Development and Evaluation of a Highly Effective Gas Particle Partitioner with Minimal Effect on the Gas Composition

Von der Fakultät für Ingenieurwissenschaften der

Universität Duisburg-Essen

zur Erlangung des akademischen Grades eines

Doktor-Ingenieurs

genehmigte Dissertation

von

Christof Asbach
aus
Essen

Referent: Prof. Dr.-Ing. Heinz Fissan
Korreferent: Prof. Dr. rer. nat. Peter Bruckmann
Tag der mündlichen Prüfung: 14. Januar 2004

Preface

Grau ist alle Theorie – wichtig ist auf'm Platz

Adi Preissler

This thesis is the result of a very nice and instructive research time during the years 2000 to 2003 at the department for Process and Aerosol Measurement Technology (AMT) of the Gerhard-Mercator-University which became part of the University Duisburg-Essen in 2003.

I wish to express my gratitude to my supervisor and mentor Prof. Dr.-Ing Heinz Fissan. His persistent support, farsighted guidance and broad scientific experience made my research work possible and highly contributed to the outcome of this work.

Further I am indebted to Dr. rer. nat. Thomas Kuhlbusch, who first introduced me to the field of aerosol technology during my "Studienarbeit" and diploma thesis. Thomas accompanied me with patience during my time at the university and supported me in countless scientific discussions and gave numerous helpful advises.

Thank you Prof. Dr. rer. nat. Peter Bruckmann for reviewing my thesis.

I wish to thank all people at the AMT who made the time here highly enjoyable. I am indebted to a number of people who contributed to the success of my work. Erik Bollow always gave useful advise concerning any computer and software issues. With Ulrich Drosten it was always nice to discuss the results of his and my experiments and the latest football matches. Heidi Giesen assisted in the administrative part. Dr. Frank Jordan helped, especially with electric field calculations. Fiete Kapitza prepared the construction drawings of the GPP for the workshop. Thank you Dr. Marcus Kennedy for numerous discussions. Christoph Kleinert always gave a helping hand for experimental set ups and two beers. With Dr. Thomas Krinke I had countless valuable discussions. His advises and reviews have always been very helpful. I want to thank Peter Müschenborn for the great time we had in the shared office. With Dr. Abhijit Roy I had numerous valuable scientific discussions, plenty of good beer and whisky and we watched several football matches (although RWO never won, when he joined). Thomas Weber was very helpful by scrutinizing many details of my work during our discussions.

I also wish to thank several people at the Institut für Energie- und Umwelttechnik (IUTA), especially Dr. Astrid John and Dr. Ulrich Quass and their students for helpful discussions and advises.

I am indebted to the mechanical workshop of the university, namely Horst Behrendt, Jens Kaminski and Hartmut Krusenbaum for manufacturing the GPP with high precision.

I thank my mother and father for their enduring encouragement and support, firstly during school, later during university time. Without my parents, I would not be in the current position.

I wish to thank my brother Dominik for preparing the photographs of the GPP in the appendix.

This way I also want to thank my friends Christiane & Holger, Thomas, Ira & Stefan, Anke & Martin, Christina & Holger and Dirk for the great time we had during the past years, wherever we were. Cheers!

Finally I wish to thank Rupprecht & Patashnick, namely Harvey Patashnick, Erich Rupprecht and Jeff Ambs, for financial support and for all good advises, especially concerning the TEOM®.

Oberhausen, March 2004 Christof Asbach

Table of Content

Figure Index

Table Index

Symbol	SI-unit	Meaning
A_c	m²	Cross section area
A_d	m²	Deposition surface area
B	s/kg	Mechanical mobility
C_c	1	Cunningham slip correction factor
c_m	kg/m³	Particle mass concentration
c_N	kg/m³	Particle number concentration
c_s	kg/s²	Spring constant
d_{ae}	m	Aerodynamic particle diameter
dr	kg	Equivalent mass change due to drift
d_t	m	Tube diameter
d_h	m	Hydraulic diameter
d_p	m	Particle diameter
E	V/m	Electric field strength
E_c	V/m	Electric field strength in a cylindrical capacitor
f	Hz	Frequency
$\bar{f}$	Hz	Average frequency
f_0	Hz	Initial frequency of the tapered element at $t = t_0$
f_1	Hz	Final frequency of the tapered element at $t = t_1$
f_{m0}	Hz	Frequency of the tapered element without filter cartridge
f_m	Hz	Frequency of the tapered element with filter cartridge
f_n	Hz	Natural Frequency of the oscillator
$\left\lvert -\Delta H_0 \right\rvert$	J	Maximum standard heat of formation of an oxide per oxygen atom for exothermic reactions
$\left\lvert -\Delta H \right\rvert$	J	Standard heat
I_i	A	Ion current
K_0	kg/s²	Spring constant of the tapered element (instrument specific)
l	m	Length
l_c	m	Length of the charging zone
l_f	m	Length of the fractionation zone
$l_{f,min}$	m	Theoretically calculated minimal length of the fractionation zone
l_{in}	m	Length of the inlet

l_{out}	m	Length of the outlet
l_{total}	m	Total length of the GPP
m	kg	Mass
$m_{A,eff}$	kg	Effective mass, determined with sensor A
$m_{B,eff}$	kg	Effective mass, determined with sensor B
m_c	kg	Mass of the filter cartridge
m_G	kg	Gaseous mass
m_p	kg	Non-volatile component of particle mass
m_{pv}	kg	(Semi-) Volatile component of particle mass
m_{real}	kg	Real airborne particle mass
m_{tf}	kg	Total mass of tapered element and filter cartridge
Δm	kg	Total mass gain of the filter during time interval Δt
n_c	1	Number of elementary charges
n_e	1	Number of free electrons
n_i	1/m³	Number concentration of ions
n_s	1	Number of free electrons at saturation charge
n_β	1/s	Impulse rate due to beta-electrons
$n_{\beta 0}$	1/s	Initial impulse rate due to beta-electrons at $t = t_0$
$n_{\beta 1}$	1/s	Final impulse rate due to beta-electrons at $t = t_1$
P	Pa	Pressure
ΔP	Pa	Pressure change
r_f	m	Radius of flow splitter
r_i	m	Radius of inner electrode
r_o	m	Radius of outer electrode
Re	1	Reynolds number
Re_{crit}	1	Critical Reynolds number
s_f	Hz/s	Average slope of the TEOM® frequency characteristic
S	A/m²	Current density
t	s	Time
t_{90}	s	Response time, until concentration or efficiency reaches 90% of final value
Δt	s	Time interval
t_r	s	Residence time
u	m/s	Velocity

$\overline{u}$	m/s	Average velocity
u_r	m/s	Radial velocity
$\overline{u}_{ti}$	m/s	Mean thermal speed of ions
u_i	m/s	Ion velocity
U	V	Voltage
U_{cor}	V	Corona voltage
U_f	V	Voltage, applied to flow splitter
U_i	V	Deflection voltage, applied to inner electrode
$\dot{V}$	m³/s	Flow rate
$\dot{V}_{Sample}$	m³/s	Sample flow rate
$\dot{V}_{Bypass}$	m³/s	Bypass flow rate
$\dot{V}_{total}$	m³/s	Total flow rate
$\dot{V}_{wash}$	m³/s	Wash flow rate
W	J	Energy
W_A	J	Activation energy
x	m	Location
z	m	Longitudinal position
Z	m²/Vs	Electrical mobility
Z_p	m²/Vs	Electrical mobility of particles
$Z_{p,\,min}$	m²/Vs	Lowest electrical mobility of particles

Greek Symbols

Symbol	SI-unit	Meaning
α	1/m	Townsend Ionisation Coefficient
α_{in}	1	Opening angle of inlet
α_{out}	1	Opening angle of outlet
α_G	1	Gas adsorption coefficient
β	1	Electron attachment coefficient
β_T	kg/K	Temperature related mass change coefficient
γ	1	Second Townsend ionisation coefficient

γ_P	kg/Pa	Pressure related mass change coefficient
δ_Φ	kg	Humidity related mass change coefficient
ε_r	1	Relative dielectric constant
ζ	V^2	Integration Constant
η	kg/ms	Dynamic fluid viscosity
η_N	1	Separation efficiency, based on number concentrations
η_m	1	Separation efficiency, based on mass concentrations
λ	m	Mean free path of gas molecules
ϑ_R	K	Room temperature
ϑ	K	Temperature
$\Delta\vartheta$	K	Temperature change
κ	1	Ratio of radii of inner and outer electrode
ν	m²/s	Kinematic viscosity
ξ	m²/kg	Extinction coefficient
ρ	As/m³	Space Charge
ρ_A	kg/m³	Density of the absorption material
ρ_P	kg/m³	Particle density
σ_G	1	Geometric standard deviation
Φ	1	Relative humidity
$\Delta\Phi$	1	Relative humidity change
φ	V	Electric potential
φ_{cor}	V	Electric potential of the corona wire
φ_i	V	Electric potential of the inner electrode

Indices

Symbol	Meaning
i	Ion
on	GPP switched on
off	GPP switched off
p	Particle

Constants

Symbol	Meaning	Value
e	Electrical elementary charge	$1.602189 \cdot 10^{-19}\ As$
k	Boltzmann constant	$1.3806 \cdot 10^{-23}\ \dfrac{AVs}{K}$
Z_i	Average electrical mobility of positively charged ions in air	$1.21 \cdot 10^{-4}\ \dfrac{m^2}{Vs}$
ε_0	Dielectric field constant	$8.854188 \cdot 10^{-12}\ \dfrac{As}{Vm}$
π	Circle constant	$3.14159265\ldots$

Chapter 1

Introduction and Motivation

The knowledge of the different parameters of airborne particles is fundamental for understanding the effect of ambient particulate matter on the climate and the health of human beings and animals. These parameters comprise e.g. number, size, surface, volume, mass, morphology or backscatter index. In order to distinguish different particle size fractions, the differentiation in total suspended particles (TSP), PM_{10}, $PM_{2.5}$ and PM_1 is widely accepted, where PM_{10} stands for all particles with aerodynamic diameters below $10\,\mu m$, $PM_{2.5}$ for particle diameters below $2.5\,\mu m$ and PM_1 for diameters below $1\,\mu m$. It has to be noted that the general definition of PM_x, as indicated in figure 1.1, only covering particles with aerodynamic diameters below $x\,\mu m$ is not strictly accurate for practical use. The value x is given by the cut-off point of standardized size selective sample inlets, i.e. impactors or cyclones. This cut off point, also called the $d_{p,50}$ is defined as the aerodynamic particle diameter where 50% of the particles get deposited in the inlet. The PM_x fractions therefore also include a small fraction of particles with diameters above the $d_{p,50}$ due to the S-shaped

Figure 1.1:   Schematic of Typical Urban Particle Mass Size Distribution
                   (John, 1993)
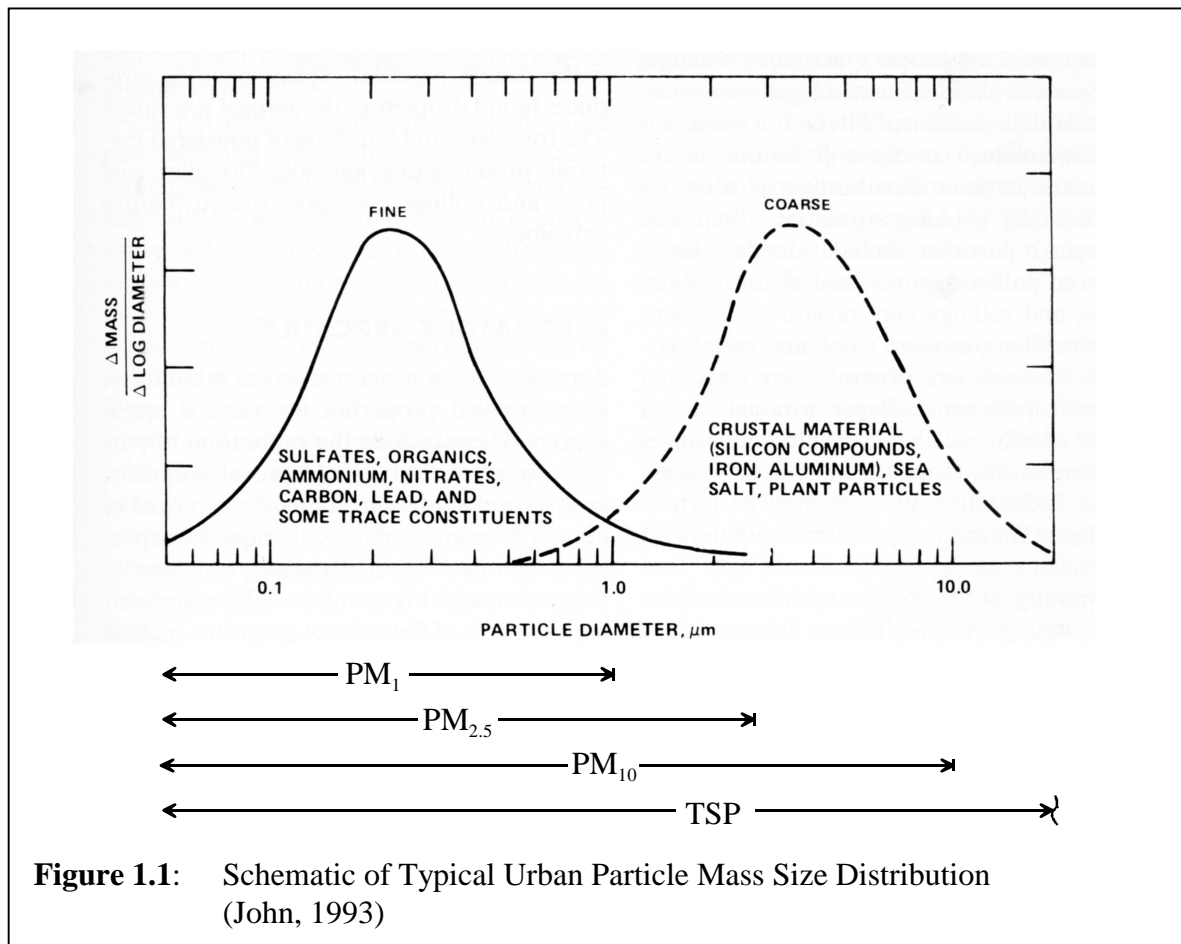
deposition curve of the inlets, (e.g. John, 2002).

The effect of airborne particles on human health has been studied by several investigators. Dockery et al. (1993) have found that air pollution with fine particulates is positively associated with death from lung cancer and cardiopulmonary disease. Schwartz et al. (1997) have found that the amount of especially particles with aerodynamic diameters below 2.5 µm, i.e. $PM_{2.5}$, is specifically related to daily mortality.

Besides the negative health effects, particles can also have an impact on the climate (Graedel and Crutzen, 1996, Hobbs and McCormick, 1988). Firstly they can scatter or adsorb the irradiation from space and therefore influence the atmosphere's albedo. Secondly they act as condensation nuclei, i.e. water in the gas phase in the vicinity of a particle condensates on the particle's surface. The formation of clouds in the atmosphere is therefore influenced by the amount of atmospheric particles.

A very common parameter to describe the amount of the particulates, suspended in the atmosphere is the particle mass concentration. Generally it is distinguished between the mass concentration of the PM_{10}, $PM_{2.5}$ and PM_1 fraction. Figure 1.1 sketches a typical bimodal urban particle mass size distributions along with the sources of the particles in the two modes.

The airborne particulate matter contains a variety of chemical species. The species can be differentiated into (semi-)volatile and non-volatile. Semi-volatile particles may sublimate at low temperature, i.e. the transition from the particle phase to the gas phase (or vice versa) can occur at ambient temperature level. The gas-particle partitioning of semi-volatile species in the atmosphere and on filters is therefore highly affected by temperature. For the measurement of ambient particle mass concentrations, it is desirable to determine the mass of all particles, non-volatile and semi-volatile.

Methods for the determination of ambient particle mass concentrations are distinguished in manual and automatic methods. Particles get deposited on a filter medium at a constant flow rate for a defined time (e.g. 12 h or 24 h) in the manual method. The average particle mass concentration is determined by pre- and post-weighing of the filter (see chapter 2.2). The manual method is accepted as reference method (e.g. DIN EN 12341, 1998) for the determination of particulate matter. Due to the long averaging time spans, manual samplers are also known as discontinuous samplers. Automatic samplers deliver data in a matter of minutes and are therefore also called continuous monitors. Commonly used continuous monitors are the Tapered Element Oscillating Micro Balance (TEOM[®]) and different versions of beta attenuation monitors. In the TEOM[®], the sample filter is fixed on a hollow oscillating tapered element. As the mass of the filter increases due to deposition of particles, the

frequency of the oscillator decreases. The frequency is recorded and the mass concentration calculated from the frequency change (see chapter 2.3.1). In a beta attenuation monitor, particles get deposited on a filter tape and the amount of deposited material is detected by the extinction of beta rays by the deposited particles (see chapter 2.3.2).

Both methods, manual and automatic, introduce changes to the particles, deposited on the sample filter (see chapter 2.4). The measured concentrations are mainly affected by the evaporation of semi-volatile particles from the sample filter. In the non-air-conditioned manual samplers, semi-volatile species can deposit in the particulate phase during a cool period, i.e. during night and morning, and evaporate during warmer periods of the day. Furuuchi et al. (2001) have found losses of semi-volatile particles from a sample filter, while the filter gets flushed with air. Witz et al. (1990) have found rapid losses of semi-volatile species from filters during storage, e.g. prior to the post-weighing of the filter.

In automatic samplers, the aerosol gets heated to a temperature above ambient level to reduce the effect of relative humidity on the measurement. Among other artefacts, this heating causes increased evaporative losses of particles from the sample filter, resulting in systematically lower mass concentrations measured by automatic than by manual samplers (e.g. Ayers et al., 1999; Williams and Bruckmann, 1999; Kuhlbusch et al., 2000).

To determine the real airborne particle mass concentration, including semi-volatile particles, two self referencing monitors, the Filter Dynamics Measurements System (FDMS) and the Differential TEOM®, have recently been developed by Rupprecht & Patashnick, Co. Inc. (Patashnick et al., 2001). The Differential TEOM® comprises a size selective inlet, a diffusion dryer to dehumidify the aerosol, a switchable electric particle remover and a TEOM® as automatic particle mass sensor. The FDMS uses a substantially similar set up, except for the particle remover which here is realized by a filter medium that can be bypassed. Both monitors can also be operated with any other automatic particle mass concentration monitor, such as a beta-gauge. As the filter, used in the FDMS system may change the thermodynamic properties of the gas which can bias the measurement, this work will only focus on the more accurate Differential TEOM®. The self referencing monitor utilizes a repeated two-step process to measure the real particle mass concentration (Asbach et al., 2003c, see also chapter 2.5). During the first step, the monitor determines the ambient particle mass concentration conventionally, i.e. including all yet unknown changes due to artefacts. In the second step, the particle remover gets switched on or the filter gets bypassed, respectively, and the mass concentration is measured while the mass sensor is operated with particle free air. Considering that the artefacts are the same during both steps, the monitor now determines

only the net effect of all artefacts, including the loss of semi-volatiles from the filter. A subtraction of the mass concentration data from both periods therefore yields to the real airborne particle mass concentration without artefacts. For a precise determination of the artefacts, the particle remover has to fulfil several requirements:

- Highly efficient separation of gas and particles

- Separation must be easily switchable

- No changes of the thermodynamic conditions of the aerosol

- The gas phase must remain substantially unaffected, otherwise chemical reactions might cause additional artefacts on the sample filter of the mass sensor

- The response time must be short compared to the duration of the two steps of the self referencing monitor

- No or low maintenance requirement

Commonly used gas particle separators are in-line filtration media or electrostatic precipitators (ESP's). Both do not fulfil the requirements. Filters introduce a pressure drop across the filter that increases with increasing filter loading and therefore change the thermodynamic properties of the aerosol and require a frequent change of the filter. As mentioned above, deposited semi-volatile material might evaporate from the filter and therefore change the gas composition. Common electrostatic precipitators use an in-line corona discharge to charge the particles and an electric field to deposit them on a precipitation electrode. It is well known from literature that corona discharge in air forms substantial amounts of ozone (e.g. Boelter et al., 1997; Chen et al., 2002) and nitrogen dioxide (e.g. Martinez and Brandvold, 1996; Griffing, 1977) that mix with the aerosol and therefore change the gas composition. A possible emission of particles by the corona may negatively affect the efficiency of an ESP. Evaporation of semi-volatile material from the precipitation electrode, which in general has direct contact to the aerosol, may also affect the gas composition of the aerosol. Further, common electrostatic precipitators require a frequent cleaning, i.e. maintenance.

The goal of this work was to develop a design for a gas-particle-separator, that fulfils all above mentioned claims. The design shall be versatile, such that the device may not only be used for the self-referencing particle mass concentration monitor, e.g. the Differential TEOM$^{®}$, but also for other applications, where an ideal gas particle separation is required.

Among others, these applications comprise pre-filtering for gas analysers to replace the commonly filter media or the artefact correction with nephelometers.

A Gas Particle Partitioner (GPP) was developed to fulfil the requirements for ideal gas particle separation based on the idea given in the patent application for the GPP. The GPP is a cylindrical set-up with inner and outer electrode. In the first section in flow direction, the particles get charged by a corona discharge, which is spatially separated from the aerosol flow. In the second section, the charged particles get deflected due to an electric field between inner and outer electrode such that the sample flow, which is withdrawn from the bottom of the GPP, is particle-free. Several measures were taken to avoid a mixing of the gases, formed by the corona with the aerosol flow.

A version of the Gas Particle Partitioner was designed and manufactured for employment in a Differential TEOM®. The realized GPP was intensively tested. The gas-particle separation efficiency was determined in the laboratory with defined monodisperse fine and coarse particles. The influence of the corona on the gas composition of the aerosol was investigated by measuring the ozone and nitrogen dioxide concentrations downstream of the GPP under different conditions. Since soiling inside the GPP is minimized and does not affect the sample flow, the maintenance requirement is mainly dominated by the lifetime of the corona wire. The lifetime of the wire was therefore investigated under realistic conditions to determine the optimal wire material.

The design of the GPP can be modified to match the requirements for applications, other than the Differential TEOM®. Currently discussed applications are a GPP for supplying the manifold for gas analysers and a GPP for implementation in a modified Differential TEOM® where the GPP is operated with lower flow rates.

Chapter 2

Background of Techniques for the Gas Particle Separation and Particle Mass Concentration Measurements

2.1 Common Gas-Particle-Separation Techniques

2.1.1 Filtration

Filtration is the most common process for separation of gas and particles. It is a simple, versatile and, in low dust concentrations, a highly economic mean for cleaning gases. Filtration is used in many different applications such as clean rooms, respiratory protection, particle sampling (see chapter 2.2) and cleaning of flue gases. Three different types of filter media are used: fibrous filters, porous membrane filters and fabric filters. All three filter types achieve a high efficiency for particles down to the sub-micrometer size range. Though all three filter types show an initial pressure drop across the filter medium, which increases with increasing filter loading. Therefore the filter media need to be replaced when a certain filter loading threshold is exceeded.

Five different mechanisms can lead to the deposition of a particle in a filter (Hinds, 1982):
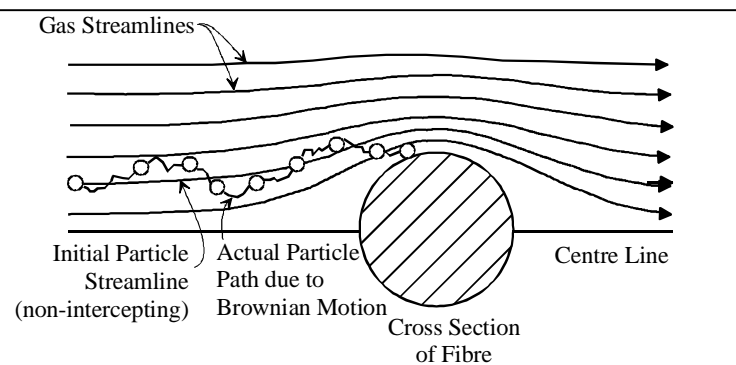
Figure 2.1.1a: Deposition due to Diffusion
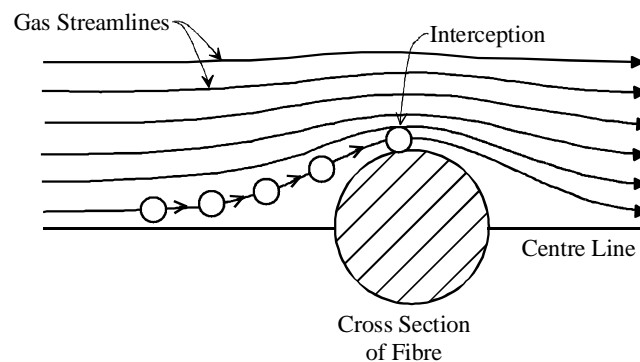
Figure 2.1.1b: Deposition due to Interception
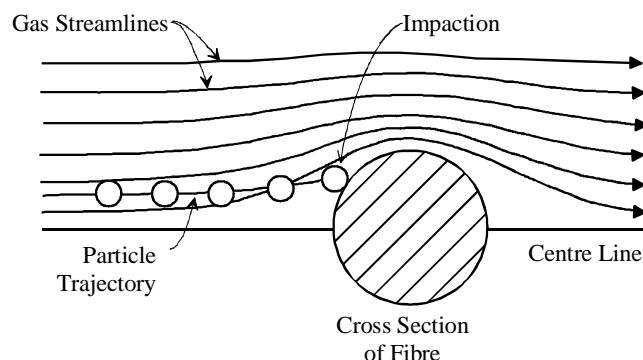
Figure 2.1.1c: Deposition due to Impaction (Hinds, 1982)

1. Diffusion
2. Inertial Impaction
3. Interception
4. Gravitational Settling
5. Electrostatic Attraction

The first three mentioned mechanisms are predominant in filters. Generally, gravitational settling can be neglected whereas electrostatic attraction becomes a major mechanism for the deposition of particles, only when an electric field is applied to the filter (Jordan, 2001). For a better understanding, the three dominant mechanisms are described for deposition on a single fibre (Hinds, 1982):

1. *Diffusion* is understood as the random motion of particles due to the collision with gas molecules. The Brownian motion of the molecules leads to a non-straight trajectory of the particles (figure 2.1.1a). As interaction with gas molecules is only applicable for particles with low inertia, diffusion is the predominant mechanism for particle sizes in the nanometer range.

2. Particle deposition due to *interception* occurs, when a particle follows a gas streamline with a minimal distance to the fibre surface less than the particle radius. The particle then collides with the fibre and is captured on its surface because of its finite size (figure 2.1.1 b). Interception is applicable for the intermediate size range between diffusion and impaction.

3. *Inertial impaction* occurs, when a particle is not able to follow a streamline around the fibre, but departs from its original streamline due to inertia (figure 2.1.1 c). Therefore, impaction is mainly applicable for large, inertial particles in the super-micrometer range. However, for high gas velocities, impaction is also be applicable for smaller particles.

2.1.2 Electrostatic Precipitation

Electrostatic Precipitation is understood as the removal of solid particles or liquid droplets from the gas in which they are suspended. The motion, necessary for the precipitation of the particles is enforced by Coulomb forces on electrically charged particles in an electric field within an electrode system. Although the term *electrostatic* is open to criticism, as the drift of the gaseous ions and the charged particles in the electric field form a current and therefore is not static, the expression *Electrostatic Precipitation* is widely accepted for this process. Therefore, although knowing that the term is not strictly accurate, the process of electrically removing particles from a gas will be referred to as *Electrostatic Precipitation* or *Electrostatic Separation* in this work.

Electrostatic Precipitators (ESP's) are widely used in e.g. scientific and industrial applications. In the scientific field, they are used to either clean a gas stream or for a well directed deposition of the suspended particles, whereas in the industrial area, ESP's are mainly used for cleaning of flue gases. Air cleaning ESP's usually include a corona discharge section to electrically charge the particles. To form the corona, a high voltage is applied to either one or more thin wire(s) or to on or more sharp tip(s). Most commonly used designs for air cleaning ESP's are: wire-tube, (multi-) wire-plate, (multi-) wire-duct and point to plane. These ESP's reach efficiencies of almost 100% with no or minimal changes
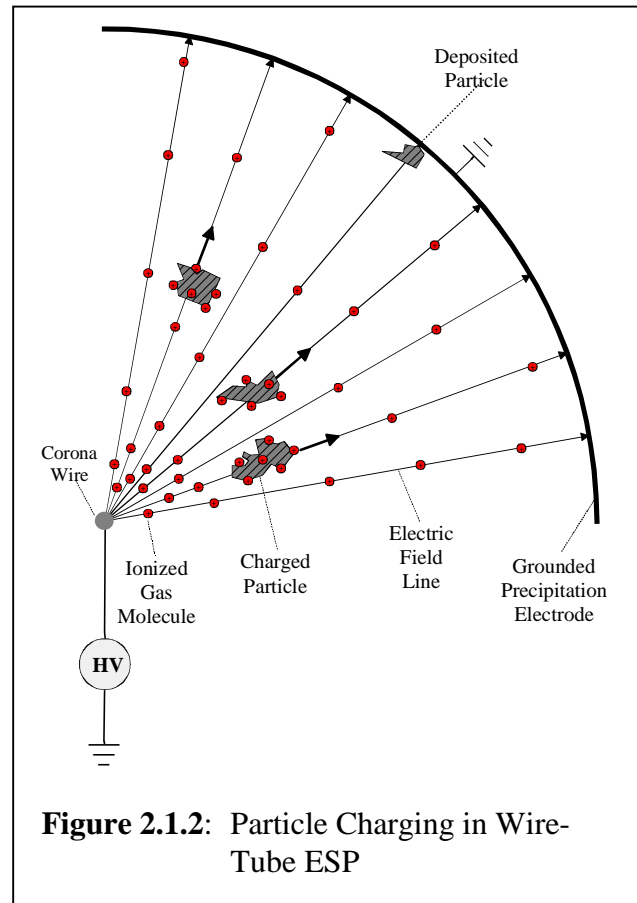
Figure 2.1.2: Particle Charging in Wire-Tube ESP

of the thermodynamic conditions, such as pressure, temperature and humidity. Due to the corona discharge, gases, such as Ozone (O_3) and Oxides of Nitrogen (NO_x), are formed (Viner et al., 1992; Martinez et al., 1996; Boelter et al., 1997) and mix with the aerosol's gas phase. Thus the corona discharge changes the gas composition of the aerosol which in some applications can be detrimental (see also chapter 2.4).The corona discharge is created by applying a high voltage to either a very thin wire or a sharp tip which is directed towards the grounded precipitation electrode, which can be a tube, plate or a duct (see chapter 3.2).The electric field strength is extremely high near the surface of the wire or tip, causing gas molecules to ionise. Due to the electric field between corona and grounded precipitation electrode, the ions are accelerated towards the precipitation electrode. On their way they collide with particles and are retained on their surface and thus electrically charge them. The process is sketched in figure 2.1.2 for a wire-tube ESP.

Two different processes lead to the collision of ions and particles: diffusion and field charging. The diffusion charging is caused by random collisions of ions and particles due to their Brownian motion (Hinds, 1982). Therefore, diffusion charging is dominant for small particles (see chapter 3.3.1). Field charging occurs due to the fact that an uncharged particle distorts the electrical field such that the field lines in the vicinity of the particle terminate on

the particle surface (see chapter 3.3.2). As the field lines are equal to the ions' trajectories, the ions are forced to fall into the particle surface. Thus, field charging is dominant for larger particles. The transition from the dominance of diffusion charging to field charging is at a particle diameter of approx. $d_p \approx 300$ nm depending on the electric field strength (Hinds, 1982). A more detailed description of the charging process is given in chapter 3.3.

2.1.3 Other Gas-Particle-Separation Techniques

Other techniques for the separation of gas and particles, such as thermal precipitators, Venturi scrubbers or cyclones are used in scientific and industrial applications. Thermal precipitators use the thermophoretic motion of particles in a temperature gradient to separate particles from a gas. Due to the difficulties of maintaining a stable temperature gradient, the sampling rate of thermal precipitators is rather low. They are mainly used in scientific applications for sampling small particle quantities, e.g. for analysis with light or electron microscopes (Hinds, 1982). Venturi scrubbers are used to clean flue gases from industrial processes, such as the combustion emissions in power plants. In a Venturi scrubber, a scrubbing liquid is introduced into the flue gas flow to wash out particles and for desulphurisation (Singer, 1982). Cyclones are widely used in both, scientific and industrial processes. In cyclones the particle removal is achieved by centrifugal, inertial, and gravitational forces developed in a vortex separator. In scientific applications they are mainly used as pre-selector for the determination of particle concentrations, i.e. to separate all particles above a certain particle diameter from the sample flow (e.g. Marple et al., 1993). In industrial processes they are mainly applied for deposition of large particles prior to the main emission control system (Singer, 1982). In all aforementioned applications, a particle chopping capability is not required.

However, the GPP is designed for separating all particles from a gas without affecting the thermodynamic conditions, such as pressure, temperature or relative humidity. Since the aforementioned techniques for gas-particle separation either change the thermodynamic conditions of the aerosol (Venturi scrubber, thermal precipitator) or only reach low collection efficiency (cyclone), they cannot be considered to be comparable to the GPP. A more detailed description of Gas-Particle-Separation mechanisms, other than filtration and electrostatic precipitation is therefore not given in this work.

2.2   Discontinuous Manual Samplers for Determination of Ambient Particle Mass Concentrations

The manual method is acknowledged as reference method for the determination of particle mass concentrations. It is based on deposition of ambient particles on mainly fibrous filter

media during a well known time period Δt (usually 12 h or 24 h) at a known flow rate $\dot{V}_{Sample}$. The mass gain Δm of the filter is determined by pre- and post-weighing of the filter. The average mass concentration during the sample time period Δt can then be expressed as:

$$c_m = \frac{\Delta m}{\dot{V}_{Sample} \cdot \Delta t} \qquad \text{(eq. 2.2.1)}$$

German reference samplers for manual determination of ambient PM_{10} particle mass concentrations have to comply with the standard DIN EN 12341 (1998). According to the standard, a reference sampler must be equipped with a standardized PM_{10} sample inlet, directly connected to the sample filter holder, followed by a volume flow control unit. A new European standard for manual sampling of $PM_{2.5}$ is currently being discussed.

The total particle mass, collected on the filter must be determined gravimetrically. The filters need to be equilibrated for 48 h in a defined standard atmosphere, i.e. at room temperature $\vartheta_R = 20°C \pm 1°C$ and relative humidity $\Phi = 50\% \pm 5\%$, prior to pre- and post- weighing.

Since during sampling, the filter is exposed to diurnally varying temperature and pressure conditions, volatilisation of semi-volatile material (e.g. Zhang and McMurry, 1991) can bias the results of the reference method. Witz et al. (1990) have also found significant losses of particulate Nitrate, Chloride and Ammonium during storage. The retention of gaseous ammonium, sulphate and organic carbon can also result in positive artefacts (Appel, 1993). A more detailed description of artefacts in the determination of particle mass concentration is given in chapter 2.4.

2.3 Continuous Online Monitors for Measurement of Ambient Particle Mass Concentrations

Continuous monitors for the determination of ambient particle mass concentrations (also called automatic or online monitors or samplers) are widely used in air quality supervision stations around the world. Compared to manual sampling, automatic sampling offers several advantages. Firstly, it delivers data with a high time resolution in almost real-time, e.g. the currently airborne particle mass concentration data is available within a matter of minutes (depending on the averaging time span) and can be plotted as diurnal variation. Secondly, the service demand is lower with automatic samplers, since the mass of the deposited particles on the internal filter media is determined continuously and the filter does not need to be replaced and handled as often as with the manual method, i.e. every 12 or 24 hours.

To overcome the problem of meteorological influences, such as fluctuation of relative humidity and ambient temperature, on the automatic sampler the aerosol inside automatic samplers gets heated to a temperature above the ambient temperature level. The elevated temperature causes an increased volatilisation of semi-volatile material from the sample filter, resulting in lower mass concentrations being measured with automatic samplers than with manual samplers. Other artefacts, such as gas phase adsorption or desorption or a drift of the sensor may also affect the output of automatic samplers (see chapter 2.4).

Most commonly used continuous monitors for the determination of ambient particle mass concentrations are the Tapered Element Oscillating Microbalance (TEOM[®1], chapter 2.3.1) and different versions of beta-attenuation monitors (also called beta-gauges, chapter 2.3.2).

2.3.1 The Tapered Element Oscillating Microbalance (TEOM[®])

The TEOM[®] is an inertial instrument for continuous measurement of ambient particle mass concentrations. It mainly consists of three components: a size selective inlet with e.g. PM_{10} or $PM_{2.5}$ characteristic, a sensor unit and a control unit. The TEOM[®] set up is shown in figure 2.3.1 .

For measurements of particulate matter with particle diameters below 10 µm (PM_{10}) an impactor, is used as size selective inlet. The impactor is essentially identical to the widely used and US EPA approved Sierra Andersen SA246b inlet (D.W. van Osdel, 1991). For particle diameters below 2.5 µm ($PM_{2.5}$) an additional sharp cut cyclone can be mounted downstream of the impactor (Kenny, 1998). Both inlets operate at a flow rate of 16.67 l/min, i.e. 1 m³/h. Since the flow rate of the inlet is higher than the sensor flow of the TEOM[®], the total flow of 16.67 l/min is split into the 3 l/min sample flow and a 13.67 l/min bypass flow.

In the sensor unit, the air is continuously drawn through a filter, which is located in an exchangeable filter cartridge on the
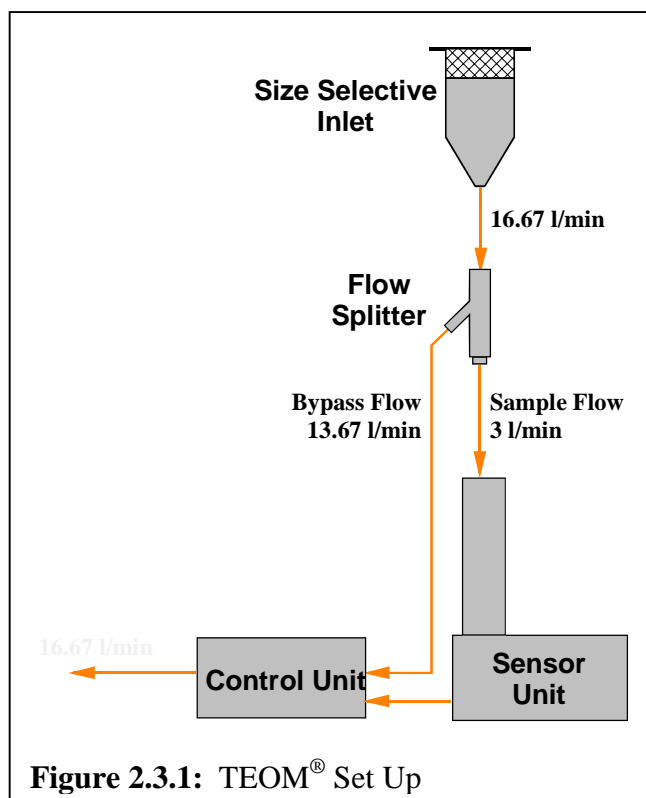
Figure 2.3.1: TEOM[®] Set Up

---

[1] TEOM[®] is a registered trademark of Rupprecht & Patashnick Co., Inc.

top end of a tapered element. The tapered element is a hollow tube, clamped on one end and free to vibrate on the other (see figure 2.3.2). The oscillation of the tapered element is excited with a constant energy, causing the system, containing the tapered element and the filter cartridge, to vibrate precisely at its natural frequency f_n, if the total mass remains constant. The system can be compared to a spring-mass system with the natural frequency f_n:

$$f_n = \sqrt{\frac{c_s}{m}}$$

(eq. 2.3.1)

where c_s is the spring constant and m the mass of the system. The natural frequency of the tapered element is different for each single device and ranges from approx. 200 Hz and 300 Hz. As the mass of the spring-mass system, i.e. of the tapered element with filter increases, the total mass gain Δm can be expressed as (Patashnick et al, 1991):

$$\Delta m = K_0 \left(\frac{1}{f_1^2} - \frac{1}{f_0^2} \right)$$

(eq. 2.3.2).

The spring constant K_0 of the tapered element can therefore be determined by measuring the oscillation frequency f_{m0} without and f_m with filter cartridge of know mass m_c as

$$K_0 = \frac{m_c}{\left(\dfrac{1}{f_m^2} - \dfrac{1}{f_{m0}^2} \right)}$$

(eq. 2.3.3).

During normal operation, the mass gain of the system is only due to deposition of particles on the sample filter. The particle mass, deposited during time interval Δt can be expressed by equation 2.3.2, where f_0 is the oscillation frequency at time t_0 and f_1 is the frequency at time $t_1 > t_0$. The average mass concentration c_m during the time interval $\Delta t = t_1 - t_0$ can be derived from equation 2.2.1.

The time resolution is theoretically only limited by the resolution of the frequency recording, which in the TEOM® is 2 seconds. In practice, a noise frequency, which is not
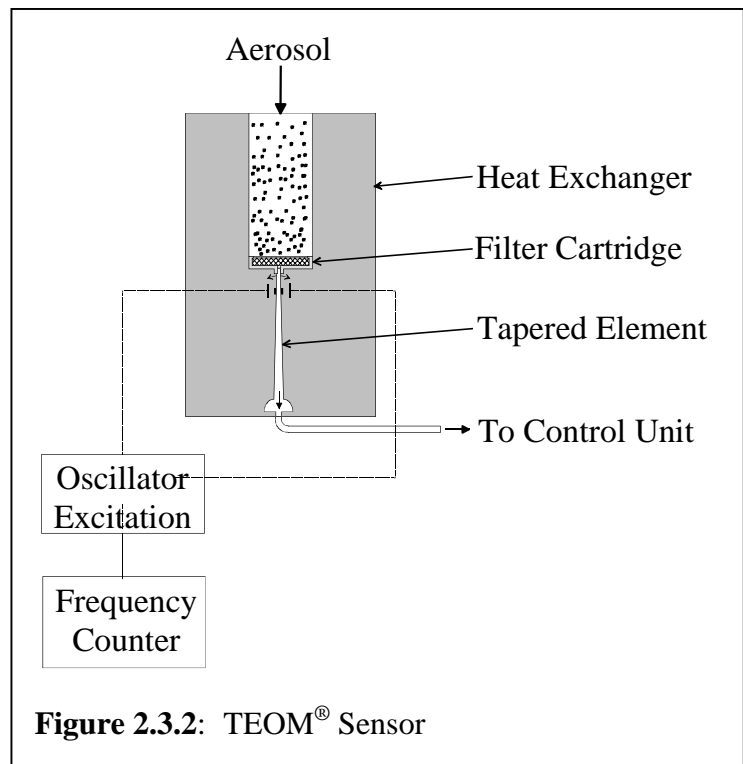
Figure 2.3.2: TEOM® Sensor

related to the mass gain of the filter, is superposed to the oscillation of the tapered element. Since the noise creates a balance of positive and negative artefacts, it can be eliminated by averaging over longer time intervals. For regulatory measurements, the averaging time interval is usually set to 5 minutes or longer.

To reduce the effect of fluctuating ambient relative humidity and temperature on the measurement, the aerosol upstream of the sensor, and the sensor compartment are heated and maintained at a constant temperature (generally 40°C or 50°C) above ambient level. The elevated temperature causes enhanced evaporation of semi-volatile particles. Therefore, in

Figure 2.3.3: Comparison of TEOM and Manual Sampler for a Rural (Spellen) and an Urban Background Site (Oberhausen), Without (top) and With (Bottom) Correction of Semi-Volatile Material (Kuhlbusch et al., 2000)
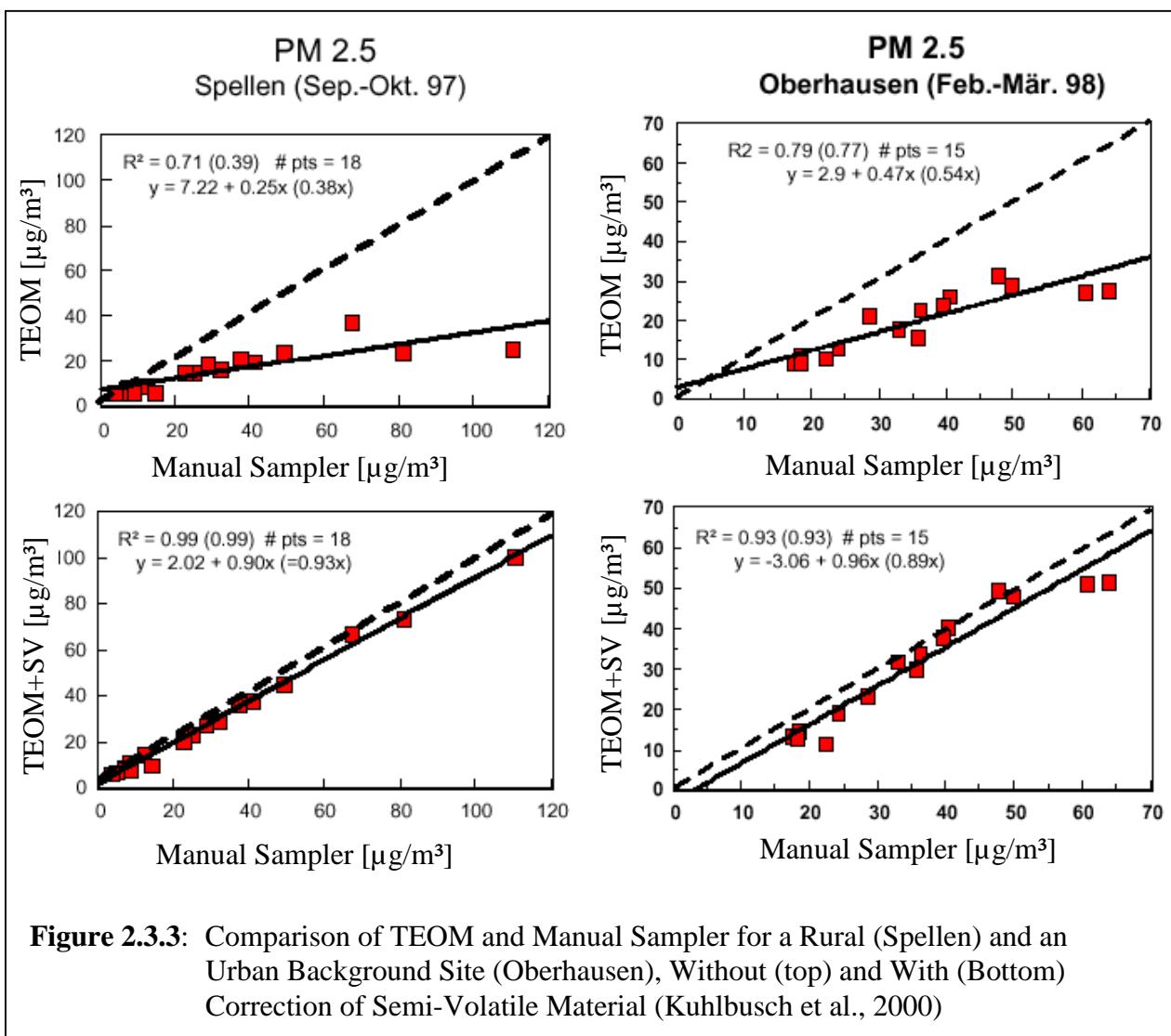
presence of particulate semi-volatile material in the atmosphere, the TEOM[®] measures lower particle mass concentrations than actually airborne (Ayers et al., 1999; Williams and Bruckmann, 2002) . In figure 2.3.3, the mass concentrations, measured with a TEOM[®] at an operating temperature of 50°C are plotted versus the mass concentrations, obtained with

manual samplers for a rural site in Voerde-Spellen, and an urban background site in Oberhausen. It can be seen that in both cases the TEOM® mass concentrations are significantly lower than those from the reference method (upper graphs). As the major components of semi-volatile material in the atmosphere are Ammonium Nitrate (NH_4NO_3) and Ammonium Chloride (NH_4Cl) the amount of sampled NH_4^+, NO_3^- and Cl^- were chemically analysed from the filters of the manual samplers and their sum added to the mass concentrations, measured with the TEOMs (lower graphs). It can be seen that the corrected TEOM data now almost match the data from the manual samplers. A more detailed description of the discrepancies between the measured data from automatic and manual samplers is given in chapter 2.4.

2.3.1.1   Sample Equilibration System

During normal operation, the TEOM® operates at an elevated temperature to reduce the effect of relative humidity on the sensor. Due to the high temperature, semi-volatile material can evaporate from the sample filter, resulting in mass concentrations lower than ambient being measured with TEOM's. One approach to overcome the discrepancies in the mass concentrations, measured with the manual method and the TEOM® is the use of a Nafion® diffusion dryer, called SES (Sample Equilibration System) upstream of the sensor (Rupprecht & Patashnick, 2000). When the SES is installed in the TEOM® set up as shown in figure 2.3.4, it allows the mass collected on the filter to equilibrate more rapidly than in the presence of high relative humidity levels. Due to the decreased humidity, the TEOM® can operate at a temperature slightly above ambient temperature, e.g. at 30°C.

Figure 2.3.4: TEOM® Set Up with SES
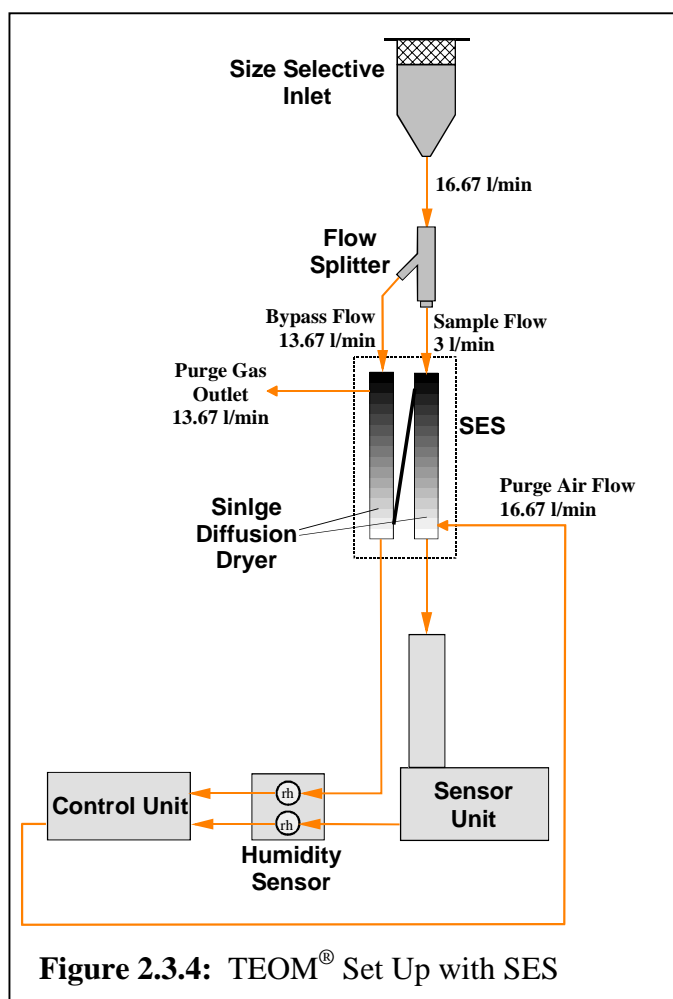
The diffusion dryer utilizes a bundle of Nafion® tubes inside a stainless steel tube. Sample inlet and outlet are designed such that the sample flow is transported through the interior of the Nafion® tubes, while the exterior of the Nafion® tubes gets flushed by a purge gas in counter flow direction. Nafion® is a Teflon® material with occasional side chains of another fluorocarbon called a sulfonic acid group. It is the sulfonic acid group's high affinity to water that allows Nafion® dryers to function. The driving force for the reaction inside the Nafion® dryer is the difference in water vapour content between the sample and the purge gas streams. When water strikes an exposed sulfonic acid group on the surface of the Nafion® dryer tube, the water is initially bound. Additional sulfonic acid groups deeper in the wall of the tubing have less water attached to them, and consequently a higher affinity to water. Water molecules absorbed onto the surface of the tubing are therefore quickly passed on to the underlying sulfonic acid groups until the water reaches the opposite side. This process continues until the vapour pressure gradient across the tubing wall is eliminated. If a dry purge gas flows over the exterior surface of the Nafion® tubing, water vapour will be continuously extracted from the sample gas stream inside the tubing.

Figure 2.3.5: Mass Concentration Measured with SES Equipped TEOM® Versus Reference Method (courtesy: Rupprecht & Patashnick Co., Inc.)
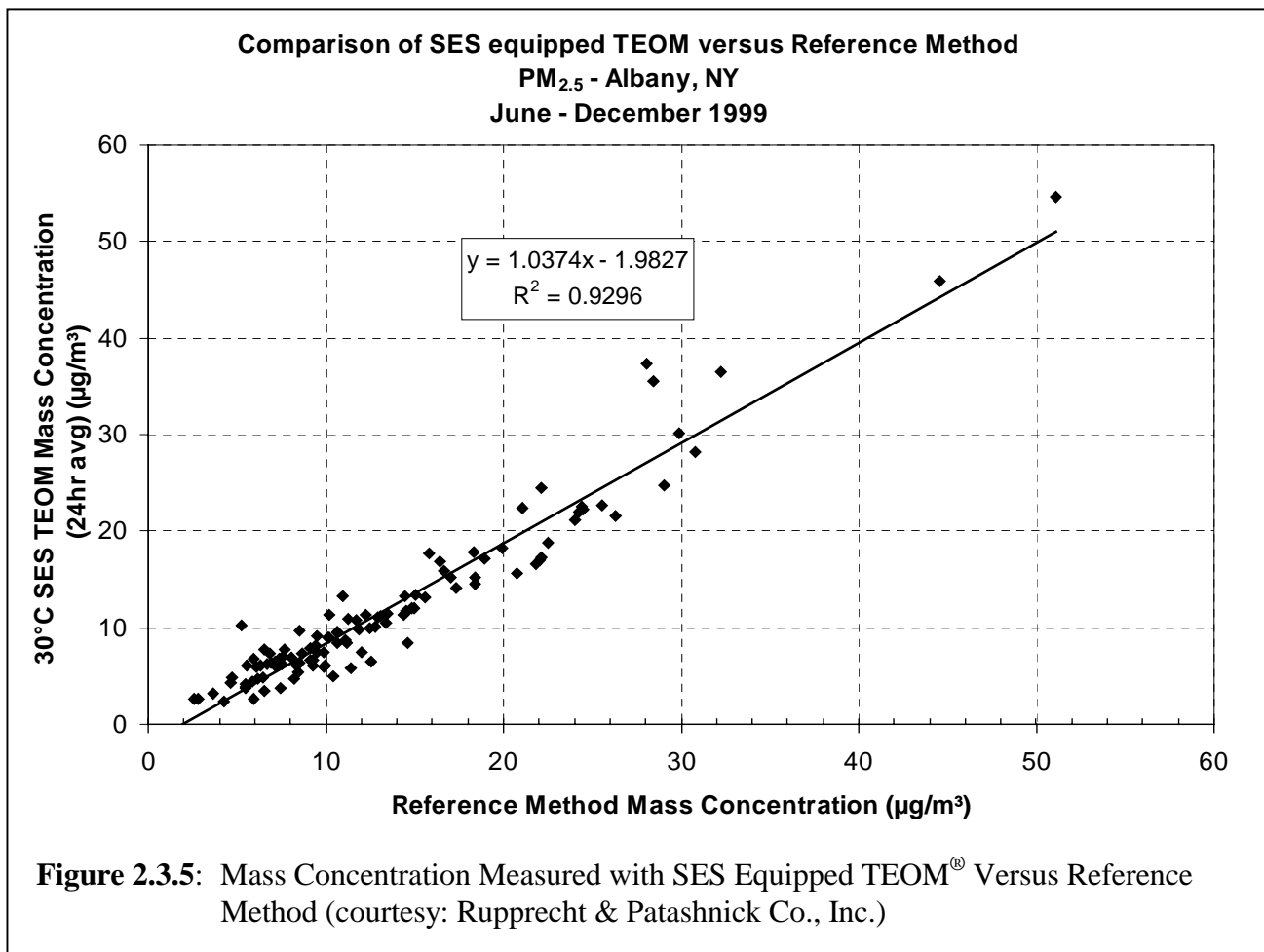
As shown in figure 2.3.5, the SES along with the lower sampling temperature is able to reduce the losses due to evaporation of semi-volatile particles from the filter effectively. Although, in both cases artefacts are most likely still present, i.e. the measured mass concentrations do not accurately represent the real airborne particle mass concentrations for both, manual sampling and SES equipped TEOM (see chapter 2.4).

2.3.2 The Beta Attenuation Monitor

The beta attenuation monitor (also called beta gauge) uses the absorption of beta rays (electrons) by particles, collected on a filter (Williams et al., 1993). Inside the monitor, the beta rays are emitted by a radioactive source. Commonly used sources are the carbon isotope ^{14}C and Krypton (^{85}Kr).

The aerosol is drawn through a sample inlet, which might be size selective, such as an impactor or a cyclone. From there it is transported to the filter medium, where the particles are deposited on a small spot (see figure 2.3.6). As filter medium, a filter tape (similar to a tape used in an audio tape recorder) is used that is moved stepwise to create a new deposition spot, once the current spot reaches the default filter loading threshold. The radioactive source and a Geiger-Müller-Counter are located on two opposite sides of the deposition spot. The Geiger-Müller-Counter counts impulses of incoming beta-electrons. Due to the absorption of beta rays by the particles, the impulse rate n_β decreases as the mass of deposited particles on the filter increases. Considering a homogenous distribution of the particles on the filter medium, the law of Lambert-Beer (eq.2.3.5) can be used (e.g. Gebhart, 1993).

1 Sample Inlet
2 Tube Heating
3 Beta Source
4 Geiger-Müller-Counter
5 Filter Housing
6 Microprocessor, Data Evaluation
7 Filter Tape
8 Mass Flow Controller
9 Vacuum Pump
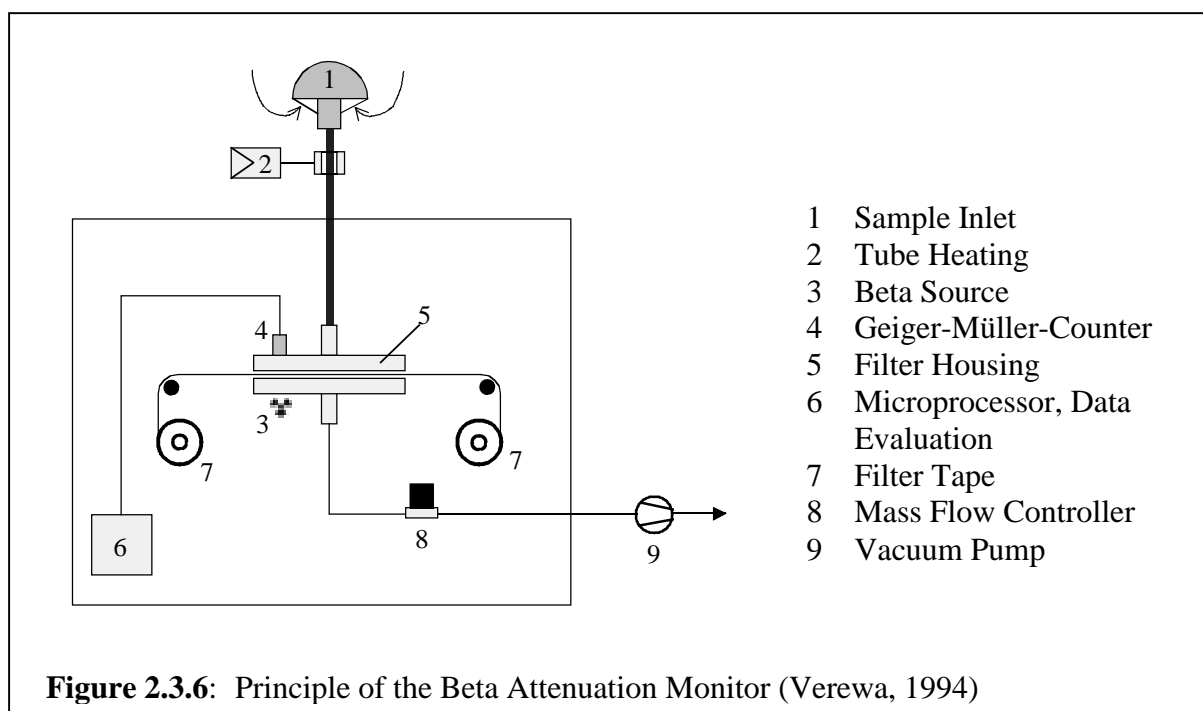
Figure 2.3.6: Principle of the Beta Attenuation Monitor (Verewa, 1994)

$$\ln\left(\frac{n_{\beta 0}}{n_{\beta 1}}\right) = \xi \cdot \frac{\Delta m}{A_d}$$ (eq. 2.3.4)

Where ξ is the extinction coefficient and A_d is the surface area of the deposition spot. Along with equation 2.2.1 the average mass concentration c_m during a time interval Δt can be expressed as

$$c_m = \frac{A_d \cdot \ln\left(\dfrac{n_{\beta 0}}{n_{1\beta}}\right)}{\xi \cdot \dot{V}_{Sample} \cdot \Delta t}$$ (eq. 2.3.5).

2.4 Artefacts in Particle Mass Measurements and Resulting Discrepancies of Measured Data From Discontinuous and Continuous Particle Mass Concentration Samplers

2.4.1 Artefacts in Particle Mass Concentration Measurements

Different artefacts can bias the measurement of ambient particulate mass concentrations with both, manual (Pang et al., 2002) and automatic samplers (Chang et al., 2001; Ayers et al., 1999; Salter et al., 1999; Pang et al. 2002). The main filter-influencing factors can be differentiated into:

- Influence of ambient relative humidity on particle size distribution and particle mass
- Evaporation of particulate semi-volatile material from the sample filter
- Adsorption of semi-volatile material in the gas phase during sampling
- Chemical reactions on the sample filter during sampling

Further, the sensor of an automatic samplers itself can be affected, by changing thermodynamic properties, e.g. temperature or pressure.

Influence of Ambient Relative Humidity on the Particle Size Distribution and Particle Mass

Relative humidity is a determining factor, influencing the size and mass of especially hygroscopic particles (Horodecki, 1999). Fine particles with diameters below 2.5 µm and especially below 1 µm are extremely prone to this effect. Due to their chemical composition, these particles generally show a higher hygroscopicity than mechanically produced large particles.

The particle mass change due to relative humidity is shown for ammonium nitrate particles in figure 2.4.1 and for sodium chloride particles in figure 2.4.2. In both cases, the particles were deposited on a sample filter, which was exposed to different relative humidity levels. A

hysteresis can be observed for both substances, i.e. the deliquescence point during increasing relative humidity is different from the point of recrystillization during decreasing humidity (Horodecki, 1999; Winkler and Junge, 1970). The mass of hydroscopic particles is therefore not only affected by the current humidity level but also by its history. Table 2.4.1 gives an overview of the deliquescence points for selected compounds.

Figure 2.4.1: Particle Mass Change of Ammonium Nitrate with Relative Humidity (Horodecki, 1999)
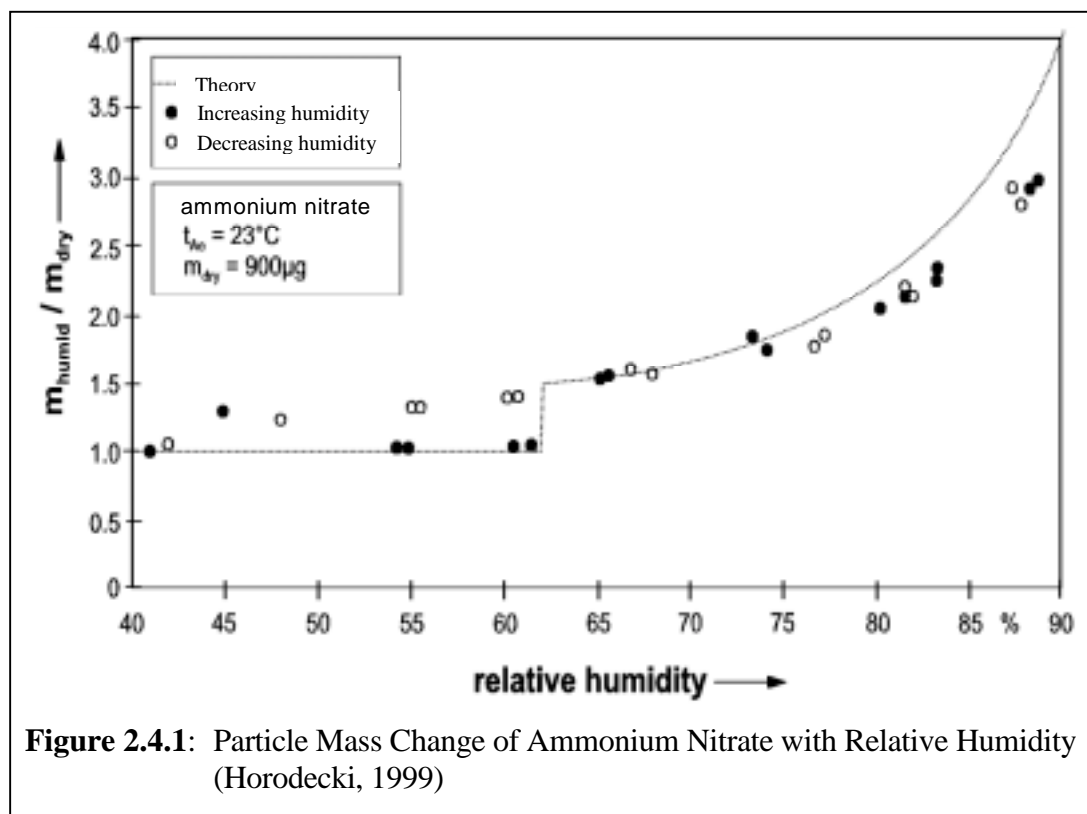
Table 2.4.1:   Points of deliquescence (p_d) for selected compounds

Substance	r.H. at p_d	Reference
NaCl	75%	Robinson and Stokes, 1955
$MgCl_2$	33%	Winkler, 1973
$(NH_4)_2SO_4$	80%	Winkler, 1973
$(NH_4)NO_3$	63%	Horodecki, 1999
Ambient Aerosols	none	Winkler, 1973

To reduce the effect of relative humidity and thus moisture on the measured particle mass, it may be advisable to reduce the relative humidity for equilibration of the sample filter to 30%. Besides the overestimation of the particle mass due to the water content of the particles, high relative humidity can also result in a negative artefact, if the size of a particle grows to a value above the cut-off diameter of the size selective inlet of the sampler.

Figure 2.4.2: Particle Mass Change of Sodium Chloride with Relative Humidity (Horodecki, 1999)
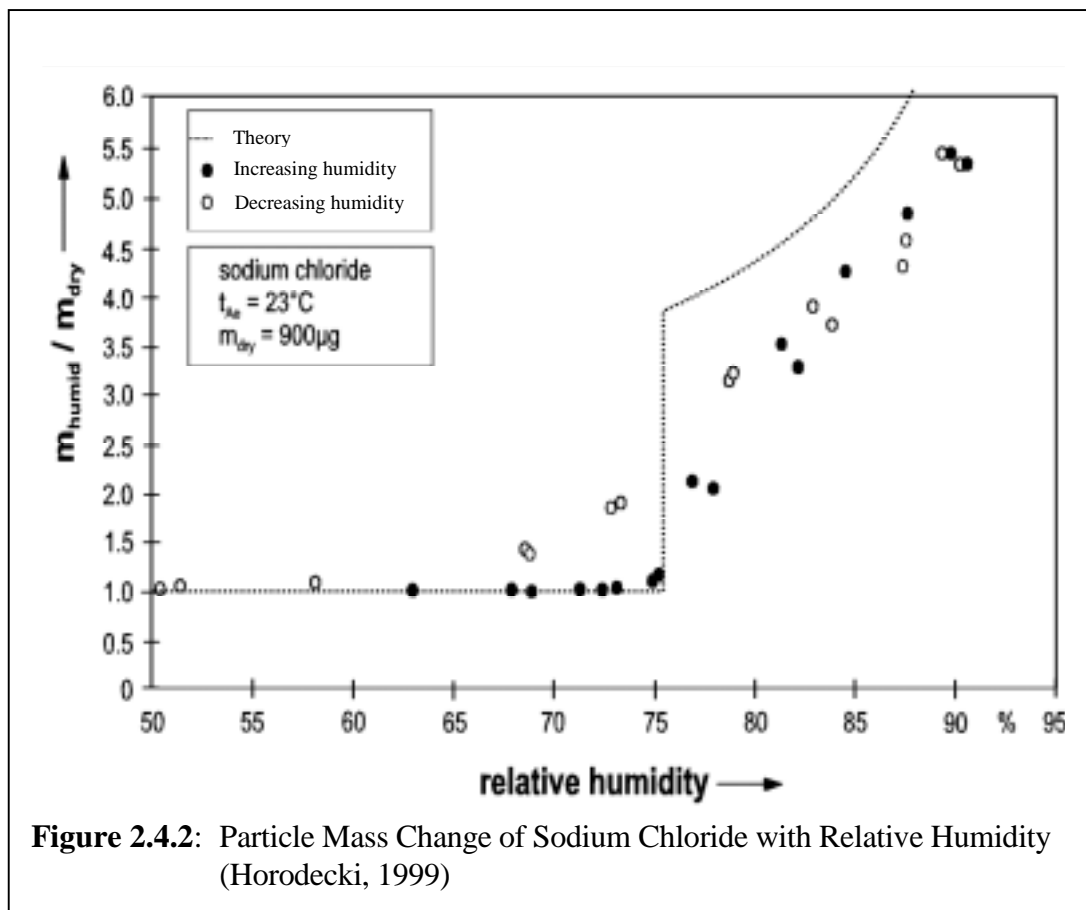
Evaporation of Particulate Semi-Volatile Material From the Sample Filter

The particles in the atmosphere can be differentiated into non-volatile and (semi-)volatile. Semi-volatile species sublimate at temperature in the ambient temperature range and may therefore be captured on sample filter in the particle phase but evaporate from the filter during sampling. The main semi-volatile species in the atmosphere are ammonium nitrate $(NH_4)NO_3$ and ammonium chloride $(NH_4)Cl$. The losses of semi-volatile material from sample filters have been investigated and discussed by several investigators. Furuuchi et al. (2001) have found significant losses of semi-volatile particulate matter from a sample filter, flushed with clean air. Witz et al. (1990) have studied the losses of semi-volatile substances during storage of loaded fibre filters. They found rapid and substantial losses of particulate nitrate, chloride and ammonium from the sample filter of 19%, 65% and 51%, respectively during storage periods of one week. Zhang and McMurry (1991) showed the nearly complete evaporative loss of fine particulate nitrate from Teflon filters during sampling. The latter was confirmed by Chow et al. (1994). They showed that the losses of nitrate during manual sampling were temperature dependent with highest losses during summer days and lowest during winter nights.

Tsai and Perng (1998) studied the sampling and weighing artefacts of ionic species, using a high-volume manual sampler (HV), a dichotomous sampler (DC) and two annular denuder systems (ADS). They found significantly lower amounts of ionic ammonium, nitrate and chloride on the sample filters than measured with the denuders for both PM_{10} and $PM_{2.5}$. Their results are summarized in table 2.4.2.

Table 2.4.2: Volatilisation Losses of Ionic Species (Tsang and Perng, 1998)

Substance	PM^{HV}_{10} % of ADS	PM^{DC}_{10} % of ADS	$PM^{DC}_{2.5}$ % of ADS
NO_3^-	-16	-21	-21
NH_4^+	-17	-21	-18
Cl^-	-24	-32	-54

Horodecki (1999) has studied the evaporation behaviour of semi-volatile particles, deposited on a filter. Figure 2.4.3 shows his results, concerning the change in mass loading of ammonium nitrate on a filter at 50°C and relative humidity below 5%, standardized to the initial mass M_0. It can be seen that the initial relative loss in particle mass is linear with time and independent from the total loading of the filter. A clear change towards lower loss rates at lower total mass of the filter can be observed as well.

An increase in pressure drop across a sample filter during sampling can also promote volatilisation artefacts, if enough particulate matter is collected (Van Vaeck, 1984).

Figure 2.4.3: Particle Mass Change of Deposited Ammonium Nitrate With Time (Horodecki, 1999)
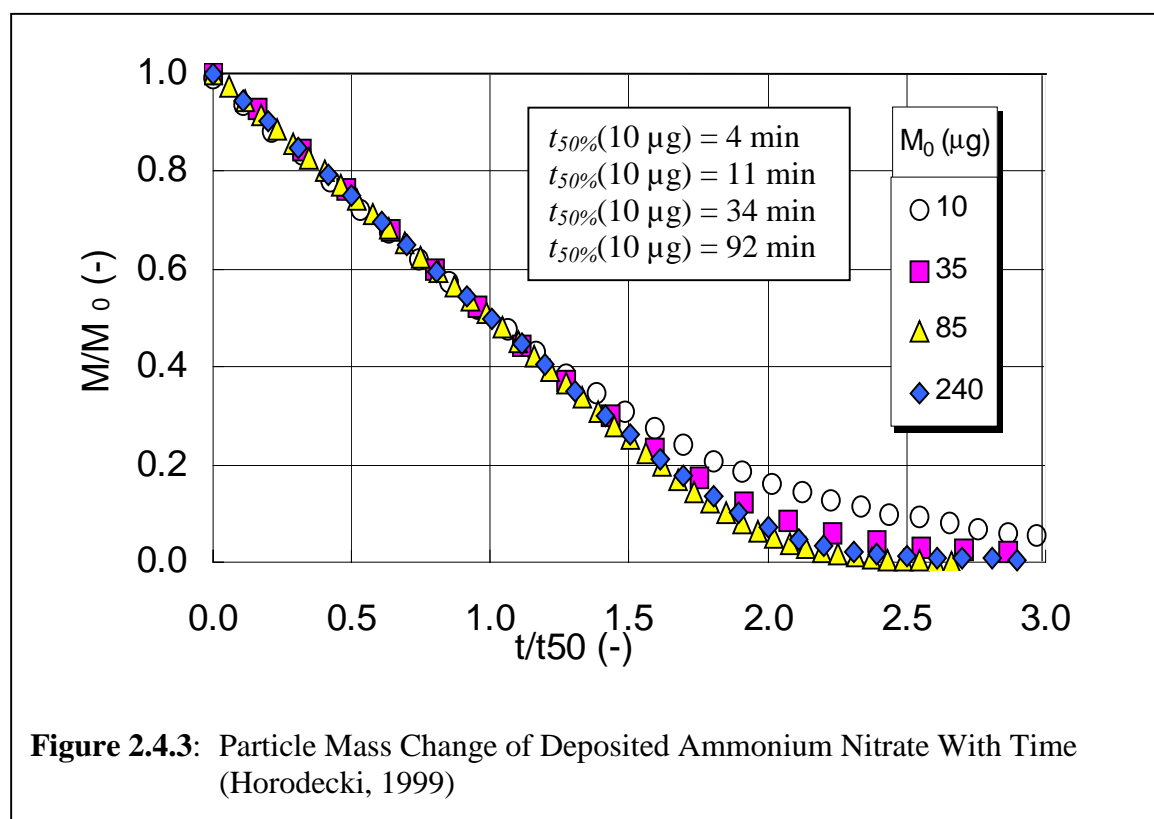
Adsorption of Semi-Volatile Material in the Gas Phase During Sampling

The latter findings give rise to the question of the importance of condensation of semi-volatile material in the gas phase on the sample filter. From the amount of semi-volatile organic compounds in the atmosphere, it can be estimated that a significant amount of these compounds can be adsorbed on sample filters and bias the measurement result.

The compounds, being adsorbed are dependent on the filter media used for filtration. Lipfert (1994) has found that if nitric acid is present at a sampling location, it can deposit on Teflon filters and cause small weight gains in proportion to the amount of nitric acid present in the atmosphere.

However, no further detailed information on the influence of the filter material on adsorption or desorption processes could be found in the literature.

Chemical Reactions on the Sample Filter During Sampling

Chemical reactions on the filter during sampling and equilibration may lead to changes in the particle mass. Reactions that have been shown to occur are:

- Transformation of nitrites to nitrates in presence of ozone (Sickles et al., 1989)
- Chemical degradation/oxidation of organic matter during sampling (compound specific)
- Formation of sulphate-containing particles by chemical reactions of sulphur dioxide gas at the surface of alkaline media such as glass fibre media
- Chemical reactions, e.g.: (Appel and Tokiwa, 1981)

  $$2NH_4NO_{3\,(s)} + H_2SO_{4\,(l)} \quad \rightarrow \quad (NH_4)_2SO_{4\,(s)} + 2HNO_{3\,(g)}$$
  $$2NaNO_{3\,(s)} + H_2SO_{4\,(l)} \quad \rightarrow \quad Na_2SO_{4\,(s)} + 2HNO_{3\,(g)}$$
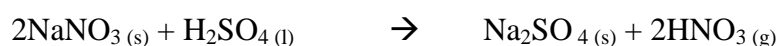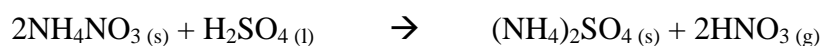
Tsai and Perng (1998) quantified the sum of the positive artefact for sulphate. They determined +11%, +8% and +15% for PM_{10} measured with a high volume sampler, PM_{10} measured with a dichotomous sampler and $PM_{2.5}$ measured with a dichotomous sampler, respectively.

2.4.2 Discrepancies of Measured Data From Discontinuous and Continuous Particle Mass Concentration Samplers

The TEOM®, as described in chapter 2.3.1, and beta attenuation monitors, as described in chapter 2.3.2, are widely used automatic samplers for continuously measuring ambient particulate matter (PM). Recent studies have shown that in presence of semi-volatile PM in

the atmosphere, these automatic monitors show lower mass concentrations than the manual reference method (see figure 2.3.3) and other methods for the determination of PM. Salter et al. (1999) have found the non-linear relationship $\text{Partisol} = 0.70 \cdot \text{TEOM}^{1.179}$ between the measured TEOM$^{®}$ and Partisol (manual reference sampler) data for PM_{10}, while Soutar et al. (1999) have come to the linear function $PM_{10} = 1.5 \cdot \text{TEOM} + 5.9$ to describe the relationship between a personal PM_{10} sampler and a TEOM$^{®}$. Ayers et al. (1999) have compared TEOM$^{®}$ data for $PM_{2.5}$ to that of a low volume filter sampler and a Micro Orifice Uniform Deposit Impactor (MOUDI). They have found the difference in the measured mass concentration to be >30%. Cyrys et al. (2001) have compared a TEOM$^{®}$, operating at 50°C and a Harvard impactor (HI), which could either be operated at ambient temperature or at 50°C. They found the ratio of mass concentration TEOM/HI to be 0.74 for the Harvard impactor at ambient temperature, whereas no systematic differences were observed, when the impactor was heated to 50°C. The investigators concluded that the observed differences are mainly due to evaporation of semivolatile PM.

Chang et al. (2001) have found a strong impact of relative humidity on the measurement results of a beta-gauge monitor. They compared data, obtained from one beta-gauge to that from two different hi-vol reference samplers and concluded that when the deliquescence point is exceeded, the beta-gauge reading was by more than 20% higher than that of the investigated manual samplers, whereas below the deliquescence point the ratio of the measured mass concentrations was approximately 1.

Inside the automatic samplers the aerosol commonly is heated (40-50°C) during sampling to minimize the effect of changing relative humidity and particle bound water on the determination of particle mass concentrations. This heating, besides reducing the above mentioned effect, also enhances the volatilisation of volatile and semi-volatile material, causing lower concentrations being measured with the automatic monitors. Hence, results obtained with automatic samplers are not simply comparable to those obtained with manual samplers which in turn also show unquantifiable losses, e.g. due to diurnally fluctuating temperature. The introduction of mathematical conversion functions for the correction has often been discussed in the past (e.g. Chang et al., 2001). The *EC Working Group on Particulate Matter* suggests as an interim solution the use of a default correction factor for member states that have not yet carried out intercomparison studies for different sampler types at different sampling locations (Williams and Bruckmann, 2001). The group concludes that a default correction factor of 1.3 could be applied to PM_{10} measurement data from both,

TEOM® instruments and beta-attenuation techniques, bearing in mind that this factor rather overestimates PM_{10} mass concentrations.

Such conversions depend on different factors, mainly the amount of semi-volatile particulate material. The composition of the atmospheric aerosol (Kuhlbusch et al., 2001) as well as the amount of the semi-volatile particulate matter, mainly Nitrate (Danalatos et al., 1999; Mehlmann et al., 1995), is not stable for a given sampling site but shows diurnal and seasonal variations. Therefore it is impossible to determine a reliable general conversion function to correct data obtained with automatic monitors.

One approach to minimize the effect of humidity and moisture on continuous particle mass concentration measurements is the use of a diffusion dryer upstream of the particle sensor (see chapter 2.3.1.1). The dryer dehumidifies the aerosol before the sensor and allows a temperature reduction to slightly above ambient temperature, causing lower losses of semi-volatile material from the filter.

2.5 A new Self-Referencing Technique for Quasi-Continuous Determination of the True Airborne Particle Mass Concentration Including Semi-Volatile Particulate Matter

To overcome the problem of not accurately measuring ambient particle mass concentration, Rupprecht & Patashnick have introduced the patented idea of the Differential TEOM® (United States Patent: Patashnick, et al., 2001; Patshnick et al., 2001), which allows the determination of the "real" particle mass concentration by monitoring the effect of the sum of all artefacts along with the conventional PM mass concentration.

The real particle mass m_{real} in ambient air can be described as the sum of the non-volatile component m_p and the (semi-) volatile component m_{pv} of the total particle mass:

$$m_{real} = m_p + m_{pv} \qquad (eq\ 2.5.1)$$

Figure 2.5.1: Differential TEOM® (Patashnick et al., 2001)

The Differential TEOM® uses two TEOM® units A and B as well as two upstream electrostatic precipitators (ESP) A and B. The air is sucked into the system through a standard size selective inlet, followed by an SES dryer, a flow splitter, two ESP's A and B and two

sensor units A and B (figure 2.5.1). The dryer dehumidifies the air and allows to reduce the sample temperature in the TEOM® sensor to e.g. 30°C (see chapter 2.3.1.1). The two ESP's are alternatively switched on and off and out of phase with each other. I.e. alternatively one sensor is driven with particle free air, the other with particle laden air. After a time interval Δt both ESP's change their status. Consider ESP A is switched off and ESP B is switched on, thus sensor A is driven with particle laden air while air in sensor B is particle free. The effective mass $m_{A,eff}$ measured by sensor A including all changes due to artefacts, can then be expressed as

$$m_{A,eff} = m_{A,p} + m_{A,pv} + \alpha_G m_G + \beta_T \Delta\vartheta + \gamma_P \Delta P + \delta_\Phi \Delta\Phi \qquad \text{(eq. 2.5.2)}$$

where $\alpha_G m_G$ is the gaseous mass gain or loss due to gas phase adsorption or desorption, $\beta_T \Delta\vartheta$ is the equivalent mass change due to temperature changes, $\gamma_p \Delta P$ is the equivalent mass change due to pressure changes and $\delta_\phi \Delta\phi$ is the equivalent mass change due to changes in relative humidity.

During said time interval, sensor B is driven with particle free air, hence $m_{Bp} = 0$ and $m_{Bpv} = 0$. The effective mass $m_{B,eff}$ of sensor B is given by equation 2.5.3:

$$m_{B,eff} = \alpha_G m_G + \beta_T \Delta T + \gamma_P \Delta P + \delta_\Phi \Delta\Phi \qquad \text{(eq. 2.5.3)}$$

Therefore:

$$m_{A,eff} - m_{B,eff} = m_p + m_{pv} = m_{real} \qquad \text{(eq. 2.5.4)}$$

Equation 2.5.4 gives the real total particle mass in the sampled aerosol. The average particle mass concentration during time interval Δt can be derived from equation 2.2.1. It should be noted here that a possible drift of one or both sensor(s) cannot be corrected with this system, as such a drift is specific for each single device. A sensor drift can only be corrected by a set-up with a single sensor, as described in chapter 2.5.1.

In figure 2.5.2 the mass concentration calculated from the data obtained with a differential TEOM® is plotted along with the mass concentration obtained with an SES equipped TEOM®. It can be seen that the mass concentration, determined with the differential TEOM® was consistently higher than that obtained with an SES equipped TEOM®. Since the differential TEOM® determines the real airborne particle mass concentration, this proves that the TEOM®, even when equipped with an SES, rather underestimates the ambient concentration, most likely due to the elevated sensor temperature or possible losses in the dryer. With respect to figure 2.3.5 this also shows that the reference method, which generally

Differential TEOM vs. SES equipped TEOM
PM$_{2.5}$ - Supersite Queens, NY
1 hour average

Figure 2.5.2: Mass Concentration, Measured With Differential TEOM® and SES Equipped
TEOM®
(courtesy: Rupprecht & Patashnick, Co., Inc.)
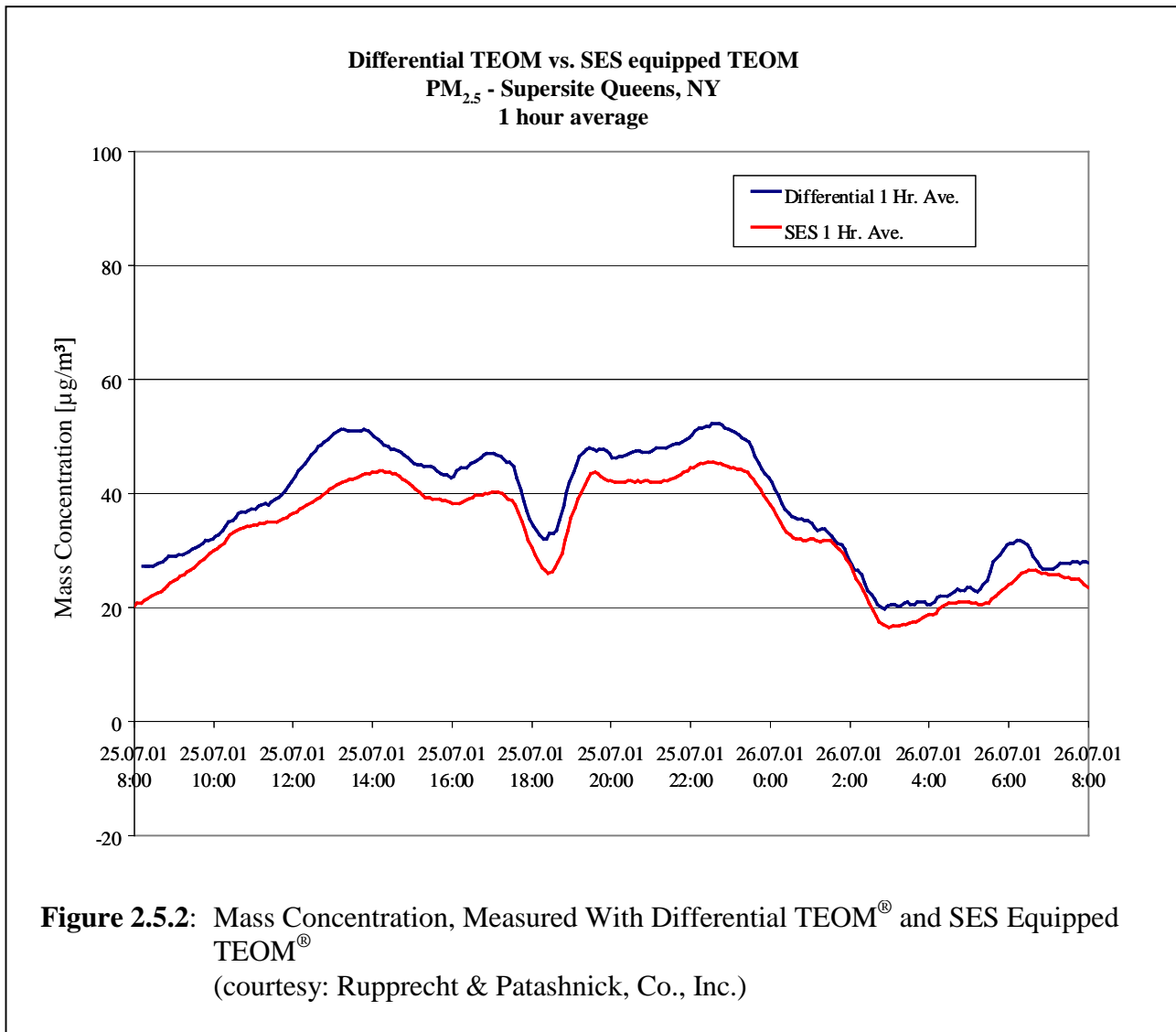
shows results, comparable to the SES equipped TEOM®, is not able to represent the true

airborne particle mass concentrations.

2.5.1 An Improved Differential TEOM® with Single Sensor and GPP

The Differential TEOM® as described in the previous chapter has several major

disadvantages. Firstly the set up comprises two full TEOM® units and therefore becomes

quite space-consuming and expensive. Secondly, the artefacts are assumed to be identical for

both devices, which e.g. in case of changing amount of semi-volatile material in the

atmosphere might not be very accurate. A possible sensor drift, which is not related to

particles or meteorological influences, is different for each sensor and can therefore not be

corrected by means of the correction method (equations 2.5.2. through 2.5.4). Thirdly, the

corona discharge in the ESP's generally produces gases like ozone and oxides of nitrogen (see

chapter 3.4) which might change the evaporation and gas phase absorption rate on the sample

filter and can therefore change the artefacts due to gaseous mass gain or loss. Further common

ESP's require frequent maintenance, mainly cleaning. A particle remover, that minimizes the

effect on the sample's gas phase and the maintenance requirements therefore highly improves the output, practicability and scientific value of the Differential TEOM®.

One approach to overcome these problems is to reduce the entire set up of the Differential TEOM® as shown in figure 2.5.1 to a set up with only one single TEOM® and one GPP as particle remover (see figure 2.5.3). The GPP gets alternately switched on and off. During the period, when it is switched off, the sensor measures the particle mass conventionally including all yet unknown changes due to artefacts and a possible drift dr (Asbach et al., 2003c)

$$m_{off} = m_p + m_{pv} + \alpha_G m_G + \beta_T \Delta\vartheta + \gamma_P \Delta P + \delta_\Phi \Delta\Phi + dr \qquad \text{(eq. 2.5.5)}$$

With the GPP switched on, the sensor measures the net effect of all artefacts, including the drift dr

$$m_{on} = \alpha_G m_G + \beta_T \Delta T + \gamma_P \Delta P + \delta_\Phi \Delta\Phi + dr \qquad \text{(eq. 2.5.6)}$$

In accordance with equation 2.5.4, the subtraction of equations 2.5.5 and 2.5.6 now gives a very accurate value for the particle mass, as all artefact related coefficients are for the same sensor. Further this set up also allows to correct the data for a possible drift of the sensor. Only the single sensor Differential TEOM® can therefore be considered to be a real self-referencing monitor.

Still one (minor) uncertainty remains with the single sensor Differential TEOM®. Since the sensor operates at an elevated temperature (suggested operating temperature is 30°C for ambient temperature below 30°C), semi-volatile particulate matter might evaporate in the heat exchanger directly upstream of the sample filter and would therefore not be captured on the filter. The heat exchanger is used to condition the aerosol before entering the sensor chamber. The evaporation in the heat exchanger increases with decreasing ambient temperature due to the higher amount of semi-volatile material in the particulate phase. The only way to prevent evaporation in the heat exchanger is to operate the sensor at ambient
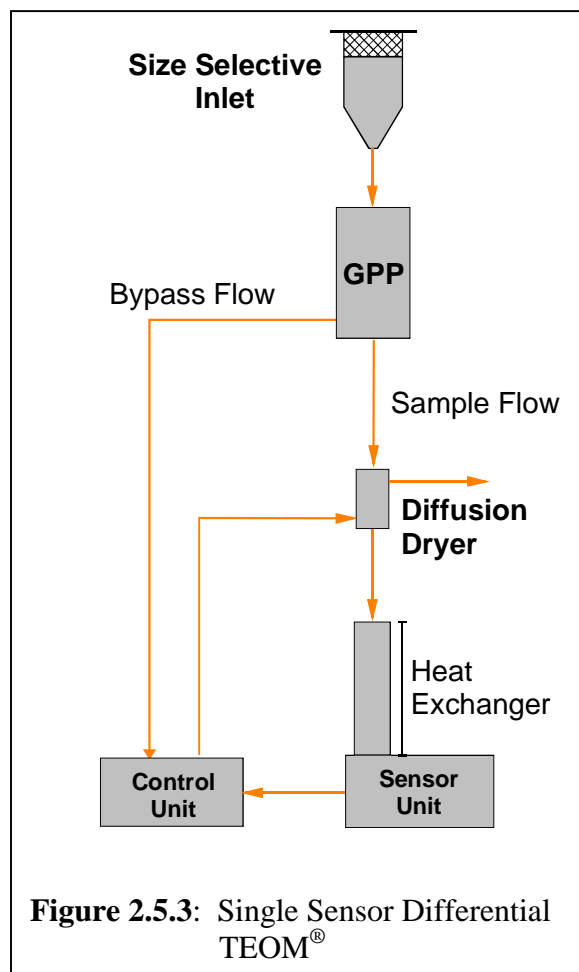
Figure 2.5.3: Single Sensor Differential TEOM®

temperature, i.e. without any temperature conditioning in the heat exchanger and sensor chamber. Studies on the behaviour of the non-heated TEOM® sensor, floating at ambient temperature, have shown that the frequency output of the TEOM® is highly affected by the temperature of the sensor. Changes of the ambient temperature would result in changing sensor temperature and therefore in fluctuating mass concentrations, delivered by the TEOM®, that do not represent the ambient concentrations. Only if the temperature changes slowly, this artefact could be corrected by the correction method of the Differential TEOM®. Since the ambient temperature does not only change diurnally but also shows quick changes, e.g. due to beginning rain or a cloud that hides the sun, the only solution that allows to correct temperature changes of the sensor is to study the temperature behaviour of the oscillation frequency analytically and develop a correction function.

Chapter 3

Theoretical Description of Physical and Chemical Processes Inside Electrostatic Gas Particle Separators

3.1 Ionisation of Gas Molecules

In order to obtain an electric current in a gas, ions have to be formed from the gas molecules. This process is known as ionisation and requires an external source of energy. The energy can be supplied by either an electric field, electromagnetic irradiation or highly energetic free electrons or ions. Two different basic mechanisms for ionisation of gas molecules are known: 1) ionisation, where one or more electrons are extracted from the molecule to form cations and 2) ionisation, due to free electrons falling into the gas molecules where they are captured to form anions. Because of the quantum nature of the ionisation process, only small objects and light quanta can interact with the gas molecules to form ions. Therefore only free electrons, atomic and molecular ions, excited atoms, neutrons and photons (UV-rays, x-rays, γ-rays) are actively participating in the ionisation process (e.g. Reist, 1993).

Many different types and forms of ionisation exist, whose description would exceed the scope of this work. Therefore only those types, applicable for corona discharge are discussed here.

The dominant ionisation mechanism in the vicinity of a corona discharge is collision ionisation, where free electrons acquire energy from the applied electric field and collide with the gas molecules. If the energy of the electron exceeds a certain level, which is characteristic for each gaseous element and called the ionisation energy, it releases one (or more) electrons from the molecule, leaving two (or more) free electrons and a positively charged ion. The first researcher to investigate the collision ionisation was Sir John Sealy Edward Townsend in the beginning of the 20th century (Townsend, 1910). He found that the increase dn_e of the number of electrons during collision ionisation is given by the general differential equation

$$dn_e(x) = \alpha(x) \cdot n_e(x) \cdot dx \qquad \text{(eq. 3.1.1)}$$

where α is the so called Townsend ionisation coefficient. α is equal to the reciprocal mean free path of electrons between two collisions. The mean free path of an electron is a function of the pressure, temperature and viscosity of the gas as well as a function of the electric field strength, which in general is a function of the location x. For a given gas at stable thermodynamic conditions and a constant electric field distribution the ionisation coefficient α is consequently only a function of the location x. The total number of free electrons, generated within the distance x can then be expressed as

Figure 3.1.1: Townsend Ionisation Coefficient α for Air at Different Temperatures and
$P = 1013.25$ mbar (White, 1969)
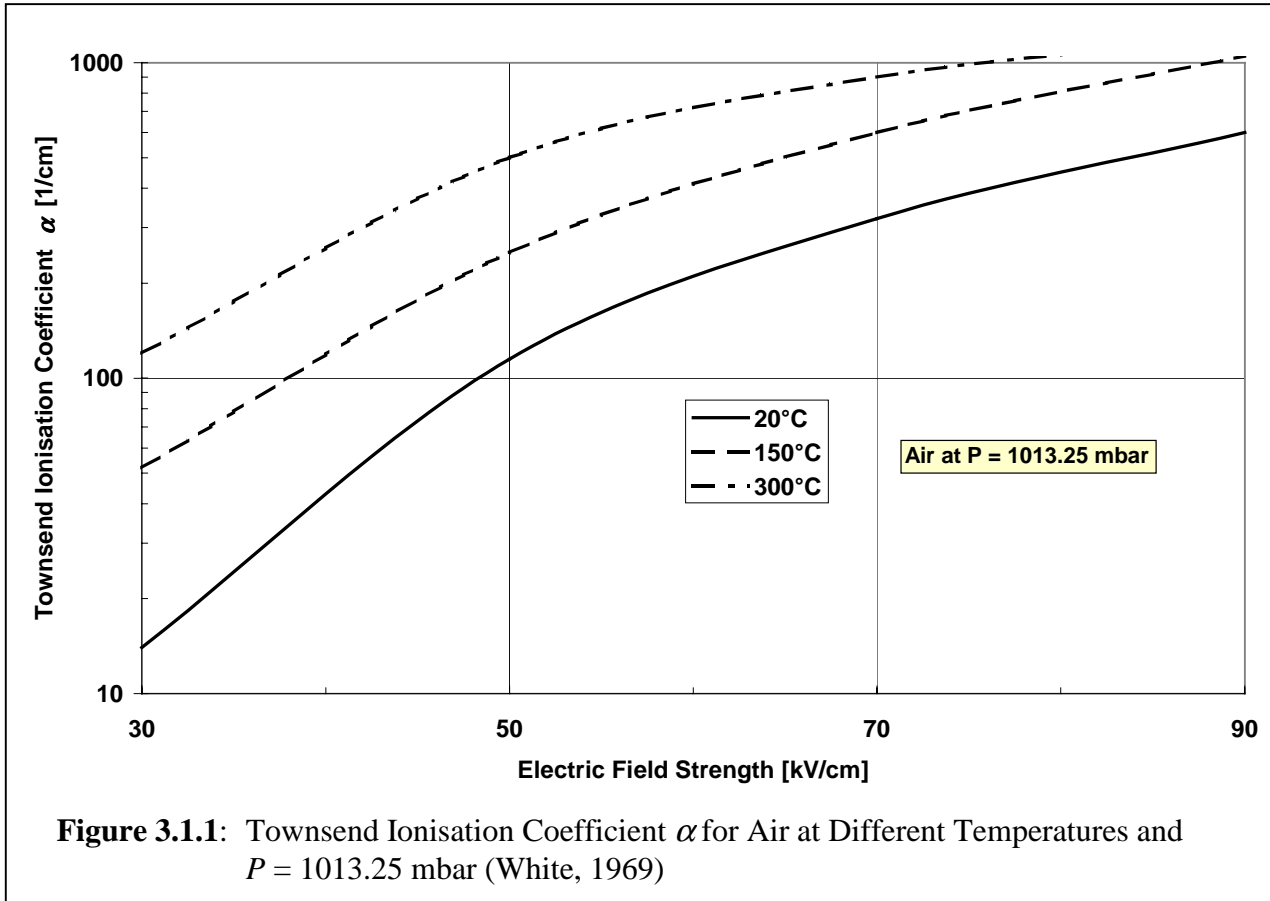
$$n_e(x) = n_e(x=0) \cdot e^{\int_0^x \alpha(x)dx}$$
(eq. 3.1.2).

The Townsend ionisation coefficient α is shown in figure 3.1.1 as a function of the electric
field strength E for air at different temperatures but stable pressure ($P = 1013,25$ mbar).

A second process that occurs near a corona discharge is the attachment of free electrons to gas
molecules to form negatively charged ions. It is mostly applicable for those elements with
high electron affinity, i.e. with a non-complete outer shell, such as halogens, oxygen and
sulphur. These elements, called electronegative elements, remain their high affinity to
electrons also when bound. The electron attachment can be described by means of the electron
attachment coefficient β, which is equal to the reciprocal mean path of an electron before
attachment to a molecule. β is characteristic for each gas and a function of the applied electric
field. The number of free electrons only in presence of electron attachment can be expressed
as:

$$n_e(x) = n_e(x=0) \cdot e^{-\int_0^x \beta(x)dx}$$
(eq. 3.1.3).

Therefore, in the presence of α- and β- ionisation, the number of electrons is given by:

$$n_e(x) = n_e(x = 0) \cdot e^{\int_0^x (\alpha(x) - \beta(x))dx}$$ (eq. 3.1.4)

In general, for a low electric field strength, α is smaller than β, causing the number of electrons to decrease with increasing x, whereas for high electric field strength, as in the corona discharge region, α is larger than β, i.e. the number of electrons increases with increasing x.

Although collision ionisation is the primary process for the formation of ions, it is not able to maintain a stable discharge. For a continuous autonomous discharge, a regeneration process for the supply of primary electrons is required. In the case of corona discharge, the most likely sources of primary electrons are: 1) release of electrons from the cathode due to collision with positive ions, 2) photoelectric emission of electrons from the cathode due to UV-irradiation from the gas, 3) photo-ionisation of the gas due to UV-irradiation from the gas, 4) ionisation due to meta stable gas atoms (White, 1969). All the processes that lead to the release of primary electrons are combined in the second Townsend ionisation coefficient γ (Townsend, 1915). γ is the probability of ionisation due to γ- processes. Since in the α- ionisation process each primary free electron releases an avalanche of secondary free electrons, the γ- process only needs to create a quite small number of primary electrons to maintain the discharge. As the number of free electrons increases with the factor $e^{\int_0^x \alpha(x)dx}$ due to α- ionisation, the requirement for a continuous corona discharge can be expressed as:

$$e^{\int_0^\infty \alpha(x)dx} - 1 = \frac{1}{\gamma}$$ (eq. 3.1.5).

3.2 Corona Discharge

The corona, used for electrical charging of particles is an autonomous, unipolar discharge due to the inhomogeneous electric field between an active corona electrode, such as a thin wire or a sharp tip, and a passive precipitation electrode, such as a tube, duct or plate (Loeb, 1965). A corona starts, when a critical electric field strength is exceeded. The application of a suitable potential difference between the two electrodes results in the electrical breakdown of the gas in the region of high electric field strength, i.e. near the corona electrode. A further increase of the voltage above a critical voltage level, will result in a spark over, causing the two electrodes to be short circuited. Generally, depending on the polarity of the corona electrode, two types of unipolar corona discharge, have to be distinguished: positive and negative corona. In both, the ionisation processes, as described in chapter 3.1, are spatially limited to

the zone of high electric field strength, i.e. to the corona region and its direct vicinity. In the corona region, which optically can be detected by its blue glow, free electrons play the major

role in the ionisation processes. These free electrons acquire a high energy from the electric field and ionise the gas molecules by collision. In agreement with equation 3.1.4, each free electron in the vicinity of the corona electrode releases an avalanche of additional free electrons and positively

Figure 3.2.1: Active and Passive Region of the Positive Corona Discharge
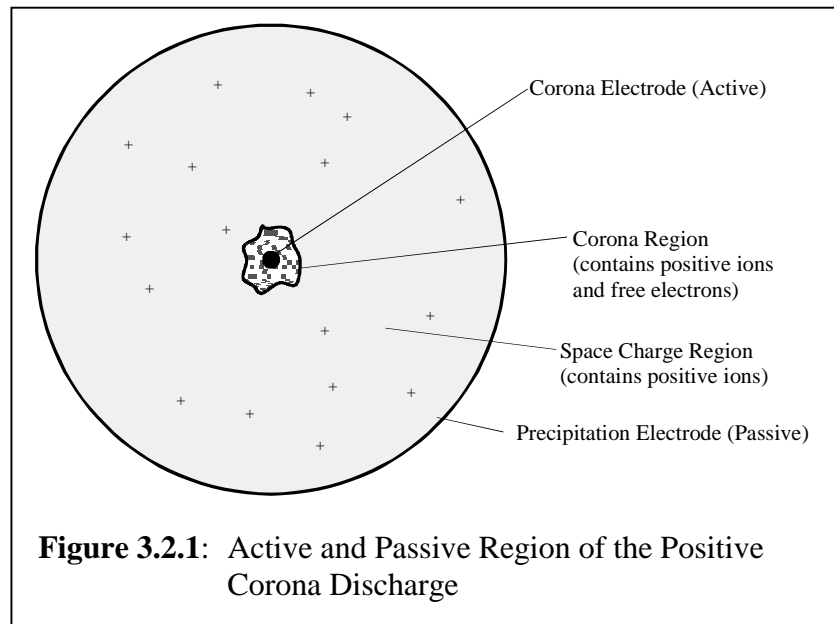
charged ions. Figure 3.2.1 schematically illustrates the active and passive regions of a positive corona discharge (e.g. Reist, 1993). In case of positive polarity of the corona electrode, the ions are transported towards the precipitation electrode while the free electrons move in direction of the corona wire. In the case of negative corona, the motion of ions and electrons is vice versa. On their way to the oppositely charged electrode, the ions impact with the suspended particles and electrically charge them (see chapter 3.3).

Positive and negative coronae can be distinguished by their optical appearance. While the positive corona exhibits a smooth and continuous glow along the corona electrode, the negative corona takes the form of tufts and beads distributed along the electrode (Rose et al., 1966). With negative coronae, a higher voltage than with positive coronae can be used before a spark over occurs. Therefore, higher ion concentrations and hence higher charging efficiencies can be achieved. On the other side, the formation of gases, mainly ozone (Viner et al., 1992; Boelter et al., 1997; Nashimoto, 1988) and oxides of nitrogen (Martinez and Brandvold, 1997; Griffing, 1977; Nashimoto, 1988) is higher in negative coronae than in positive coronae. The latter is due to the fact that the initial reaction for the formation of both, ozone and oxides of nitrogen is the electron impact dissociation of oxygen and nitrogen, respectively (Boelter et al., 1997; Nashimoto, 1988). The electron impact dissociation is directly related to the number of free electrons, which is higher in the case of negative compared to positive coronae (see chapter 3.4).

Thus, negative corona polarity is mainly used for cleaning of industrial flue gases, where the O_3 and NO_x concentrations only play a minor role, whereas positive coronae are mainly applied in indoor and scientific applications.

3.3 Electrical Charging of Particles in an Ion Environment

Generally particles may acquire electrical charge by means of three different mechanisms: static electrification, diffusion charging and field charging. Static electrification is not applicable for particle charging with a corona discharge and will therefore not be covered in this work. Diffusion charging occurs because of random collisions of particles and gas ions due to their Brownian motion and hence is applicable mainly for small particles. For a detailed description, see chapter 3.3.1. Field charging of particles occurs due to the distortion of the electric field adjacent to a particle such that the field lines terminate on the particle surface and force the ions to fall onto the particle. The field charging mechanism is described in detail in chapter 3.3.2.

For the derivation of the formulae for the number of elementary charges, acquired by diffusion and field charging, given in the next two chapters, the assumption was made that the mean distance between the dispersed particles is much larger than the particle diameter. This is necessary to exclude any interaction between the particles. Considering a monodisperse aerosol with a particle mass concentration of $c_m = 500 \frac{\mu g}{m^3}$ and a particle density of $\rho_p = 1.8 \frac{g}{cm^3}$, the mean distance between two particles is 1235 fold the particle diameter. Bearing in mind that the atmospheric particle mass concentrations are rather much lower than $c_m = 500 \frac{\mu g}{m^3}$, this proves that the aforementioned assumption is correct.

3.3.1 Diffusion Charging

As described in chapter 3.1 and 3.2, unipolar ions are produced in a corona discharge. Besides their electrically enforced motion in an applied electric field due to Coulomb forces, ions and small particles show Brownian motion. Brownian motion is a random, zigzag motion due to the collision with other gas molecules (e.g. Reist, 1993). As a result of their Brownian motion, ions may collide with particles and transfer their charge. The probability of such collisions at constant atmospheric conditions mainly depends on the particle diameter d_p, the ion concentration n_i and the residence time t_r of the particle in the ion environment. Since this charging mechanism is based on the Brownian motion of ions and particles, it is referred to as

diffusion charging. The diffusion charging mechanism does not require an external electric field.

The charges, accumulated on a particle, build up an electric field around the particle surface that repels additional ions, reducing the rate at which ions arrive. Due to the repulsion forces, only ions above a certain velocity level, will overcome the electrical barrier and reach the particle surface. This velocity threshold increases with increasing charge level of the particle. The expression for the number n_c of elementary charges, acquired by a particle, as given in equation 3.3.1 (Hinds, 1982), is based on a Boltzmann distribution of ion velocities, which does not include an upper velocity limit for the ions. Therefore no theoretical upper limit for the particle charge, acquired due to diffusion charging exists. It has to be pointed out that equation 3.3.1 is a theoretical approach to estimate the number of elementary charges and therefore for the particle size range $d_p \leq 2\ \mu$m is only accurate within a factor of 2.

$$n_c = \frac{2\pi\varepsilon_0 d_p k\vartheta}{e^2} \cdot \ln\left(1 + \frac{d_p \bar{u}_{ti} e^2 n_i t_r}{8\varepsilon_0 k\vartheta}\right)$$

(eq. 3.3.1).

The number n_c of elementary charges, acquired by particles with a diameter of $d_p = 10$ nm, $d_p = 50$ nm and $d_p = 100$ nm is plotted versus the residence time t_r in the ion environment in figure 3.3.1.
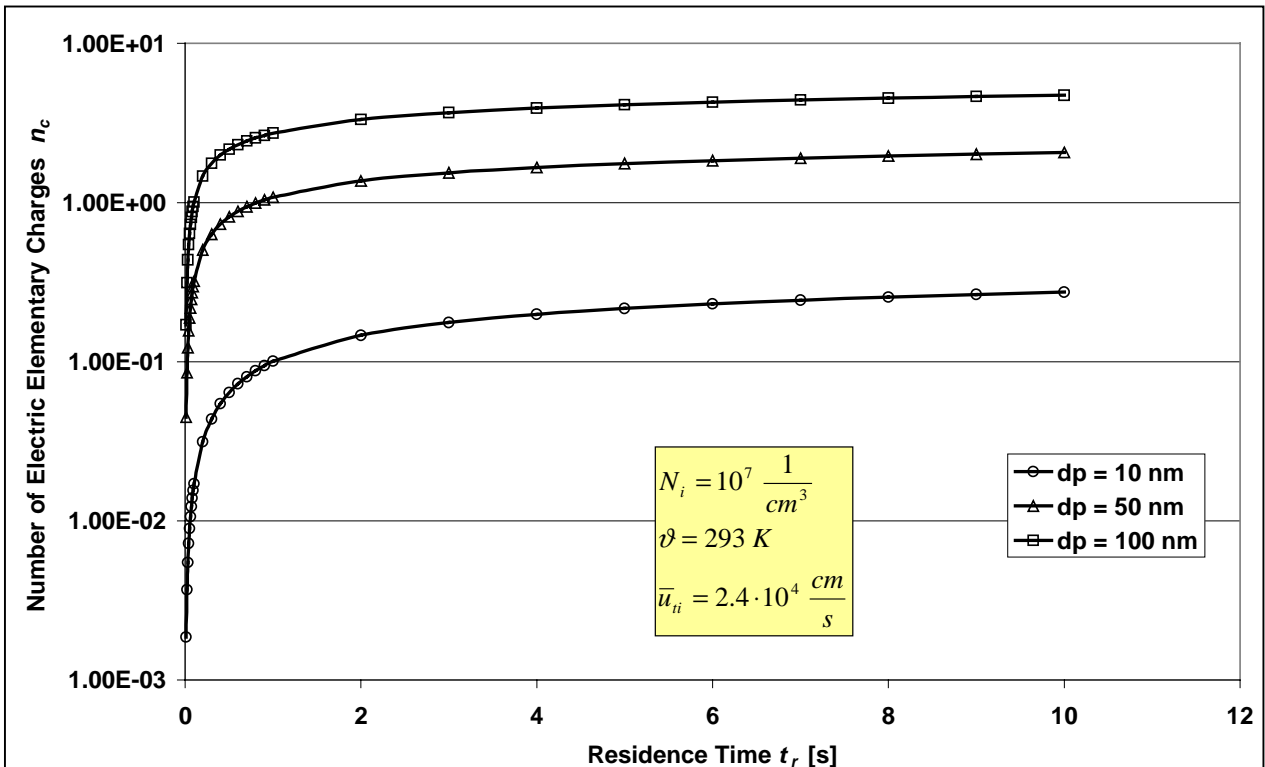
Figure 3.3.1: Number of Elementary Charges Acquired by Diffusion Charging

3.3.2 Field Charging

Field charging occurs, when particles and unipolar ions are present in a strong electric field. Figure 3.3.2 shows an uncharged spherical particle of electrically conducting material in a uniform electric field. It can be seen that the particle distorts the electric field in the vicinity of the particle surface such that the adjacent field lines terminate on the particle surface. Due to the high electric mobility of the ions, the field lines represent the ion's trajectories. Therefore the ions are electrically
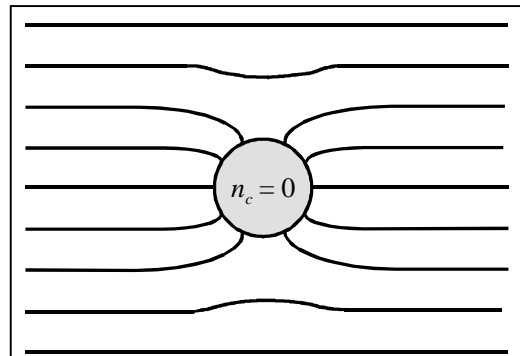
Figure 3.3.2: Electric Field in the Vicinity of an Uncharged Particle

enforced to collide with the particle. Equation 3.3.2 describes the field charging over time of an initially uncharged particle in an electric field of field strength E (Hinds, 1982).

$$n_c = \left(\frac{3\varepsilon_r}{\varepsilon_r + 2} \right) \left(\frac{\pi \varepsilon_0 E d^2}{e} \right) \left(\frac{e Z_i n_i t}{4\varepsilon_0 + e Z_i n_i t} \right) \qquad \text{(eq. 3.3.2)}$$

ε_r is the relative dielectric constant of the particle material. Therefore the first term is material specific and ranges from 1 for $\varepsilon_r = 1$ (vacuum) to 3 for $\varepsilon_r \rightarrow \infty$ (electrically conducting material).
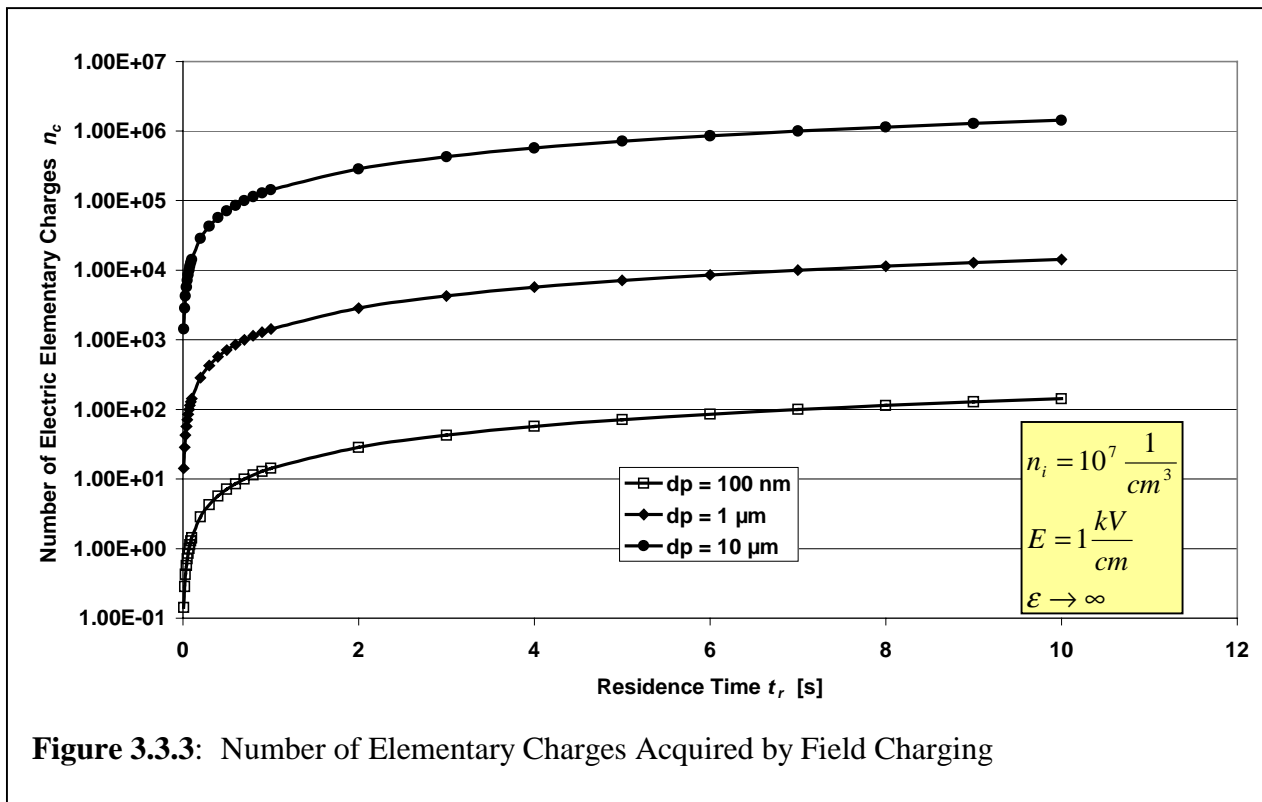
Figure 3.3.3: Number of Elementary Charges Acquired by Field Charging

The number n_c of elementary charges, acquired by particles with a diameter of $d_p = 100$ nm, $d_p = 1$ µm and $d_p = 10$ µm is plotted versus the residence time t_r in the ion environment with ion concentration $n_i = 10^7 \dfrac{1}{cm^3}$ in figure 3.3.3.

As the number of the elementary charges, captured by the particle increases, the density of terminating field lines near the particle surface decreases, whereas the density of field lines that begin on the opposite side of the particle increases (figure 3.3.4). Once the particle reaches the saturation charge level, no more field lines end on the particle, whereas the density of field lines that begin on the particle surface reaches its maximum (figure 3.3.5). The saturation charge level is reached after a long period of time, i.e. for $t \to \infty$. Therefore, the number of elementary charges n_s at saturation charge level can be expressed by the first two terms on the right side of equation 3.3.2:

$$n_s = \left(\frac{3\varepsilon_r}{\varepsilon_r + 2} \right)\left(\frac{\pi\varepsilon_0 E d^2}{e} \right) \qquad \text{(eq. 3.3.3)}$$

Figure 3.3.4: Electric Field in the Vicinity of a Partially Charged Particle
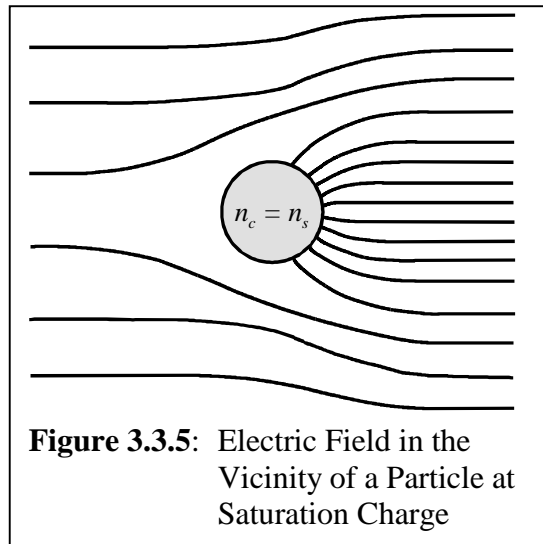
Figure 3.3.5: Electric Field in the Vicinity of a Particle at Saturation Charge

As the particle motion in an electric field is not only dependent on the electrical charge $n_c \cdot e$, carried by the particle, but also on its mechanical mobility B, the electrical mobility Z_p of particles has to be regarded to evaluate the efficiency of diffusion and field charging with respect to electrostatic separation or precipitation. The electrical mobility of particles can be expressed as

$$Z_p = n_c \cdot e \cdot B \qquad\qquad\qquad\qquad\qquad\qquad\qquad \text{(eq. 3.3.4)}$$

where

$$B = \frac{C_c(d_p)}{3\pi\eta d_p} \qquad\qquad\qquad\qquad\qquad\qquad\qquad \text{(eq. 3.3.5)}$$

with the empirical Cunningham slip correction factor C_c used to correct the distortion of the particle motion due to the interaction with gas molecules. It is mainly applicable for particle

diameters below $d_p = 1$ µm and approaches a value of 1 for $d_p > 1$ µm. The Cunningham factor is given by equation 3.3.6 (Hinds, 1982):

$$C_c(d_p) = 1 + \frac{\lambda}{d_p}\left[2.514 + 0.800 \cdot \exp\left(-0.55\frac{d_p}{\lambda}\right)\right] \qquad \text{(eq. 3.3.6)}.$$

The electrical mobility of particles after diffusion charging, field charging and combined diffusion and field charging are plotted versus the particle diameter in figure 3.3.6 for $E = 1$ kV/cm. It can be seen from the graph that the charging efficiency has a minimum for a particle diameter of approximately $d_p = 300$ nm.

Figure 3.3.6: Electrical Mobility of Particles after Diffusion Charging, Field Charging and Combined Diffusion and Field Charging
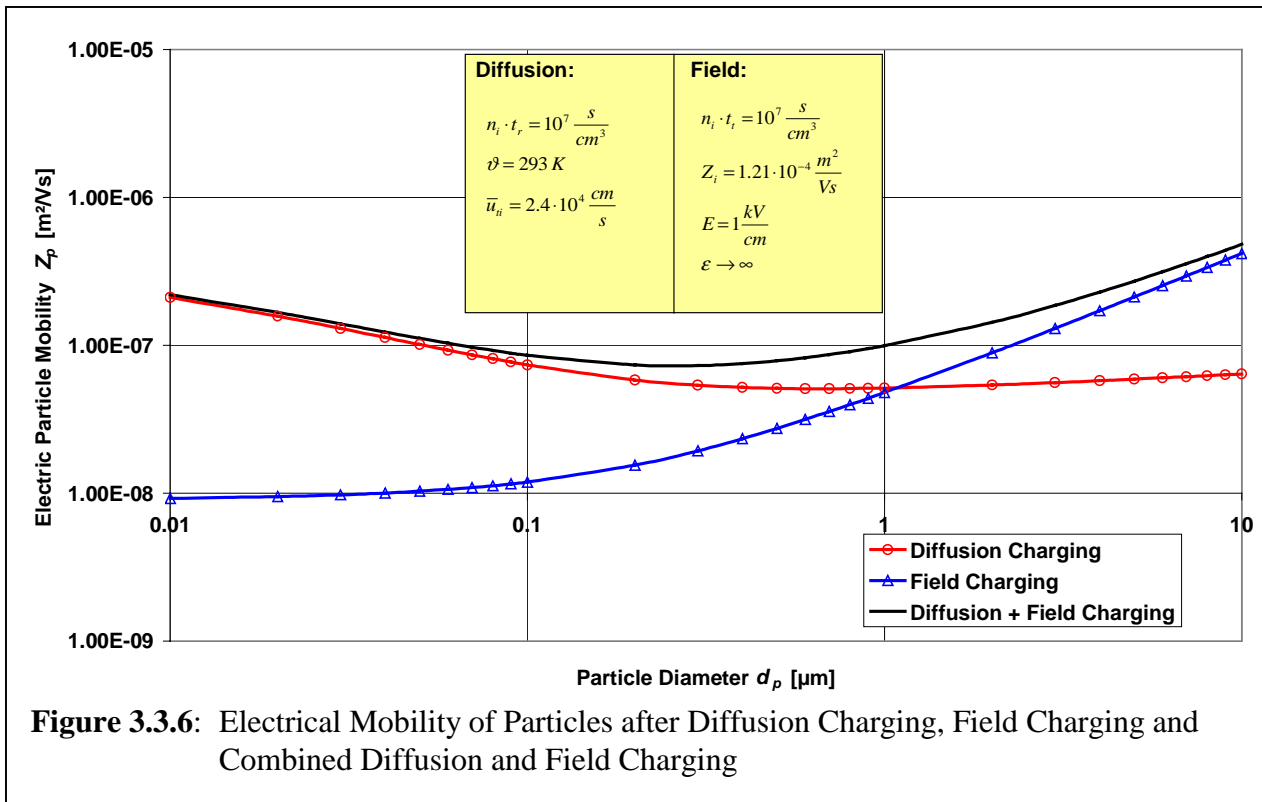
3.4 Gas Formation due to a Corona Discharge

In a corona discharge region, chemical reactions lead to the formation of gases, mainly ozone (Boelter et al., 1997; Viner et al., 1992) and oxides of nitrogen (Brandvold et al., 1989; Martinez et al., 1996). This gas formation is of minor interest, as long as the corona charging is used in industrial applications for air cleaning of flue gases, whereas when used for indoor applications, such as particle charging in scientific purposes, indoor air cleaners, laser printers or photocopiers, the elevated O_3 and NO_x concentrations can be detrimental for the downstream process or insalubrious for the user (US EPA, 1997).

3.4.1 Formation of Ozone

Ozone is a natural component of ambient air that appears as a trace gas. In the atmosphere, the ambient ozone is dissociated due to reaction (1):

$$O_3 + M \rightarrow O + O_2 + M \qquad (1)$$
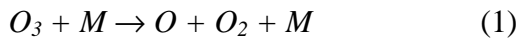
Where M is an arbitrary body for the purpose of supplying the activation energy W_A or removing the standard heat $\left|-\Delta H\right|$. It has been found that the reverse of reaction (1), reaction (2), is dominant for the formation of ozone in coronae (Boelter et al., 1997; Viner et al., 1992; Chen et al., 2002):

$$O + O_2 + M \rightarrow O_3 + M \qquad (2)$$

Figure 3.4.1: Formation and Dissociation of O_3

Reactions (1) and (2) are sketched in figure 3.4.1. It can be seen from the figure that for the formation or dissociation of ozone, a certain activation energy W_A is required.

The atomic oxygen for reaction (2) is most likely being delivered by dissociation of O_2 by electrons as shown in reaction (3) (Boelter et al., 1997):

$$e + O_2 \rightarrow 2O + e \qquad (3)$$

Therefore the ozone formation in a corona discharge is a 2-step process of reaction (3) followed by reaction (2). Regarding reaction (3), it is obvious that an increased corona current, with other words a higher electron density, causes a higher formation of atomic oxygen and thus a higher formation of ozone (Boelter et al., 1997; Viner et al., 1992; Chen et al., 2002).

Besides reaction (1), ozone is dissociated by reaction (4)

$$O + O_3 \rightarrow 2O_2 \qquad (4).$$

As in a corona discharge the formation rate of atomic oxygen as per reaction (3) is higher than the dissociation rate of ozone as described by reaction (4) (Boelter et al., 1997), the ozone concentration in the vicinity of the corona steadily increases, when the corona is situated in still air. When the corona is air-fed, as it is in most applications, the ozone concentration of the air is elevated to a level higher than ambient.

The ozone formation rate is highly affected by the polarity of the corona. Brandvold et al. (1989) have found that for a point-to-plane precipitator, the ozone concentration for negative polarity is 7.2 ± 0.2 times higher than for positive polarity. Boelter et al. (1997) have measured an approximately 6 fold higher ozone concentration for negative polarity than for positive polarity in a wire-plate precipitator.

Nashimoto (1988) has found a strong impact of the corona electrode material on the O_3 and NO_x emissions by corona discharging. Boelter et al. (1997) have approved Nashimotos theory that the ozone generation rate is linked to electrode material by the rate of formation of an oxide layer on the wire surface. The oxide formation rate can be quantified by means of the *maximum standard heat of formation of an oxide per oxygen atom for exothermic reactions* $(|-\Delta H_0|)$ of the wire material. Both investigators have found that silver produced the lowest amount of ozone among the tested wire materials, as it has the lowest value of $(|-\Delta H_0|)$. With increasing $(|-\Delta H_0|)$ of the wire material the ozone formation rate increases. Since the formation rate of ozone is based on the easy oxidation of silver, the low value of $(|-\Delta H_0|)$ turns out to be disadvantageous for practical use, as the strong oxidation of the silver wire makes the wire break very quickly (see chapter 5.6).

Several investigators (Boelter et al., 1997; Nashimoto, 1988; Viner et al., 1992) have studied the influence of wire diameter on the O_3 and NO_x formation. All have come to the conclusion that the specific formation of ozone is lower the smaller the wire diameter is. Specific formation means in that case the formation of ozone related to the corona current.

The dissociation of ozone in a corona discharge is affected by thermodynamic conditions of the air in the corona region. As the temperature of the gas increases, the ozone dissociation rate, as described in reaction (4) increases, whereas the ozone formation rate as per reaction (2) decreases (Boelter et al., 1997; Awad et al., 1975). Therefore, the ozone concentration downstream of the corona is decreasing for increasing temperature (Ohkubo et al., 1990).

Water vapour in the gas also affects the ozone concentration due to reaction with ozone molecules as well as by competing for the atomic oxygen as shown in reactions (5) and (6) and therefore reducing the generation rate of ozone (Viner et al., 1992).

$$O + H_2O \rightarrow 2OH^* \tag{5}$$

$$OH^* + O_3 \rightarrow HO_2 + O_2 \tag{6}$$

$$HO_2 + O_3 \rightarrow OH^* + 2O_2 \tag{7}$$
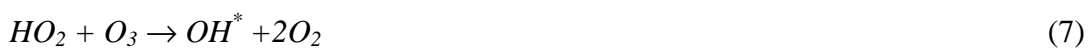
Where OH^* is a highly unstable intermediate species.

As can be concluded from reaction (5), the number of atomic oxygen is lower in presence of water vapour, causing a lower formation of ozone as per reaction (2) and an enhanced formation of OH^* radicals. The OH^* radicals dissociate the ozone (reaction 6) to form HO_2 and an oxygen molecule. The so formed HO_2 reacts with ozone to from OH^* radicals plus two oxygen molecules (reaction 7). Thus, it can be concluded that the presence of water vapour decreases the formation and increases the dissociation of ozone, resulting in a lower ozone

concentration compared to dry air. However, the formation of OH^* instead of ozone is rather more critical, as OH^* radicals are even more reactive than ozone. Therefore, in presence of OH^*, chemical reactions in the aerosol and on the sample filter may be enhanced.

Anyhow, since the GPP must not change the thermodynamic conditions of the aerosol, increased temperature and relative humidity cannot be applied in the instrument to reduce the formation of O_3.

3.4.2 Formation of Nitrogen Dioxide

Besides the formation of ozone, a corona produces oxides of nitrogen, mainly nitrogen dioxide. While the formation of ozone has been intensively investigated, only very few publications cover the chemical reactions that form NO_2 near a corona. Griffing (1977) has studied the formation of oxides of nitrogen during thunderstorms and found that the same reactions as Nashimoto (1988) that lead to the production of NO_2. This is explainable, as lightning is just like a corona an electrical breakthrough of the air. Both, Griffing and Nashimoto found the electron impact dissociation of molecular nitrogen as per reaction (8) to be the initial step in the formation of NO_2.

$$N_2 + e \rightarrow 2N + e \tag{8}$$

The so formed atomic nitrogen reacts with either molecular oxygen or ozone to form nitric oxide

$$N + O_2 \rightarrow NO + O \tag{9}$$

$$N + O_3 \rightarrow NO + O_2 \tag{10}$$

In presence of an arbitrary molecule (M) that takes up the reaction energy from the exothermic reaction 11, the nitric oxide then reacts with atomic oxygen to form NO_2

$$NO + O + M \rightarrow NO_2 + M^* \tag{11}$$

The nitric oxide might also react with ozone to form nitrogen dioxide and molecular oxygen

$$NO + O_3 \rightarrow NO_2 + O_2 \tag{12}$$

However, most of the atomic oxygen, formed by reaction (1) reacts with molecular oxygen to form ozone. Therefore the ozone concentration, caused by a corona discharge, reaches a higher level than the concentration of nitrogen dioxide.

Chapter 4

Concept of a Gas Particle Partitioner with Minimal Effect on the Gas Phase

4.1 General Criteria and Overall Design of the GPP

The GPP is a cylindrical and coaxial arrangement that is separated into four zones: aerosol inlet, charging zone, fractionation zone and aerosol outlet (see figure 4.1.1). The charging and fractionation zone are the heart of the instrument. In this section, the GPP consists of an inner and an outer electrode. In the charging zone, the inner electrode is a metal grid with centred corona wire. In the fractionation zone, the inner electrode is a solid cylinder, electrically connected to the grid. In the charging and fractionation zone, the aerosol flows in the annular space between inner and outer electrode. When a high voltage is applied to the corona wire and a lower voltage of same polarity is applied to the inner electrode, the particles get electrically charged (see chapter 4.6.2). The charged particles get deflected towards the grounded outer electrode in both, charging and fractionation zone. The total aerosol flow is internally split into a sample
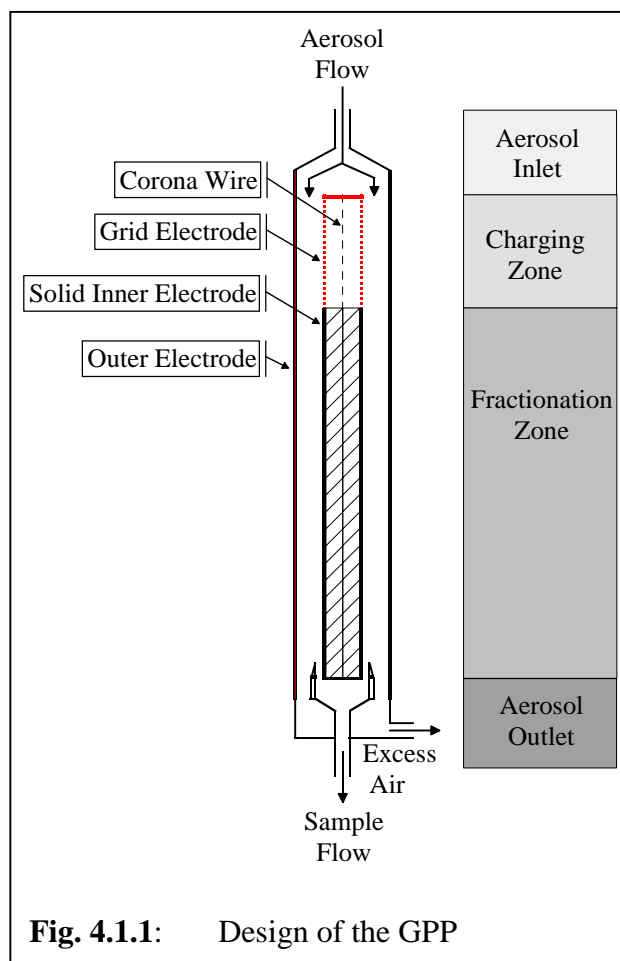
Fig. 4.1.1:   Design of the GPP

flow and an excess air flow at the lower end of the fractionation zone. The flow splitter is designed such that no change of the particle size distribution in the aerosol occurs when the GPP is switched off (see figure 4.1.2 a), but all particles either reach the excess air flow or get deposited on the outer wall when it is switched on (see chapter 4.6.3). Therefore, when switched on, the sample flow is particle free (see figure 4.1.2 b).

Several measures were taken to minimize an effect of the corona discharge and evaporation of deposited particles on the gas phase of the sample flow (see chapter 4.7).

The design of the GPP can be flexibly adjusted to different applications. The currently realized version is designed for employment in a Differential TEOM® with single TEOM® set

Figure 4.1.2: GPP in Inactive (a) and Active Mode (b)
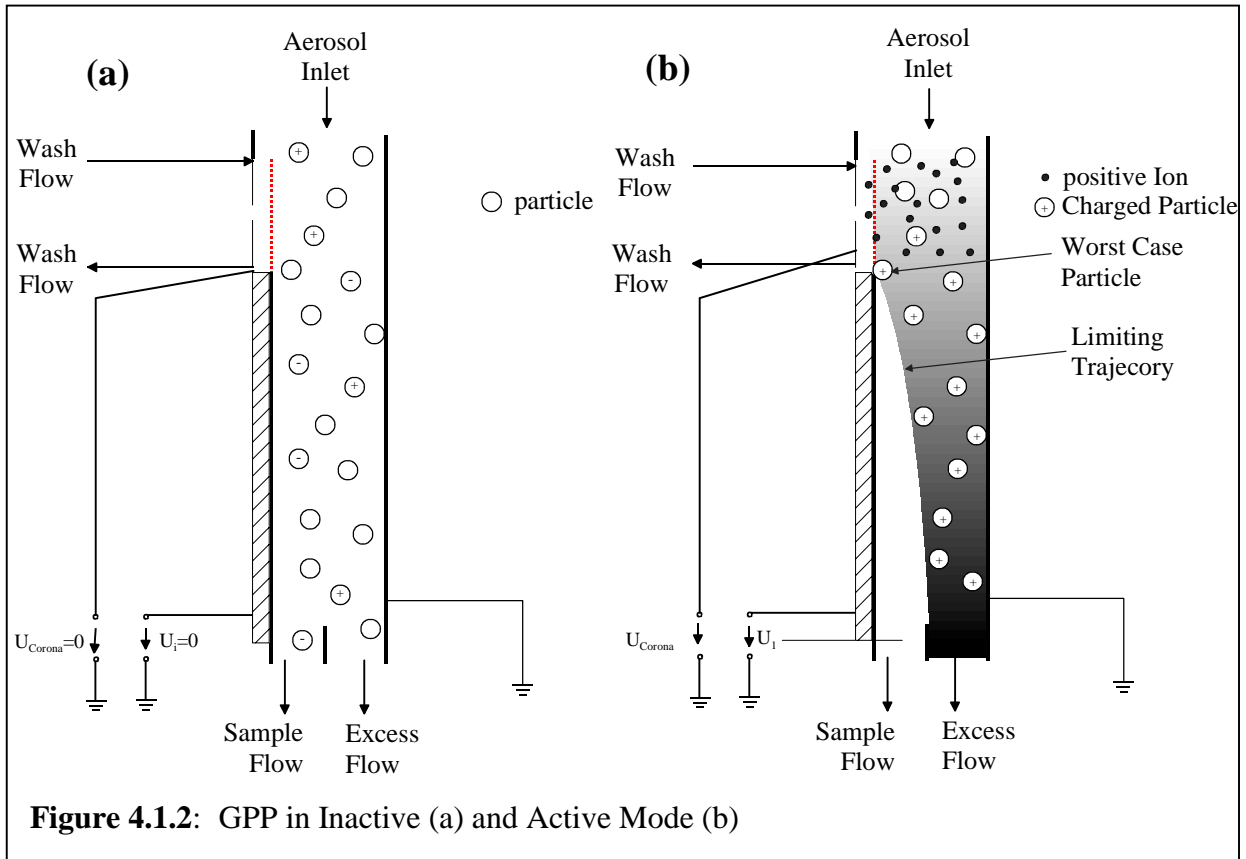
up as described in chapter 2.5.1. Therefore the required flow rates are 3 l/min for the sample flow and 13.67 l/min for the excess flow (see chapter 2.3.1). All data and results given in this and the next chapter are based on the realized version of the GPP. A description of different GPP designs for other applications is given in appendix D.

4.2 Electrical Properties of the GPP

4.2.1 Electric Field Distribution *E(r)* in the charging zone between Grid and Outer Electrode With Ionic Space Charges

By applying a high voltage to the wire (corona voltage), air molecules in the vicinity of the wire get ionised and deflected towards the grid electrode. Since a voltage of same polarity as the corona voltage is applied to the grid electrode while the outer wall of the GPP is grounded, the ions penetrate through the grid into the charging zone between the grid and the outer wall. Here the particles get charged due to both, diffusion and field charging (Hinds, 1982).

The electric field in a cylindrical capacitor can be described by equation 4.2.1.:

$$E_c(r) = \frac{U}{\ln\left(\frac{r_o}{r_i}\right)} \frac{1}{r}$$

(eq. 4.2.1)

Equation 4.2.1 is valid only for an undistorted electrical field between an inner electrode of radius r_i and an outer electrode of radius r_o. As the ions, present within the electrode system bear electric charges, they form a space charge distribution in the charging zone. The electric field of the space charge distorts the electrical field between inner and outer electrode and therefore equation 4.2.1 cannot be used. For the derivation of the resulting electric field, Maxwell's Theory has to be taken into account.

After a transition time, the space charge reaches a stable distribution in the charging zone and the overall electric field can be regarded as static and independent of time. The general differential equation 4.2.2 (Wolff, 1997) describes the electric field in presence of space charges.

$$ div\ \vec{E} = \frac{\rho}{\varepsilon_0} \qquad\qquad (eq.\ 4.2.2) $$

with the divergence in cylinder coordinates

$$ div\ \vec{E} = \frac{1}{r}\frac{\partial(r \cdot E(r))}{\partial r} + \frac{1}{r}\frac{\partial E(\alpha)}{\partial \alpha} + \frac{1}{r}\frac{\partial E(z)}{\partial z} \qquad\qquad (eq.\ 4.2.3) $$

If scatter of the electrical field at the upper and lower end of the charging zone is neglected, and the corona produces a uniform ion concentration, independent of the angle α and the longitudinal position z, the three-dimensional differential equation 4.2.3 turns into a one-dimensional equation, since then $\frac{\partial E(\alpha)}{\partial \alpha} = 0$ and $\frac{\partial E(z)}{\partial z} = 0$. Therefore equations 4.2.2 and 4.2.3 can be simplified to

$$ div\ \vec{E} = \frac{1}{r}\frac{d}{dr}(r \cdot E(r)) = \frac{\rho(r)}{\varepsilon_0} \qquad\qquad (eq.\ 4.2.4). $$

The current density $\vec{S}$ of the ions, that are transported from the inner to the outer electrode, can be described as

$$ \vec{S} = \rho(r) \cdot \vec{u}_i \qquad\qquad (eq.\ 4.2.5) $$

Since the electric field is assumed to be independent of the angle α and longitudinal position z, the current density only has a component in direction of $\vec{e}_r$. The ion velocity, which is facing in the same direction, can be expressed by the electric ion mobility Z_i and the electric field strength $E(r)$:

$$ \vec{u}_i = Z_i \cdot E(r) \cdot \vec{e}_r \qquad\qquad (eq.\ 4.2.6) $$

The continuity requirement $div\ \vec{S} = 0$ is fulfilled, if all charges that leave the corona region through the grid reach the outer electrode in the charging zone. If the convective transport of ions by the perpendicular flow can be neglected, this assumption is always true, when no

particles are present. Since the number of particles that acquire charges and are not deposited on the outer wall in the charging zone is in general three ore more orders of magnitude smaller than the number of ions, it can be assumed that the continuity requirement is also fulfilled with particles present in the charging zone. Therefore the one dimensional current density can be expressed as:

$$\vec{S}(r) = \frac{I_i}{2\pi l_c r}\vec{e}_r \qquad \text{(eq. 4.2.7)}$$

Along with equations 4.2.5, 4.2.6 and 4.2.7, the relation between ionic current I_i and electrical field strength $E(r)$ is given by:

$$\frac{I_i}{2\pi l_c r} = \rho(r)\cdot Z_i \cdot E(r) \qquad \text{(eq. 4.2.8)}$$

Inserting $\rho(r)$ from equation 4.2.4 gives the Bernoulli differential equation:

$$\frac{d}{dr}\left(r\cdot E(r)\right) = \frac{I_i \cdot r}{2\pi\cdot\varepsilon_0\cdot l_c\cdot Z_i}\cdot\frac{1}{r\cdot E(r)} \qquad \text{(eq.4.2.9)}$$

with the solution (Büscher et al., 1994)

$$E(r) = \sqrt{\frac{I_i}{2\pi\cdot\varepsilon_0\cdot l_c\cdot Z_i} + \frac{\zeta}{r^2}} \qquad \text{(eq.4.2.10)}$$

The detailed derivation of equation 4.2.10 is given in appendix A. ζ is an integration constant, that defines the limitations for the electric field strength. As the argument in the square root cannot get negative, the lower limit for the integration constant is for the case that the electric field strength gets to zero at the surface of the grid electrode. Due to their polarity, the space charges can only decrease but not increase the electric field strength compared to an undistorted field in a cylindrical capacitor. Thus the upper boundary for ζ is the case, when no ions are present, therefore $I_i = 0$ and equation 4.2.10 is equal to equation 4.2.1. Hence the scope of validity for ζ is:

$$-\frac{I_i}{2\pi\cdot\varepsilon_0\cdot l_c\cdot Z_i}r_i^2 \le \zeta \le \left(\frac{U_i}{\ln\left(\frac{r_o}{r_i}\right)}\right)^2 \qquad \text{(eq. 4.2.11)}$$

The integration constant ζ varies in each case and depends on the ion current I_i and the resulting space charge distribution $\rho(r)$. For determination of ζ, equation 4.2.10 has to be integrated to obtain the potential difference between inner and outer electrode, which is the deflection voltage U_i.

$$U_i = \int_{r_i}^{r_o} \sqrt{\frac{I_i}{2\pi \cdot \varepsilon_0 \cdot l_c \cdot Z_i} + \frac{\zeta}{r^2}} \, dr \qquad \text{(eq. 4.2.12)}$$

For a given situation, the ion current is constant and therefore the first addend of the square root is constant and can be substituted:

$$A = \frac{I_i}{2\pi \cdot \varepsilon_0 \cdot l_c \cdot Z_i} \qquad \text{(eq. 4.2.13)}$$

For a solution of the integral in equation 4.2.12, it has to be distinguished, whether $\zeta < 0$ or $\zeta \geq 0$.

For $\zeta < 0$:

$$U_i = \sqrt{A \cdot r_o^2 + \zeta} - \sqrt{A \cdot r_i^2 + \zeta} + \sqrt{-\zeta}\left[\arcsin\sqrt{\frac{-\zeta}{A \cdot r_o^2}} - \arcsin\sqrt{\frac{-\zeta}{A \cdot r_i^2}} \right] \qquad \text{(eq. 4.2.14)}$$

For $\zeta \geq 0$

$$U_i = \sqrt{A \cdot r_o^2 + \zeta} - \sqrt{A \cdot r_i^2 + \zeta} + \sqrt{\zeta}\left[ar\sinh\sqrt{\frac{\zeta}{A \cdot r_i^2}} - ar\sinh\sqrt{\frac{\zeta}{A \cdot r_o^2}} \right] \qquad \text{(eq. 4.2.15)}$$

For $\zeta < 0$, the electric field strength in the charging zone increases with increasing r, whereas for positive values of ζ the electric field strength decreases with increasing r. For $\zeta = 0$, the inhomogeneity of the electric field distribution due to the space charges compensates the inhomogeneity of the electric field of the cylindrical capacitor and therefore the overall electric field strength in the charging zone becomes constant and independent of the radial position r. Both, equation 4.2.14 and equation 4.2.15 cannot be solved analytically for ζ but have to be solved iteratively. Since all other parameters are known, the value for ζ has to be varied until the result of either equation 4.2.14 or equation 4.2.15 matches the known deflection voltage U_i.

4.2.2 Spatial Ion Number Concentration $n_i(r)$ in the Charging Zone Between Grid and Outer Electrode With Ionic Space Charges

Looking at the ion distribution in the charging zone from a macroscopic point of view, the charge distribution $\rho(r)$ can be regarded as a space charge distribution that can be expressed as

$$\rho(r) = n_i(r) \cdot e \qquad \text{(eq. 4.2.16)}$$

Along with equation 4.2.8, the distribution of the ion concentration $n_i(r)$ is

$$n_i(r) = \frac{I_i}{2\pi \cdot e \cdot l_c \cdot Z_i} \cdot \frac{1}{r \cdot E(r)} \qquad \text{(eq. 4.2.17)}$$

where the ion current I_i is a function of the applied deflection voltage U_i and $E(r)$ is given by equation 4.2.10.

4.3 Flow Profile in the GPP

The average flow velocity in a tube or an annulus can be described by the ratio of the flow rate $\dot{V}$ and the cross sectional area A_c:

$$\bar{u} = \frac{\dot{V}}{A_c} \qquad \text{(eq. 4.3.1)}$$

Although often assumed, the *laminar* flow velocity in an annular ring is not constant but shows an approximately parabolic radial dependency. For the determination, whether a flow is laminar or turbulent, the Reynolds number Re has to be taken into account. The Reynolds number is the ratio of the inertial force and the friction force. For the flow in a tube, it can be calculated by means of the average fluid velocity $\bar{u}$, the tube diameter d_t and the kinematic viscosity of the fluid ν (Verein Deutscher Ingenieure, 1988)

$$\text{Re} = \frac{\bar{u} \cdot d_t}{\nu} \qquad \text{(eq. 4.3.2).}$$

For flow in an annulus, like the GPP, an equivalent diameter, the so called hydraulic diameter d_h, has to be taken into account. For an annulus, the hydraulic diameter is given by the subtraction of the diameters of the inner and outer cylinder

$$d_h = 2 \cdot (r_o - r_i) \qquad \text{(eq. 4.3.3)}$$

Therefore the Reynolds number for flow in an annulus can be expressed as

$$\text{Re} = \frac{2 \cdot \dot{V}_{total}}{\pi \cdot (r_o + r_i) \cdot \nu} \qquad \text{(eq. 4.3.4)}$$

If the Reynolds number does not exceed a critical value, the flow is considered to be laminar. For tubes or annuli, the critical Reynolds number is $\text{Re}_{crit} = 2320$ (Hering et al., 1988). For the realized version of the GPP with $r_o = 5$ cm, $r_i = 2.5$ cm, $\dot{V}_{total} = 16.67 \frac{l}{\text{min}}$ and the kinematic viscosity of air at standard conditions of $\nu = 1.54 \cdot 10^{-5} \frac{m^2}{s}$, the Reynolds number is Re = 153.1. Hence the flow in the GPP is laminar.

Figure 4.3.1: Flow Velocity Distribution in an Annulus with $r_i = 2.5$ cm and $r_o = 5$ cm,
Flow Rate $\dot{V} = 16.67$ l/min
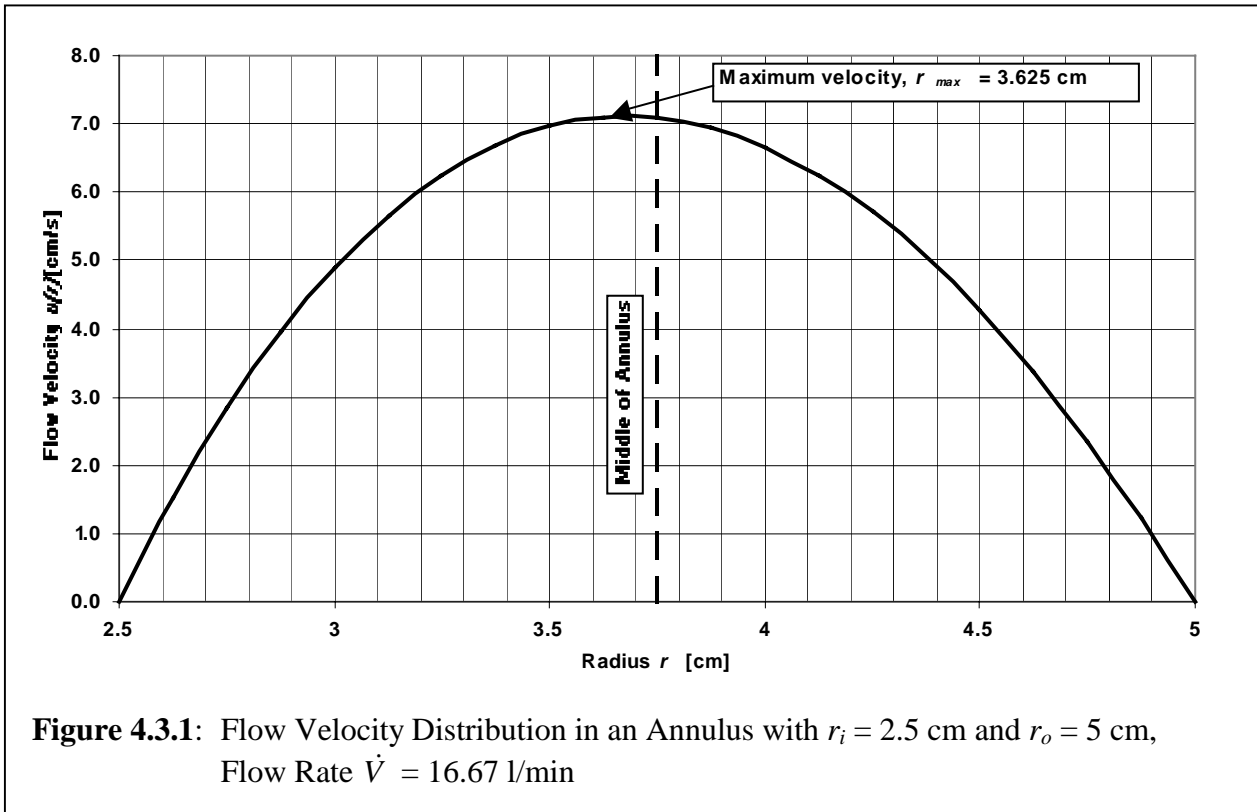
For a precise description of particle trajectories in the superposed electric and laminar flow field in the GPP, an accurate expression for the flow distribution in the GPP has to be taken into account. Bird (1960) has found an expression for the laminar flow distribution in an annulus

$$u(r) = \frac{2\dot{V}_{total}}{\pi r_o^2 \left(1 - \kappa^4 - \frac{\left(1 - \kappa^2\right)^2}{\ln\left(\frac{1}{\kappa}\right)} \right)} \left[1 - \left(\frac{r}{r_o}\right)^2 + \frac{1 - \kappa^2}{\ln\left(\frac{1}{\kappa}\right)} \ln\left(\frac{r}{r_o}\right) \right]$$

(eq. 4.3.5)

where $\dot{V}_{total}$ is the total flow through the annulus and $\kappa = \dfrac{r_i}{r_o}$ is the ratio of the radii r_i and r_o of the inner and outer cylinder, respectively. The velocity distribution is shown in figure 4.3.1 for an inner radius of $r_i = 2.5$ cm, an outer radius of $r_o = 5$ cm and a total flow rate of $\dot{V}_{total} = 16.67 \dfrac{l}{\min}$. As can be seen from the graph, the flow velocity gets zero at the surfaces of the inner and outer cylinder and increases towards the middle of the annulus. The maximum velocity at a radius of $r = 3.625$ cm is shifted inwards from the middle of the annulus, therefore the flow profile is not strictly parabolic.

4.3.1 Residence Time t_r

As shown in chapter 4.3, the gas velocity in the GPP shows a radial dependence. Therefore the residence time t_r of particles, convectively transported with the gas flow, depends on the particle's radial position r. In laminar flow conditions and with no electric field in the GPP,

Figure 4.3.2: Particle Residence Time Distribution in an Annulus with $r_i = 2.5$ cm and $r_o = 5$ cm, length $l = 5$ cm, Flow Rate $\dot{V}$ = 16.67 l/min
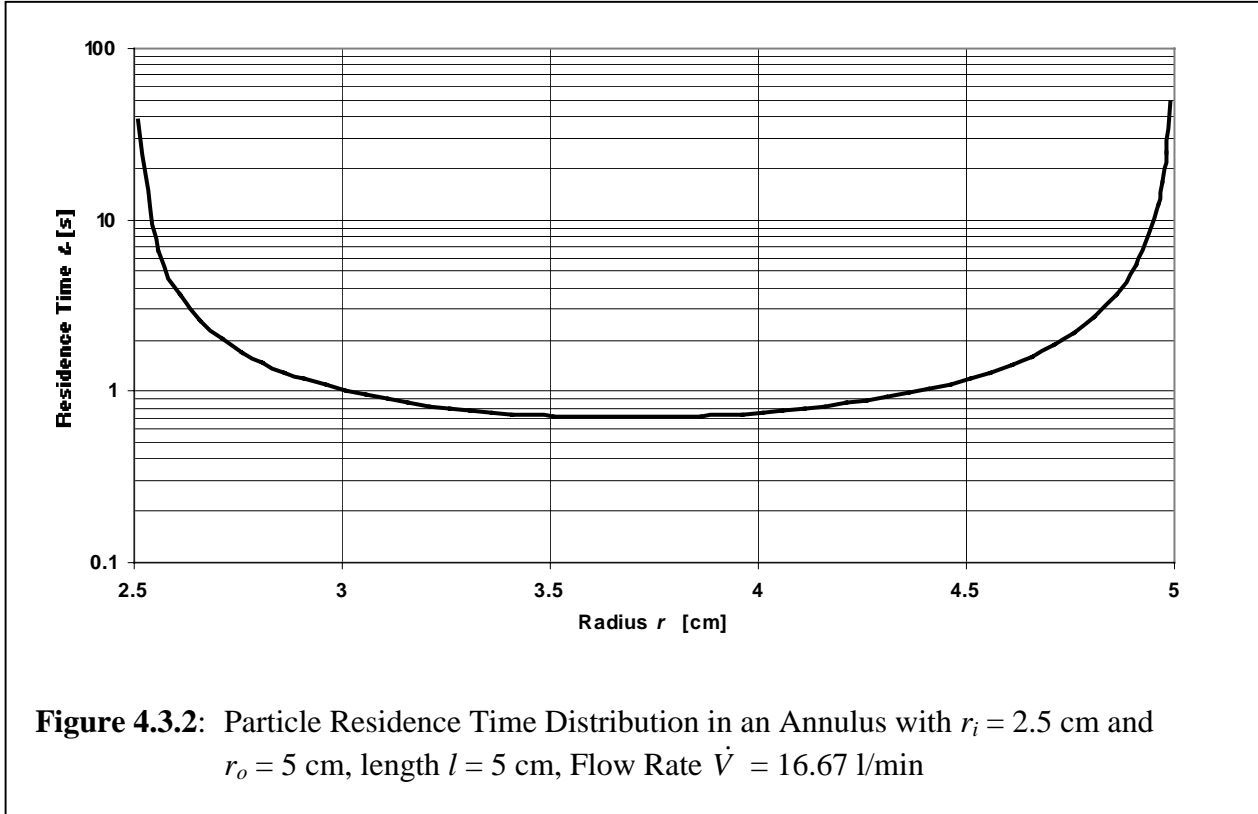
the radial position does not change during the transport. Along with equation 4.3.5 the residence time of a particle within an arbitrary length l can be expressed as

$$t_r(r) = \frac{l}{u(r)} = \frac{\pi \cdot l \cdot r_0^2}{2 \cdot \dot{V}_{total}} \cdot \frac{1 - \kappa^4 - \dfrac{\left(1 - \kappa^2\right)^2}{\ln\left(\dfrac{1}{\kappa}\right)}}{1 - \left(\dfrac{r}{r_0}\right)^2 + \dfrac{1 - \kappa^2}{\ln\left(\dfrac{1}{\kappa}\right)}\ln\left(\dfrac{r}{r_o}\right)} \qquad \text{(eq. 4.3.6)}$$

The residence time, resulting from the flow velocity distribution as shown in figure 4.3.1 is illustrated in figure 4.3.2.

4.4 The $n_i t_r$ product in the Charging Zone

The product of the ion concentration n_i and the residence time t_r of particles in the ion environment is widely accepted as a measure for the particle charging efficiency. A value of $n_i \cdot t_r = 10^7 \dfrac{s}{cm^3}$ is supposed to be sufficient for an efficient charging of the particles (Hinds, 1982).

Since both, the ion concentration and the particle residence time have a radial dependence, the $n_i t_r$ product shows a radial distribution. Along with equations 4.2.17 and 4.3.6 it can be expressed as

$$n_i(r) \cdot t_r(r) = \frac{I_i \cdot r_0^2}{4 \cdot e \cdot Z_i \cdot \dot{V}_{total}} \cdot \frac{1}{r \cdot E(r)} \cdot \frac{1 - \kappa^4 - \dfrac{\left(1 - \kappa^2\right)^2}{\ln\left(\dfrac{1}{\kappa}\right)}}{1 - \left(\dfrac{r}{r_0}\right)^2 + \dfrac{1 - \kappa^2}{\ln\left(\dfrac{1}{\kappa}\right)} \ln\left(\dfrac{r}{r_o}\right)} \qquad \text{(eq. 4.4.1)}$$

4.5 Motion of Charged Particles in the Superposed Electric and Flow Field Between the Inner and Outer Electrode in the Fractionation Zone

In the fractionation zone, the charged particles get deflected due to an electric field between inner and outer electrode. If space charge effects due to the charges, carried by the particles can be neglected, the field distribution $E(r)$ can be described by equation 4.2.1. The radial velocity of each particle is then given by the product of the electrical mobility Z_p of the particle and the electric field strength $E(r)$ at the current radial position r.

$$u_r(r) = Z_p \cdot E(r) \qquad \text{(eq. 4.5.1)}$$

As the radial velocity $u_r(r)$ is the first derivative of the radial position r, the radial motion of a particle, initially at the radial position $r(t=0)$ can be expressed as

$$\int_{r(t=0)}^{r(t)} \Re d\Re = \frac{Z_p \cdot U_i}{\ln\left(\dfrac{r_o}{r_i}\right)} \int_0^t d\tau \qquad \text{(eq. 4.5.2)}$$

Therefore (Asbach et al., 2003a)

$$r(t) = \sqrt{2 \cdot Z_P \frac{U_i}{\ln\left(\dfrac{r_o}{r_i}\right)} \cdot t + r^2(t=0)} \qquad \text{(eq. 4.5.3)}$$

Equation 4.5.3 describes the time dependent radial motion of a charged particle in the GPP. To determine particle trajectories inside the GPP, the radial and the longitudinal motion of the particles have to be superposed. If the sedimentation velocity of the particle can be neglected, the longitudinal position $z(t)$ is given by the integral of the longitudinal gas velocity $u(r)$ given in equation 4.3.5 with r being the time dependent radial position $r(t)$ in equation 4.5.3:

$$z(t) = \int u(r(t)) dt \qquad \text{(eq. 4.5.4)}$$

with the substitutions

$$C \equiv \frac{2\dot{V}_{total}}{\pi r_o^2 \left(1 - \kappa^4 - \dfrac{\left(1 - \kappa^2\right)^2}{\ln\left(\dfrac{1}{\kappa}\right)}\right)} \qquad \text{(eq. 4.5.5)}$$

$$a \equiv \frac{2 \cdot Z_P U}{r_o^2 \ln\left(\dfrac{1}{\kappa}\right)} \qquad \text{(eq. 4.5.6)}$$

and

$$b \equiv \frac{1 - \kappa^2}{\ln\left(\dfrac{1}{\kappa}\right)} \qquad \text{(eq. 4.5.7)}$$

the time depending longitudinal position $z(t)$ can be expressed as

$$z(t) = C\left\{ t - \frac{1}{2}\frac{at^2}{r_o^2} - \kappa^2 t + bt\left[\ln\left(\frac{\sqrt{at + r_i^2}}{r_o}\right) - \frac{1}{2}\right] + \frac{b}{a}r_i^2\left[\ln\left(\frac{\sqrt{at + r_i^2}}{r_o}\right) - \ln(\kappa)\right] \right\} \text{(eq. 4.5.8)}$$

Equation 4.5.8 is valid only for particles with terminal settling velocities v_{TS} negligible compared to the gas velocity. The terminal settling velocity is given by equation 4.5.9 (Hinds, 1982)

$$v_{TS} = \frac{\rho_p \cdot d_p^2 \cdot g}{18 \cdot \eta} \qquad \text{(eq. 4.5.9)}$$
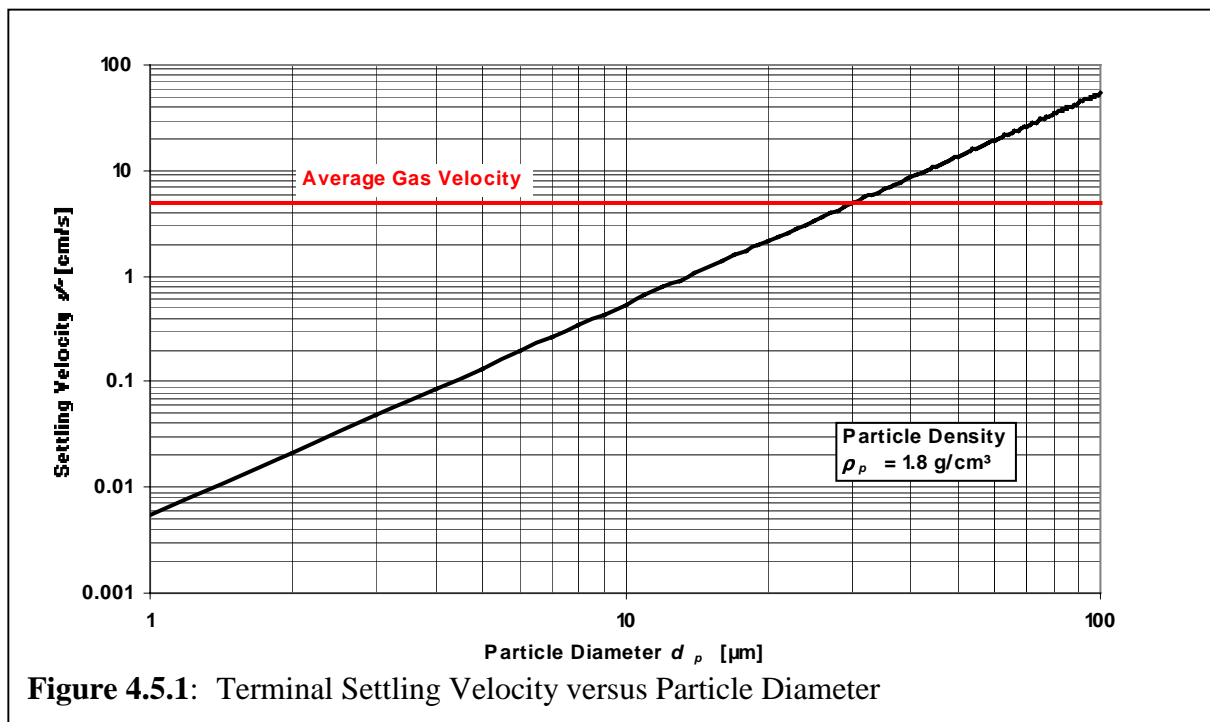
Figure 4.5.1: Terminal Settling Velocity versus Particle Diameter

Figure 4.5.1 shows the terminal settling velocity of particles versus the particle diameter for a particle density of $\rho_p = 1.8$ g/cm³. As can be seen from the graph, the settling velocities of PM_{10} particles are in any case far below the average gas velocity in the GPP of approximately 5 cm/s.

The particle trajectories of six particles of different diameter <10 µm d_{ae}, as specified in table 4.5.1, are illustrated in figure 4.5.2. For the radii of the inner and outer electrode, the actually realized diameters of $r_i = 2.5$ cm and $r_o = 5$ cm were chosen. The length of the fractionation zone was assumed to be long enough that the particle of lowest mobility can reach the outer electrode. All particles were assumed to initially be at the surface of the inner electrode, therefore $r(t=0) = r_i$. The deflection voltage, applied to the inner electrode is $U_i = 2000$ V. The Cunningham correction factor C_c has been calculated, using equation 3.3.6. For the number n_c of elementary charges, it has been assumed that the particles were exposed to diffusion charging and field charging (see chapter 4.3). The particles were assumed to spend 1 second in an ion concentration of $10^7 \frac{1}{cm^3}$ with an average electric field strength of $E = 1 \frac{kV}{cm}$. In that case, the electric mobility of the particles, resulting from the charging process is the lowest for a particle diameter of 300 nm. Therefore the trajectory of the 300 nm particle shown in figure 4.5.2 represents the slowest radial motion.

Figure 4.5.2: Particle Trajectories in the Superposed Electrical and Flow Field with Radii $r_i = 2.5$ cm and $r_o = 5$ cm and a Deflection Voltage $U_i = 2000$ V
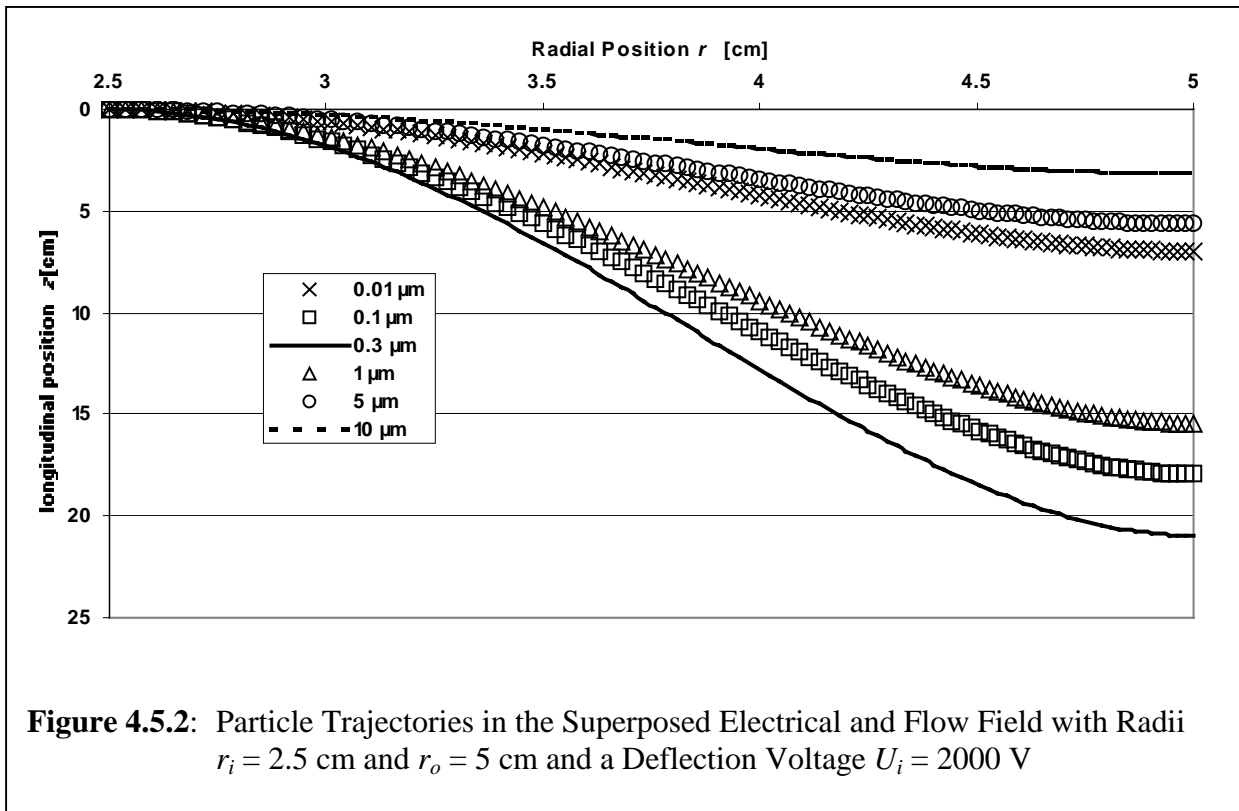
Table 4.5.1:   Particle Data for Figure 4.5.1

d_p [µm]	0.01	0.1	0.3	1	5	10
C_c	22.45	2.89	1.57	1.17	1.03	1.02
n_c	0.105	3.17	15	91.3	1410	5080
Z_p [m²/Vs]	2.20E-07	8.54E-08	7.31E-08	9.93E-08	2.72E-07	4.82E-07

4.6 Design of the Different Zones of the Gas Particle Partitioner

This chapter is to describe the design of the realized version of the GPP. This version was designed for the Differential TEOM® with a single sensor set-up as described in chapter 2.5.1. Therefore the total flow rate is 16.67 l/min as required by the size selective sample inlet. The total flow gets internally split into a 3 l/min sample flow that is directed to the sensor, and a 13.67 l/min excess flow.

As described in chapter 4.1, the GPP is separated into four different zones, aerosol inlet zone, charging zone, fractionation zone and sample and excess outlet zone. The inlet zone serves to spread the total aerosol flow, coming from the tubing, over the annular space between inner and outer electrode. The charging zone comprises the corona wire in axial position, surrounded by a permeable grid that lets only ions penetrate into the space between inner and outer electrode, where some ions impart their charge on the particles. In the fractionation zone, the so-charged particles get deflected towards the outer wall due to an electric field between inner and outer electrode. At the lower end of the fractionation zone, the total flow is split into the sample flow and the excess flow, which in the sample and excess outlet zone are led out of the GPP.

The radii of inner and outer electrode were chosen to minimise the total length and the response time of the GPP. The values for the radii are $r_i = 2.5$ cm for the inner and $r_o = 5$ cm for the outer electrode.

4.6.1 Aerosol Inlet Zone

The inlet is designed as a cone with an upper opening of ½" to easily connect commonly used ½" tubes. The lower end opens to a radius of 5 cm to match the size of the outer electrode.

The aperture angle α of the aerosol inlet cone was chosen to be 15° in accordance with the VDI guideline for similarly designed plane filter devices (VDI 2066 Part 7, 1993) to assure laminar flow conditions in the inlet.

The inlet is sketched in figure 4.6.1, where α is the opening angle, a is the difference between outer radius r_o of the GPP and the radius of the inlet tube ($a_{in} = r_o - \frac{1}{4}"$) and l_{in} is the length of the inlet. The required length l_{in} of the inlet can then be expressed as

$$l_{in} = \frac{r_o - \frac{1}{4}"}{\tan \alpha_{in}} \qquad \text{(eq. 4.6.1)}$$

With an outer radius of $r_o = 5$ cm and an aperture angle of $\alpha_{in} = 15°$, the length of the inlet comes out to $l_{in} = 16.3$ cm plus an approximately 30 mm tube connection of ½" diameter .
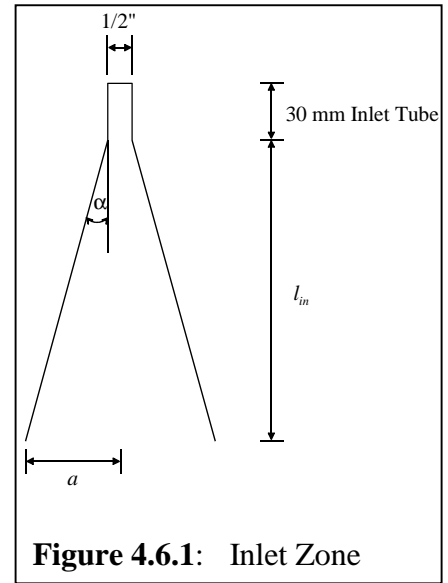
Figure 4.6.1: Inlet Zone

4.6.2 Particle Charging Zone

In the charging zone, the inner electrode is a permeable grid with a coaxial corona wire (see figure 4.6.2). If a high electric potential is applied to the wire and a lower potential of same polarity is applied to the grid, while the outer electrode is grounded, ions are produced in the vicinity of the corona wire and transported towards the grid electrode. Since the grid potential has the same polarity as the ions, they penetrate through the grid into the section between inner and outer electrode, where they collide with the particles and transfer their charge (see chapter 4.3). The charging efficiency depends mainly on the ion concentration n_i in the charging zone and the particle residence time t_r within the ion environment. Since the ion concentration cannot be determined in advance, but can only be calculated from the measured ionic current, the concentration was assumed to be $n_i = 10^7 \frac{1}{s}$. The product $n_i \cdot t_r$ of ion concentration and residence time is a widely accepted measure for the effectiveness of the corona charging process. An $n_i \cdot t_r$ product of $10^7 \frac{s}{cm^3}$ is assumed to be sufficient for efficient particle charging (Hinds, 1982). With the assumed ion concentration the required residence time in the charging zone is therefore 1 second.

The average gas velocity in the GPP can be described by equation 4.6.2

$$\overline{u} = \frac{\dot{V}_{total}}{\pi \left(r_o^2 - r_i^2 \right)} \qquad \text{(eq. 4.6.2)}$$
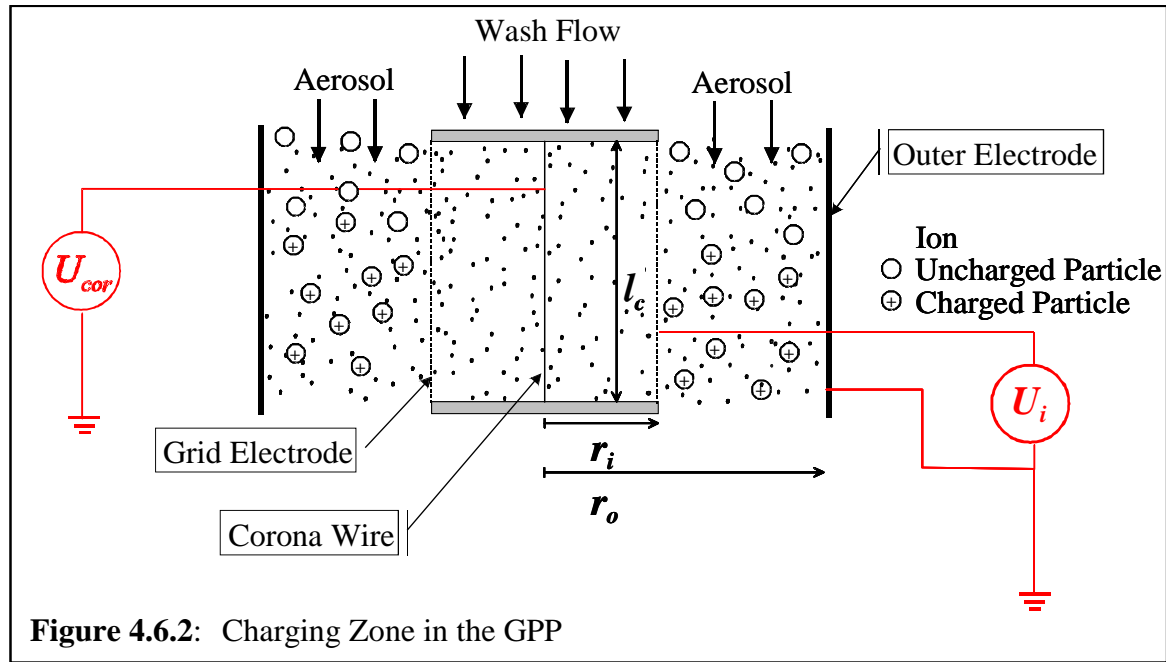
Figure 4.6.2: Charging Zone in the GPP

With the total flow rate of 16.67 l/min and the radii $r_i = 2.5$ cm and $r_o = 5$ cm, the average gas velocity in the GPP is $\bar{u} \approx 4.7 \, \frac{cm}{s}$. The theoretically required minimum length of the charger is therefore $l_c = 4.7$ cm. The actually realized length is 5 cm. The slightly longer length was chosen in order to be on the safe side.

4.6.2.1   Wash Flow

Since several investigators have found that corona discharge forms gases like Ozone (Boelter et al., 1997; Viner et al., 1992) and oxides of Nitrogen (Brandvold et al., 1989; Martinez et al., 1996), the area in-between the grid gets flushed with a particle free wash flow. The wash flow is intended to transport the gases, formed by the corona, convectively out of the GPP and avoid a mixing of these gases with the sample flow. Particles that might be emitted by the corona are also transported away with the wash flow and do not affect the sample flow. To minimize mixing of the wash flow and the sample flow, the wash flow rate was chosen such that sample flow and wash flow have the same average velocity. Therefore the wash flow rate is

$$\dot{V}_{wash} = \bar{u} \cdot \pi \cdot r_i^2 \qquad\qquad \text{(eq. 4.6.3)}.$$

With the given values, the wash flow rate is 5.6 l/min. The wash gas flows in-between the grid electrode and continues inside the hollow inner electrode in the fractionation zone. Between the fractionation zone and the aerosol outlet zone, the wash flow is withdrawn from the inner electrode.

4.6.3 Particle Fractionation Zone

In the fractionation zone, the inner and outer electrode are concentric cylinders (see figure 4.6.3). The inner electrode is electrically connected to the grid electrode in the charging zone and therefore has the same electric potential. The outer cylinder is grounded.

At the lower end of the fractionation zone, the total aerosol flow is split into the sample flow of $\dot{V}_{Sample} = 3\,\frac{l}{min}$ and the excess flow of $\dot{V}_{Excess} = 13.67\,\frac{l}{min}$. The fractionation zone is designed such that the all particles either reach the excess flow or get deposited on the outer wall when switched on. The flow splitter is designed such that when the GPP is switched off, the aerosol remains unaffected, i.e. also the particle size distribution remains unaltered.

4.6.3.1   Design of the Internal Flow Splitter

The internal flow splitter is designed such that it splits the total flow into the sample flow and the excess flow without influencing the aerosol's particle size distribution. To determine the radial position r_f of the flow splitter the radial distribution of the gas velocity $u(r)$ as per equation 4.3.5 has to be taken into account. The infinitesimal flow rate $d\dot{V}(r)$ that flows within an infinitesimal annular cross section $dA(r)$ is the given by

$$d\dot{V}(r) = u(r) \cdot dA(r) \qquad\qquad \text{(eq. 4.6.4)}$$

where the cross section is (see figure 4.6.4)

$$dA(r) = 2\pi r dr \qquad\qquad \text{(eq. 4.6.5)}$$
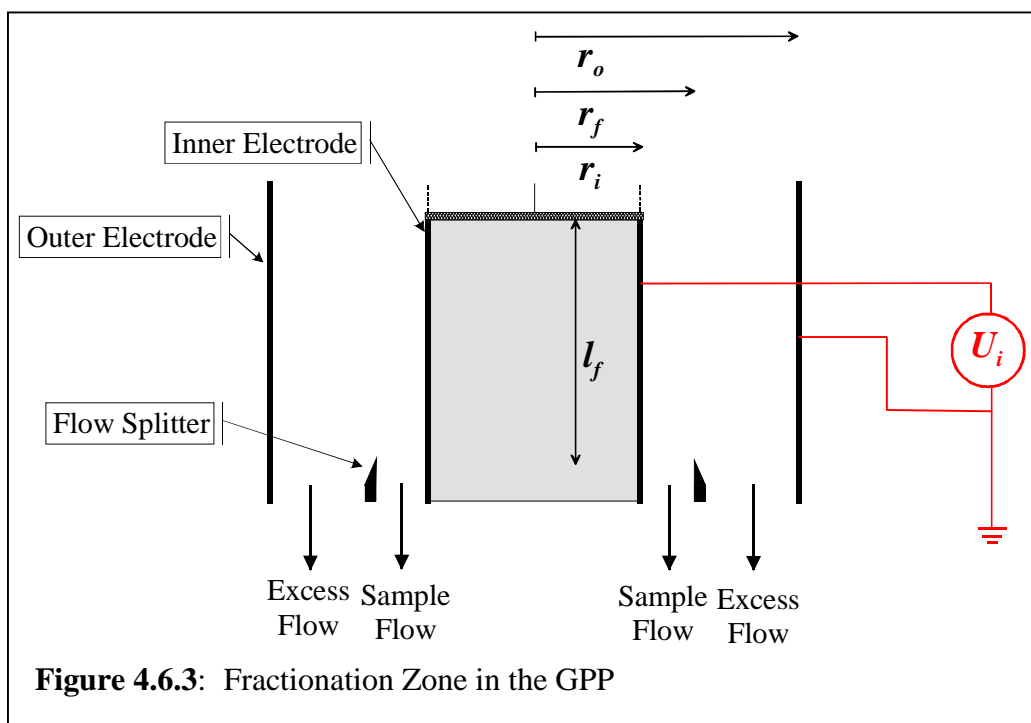
Figure 4.6.3: Fractionation Zone in the GPP

The flow rate between two arbitrary radii r_1 and r_2 can then be expressed as

$$\dot{V}(r) = 2\pi C \int_{r_1}^{r_2} r \left[1 - \left(\frac{r}{r_o} \right)^2 + \frac{1 - \kappa^2}{\ln\left(\frac{1}{\kappa}\right)} \ln\left(\frac{r}{r_o} \right) \right] dr \qquad \text{(eq. 4.6.6)}$$

The factor C is given by equation 4.5.5. By setting $r_1 = r_i$ and $r_2 = r_f$ equation 4.6.6 gives an expression for the sample flow

$$\dot{V}_{Sample} = 2\pi C \left\{ \frac{r_f^2}{2} \left[1 + b \cdot \ln\left(\frac{r_f}{r_o} \right) - \frac{b}{2} \right] - \frac{r_f^4}{4 r_0^2} - \frac{r_i^2}{4} \left[\kappa^2 - b \right] \right\} \qquad \text{(eq. 4.6.7)}$$

setting $r_1 = r_f$ and $r_2 = r_o$ leads to an expression for the excess air flow.

$$\dot{V}_{Excess} = 2\pi C \left\{ \frac{r_o^2}{4} \left[1 - b \right] - \frac{r_f^2}{2} \left[1 + b \cdot \ln\left(\frac{r_f}{r_o} \right) - \frac{b}{2} \right] + \frac{r_f^4}{4 r_o^2} \right\} \qquad \text{(eq. 4.6.8)}$$

Equations 4.6.7 and 4.6.8 cannot be solved analytically for r_f. The iterative solution gives one single value of r_f, where the flow rates match the required sample flow and excess flow, respectively. With the given flow rates and radii, the position of the flow splitter is $r_f = 3.24$ cm.

Voltage of the Flow Splitter

The ring for the flow splitter is made from electrically conducting material, with a partial voltage U_f applied to it. This partial voltage, derived from the electric field distribution (equation 4.2.1) and the radial position r_f, assures a non-distorted electric field between inner and outer electrode. The partial voltage U_f can be expressed as

$$U_f = U_i - \int_{r_i}^{r_f} E(\rho) d\rho \qquad \text{(eq. 4.6.9)}$$

Figure 4.6.4: Determination of the Infinitesimal Annular Cross Section

Therefore

$$U_f = U_i - \frac{U_i}{\ln\left(\frac{r_o}{r_i}\right)} \ln\left(\frac{r_f}{r_i} \right) \qquad \text{(eq. 4.6.10)}$$

With a deflection voltage of $U_i = 2000$ V and the abovementioned radii, the voltage of the flow splitter is $U_f = 1255.4$ V. To realize both voltages U_i and U_f with only one voltage supply, a voltage divider, comprising two appropriate resistors is used.

If the flow splitter would be made from insulating material, charged particles could deposit on the flow splitter, electrically charge it, and therefore distort the electric field in both cases, when the GPP is switched on and off. When switched off, this would yield to unquantifiable particle losses. When switched on, the field could be disturbed such that not all particles reach the excess flow and therefore decrease the separation efficiency of the GPP.

4.6.3.2 Limiting Particle Trajectory to Determine the Required Length of the Fractionation Zone

For the determination of the required length of the fractionation zone, the limiting trajectory of a "worst case particle" has to be considered. The definition of the "worst case particle" is I) lowest possible electrical mobility for PM_{10} particles (due to the impactor characteristic, the PM_{10} fraction includes particles of up to approx. 13 µm), and II) particle initially ($t = 0$) situated directly at the surface of the inner electrode ($r = r_i$) at the transition from charging zone to fractionation zone (see figure 4.6.5). As shown in chapter 4.5, the lowest mobility was estimated by means of the charge distribution of particles after combined field and diffusion charging. With an assumed average field strength of $E = 1$ kV/cm and an ion concentration of $n_i = 10^7$ cm^{-3} the mobility of the "worst case particle" is

$$Z_{p,min} = 7.3 \cdot 10^{-8} \frac{m^2}{Vs} \quad \text{(for} \quad d_p = 0.3 \text{ µm,} \quad n = 15$$

elementary charges). The trajectory of that particle was then calculated by the superposition of the radial motion $r(t)$ (eq. 4.5.3) and the longitudinal motion $z(t)$ (eq. 4.5.8). In order to obtain the minimal length of the fractionation zone, the "worst case particle" has to just reach the excess flow. Therefore the longitudinal position $z(r_f)$, when the particle reaches the radial position r_f of the flow splitter determines the minimal required length of the fractionation zone (see trajectory of worst case particle in figure 4.6.6). As can be seen from the graph, the required length of the fractionation zone is $l_{f,min} = 3.81$ cm. The total time the "worst case particle" needs to travel from the inner electrode to r_f can be calculated by solving equation 4.5.3 for t_{rf}
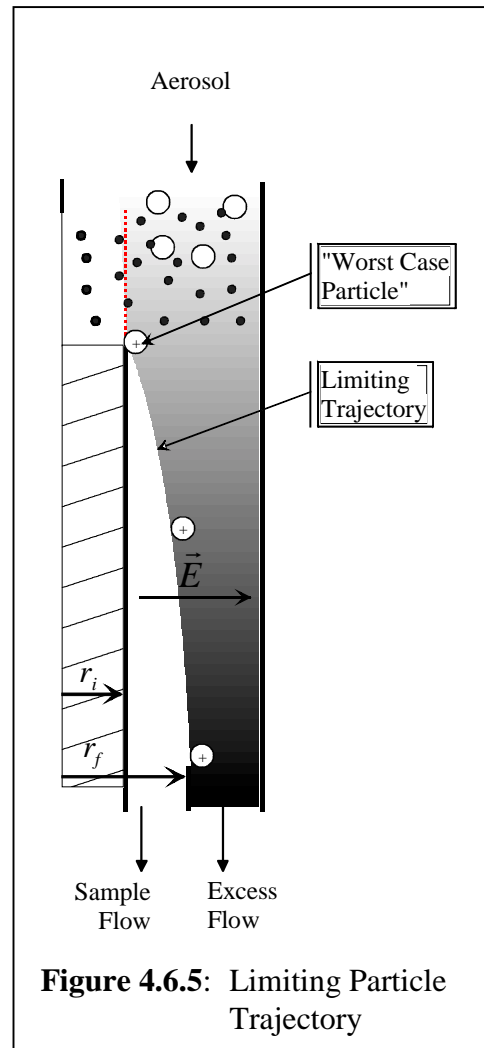
Figure 4.6.5: Limiting Particle Trajectory

$$t_{rf} = \frac{r_f^2 - r_i^2}{2 \cdot Z_p \cdot U_i} \cdot \ln\left(\frac{r_o}{r_i}\right) \qquad\qquad (\text{eq. 4.6.11})$$

Radial Position r [cm]

Figure 4.6.6: Trajecory of a Worst Case Particle for the Determination of the Minimal Length of the Fractionation Zone
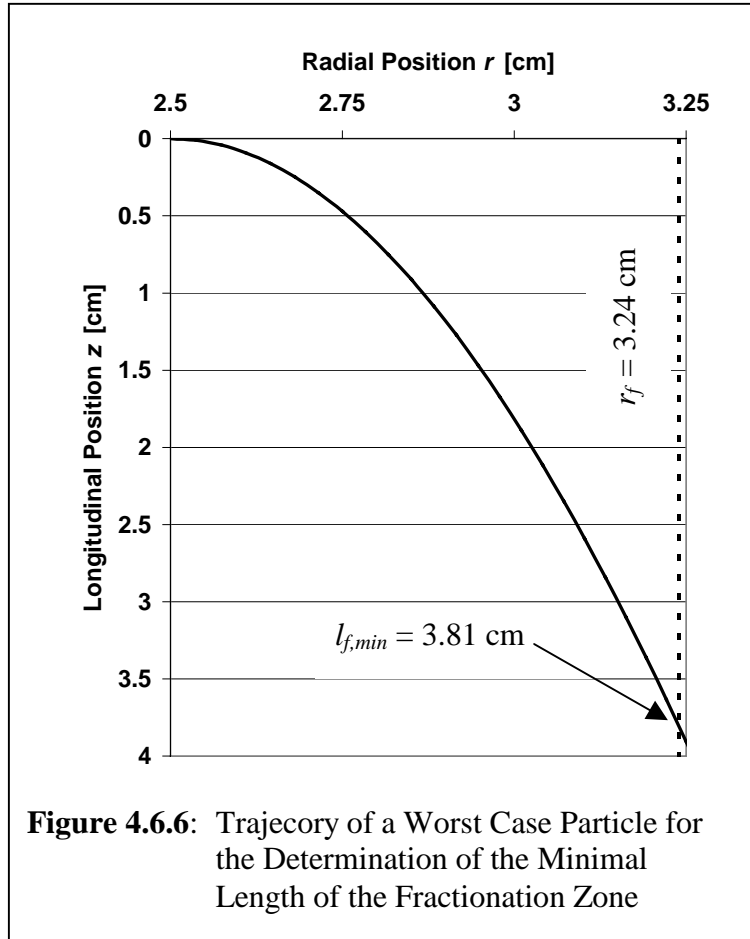
4.6.4 Sample and Excess Outlet Zone

The sample and excess outlet serves to lead the sample and the excess gas flow out of the GPP. The design of the outlet is sketched in figure 4.6.7. The aperture angle is the same as in the inlet, i.e. $\alpha_{out} = 15°$. The length a is the difference between the radius of the flow splitter r_f and the radius of the outlet tube ($a_{out} = r_f - \frac{1}{4}''$). Therefore

$$l_{out} = \frac{r_f - \frac{1}{4}''}{\tan\alpha_{out}} \qquad\qquad (\text{eq. 4.6.12})$$

With the given values, the length of the outlet is $l_{out} = 9.71$ cm.

In order to obtain a homogenous flow distribution of the excess flow in the fractionation zone, it is withdrawn through two opposite outlets. A fine mesh is used to laminize the flow. The sample flow is led out of the GPP straight in order to minimize particle losses due to impaction. To prevent the formation of turbulences in the outlet, the inner electrode does not

end abruptly, but reaches conically into the outlet to smoothly route the streamlines of the sample flow.

Figure 4.6.7: Design of the Sample and Excess Outlet
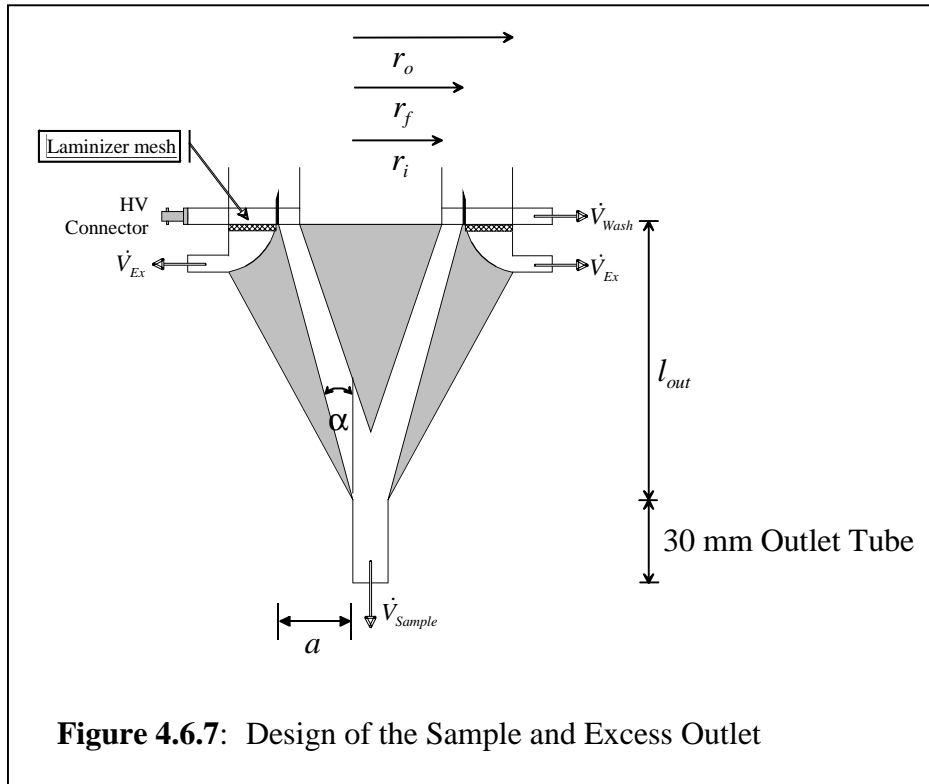
4.6.5 Final Design of the GPP and Summary of Geometric, Electric and Flow Rate Values

In the previous chapters, the design of the four single zones of the GPP have been described. Tables 4.6.1 through 4.6.3 summarise the electrical and geometric values as executed for the design as well as the required flow rates. The final design of the assembled GPP is illustrated in Figure 4.6.8. Photographs of the manufactured GPP are given in appendix E.

Table 4.6.1: Geometric Values for the GPP Design

r_i	r_f	r_o	l_{in}	l_c	l_f	l_{out}	Flanges	l_{total}
2.5 cm	3.24 cm	5.0 cm	16.3 cm	5.0 cm	5.0 cm	9.71 cm	1.5 cm	45.01 cm

Table 4.6.2: Nominal Electric Values for the GPP Design

U_i	U_f	U_{cor}
2 kV	1.255 kV	≤ 13 kV

Table 4.6.3:   Flow Rates of the GPP

$\dot{V}_{total}$	$\dot{V}_{Sample}$	$\dot{V}_{excess}$	$\dot{V}_{wash}$
16.67 l/min	3 l/min	13.67 l/min	5.6 l/min

Figure 4.6.8: Overall Design of the GPP
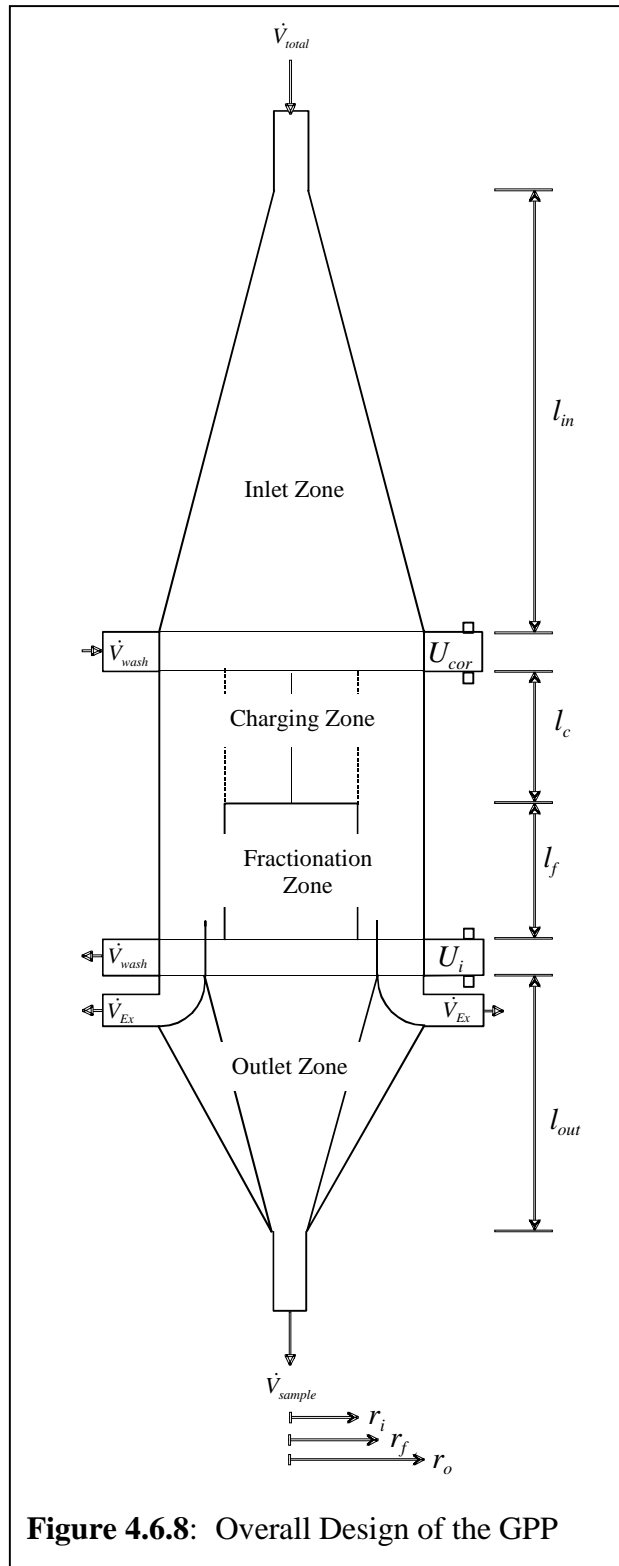
4.7   Summary of the Measures to Minimize the Effect on the Gas Phase

Several measures were taken to minimise the influence on the gas composition. In common electrostatic precipitators, the gas phase gets affected mainly due to two mechanisms. The first mechanism is the influence of the gas composition of the aerosol by the formation of gases, mainly ozone and oxides of nitrogen (see chapter 3.4) by the corona that mix with the sample flow. The second mechanism is evaporation of deposited (semi-)volatile particles from the precipitation electrode.

To minimise mixing of the corona gases with the sample flow, the corona wire is spatially separated from the sample flow. The spacing between corona wire and sample flow, i.e. the space in-between the grid electrode, gets flushed with a particle free "wash flow". The wash flow shall convectively transport the gases, formed by the corona, out of the GPP.

In order to reduce the formation of gases, the corona was optimised. Firstly, positive polarity was chosen for the corona, since several investigators (e.g. Brandvold et al., 1989; Martinez et al., 1996) have shown that positive corona produces a lower amount of ozone and nitrogen oxides. Secondly, a 25 µm silver wire has been chosen for the corona wire. Nashimoto (1989) has found that among eight tested wire materials, silver formed the lowest amount of ozone (approx. 70% less than gold) whereas the formation of nitrogen oxides was just slightly higher (+10%). However, as will be described in chapter 5.5, silver wire never lasted for more than a few days and was replaced by gold wire for longevity reasons. Boelter at al. (1997) have shown for tungsten wires that at the same efficiency, a thinner wire produces a lower amount of ozone. A wire diameter of 25 µm seems to be the lowest manageable diameter.

The flow splitter avoids a mixing of gases, formed by evaporation of deposited particles with the sample flow, as the outer wall, where particles deposit, is spatially separated from the sample flow. Evaporation of deposited particles will therefore only affect the excess flow but not the sample flow. Further, only a fraction of all particles gets deposited inside the GPP. The other fraction is transported out of the GPP with the excess flow. The amount of deposited particles and consequently evaporation of deposited material is therefore reduced.

Chapter 5

Experimental Investigations on the Performance of the Gas Particle Partitioner

5.1   Electrical Properties of the Gas Particle Partitioner

As described in chapter 4, the electric field distribution $E(r)$, distribution of the ion concentration $n_i(r)$ and the product of the ion concentration and residence time of a particle in the ion environment $n_i \cdot t_r(r)$ are the main key to predict the effectiveness of the charging and deflection process. This chapter is to describe the experimental investigation of these parameters.

5.1.1 Voltage-Current Characteristic of the GPP

The ion current is the determining value for the distributions of the electric field $E(r)$ and the ion concentration $n_i(r)$. Since both distributions determine the charging efficiency of the particles in the charging zone, it is important to know the characteristic of the ion current I_i in dependence of the applied corona voltage U_{cor}. The corona voltage U_{cor} is difference of the
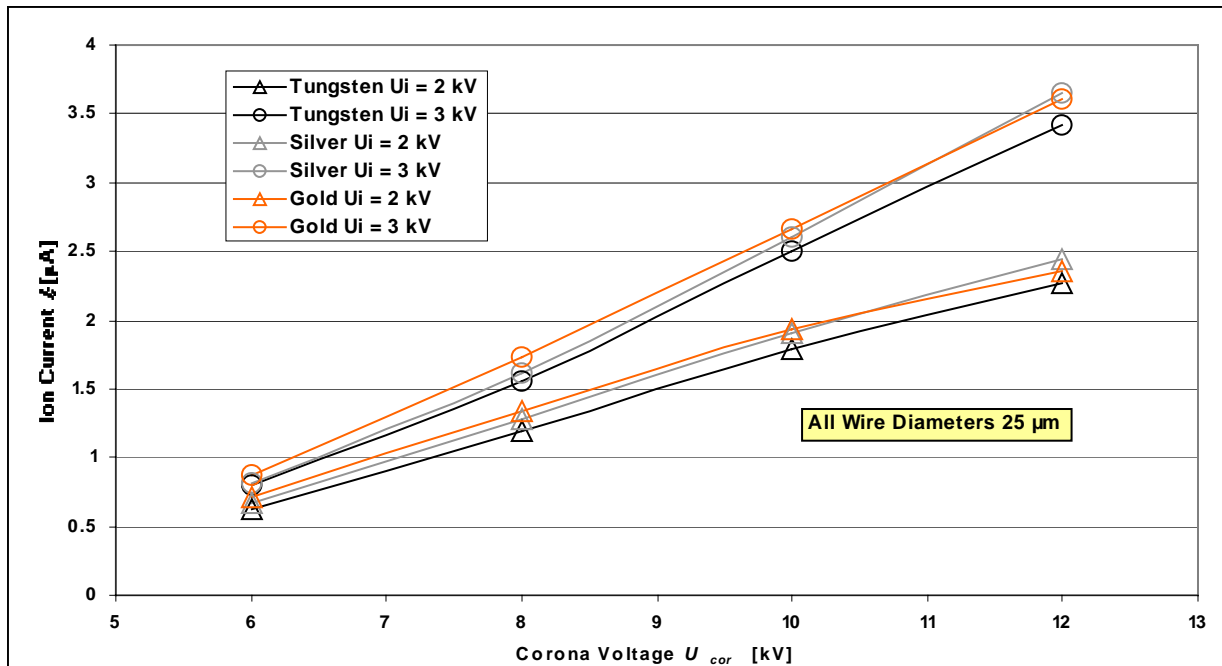
Figure 5.1.1: Voltage-Current Characteristic of the GPP for Three Different Corona Wire Materials of Same Diameter, Deflection Voltages $U_i = 2$ kV and $U_i = 3$ kV

electric potentials φ of the corona wire and the grid electrode, i.e. $U_{cor} = \varphi_{cor} - \varphi_i$. The GPP is equipped with an aluminium foil in the charging zone that allows to connect an ampere meter to monitor the ion current. As shown in figure 5.1.1, these measurements have been carried out for three different wire materials, gold, silver and tungsten and two deflection voltages of $U_i = 2$ kV and $U_i = 3$ kV. All wires had the same diameter of 25 µm. Gold and Tungsten are commonly used wire materials in e.g. ESP's or indoor electrostatic air cleaners (Boelter et al., 1997; Viner et al.; 1992). Silver wire was tested because Nashimoto (1988) has found that corona discharge around a silver wire produces the lowest amount of ozone. The formation of ozone and nitrogen dioxide from the different wire materials will be discussed in chapter 5.4. As can be seen from the graph, the current does not show a substantial dependency on the wire material. This was expected, as the corona current is mainly a function of the electric field strength at the wire surface, which is independent of the wire material. The slight differences in the measured current are most likely due to changing meteorological conditions in the laboratory that can affect the formation of ions. As can also be seen from the graph, the measured ion current is higher for a higher deflection voltage, even though the corona voltage remained the same. This can be explained by the electric forces on the ions near the grid. If a lower deflection voltage is applied to the grid, the ions are exposed to a lower electric force and therefore deposition of ions at the grid due to diffusion becomes more dominant.

To study the effect of the wire diameter on the current, the current-voltage characteristic has

Figure 5.1.2: Voltage-Current Characteristic of the GPP for Three Different Silver Wire Diameters, Deflection Voltages $U_i = 2$ kV and $U_i = 3$ kV
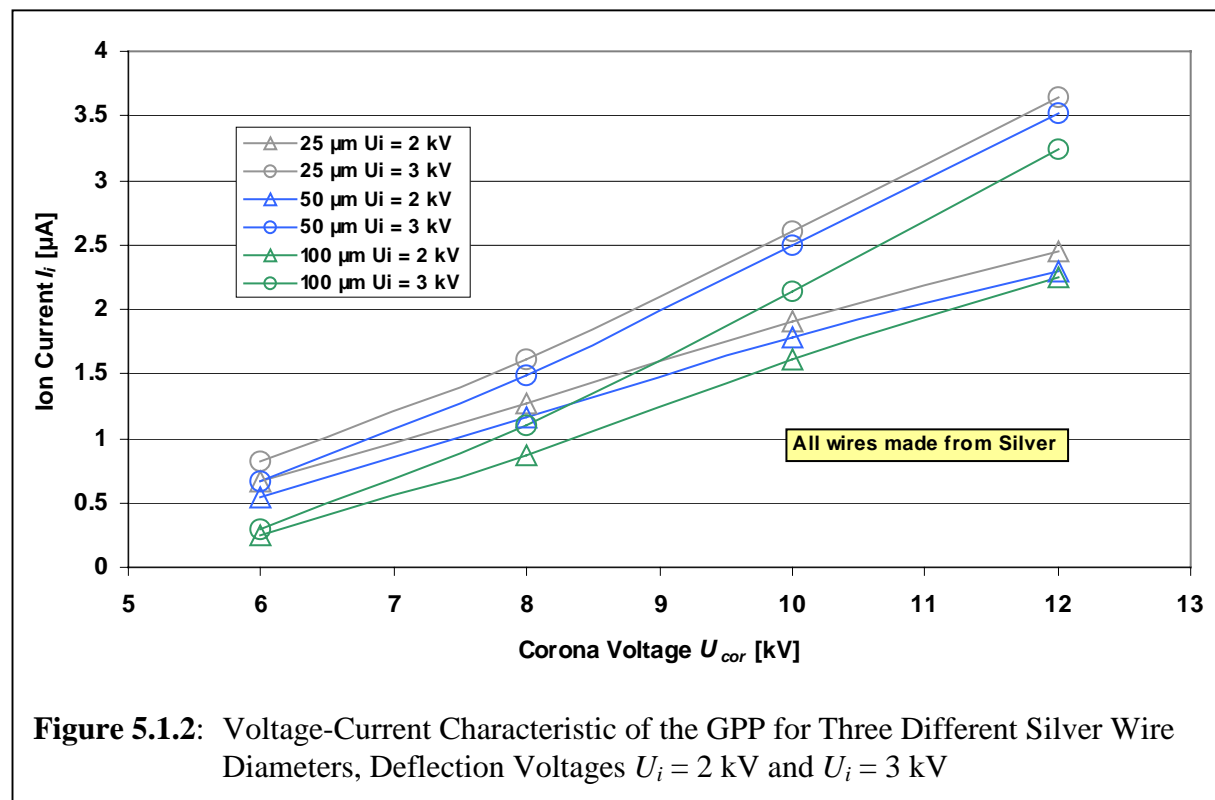
been measured for three different silver wire diameters with deflection voltages of $U_i = 2$ kV and $U_i = 3$ kV. The results are illustrated in figure 5.1.2 for wire diameters of 25 µm, 50 µm and 100 µm. Figure 5.1.2 shows that the ion current increases with decreasing wire diameter. This is expected, since the electric field strength at the wire surface is reciprocally proportional to the wire diameter.

5.1.2 Electric Field in the Charging Zone

When the ion current I_i is known, the electric field distribution in the charging zone can be calculated as explained in chapter 4.2.1. For the illustration of the electric field distribution in the charging zone in figure 5.1.3, the measured current values for corona voltage of $U_{cor} = 12$ kV and deflection voltages of $U_i = 2$ kV and $U_i = 3$ kV, respectively, were taken. For 2 kV, the average measured current is $I_i(2\ kV) = 2.4$ µA, the value for 3 kV is $I_i(3\ kV) = 3.5$ µA.

The integration constant ζ in equation 4.2.10 was determined iteratively, using equations 4.2.14 and 4.2.15. For $I_i(2\ kV) = 2.4$ µA, the integration constant is $\zeta = -9.14 \cdot 10^5\ V^2$, causing the distribution of the electric field strength for $I_i(2\ kV)$ to be slightly increasing with increasing r. For $I_i(3\ kV) = 3.5$ µA, the constant is $\zeta = +1.87 \cdot 10^6\ V^2$, causing the slightly negative slope of the distribution of the electric field strength for $I_i(3\ kV)$. The resulting electric field distributions are shown in figure 5.1.3 as solid lines. The dotted lines indicate the

Figure 5.1.3: Electric Field Distribution With and Without Ionic Space Charges for $U_{cor} = 12$ kV, $U_i = 2$ kV and $U_i = 3$ kV
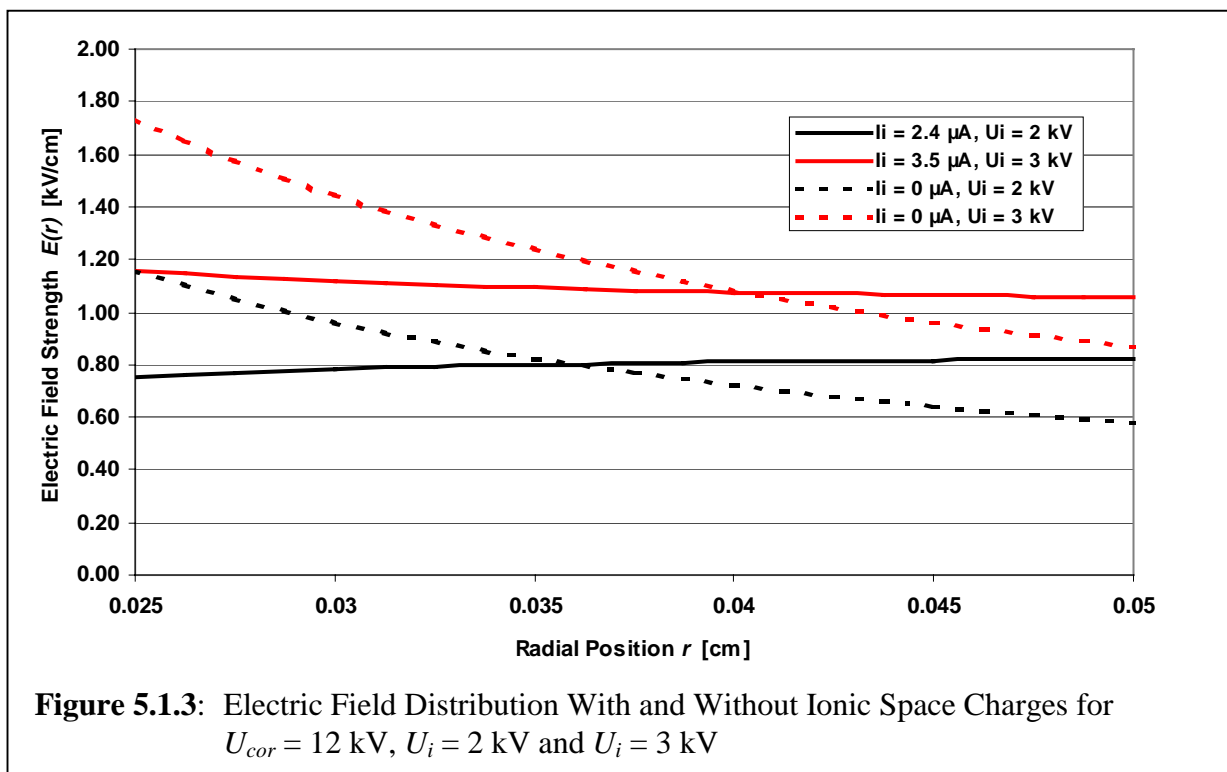
undistorted electric field in the charging zone in absence of space charges. It can be seen that the ionic space charges strongly interfere with the field distribution. In both cases, the electric field strength becomes almost constant within the entire charging zone. This means that the ionic space charges create an additional electric field distribution that has an opposite characteristic compared to the undistorted electric field of a cylindrical capacitor. Therefore, when the two fields are superposed, the inhomogeneity of the space charge field almost compensates the inhomogeneity of the undistorted electric field, resulting in an almost constant field distribution.

5.1.3 Distribution of the Ion Concentration and $n_i t_r$ Product in the Charging Zone

As described in chapter 4.4, the distribution of the ion concentration $n_i(r)$ as given by equation 4.2.17 depends on both, ion current I_i and electric field distribution $E(r)$. Figure 5.1.4 shows the spatial ion distribution in the charging zone for the two cases, illustrated in figure 5.1.3. Even though the ion current is approximately 46% higher when the GPP is operated with a deflection voltage of $U_i = 3$ kV, than when operated with $U_i = 2$ kV, the ion concentrations differ to a much lower extend. The average difference in the ion concentration is only 6.9%, ranging from –4.8% to +13.6%. The reason why the ratio of the ion concentrations does not comply with the ratio of the ion currents is the difference in the applied electric field. Since the ion concentration is reciprocally proportional to the electric field strength $E(r)$, the effect
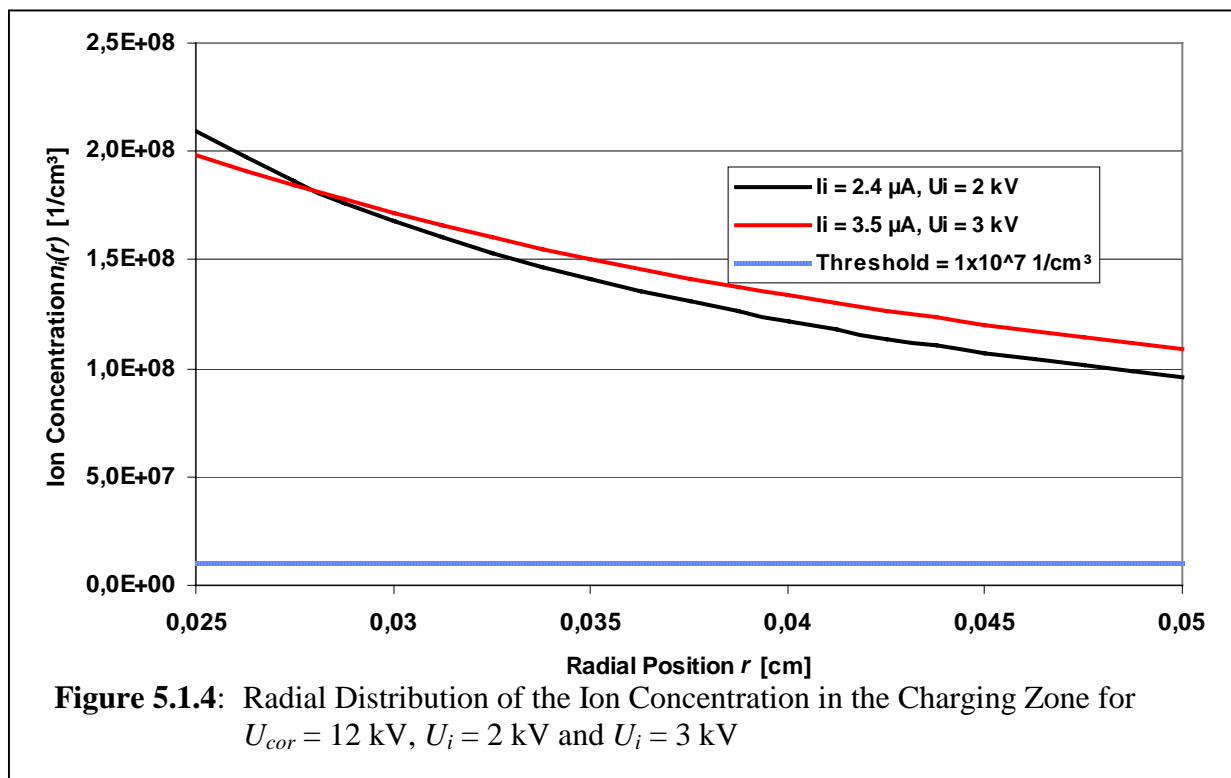
Figure 5.1.4: Radial Distribution of the Ion Concentration in the Charging Zone for $U_{cor} = 12$ kV, $U_i = 2$ kV and $U_i = 3$ kV

of the higher electric field strength almost compensates the effect of the higher ion current. As the difference in the electric field strength is the highest near the surface of the inner electrode (see figure 5.1.3), the ratio is the lowest at $r = r_i$ and the highest at $r = r_o$.

Figure 5.1.5: Radial Distribution of the $n_i t_r$ Product in the Charging Zone for $U_{cor} = 12$ kV, $U_i = 2$ kV and $U_i = 3$ kV
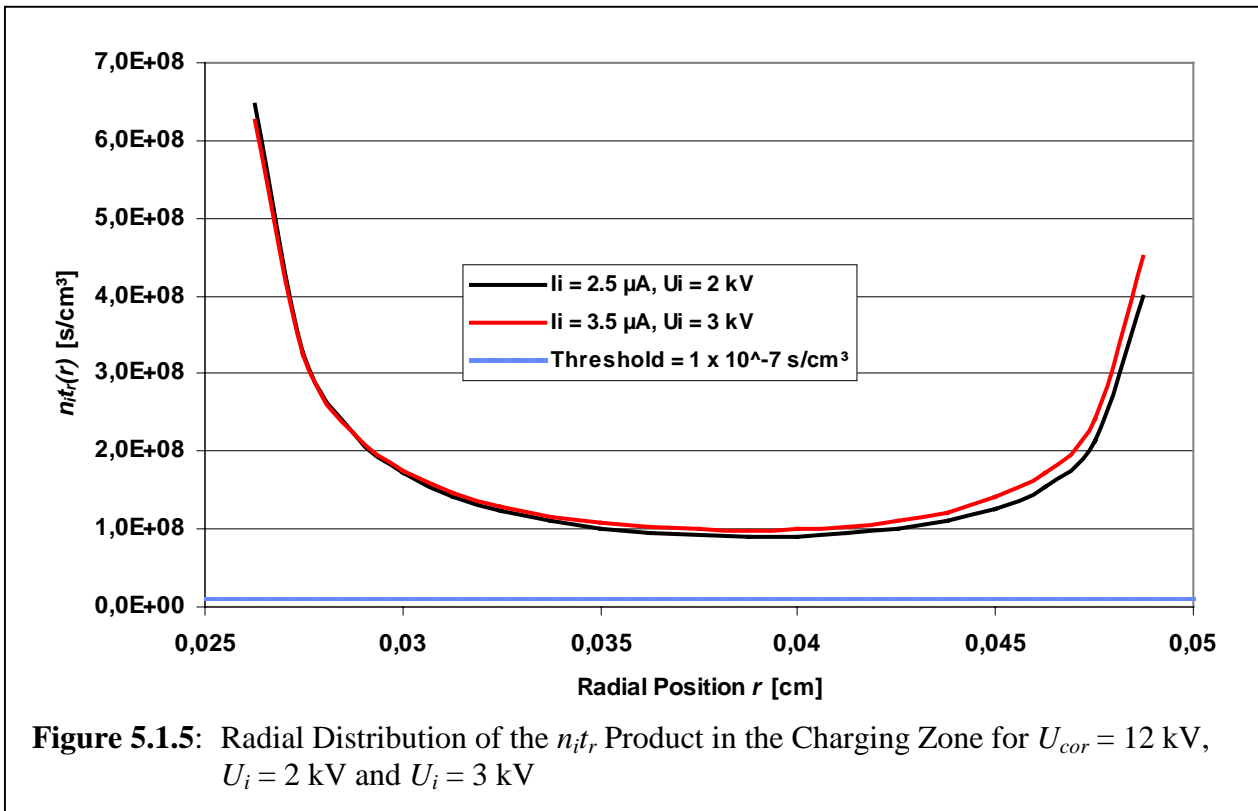
As can be seen from figure 5.1.4, the assumed ion concentration of $n_i = 10^7 \frac{1}{cm^3}$ is exceeded by a factor between 10 and 20 throughout the charging zone.

Multiplying the data of the radial distribution of the ion concentration with the data of the radial distribution of the particle residence time as shown in figure 4.3.2 gives the radial distribution of the $n_i t_r$ product in the charging zone as illustrated in figure 5.1.5. Since the radial distribution of the residence time is the same and the ion concentrations do not substantially differ for both deflection voltages, the distributions of the $n_i t_r$ product is very similar in both cases. Since the minimal value for the $n_i t_r$ product in the charging zone is approximately $1 \cdot 10^8 \frac{s}{cm^3}$, i.e. a factor of approximately 10 higher than required, the charging zone of the GPP can be considered to be a highly effective particle charger.

5.2 Gas-Particle-Separation Efficiency and Particle Losses Based on Number Concentrations

When mentioning the separation efficiency of a particle remover like the GPP, it is important to note whether it is related to the number concentration or the mass concentration of the suspended particles. Only for highly monodisperse particles these efficiencies can be considered to be identical. When talking about polydisperse atmospheric aerosols, such as the total suspended particulate matter (TSP), PM_{10} or $PM_{2.5}$, the particle mass related efficiency is dominated by a small number of *large* particles in the super-micrometer range (see volume-curve in figure 5.2.1), i.e. the efficiency for *small* particles might be underestimated. The number related efficiency is dominated by the high number of small particles in the sub-micrometer range (see number-curve in figure 5.2.1), i.e. the number related separation efficiency might underestimate the efficiency for large particles.

Figure 5.2.1: Size Distributions of Atmospheric Aerosol
(Hinds, 1982)
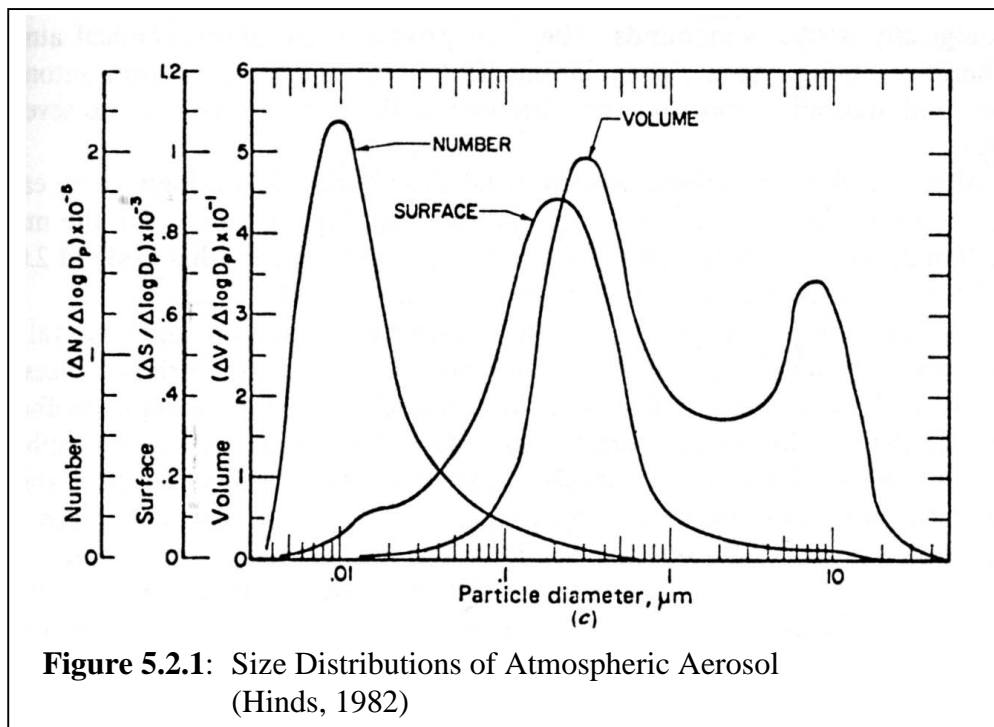
5.2.1 Investigation with Atmospheric Aerosol

As an initial measure to verify the general functionality of the GPP, measurements were performed with atmospheric aerosol to determine the separation efficiency, based on the total ambient particle number concentration and the response time of the GPP by measuring the concentration downstream of the active and inactive GPP, respectively. The set up was also used to determine the particle losses in the GPP by measuring the particle number concentration in ambient air and downstream of the inactive GPP.

5.2.1.1   Experimental Set Up

The experimental set up for the determination of the separation efficiency, based on the total ambient number concentration is shown in figure 5.2.2. The voltages are applied to the GPP by means of two high voltage supplies. The corona voltage U_{cor} could either be adjusted by computer or by hand. The supply of the deflection voltage U_i and the voltage U_f for the flow splitter was realized by means of a high resistive voltage divider. The standard values, used for these measurements are summarized in table 5.2.1.

Table 5.2.1:   Values for the Determination of the Separation Efficiency with Respect to the Total Ambient Particle Number Concentration

Deflection Voltage	Corona Voltage	Flow Splitter Voltage	Sample Flow Rate	Excess Flow Rate	Wash Flow Rate
U_i	U_{cor}	U_f	$\dot{V}_{Sample}$	$\dot{V}_{Excess}$	$\dot{V}_{Wash}$
2 kV	5 kV – 10 kV	1.255 kV	3 l/min	13.67 l/min	5.6 l/min

To measure the particle concentration in the sample flow, a condensation particle counter (TSI, CPC Model 3022) is used. Since the inlet flow of the CPC is either 0.3 l/min or 1.5 l/min and the sample flow from the GPP is 3 l/min, a flow splitter downstream of the GPP was employed (not shown in the figure). An additional three way valve between the flow splitter and the CPC allowed to alternatively measure the total particle concentration downstream of the GPP or in ambient air to allow the determination of the particle losses in the GPP. A computer software was used to read the concentrations from the CPC and to adjust the corona voltage via a relay circuit. The software allows to apply default voltage levels and to download and store the concentration in dedicated time steps.

5.2.1.2   Results

As described in table 5.2.1, the separation efficiency was determined for a corona voltage spectrum, ranging from $U_{cor} = 5$ kV to $U_{cor} = 10$ kV for a deflection voltage of $U_i = 2$ kV. A deflection voltage of $U_i = 3$ kV has also been investigated, but did not show a substantial difference to the experiments with $U_i = 2$ kV. The total number concentration in the laboratory air was quite stable at $c_N \approx 5000$ cm^{-3}. For the efficiency, the number concentrations downstream of the GPP were measured with the GPP switched on or off,

respectively. Altogether 98 experimental runs were carried out. The efficiency η_N was then calculated with equation 5.2.1

$$\eta_N = \left[1 - \frac{c_{N.on}}{c_{N,off}} \right] \cdot 100\% \qquad\qquad (\text{eq. } 5.2.1)$$

The resulting efficiency is plotted against the corona voltage in figure 5.2.3. As expected, the efficiency increases with increasing corona voltage and reaches a maximum of approximately 96% for a corona voltage of 10 kV. The standard deviation of the efficiency is given in the figure for every investigated corona voltage. The errors bars in the graph indicate the range of measured separation efficiencies, i.e. minimum and maximum.
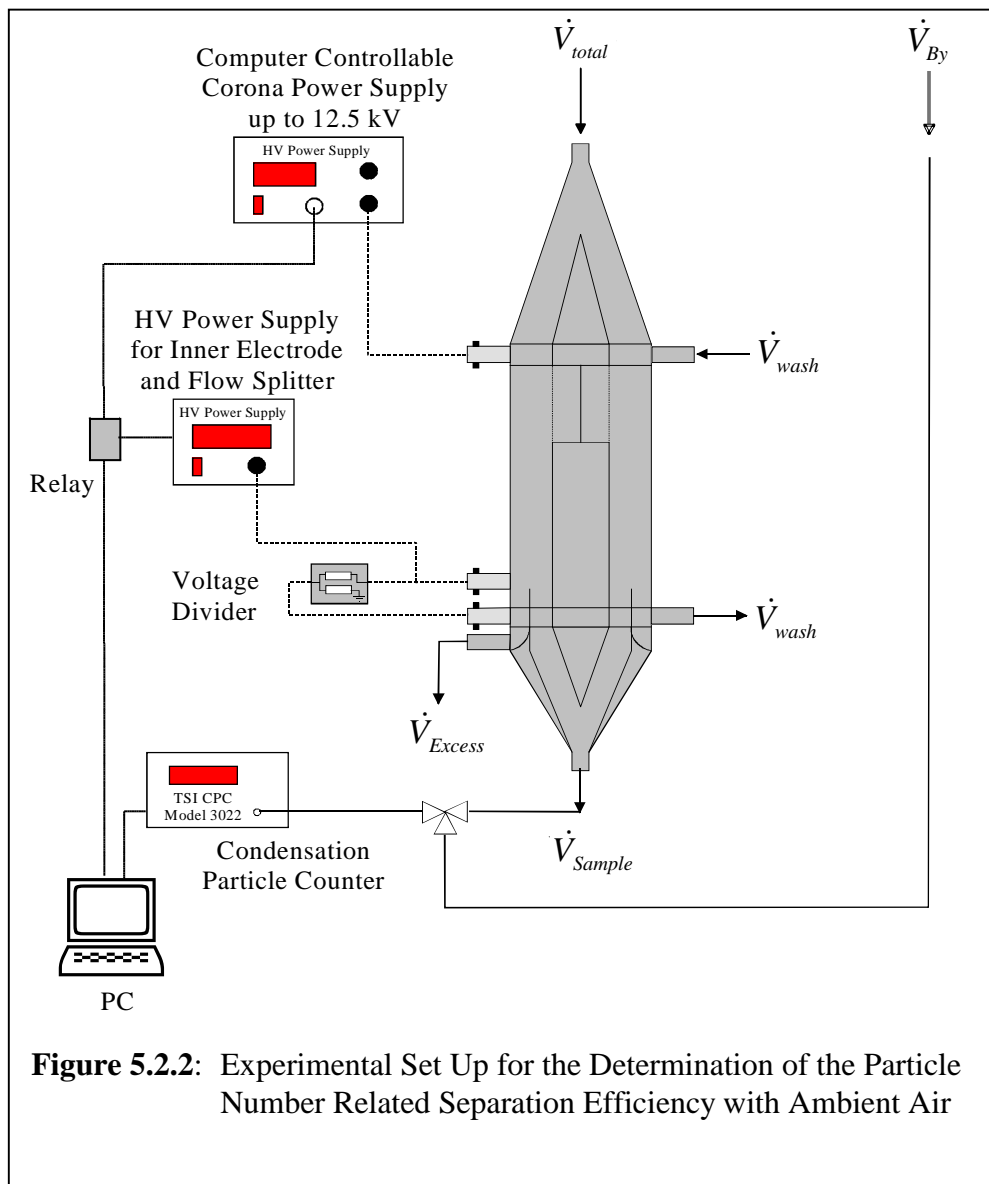
Figure 5.2.2: Experimental Set Up for the Determination of the Particle Number Related Separation Efficiency with Ambient Air

Figure 5.2.3: Separation Efficiency of the GPP Based on Total Ambient Particle Number Concentrations
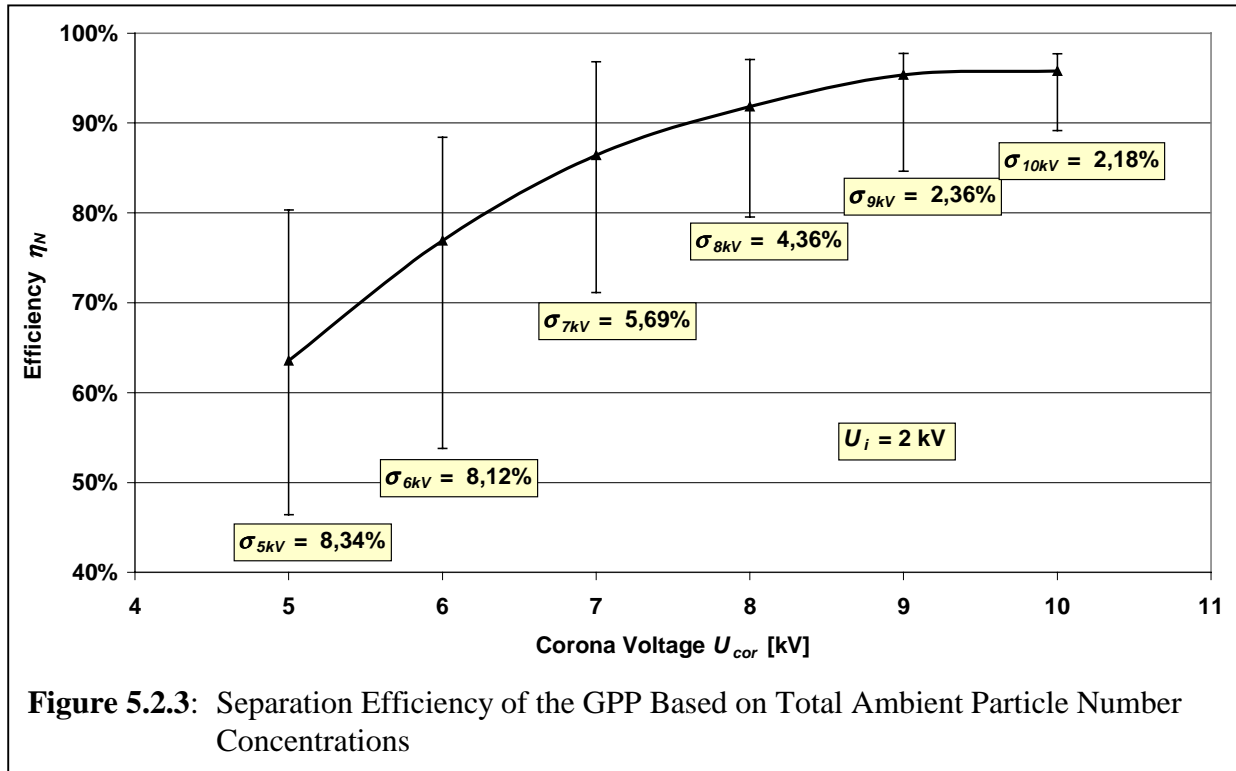
It is assumed that the remaining 4% of particles penetrating through the GPP are uncharged nanoparticles as it is well known that nanoparticles do not get efficiently charged by a corona discharge. Due to their low surface area and mass (see figure 5.2.1), nanoparticles only have a negligible effect on most of the possible downstream processes like particle mass concentration measurement in a differential mass measurement system, e.g. the Differential TEOM®.

During each experimental run, the dynamic response time and the dead time of the GPP were recorded. The t_{90} time constant, i.e. the time until the concentration reaches 90% of its final value after a switching, was found to be approximately 7 s. The dead time, i.e. the time after a switching until the particle counter showed a response, was approx. 3 s.

Figure 5.2.4 shows the measured ambient particle number concentration, measured through the bypass, against the concentration measured downstream of the inactive GPP. The dotted line indicates the 1:1 line, while the solid line shows the regression over all measured data pairs. The resulting regression function $y = 0.99 \cdot x$ shows that only approx. 1.3% of the total particle number concentration get lost in the GPP.

Figure 5.2.4: Ambient Particle Number Concentration versus Particle Number
Concentration Downstream of Inactive GPP
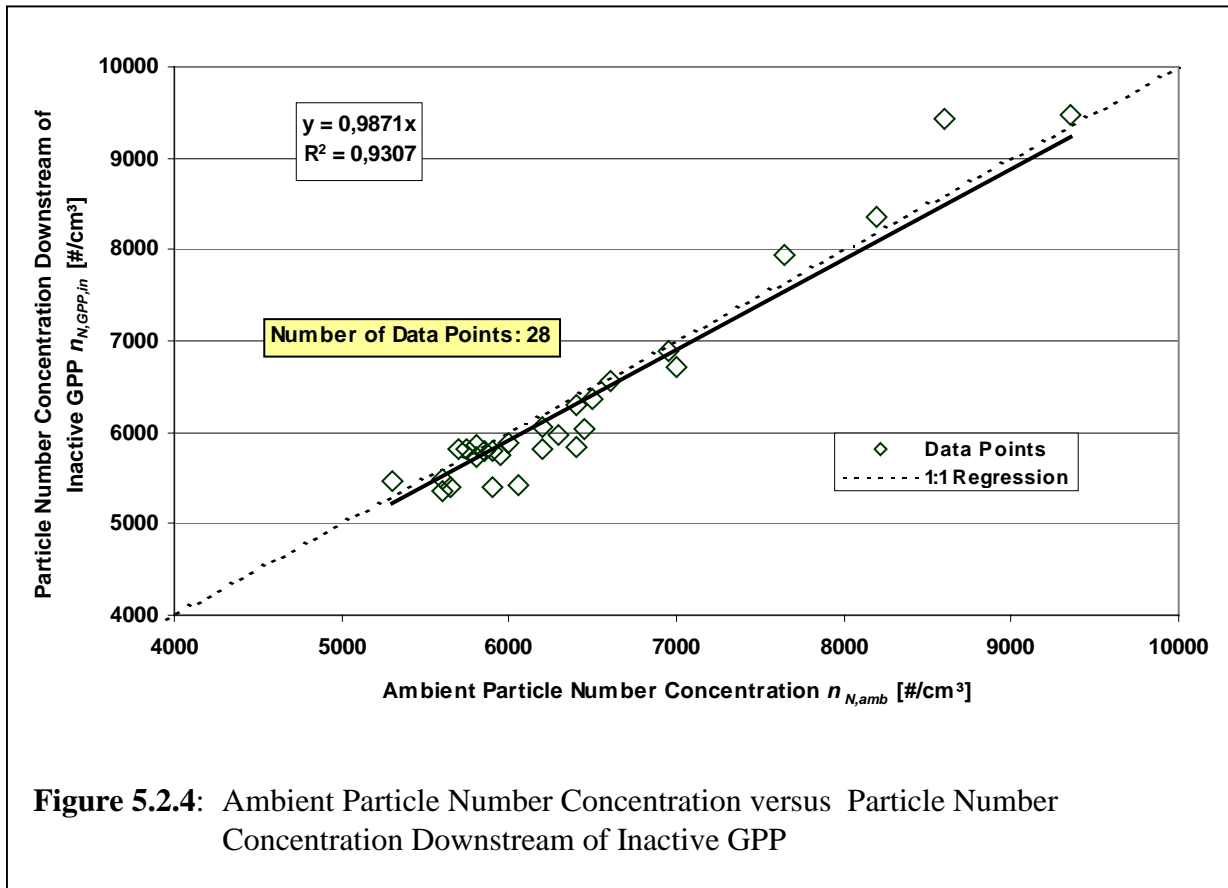
5.2.2   Investigation With Fine Particles

As the investigations with atmospheric aerosol have shown, a maximum efficiency of approximately 96% concerning the total ambient particle number could be achieved. It was assumed that the remaining 4% penetrating through the GPP are uncharged nanoparticles. The investigations with defined fine particles were carried out in order to investigate the separation behaviour of nanoparticles and to draw conclusions about the lowest diameter of particles that get efficiently charged in the GPP.

5.2.2.1   Experimental Set Up

A latex particle generator was used to produce fine particles with a defined sized distribution in compliance with VDI guideline 3491 (1980). Latex particle generators are widely used, as they produce particles with reproducible size distributions. For the generation, monodisperse latex particles were suspended in distilled water. The suspension was supplied by an injection pump to an atomizer that sprays the suspension into a drying tube. A particle free dry air flow was introduced into the drying tube in order to evaporate the droplets, containing the particles. The experimental set up is shown in figure 5.2.5. Due to the hydrophobic nature of latex, the particles do not contain any water after an efficient drying process. However, the evaporated

Figure 5.2.5: Experimental Set Up for the Determination of the
Separation Efficiency for Fine Particles
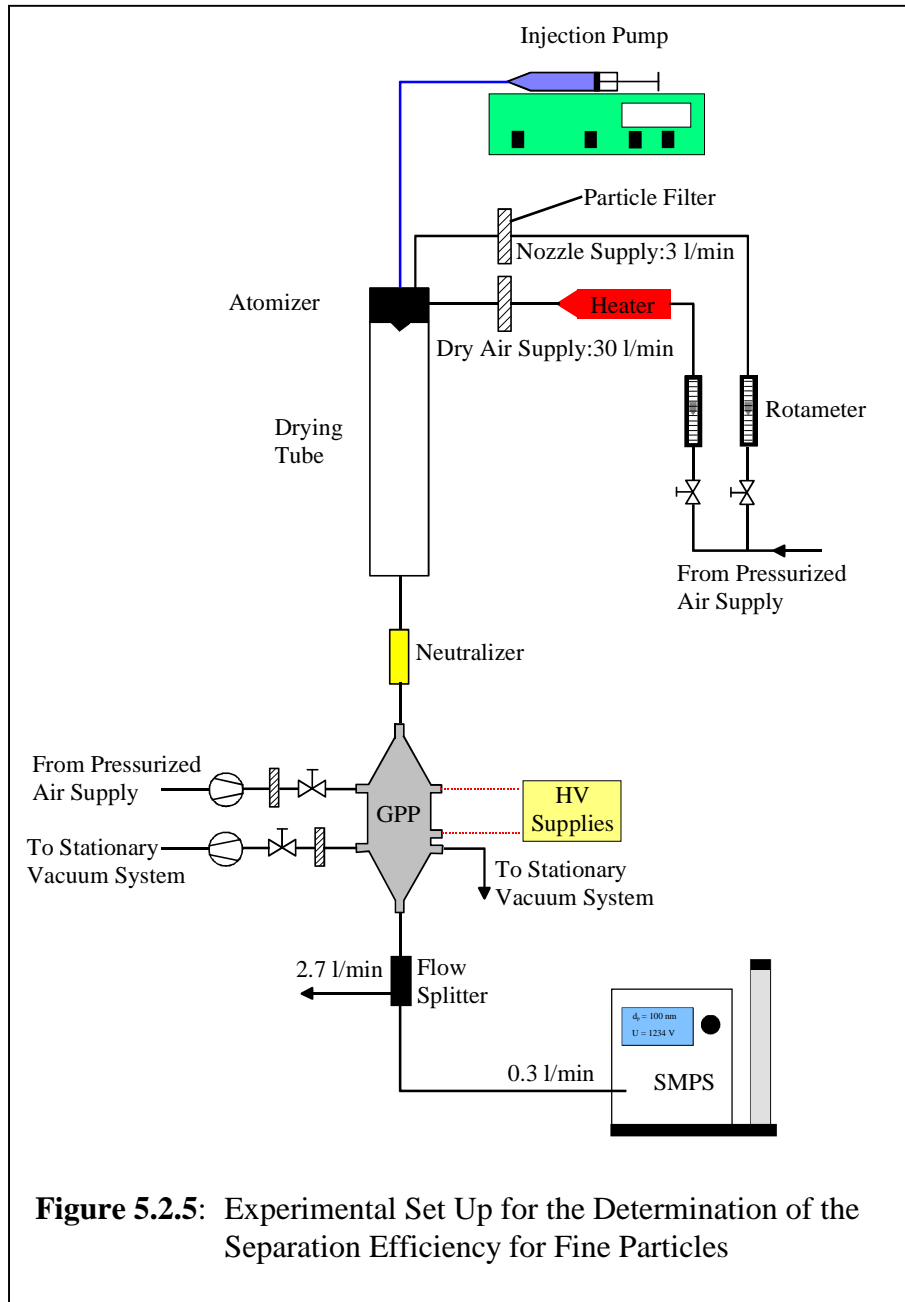
distilled water left particles with a size distribution, qualitatively similar to an atmospheric
size distribution. Therefore, the final particle size distribution comprised the background
distribution of the particles from distilled water with a high peak at the size of the latex
particles.

To determine the number size distribution of the so-produced particles, a Scanning Mobility
Particle Sizer (SMPS) was used (TSI Model 3936, 2003) along with a TSI-long Differential
Mobility Analyser (DMA). With this DMA, the SMPS system allowed to determine particle
size distributions in the size range of approximately 15 nm $\leq d_p \leq$ 700 nm. A flow splitter was
used downstream of the GPP to split the 3 l/min sample flow from the GPP into a 0.3 l/min

flow to the SMPS and a 2.7 l/min excess flow. All flow rates of the GPP were controlled with needle valves and frequently verified, using a bubble meter.

5.2.2.2 Results

Altogether five different particle sizes were investigated. Particles diameters of 24.5 nm, 48.7 nm, 89.8 nm and 254.5 nm were generated with latex particles as described above. The data for the particle size of 17.8 nm was taken from the background particles, caused by the evaporation of distilled water. The particle size of 254.5 nm was used, as this diameter is close to the diameter of the "worst case" particle (see chapter 4.6.3.2). The separation efficiency was measured with corona voltages of 6, 8, 10 and 12 kV as well as with deflection voltages of 2 and 3 kV. In figure 5.2.6, the separation efficiency is plotted versus the corona voltage for deflection voltages of 2 and 3 kV, exemplary for 89.8 nm particles. The number size distribution of the test particles is given in the lower right corner of the graph. The error bars in the graph indicate the highest and lowest measured efficiency.

It can be seen from the graph that the efficiency was consistently higher for $U_i = 3$ kV. This was observed for all investigated particle sizes (see figure 5.2.7 and 5.2.8) and gives rise to the recommendation of the use of 3 kV as deflection voltage. For 89.8 nm particles, the separation efficiency reaches 99.8% with a standard deviation of 0.19% with a corona voltage of 12 kV and deflection voltage of 3 kV. With a deflection voltage of 2 kV, the highest achieved efficiency was 98.6% with a standard deviation of 0.56%.

Figure 5.2.6: Separation Efficiency Versus Corona Voltage for $d_p = 89.8$ nm With Deflection Voltage of $U_i = 2$ kV and 3 kV

Figure 5.2.7: Separation Efficiency Versus Particle Diameter for $U_{cor} = 10$ kV and $U_i = 2$ kV and 3 kV

Figure 5.2.8: Separation Efficiency Versus Particle Diameter for $U_{cor} = 12$ kV and $U_i = 2$ kV and 3 kV
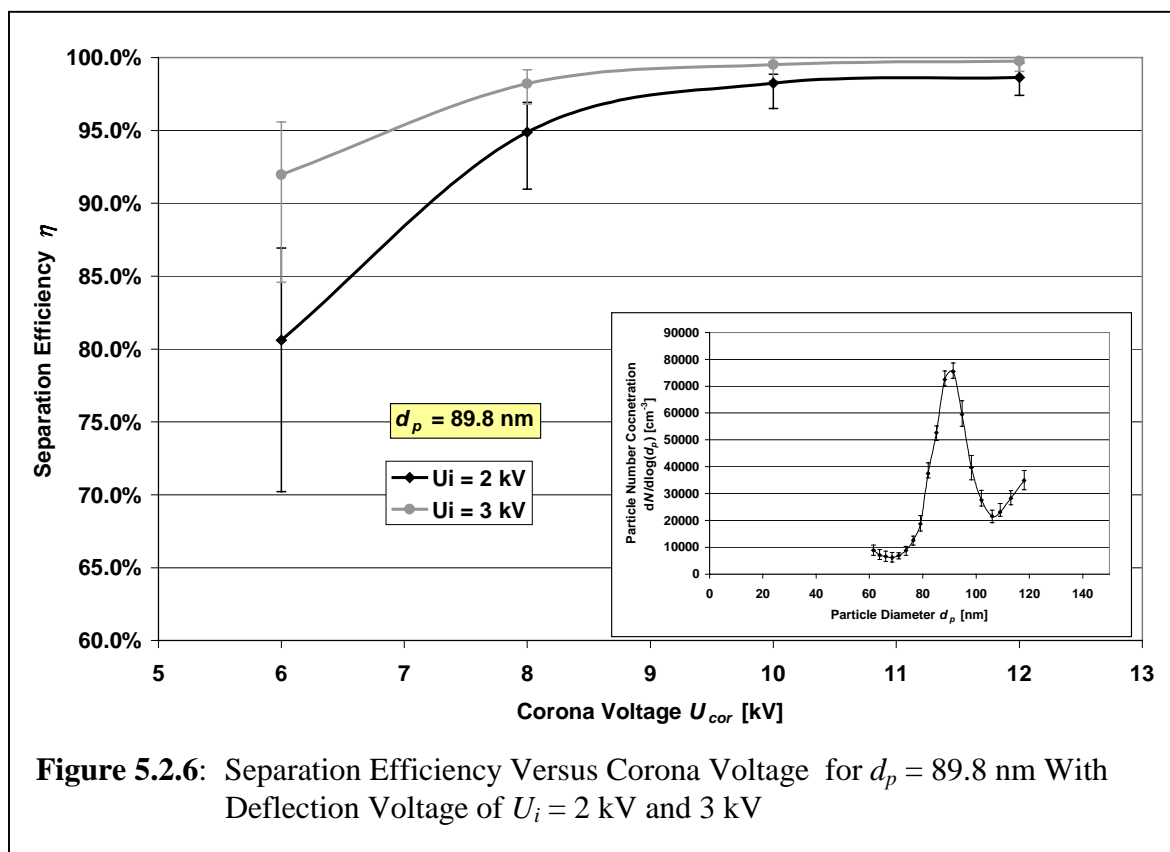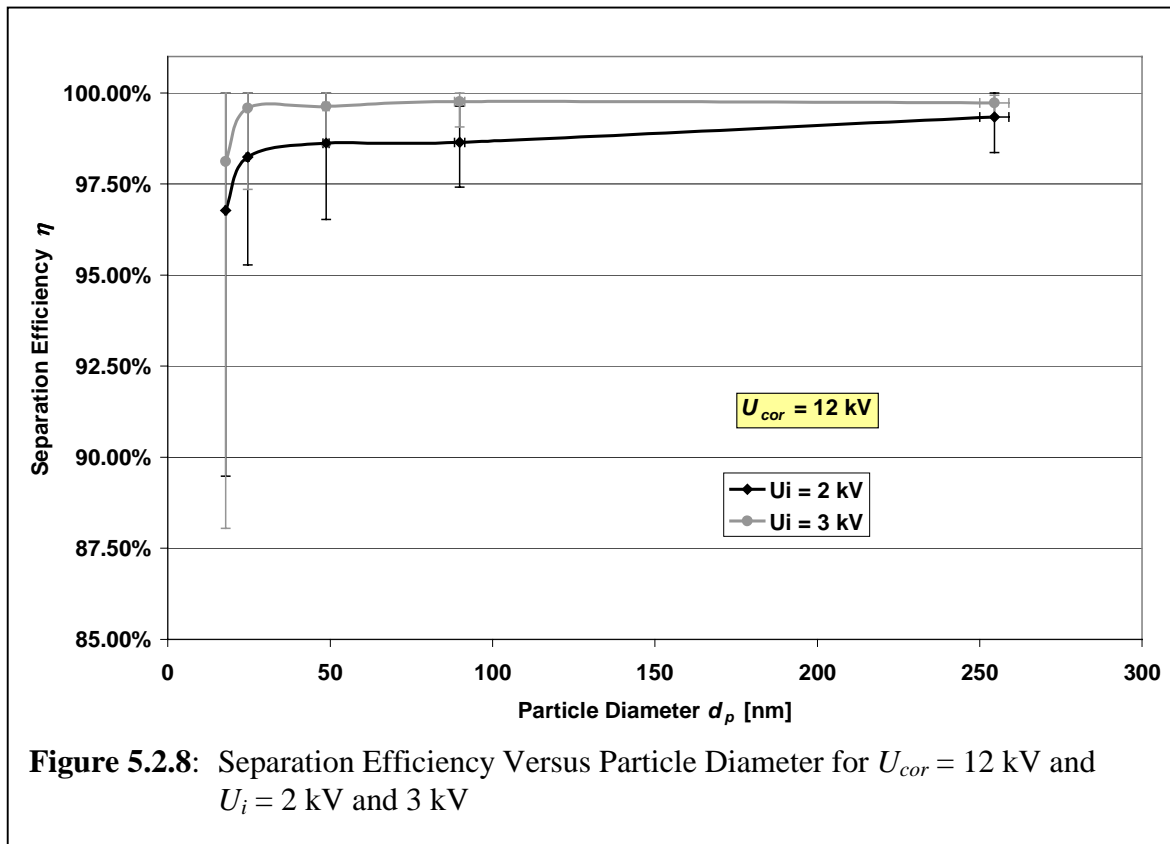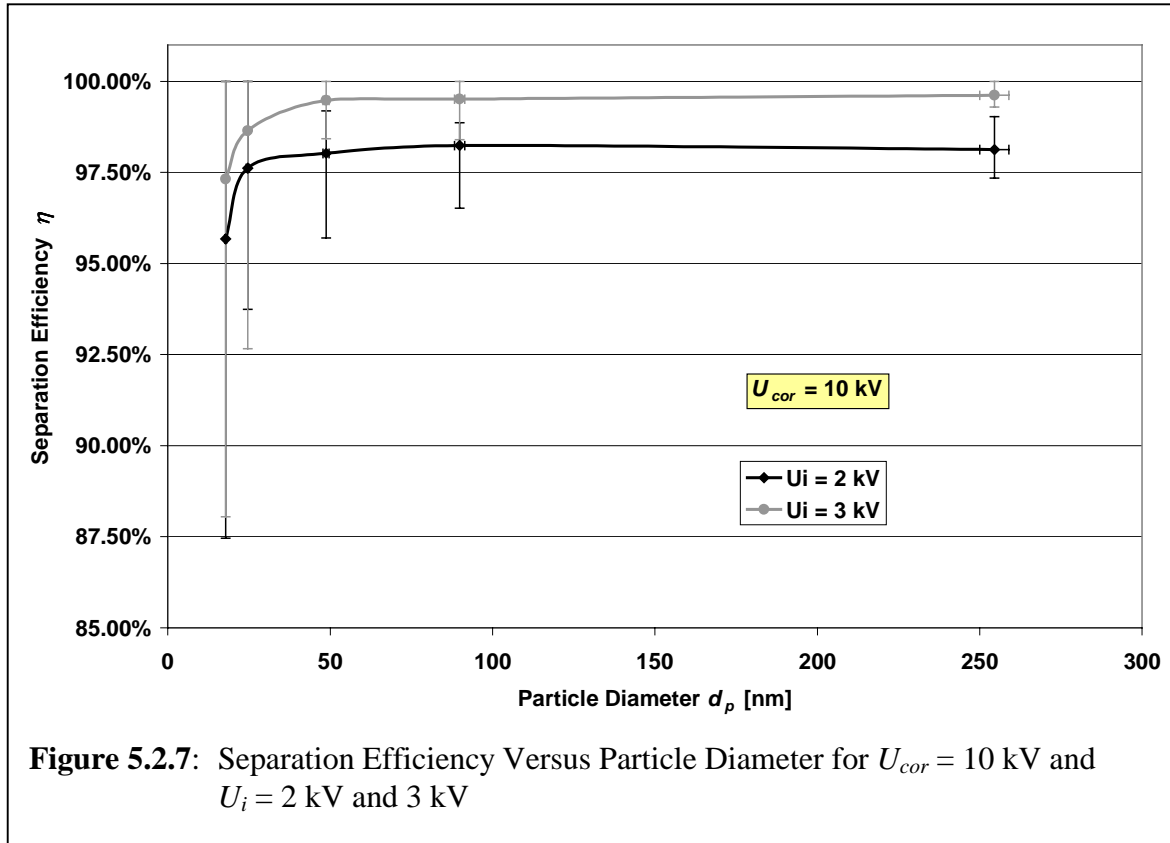
Figure 5.2.7 shows the separation efficiency versus the particle diameter for $U_{cor} = 10$ kV. For $U_{cor} = 12$ kV, the efficiency data is shown in figure 5.2.8. Both graphs show that the efficiency is significantly lower for 18 nm particles. With a corona voltage of 10 kV, the

efficiency is already decreased for a particle diameter of 25 nm. However, with corona voltage of 12 kV and a deflection voltage of 3 kV, the efficiency is >99.5% for particle diameters above 25 nm. For the investigated "worst case" particle, the separation efficiency is 99.7% with a standard deviation of 0.18% and 99.3% with a standard deviation of 0.58% for 12 kV corona voltage and a deflection voltage of 3 kV and 2 kV, respectively. It can be concluded that the GPP reaches near 100% gas particle separation efficiency for fine particles with diameters above 25 nm.

Table 5.2.1 summarizes the results for with corona voltages of 10 kV and 12 kV.

Table 5.2.2:   Separation Efficiencies With Deflection Voltages of 2 kV and 3 kV, and
Corona Voltages of 10 kV and 12 kV

	d_p[nm]	17.8	24.5	48.7	89.8	254.5
U_{cor} = 10 kV	η_{2kV}	95.7%	97.6%	98.0%	98.2%	98.1%
	σ_{2kV}	4.51%	2.24%	0.98%	0.58%	0.56%
	η_{3kV}	97.3%	98.6%	99.5%	99.5%	99.6%
	σ_{3kV}	4.25%	1.89%	0.47%	0.38%	0.23%
U_{cor} = 12 kV	η_{2kV}	96.8%	98.2%	98.6%	98.6%	99.3%
	σ_{2kV}	2.88%	1.44%	0.86%	0.56%	0.58%
	η_{3kV}	98.1%	99.6%	99.6%	99.8%	99.7%
	σ_{3kV}	2.95%	0.77%	0.40%	0.19%	0.18%

5.3 Gas-Particle-Separation Efficiency For Coarse Particles Based on Mass Concentrations

To investigate the mass related separation efficiency of the GPP, a TEOM® particle mass sensor (Series 1400a, 1991) as described in chapter 2.3.1was used. The sensor was challenged with Sodium Chloride (NaCl) particles. When operating at a low relative humidity level, NaCl particles show no substantial water content and can be considered to be inert. I.e. the mass of the sample filter inside the TEOM sensor does not get affected by evaporation of deposited material.

5.3.1 Experimental Set Up

The Sodium Chloride aerosol was generated with an ultrasonic atomiser that was fed by an injection pump containing NaCl, solved in distilled water. The atomiser produces droplets of the suspension. It is situated at the centre of the bottom of a drying tube. Dry air was
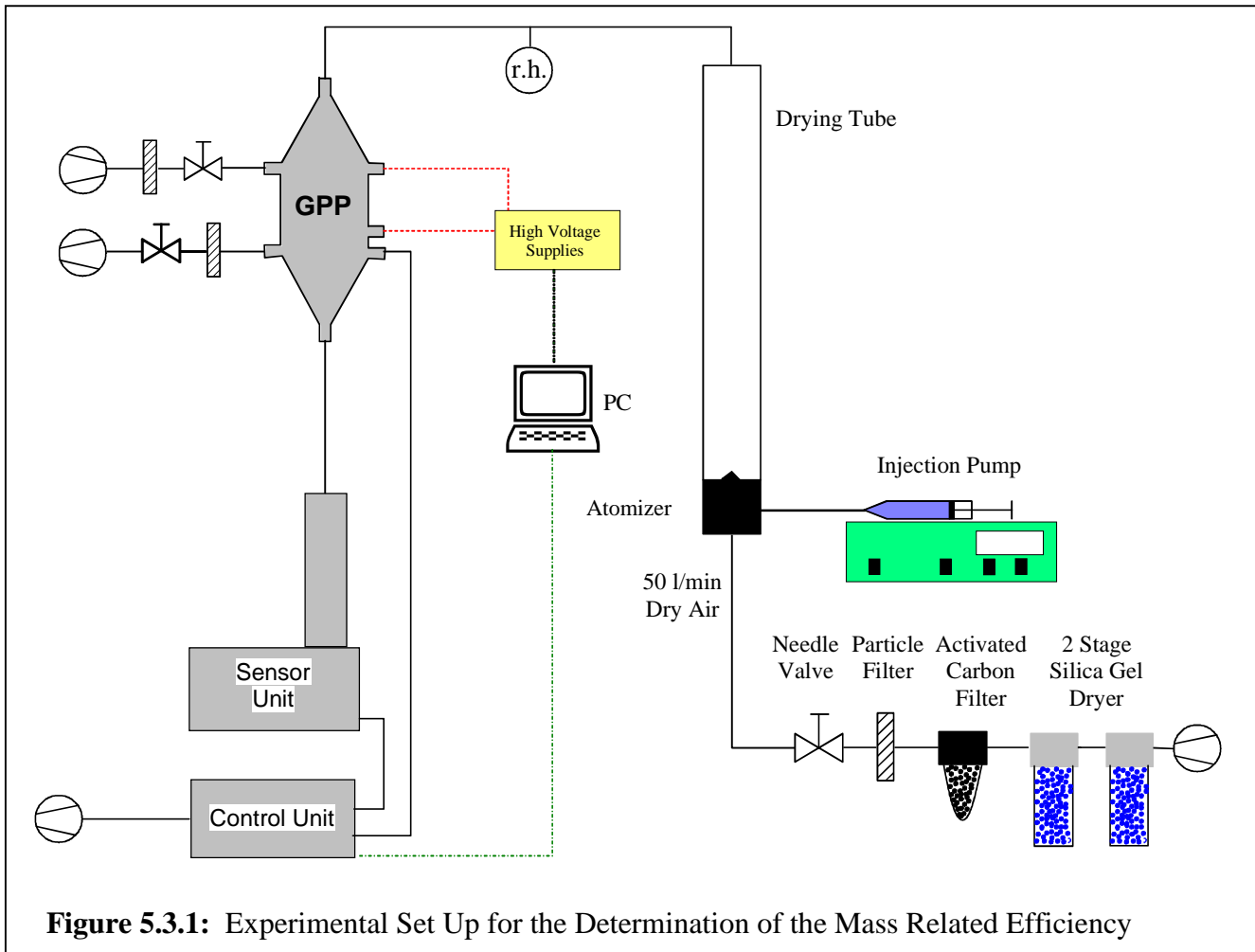
Figure 5.3.1: Experimental Set Up for the Determination of the Mass Related Efficiency

introduced into the drying tube at a flow rate of 50 l/min. Before entering the drying tube, the air passed a 2-stage silica gel dryer, an activated carbon filter and a particle filter. The flow rate was maintained with a needle valve. The relative humidity of the dry air after the dryers and filters was between 5% and 10% according to the condition of the silica gel. In the drying tube, the water droplets evaporate, leaving only Sodium Chloride particles with relatively monodisperse size distribution $(\sigma_g \approx 1.2)$. Different NaCl suspensions were used to allow investigations on variable particle diameters and concentrations.

Downstream of the drying tube, the relative humidity of the sample aerosol was measured with a humidity sensor. The wash flow rate of 5.6 l/min was maintained with needle valves at the wash flow inlet an outlet. The excess flow of 13.67 l/min and the sample flow of 3 l/min were maintained by the internal mass flow controllers of the TEOM®. A computer software was used to control the high voltage supplies for the deflection voltage U_i (which, due to the attached voltage divider, also determines the voltage U_f of the flow splitter) and the corona voltage U_{cor}.

5.3.2 Results

Altogether 5 different NaCl suspensions were used for the investigations. The solutions differed in the amount of solved NaCl (see table 5.3.1). The feed rate of the injection pump was set to 10 ml/h for all experimental runs, assuring a fairly stable relative humidity of the aerosol of approximately 20% (re-crystallization of NaCl particles at approximately 40%). The size distribution of the aerosol was measured with an Aerodynamic Particle Sizer (APS). For each suspension the size distribution was

Table 5.3.1: Aerodynamic Diameters and Standard Deviations

Solution	d_{ae}	σ_g
0.5 g/l	4.46 µm	1.19
3 g/l	4.73 µm	1.20
10 g/l	7.09 µm	1.19
30 g/l	9.25 µm	1.20
50 g/l	10.7 µm	1.22

stable and relatively monodisperse (see figure 5.3.2). The total particle mass concentrations were relatively high (>500 µg/m³) compared to ambient concentrations. This ensured that a possible drift of the sensor frequency, as observed prior to the measurements, only had a negligible impact on the measured efficiency.

Different voltage settings have been investigated for each NaCl suspension. Deflection voltages of 2 kV and 3 kV have been used along with corona voltages of 6 kV, 8 kV, 10 kV and 13 kV. During the measurements, the voltages of the GPP were switched on and off in intervals of 5 minutes. The oscillator frequency was stored and used for further calculations as it is the only original signal of the TEOM. Figure 5.3.3 shows one example of the frequency during one experimental run. The dotted lines indicate the times when the GPP got switched on or off, respectively. It can be seen that the frequency decreases constantly when the GPP is switched off, i.e. air is particle laden, while the frequency remains at a constant level when the GPP is switched on, i.e. the air is particle free.

For the determination of the mass concentration during each 5 minute time period, the characteristic of the frequency was assumed to be a straight line with a constant slope. In order to assure that the TEOM® has reached stable conditions, a rather generously scaled transition time of 100 s after each switching was taken into account. Firstly, the slope s_f of the frequency was determined. Secondly, the total time Δt and the average frequency $\bar{f}$ during said interval Δt were calculated. The initial frequency f_0 and the final frequency f_1 during Δt were then calculated by
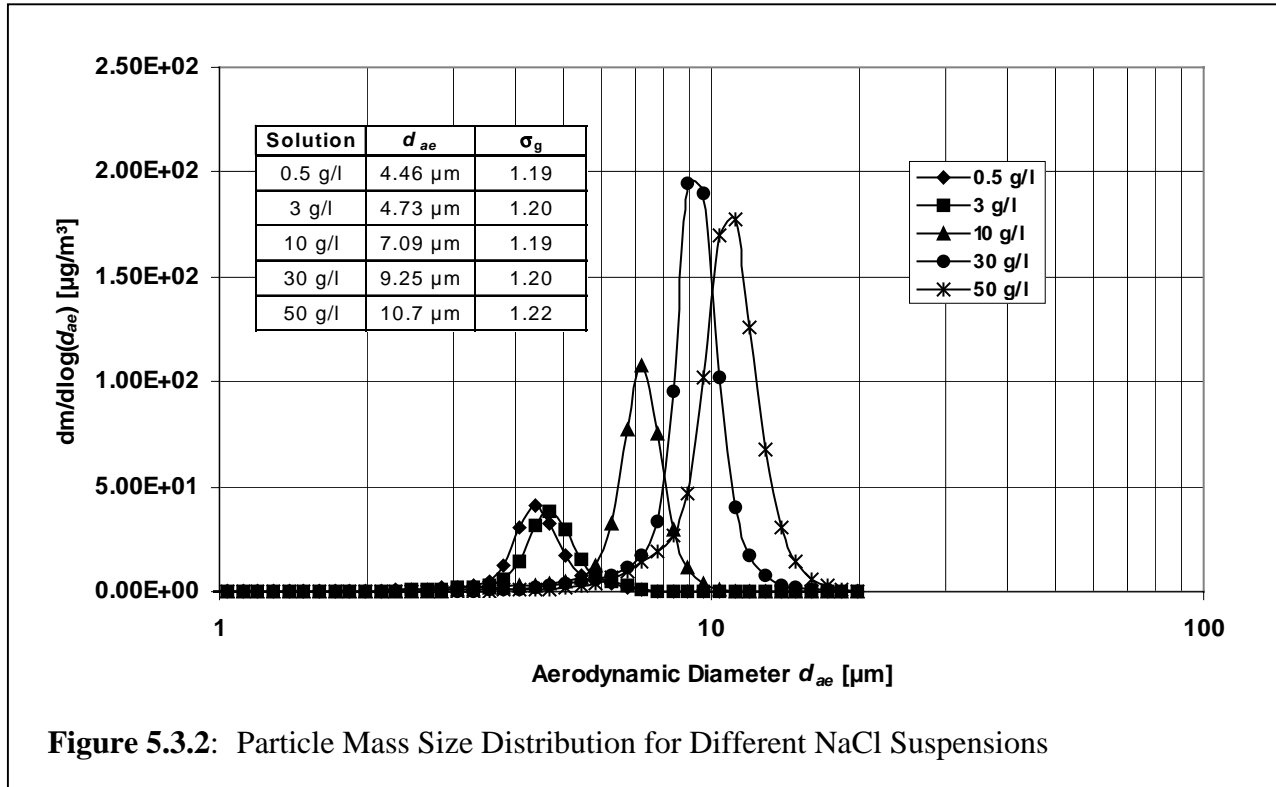
Figure 5.3.2: Particle Mass Size Distribution for Different NaCl Suspensions

$$f_0 = \bar{f} - s_f \frac{\Delta t}{2} \qquad \text{(eq. 5.3.1)}$$

$$f_1 = \bar{f} + s_f \frac{\Delta t}{2} \qquad \text{(eq. 5.3.2)}$$

The total mass gain of the filter during the time interval is then given by equation 2.3.2

$$\Delta m = K_0 \left(\frac{1}{f_0^{\,2}} - \frac{1}{f_1^{\,2}} \right) \qquad \text{(eq. 5.3.3)}$$

The average mass concentration c_m during the time interval Δt may then be expressed as

$$c_m = \frac{\Delta m}{\dot{V} \cdot \Delta t} \qquad \text{(eq. 5.3.4)}$$

The separation efficiency η is derived from the mass concentrations $c_{m,on}$ (GPP switched on) and $c_{m,off}$ (GPP switched off):

$$\eta_m = \left(1 - \frac{c_{m,on}}{c_{m,off}} \right) \qquad \text{(eq. 5.3.5)}$$

Figure 5.3.4 shows the measured separation efficiency versus the corona voltage exemplary for one particle diameter ($d_p = 9.25$ µm) for a deflection voltage of $U_i = 2$ kV. The results of the experimental runs with other particle diameters are very similar. The experimental results of the separation efficiencies are given in table 5.3.2 for the different voltage settings. The values given in the table are averages over all investigated particle diameters.
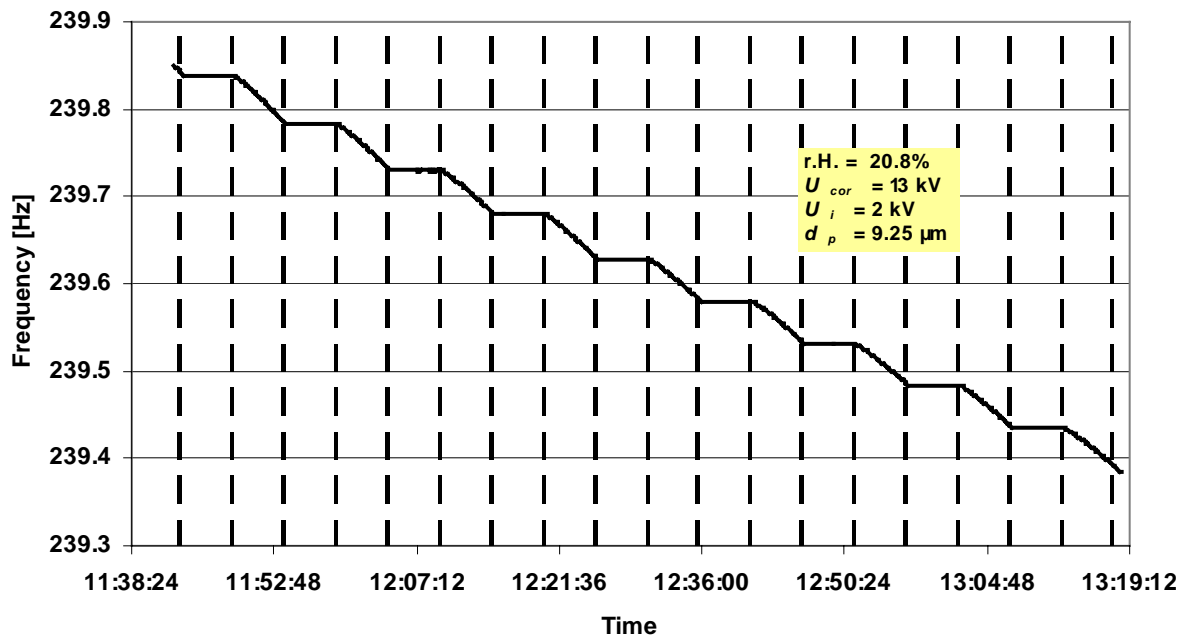
Figure 5.3.3: Frequency of the Oscillator for one Experimental Run With d_p = 9.25 µm, U_{cor} = 13 kV, U_i = 2 kV
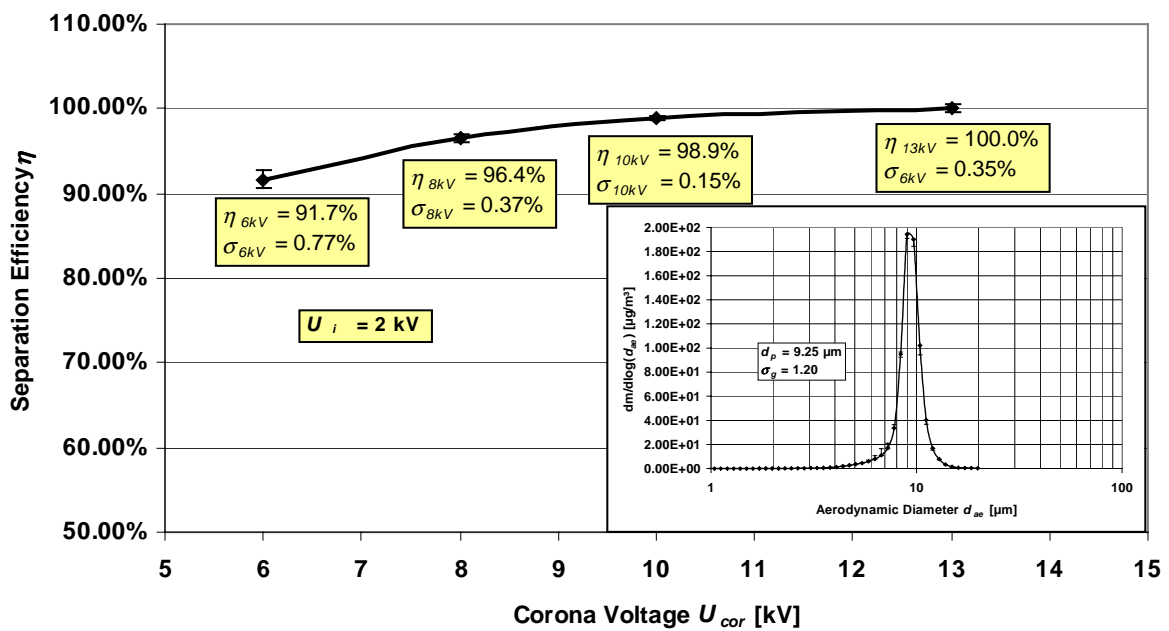
Figure 5.3.4: Separation Efficiency Versus Corona Voltage for d_p = 9.25 µm With Deflection Voltage U_i = 2 kV

Table 5.3.2: Separation Efficiencies

U_i [kV]	2				3			
U_{cor} [kV]	6	8	10	13	6	8	10	13
η	90.7%	96.2%	99.1%	100.0%	94.5%	97.7%	99.4%	99.9%

The efficiency reaches its final value of approximately 100% for a corona voltage of 13 kV. Figure 5.3.5 shows the separation efficiency of the GPP versus the particle diameter for a corona voltage of $U_{cor} = 13$ kV and deflection voltage of 2 kV and 3 kV. As can be seen from the graph, the separation efficiency is approximately 100% for all investigated particle diameters and does not get substantially affected by the deflection voltage. Separation efficiencies of above 100% are most likely due to an improper zero point of the TEOM® frequency. This is underlined by the fact that prior to the measurements, the frequency of the TEOM showed unstable behaviour when operating with particle free air. The mass concentrations as calculated by the TEOM® were mainly in a range between –0.5 µg/m³ and –3 µg/m³. The generation of high particle mass concentrations could lower but obviously not eliminate the effect.

With respect to the results with fine particles (chapter 5.2.2) it can be concluded that the GPP separates gas and particles with an efficiency of approximately 100% for all particles in the size range of 25 nm $\leq d_p \leq$ 10.7 µm. In the intermediate size range between sizes investigated in chapter 5.2.2 and here, the efficiency is not expected to be below those, reported here, as the charging efficiency shows a minimum for approx. 250 nm particles, whereas the efficiency increases for both, smaller and larger particle sizes (see figure 3.3.6). Therefore the lowest separation efficiency is expected for a particle diameter of 250 nm which has shown to be very near 100 % (see figures 5.2.7 and 5.2.8).

d_p	4.46 µm	4.73 µm	7.09 µm	9.25 µm	10.7 µm
σ_g	1.19	1.2	1.19	1.2	1.22
η_{2kV}	99.7%	100.3%	100.1%	100.0%	99.9%
σ_{2kV}	1.34%	1.41%	0.04%	0.35%	0.22%
η_{3kV}	100.4%	99.2%	99.8%	100.3%	99.9%
σ_{3kV}	1.71%	0.61%	0.28%	0.40%	0.22%
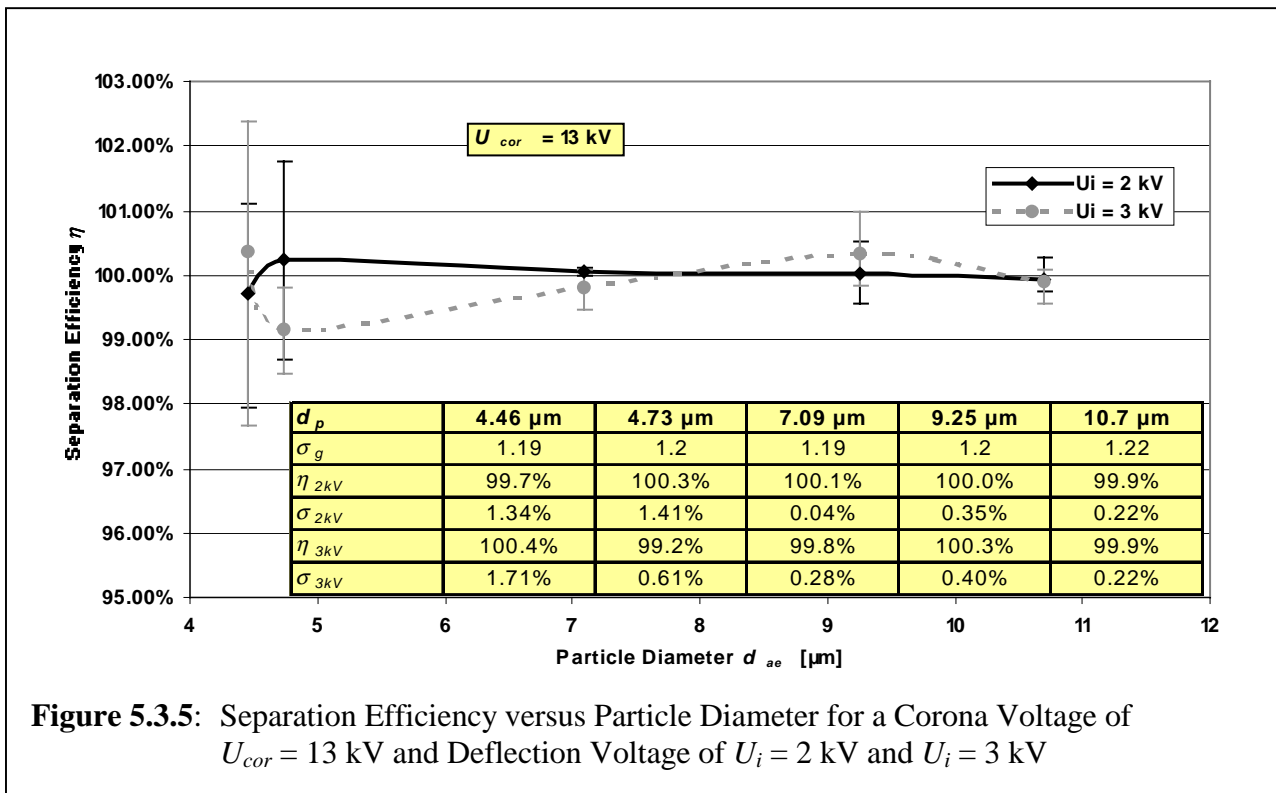
Figure 5.3.5: Separation Efficiency versus Particle Diameter for a Corona Voltage of $U_{cor} = 13$ kV and Deflection Voltage of $U_i = 2$ kV and $U_i = 3$ kV

5.4 Investigations on the Gas Phase of the Sample Flow and Wash Flow

The GPP was designed to separate gas and particles with minimal effect on the gas phase of the aerosol. The major influence on the gas phase in corona discharge regions is due to gases formed by the corona, i.e. ozone (Boelter et al., 1997; Viner et al., 1992) and oxides of nitrogen (Brandvold et al., 1989; Martinez et al., 1996). To minimize the effect on the gas phase of the sample flow, the corona was optimised with respect to the corona wire diameter and material. A particle free wash flow is introduced around the corona wire to convectively transport the corona gases out of the GPP and avoid a mixing with the sample flow (see chapter 4.7).

The formation of ozone and nitrogen oxides are multi-step reactions with polar intermediate species, i.e. ions (see chapter 3.4). The wash flow transports the non-polar final product of the reactions (O_3 or NO_x) away from the discharge region. Those ions that did not finally react within the grid electrode are transported through the grid into the charging zone due to Coulomb forces. Here they either transfer their charge to the particles or chemically react to form ozone or oxides of nitrogen in the aerosol flow. Therefore, to a certain extend, the O_3 and NO_x concentration will always be elevated in the sample flow, when the corona is active.

To determine the effectiveness of the different measures for a minimization of the influence on the gas phase, the ozone and nitrogen dioxide concentrations were measured downstream of the GPP for different wire diameters and materials as well as with different wash flow rates and different polarity. The nitrogen oxide concentrations were also measured. Since NO is an intermediate species in the formation of ozone and nitrogen dioxide, the concentration did not show a reproducible correlation to the applied voltages or the measured currents. Therefore the measurements of nitrogen oxide will not be covered in this chapter.

5.4.1 Experimental Set Up

The gas concentrations were measured, using an ozone analyser (Dasibi Environmental Corporation Model 1008, 1983) and an NO_x Analyser (Thermo Instruments, Model TE42C, 1995). Both analysers were simultaneously connected to the outlet of the GPP as shown in figure 5.4.1. The measurements were performed with laboratory air. Before and after each experimental run, the background concentration of O_3 and NO_2 in the air was measured. Since the analysers do not offer an easy download of the data to a computer, the current concentrations were recorded manually from the display on the control panel.

The wash flow rate of the GPP was maintained by needle valves at its inlet and outlet. The excess flow was controlled by an internal mass flow controller of a TEOM® as it offers to precisely adjust the flow rate in the required range.

To measure the gas concentration in the *sample* flow, the sample outlet was connected to the gas analysers. For the determination of the concentration in the *wash* flow, the wash flow outlet was connected to the gas analysers and the sample flow maintained with a needle valve. To accurately adjust the flow rate of 3 l/min or 5.6 l/min, respectively, a bypass, equipped with a precise needle valve was connected to the two gas analysers. All flow rates were frequently verified, using a bubble meter.
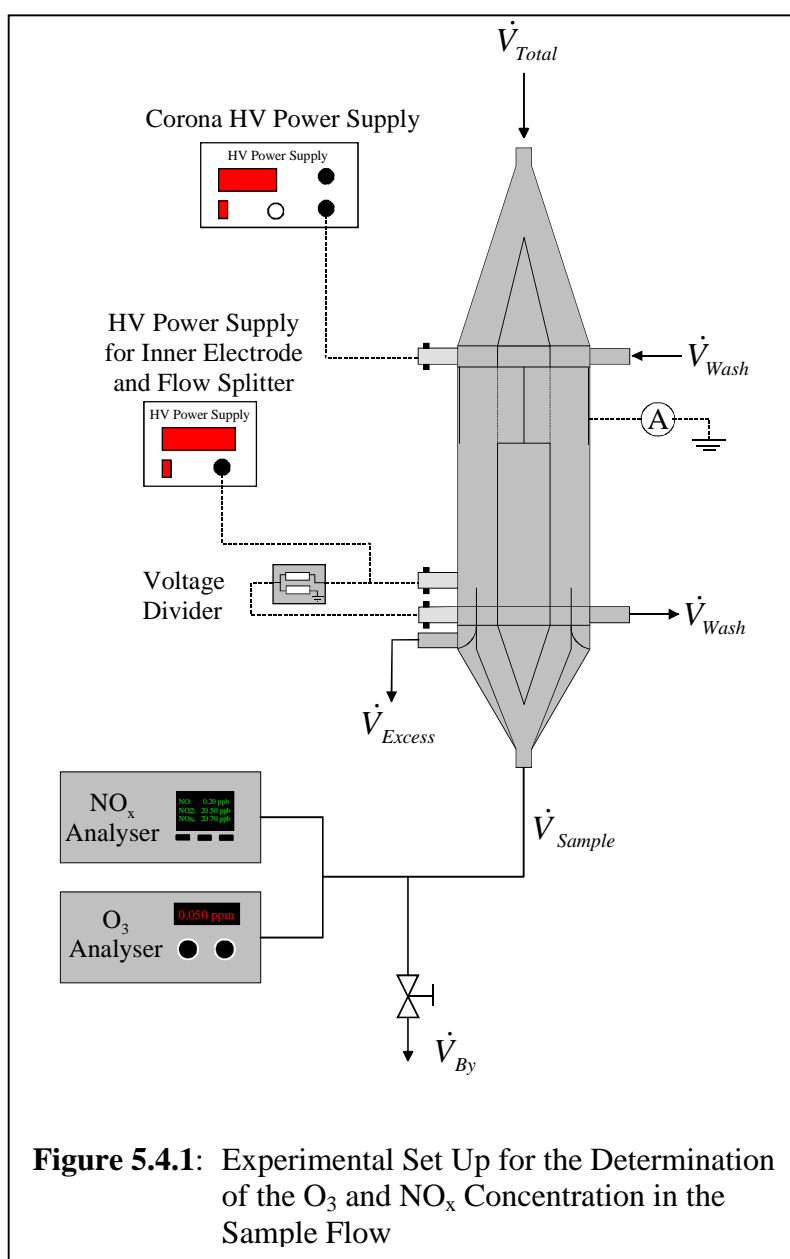
Figure 5.4.1: Experimental Set Up for the Determination of the O_3 and NO_x Concentration in the Sample Flow

5.4.2 **Verification of the Wash Flow Rate**

To minimize mixing of the wash flow with the aerosol flow, the wash flow rate was calculated such that the average velocity of the wash flow is identical to the velocity of the aerosol in the charging zone. In that case, the wash flow rate is 5.6 l/min. In order to verify that this theoretically calculated flow rate really causes the lowest mixing of the two flows, the ozone concentration in the sample flow was measured, while the wash flow rate was varied from 0 l/min to 6 l/min for a deflection voltage of $U_i = 2$ kV and corona voltage range of $6\,\text{kV} \leq U_{cor} \leq 12\,\text{kV}$. Prior to and after each experimental run, the background level of ozone in the laboratory air was determined and subtracted from the measured data for active GPP. However, the background level of ozone has shown to be quite stable during each run. The average background of ozone in the laboratory was approximately 30 ppbV. Koutrakis et al. (1993) have reported much higher ambient ozone levels in the US to be in the range between 50 ppbV and 300 ppbV. The experimental runs were performed, using a 25 µm gold wire as corona electrode. The results are shown in figure 5.4.2.

As can be withdrawn from the bar diagram, for all investigated corona voltages, the additional ozone concentration decreases with increasing wash flow rate until it reaches a minimum at 5.6 l/min. This proves that the calculated wash flow rate indeed causes the lowest mixing of the flows.

Figure 5.4.2: Additional Ozone Concentration in the Sample Flow for Different Wash Flow Rates and Different Corona Voltages
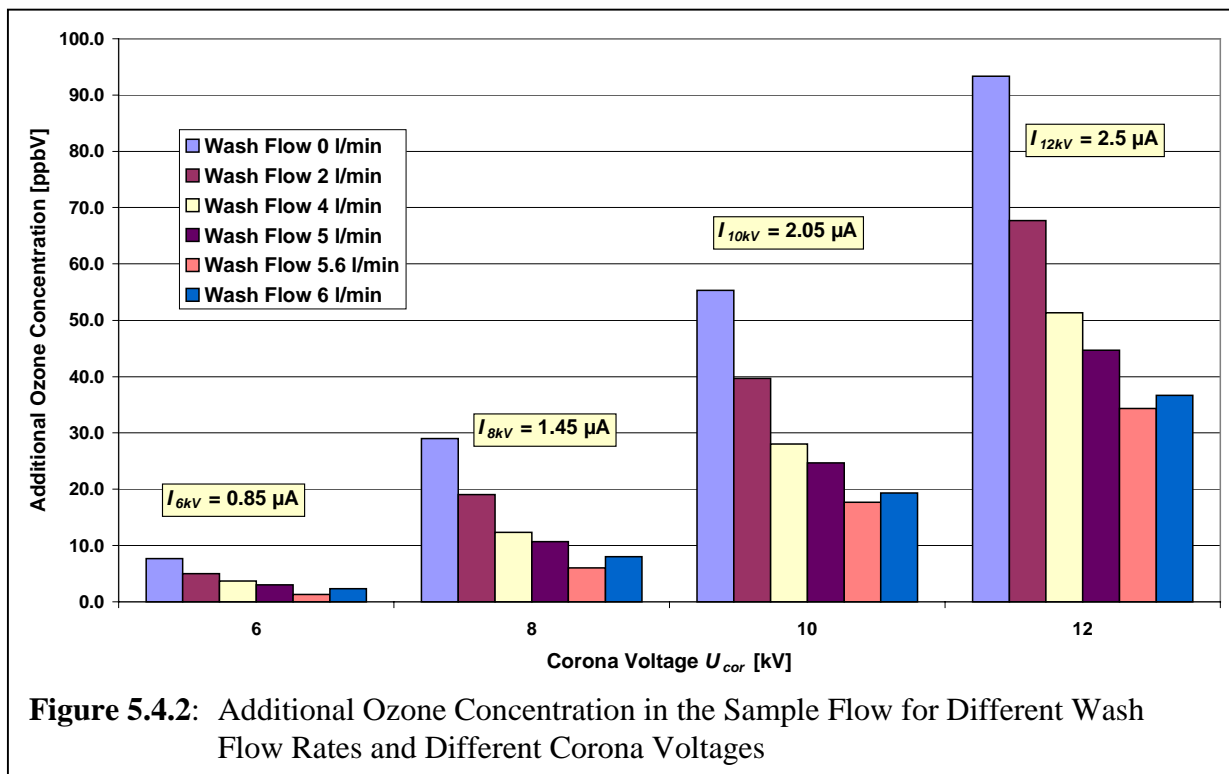
5.4.3 Measurement of Changed Gas Concentrations in the Sample Flow and Wash Flow

When talking about the changed gas concentrations due to a corona discharge, it is important to declare what is the source parameter for the elevated concentrations and which parameter determines the effectiveness of the corona. Only the knowledge of both parameters allows to evaluate the measured data and to interfere with the process to lower the specific formation of these gases. In the given geometry of the GPP, the source parameter for the gas formation by the corona is the electric field near the corona wire, which for the given geometry is determined by the corona voltage. The parameter that determines the effectiveness of the corona with respect to particle charging, is the ion concentration outside of the grid, which is determined by the ion current and the electric field distribution in the charging zone (see equation 4.2.17). As described in chapter 5.1. and in appendix C, the ion concentration, and therefore the charging efficiency, does not differ substantially for the investigated deflection voltages of $2\,kV$ and $3\,kV$, respectively, under otherwise identical conditions. The ion concentration, and thus the charging efficiency, is therefore mainly a function of the applied corona voltage U_{cor}.

Therefore the additional ozone and nitrogen dioxide concentrations are plotted versus the corona voltage in this chapter in order to demonstrate the effect of the corona on the gas phase of the sample and wash flow.

5.4.3.1 Measurement of Additional Ozone and Nitrogen Dioxide Concentration in the Sample Flow and Wash Flow

The ozone and nitrogen dioxide concentration in the sample flow were measured as shown in figure 5.4.1. Since the formation of additional ozone and nitrogen dioxide in the sample flow or wash flow, respectively, is of interest, the background concentration in the laboratory air was frequently measured and subtracted from the total concentration in the sample flow.

Different Wire Materials

Initially, the gas concentrations were measured for different corona voltage settings with $25\,\mu m$ corona wires made from gold, silver and tungsten. The investigations were carried out with deflection voltages of $U_i = 2\,kV$ and $U_i = 3\,kV$. The measurements were performed in the intended operation mode, i.e. with $5.6\,l/min$ wash flow. The ion current was simultaneously measured and the average ion concentration in the charging zone calculated, using equations 4.2.10 and 4.2.17. Figure 5.4.3. shows the additional ozone and nitrogen dioxide concentration against the corona voltage. As can be seen, the gas concentrations for $U_i = 2\,kV$ and $U_i = 3\,kV$ do not substantially differ. This was expected, as the corona voltage

that determines the total formation of ozone and nitrogen dioxide, was the same during the measurements. Due to the similarity of the results with $U_i = 2$ kV and $U_i = 3$ kV, only the results for $U_i = 2$ kV will be presented in the following to assure a better clarity of the graphs. Figure 5.4.3 also shows that among the three tested wire materials, silver wire produced the lowest amount of both, ozone and nitrogen dioxide, followed by gold and tungsten. This agrees well with the investigations of Nashimoto (1988), who also found that the formation rate of these gases is the lowest for silver wire.

Figure 5.4.3 Additional Ozone and Nitrogen Dioxide Concentration in the Sample Flow versus Corona Voltage for Silver, Gold and Tungsten Wire, Deflection Voltage $U_i = 2$ kV and $U_i = 3$ kV, With Wash Flow, Positive Corona
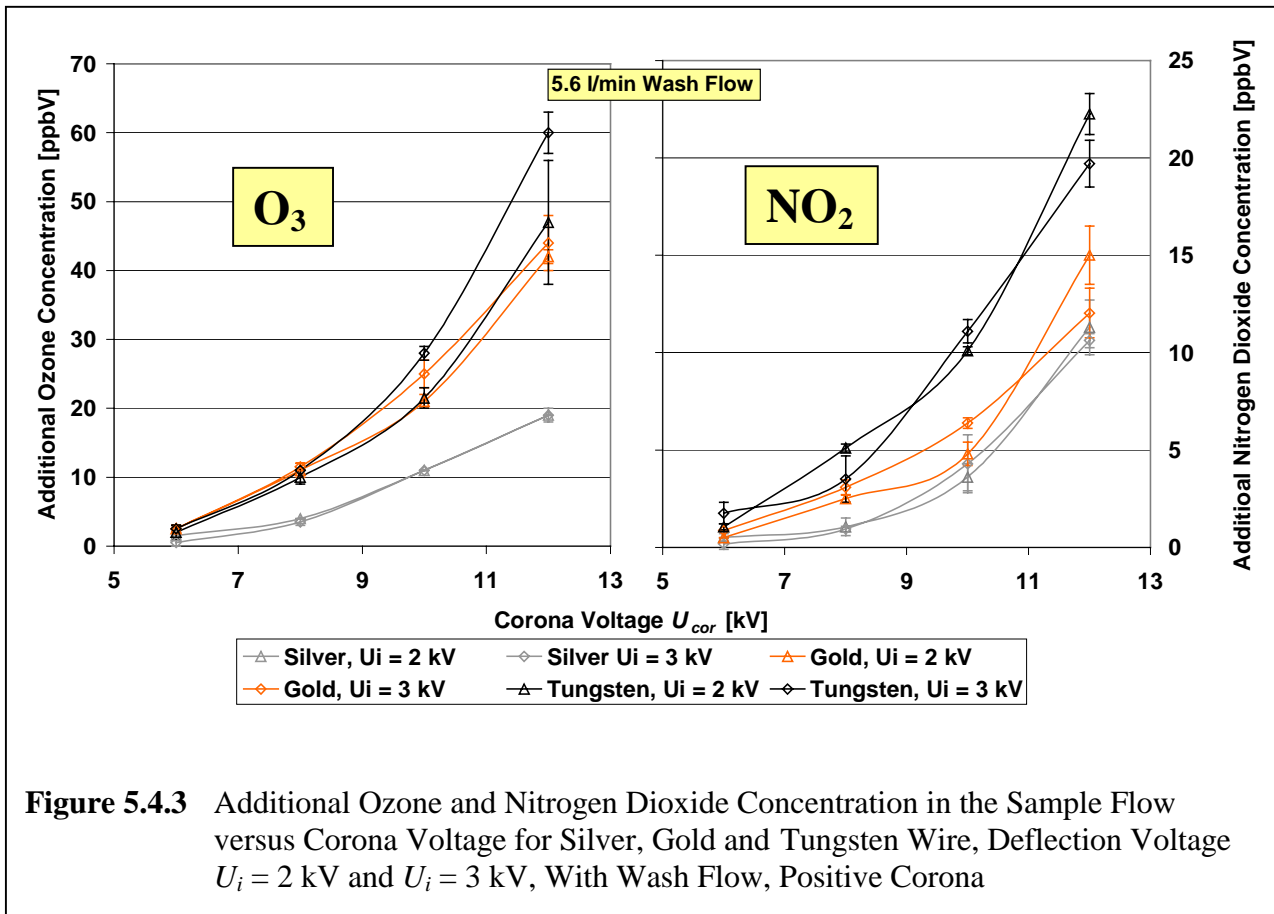
Different Wire Diameters

As a next step, the influence of the wire diameter on the ozone formation was studied. Three different silver wire diameters were used: 25 µm, 50 µm and 100 µm. The resulting additional gas concentrations are plotted versus the corona voltage in figure 5.4.4. The graph shows that the specific ozone concentration increases with increasing wire diameter. Bearing in mind that the electric field strength near the wire surface and therefore the ion concentration and charging efficiency is higher for thinner wires (see also Appendix C), this underlines the recommendation of usage of a wire diameter as low as possible for highly efficient particle charging at the lowest possible gas formation rates. Boelter et al. (1997) and Nashimoto (1988) have come to the same conclusion. The NO_2 concentration shows no substantial

dependence on the wire diameter. This has also been found by Nashimoto (1988), who stated that the formation of nitrogen dioxide is not only a function of the wire diameter, but also of the ozone concentration. Since NO_2 is oxidized to NO_3 and N_2O_5, the NO_2 concentration does not represent a simple relationship with the wire diameter.

Figure 5.4.4   Additional Ozone and Nitrogen Dioxide Concentration in the Sample Flow versus Corona Voltage for Silver Wire Diameters of 25 µm, 50 µm and 100 µm, Deflection Voltage $U_i = 2$ kV, With Wash Flow, Positive Corona
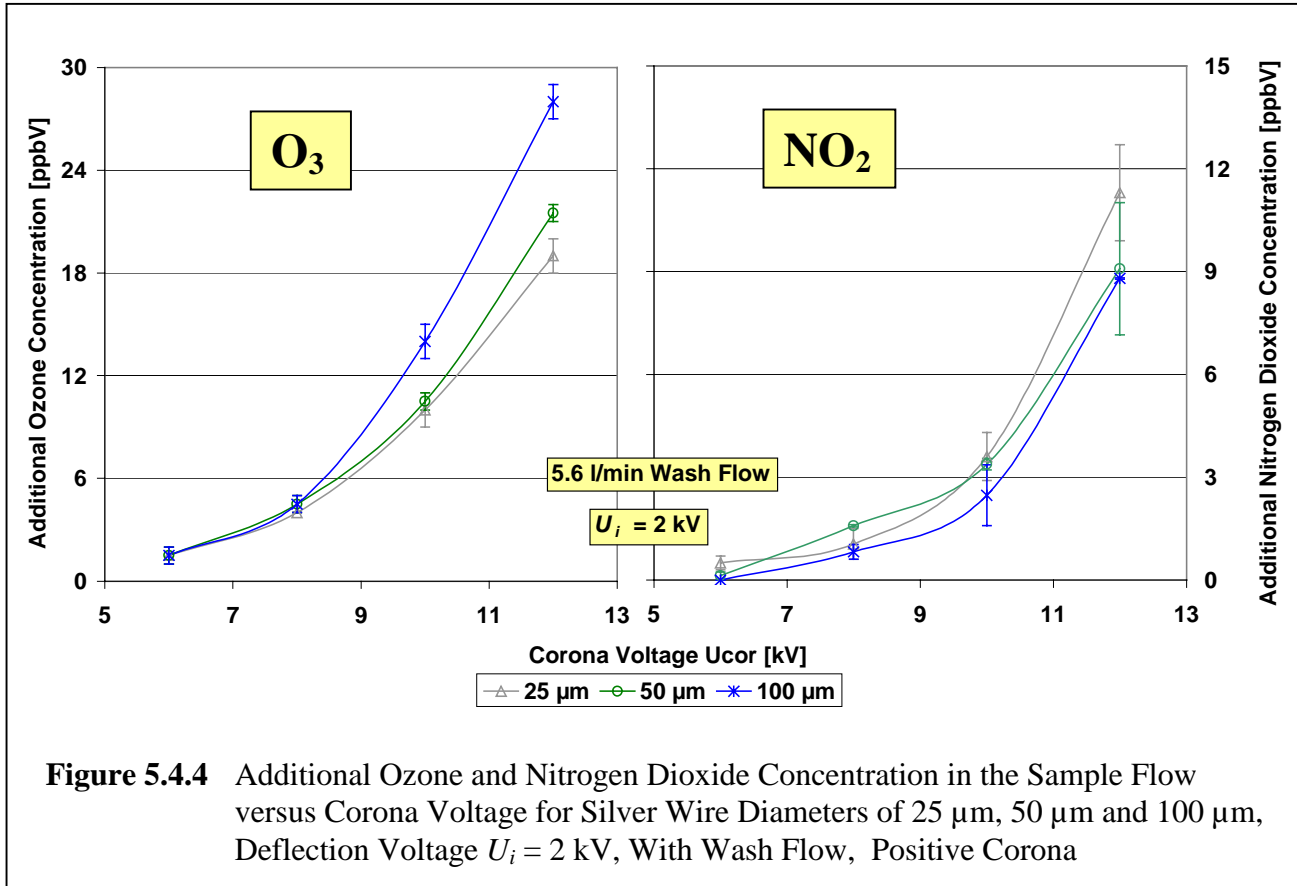
As will be described in detail in chapter 5.6, silver wire broke very frequently (average approximately every 48 hours) whereas Gold and Tungsten wires lasted for several months. For continuous, almost maintenance-free operation of the GPP, silver wire was therefore considered not to be practicable. Since the gas formation of the corona with gold wire was lower than with tungsten wire, gold was chosen as the recommended wire material. The recommended wire diameter is 25 µm, as it seems to be the lowest manageable. Therefore the graphs in the following will only present the results, obtained with 25 µm gold wire.

Different Polarity

Several investigators (e.g. Brandvold et al., 1989; Martinez et al., 1996) have found that the formation of ozone and oxides of nitrogen is highly affected by the polarity of the corona. All have come to the conclusion that the positive corona forms less gases than the negative corona. To verify their statements for the GPP, the ozone and nitrogen dioxide concentration in the sample flow were measured for positive and negative polarity of corona and deflection voltage. The GPP was operated in the intended mode, i.e. with a wash flow rate of 5.6 l/min.

As the graph in figure 5.4.5 shows, the additional ozone concentration in the sample flow is by a factor of more than 10 higher for negative compared to positive polarity. The divergence for nitrogen dioxide is lower. Here the ratio of NO_2 formation with negative compared to positive polarity is approximately 4. Anyhow, the results agree well with literature and prove that positive polarity is the better choice for a minimised effect on the gas phase.

Figure 5.4.5: Additional Ozone Concentration in the Sample Flow versus Corona Voltage for Positive and Negative Polarity, With Wash Flow, 25 µm Gold Wire
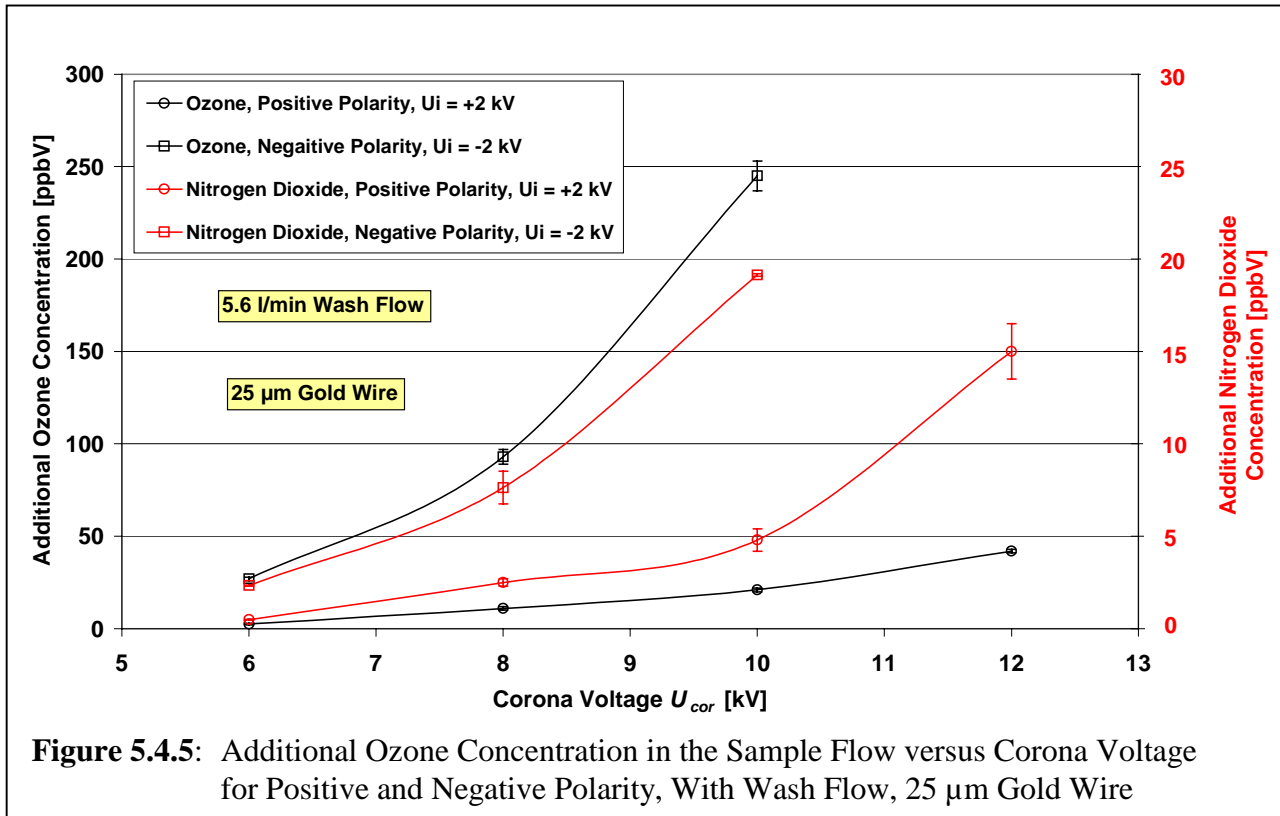
Effectiveness of the Wash Flow

The wash flow is a particle free air flow that is introduced into the space in-between the grid electrode to convectively transport the gases, formed by the corona, out of the GPP and to avoid mixing with the sample flow. To determine the effectiveness of the wash flow, the ozone and nitrogen dioxide concentration in the sample flow were firstly measured as usual, i.e. with 5.6 l/min wash flow. Secondly, the concentrations in the sample flow were measured without wash flow, i.e. the corona was operated in still air. During the measurements without wash flow, the inlet and outlet of the wash flow were sealed. Thirdly, the O_3 and NO_2 concentrations in the wash flow itself were measured at the regular flow rate of 5.6 l/min. All measurements were performed with corona voltages of 6 kV, 8 kV, 10 kV and 12 kV. Figure 5.4.6 shows that both, the ozone and nitrogen dioxide concentration in the sample flow are effectively reduced by the wash flow (see also table 5.4.1). The ozone concentration is

reduced by the wash flow to approximately one third, while the nitrogen dioxide concentration is reduced to generally less than one half. The results are summarized in table 5.4.1.

Figure 5.4.6: Additional Ozone Concentration in the Sample Flow Versus Corona Voltage, With Wash Flow, Without Wash Flow and in the Wash Flow, Deflection Voltage U_i = 2 kV, 25 µm Gold Wire, Positive Corona
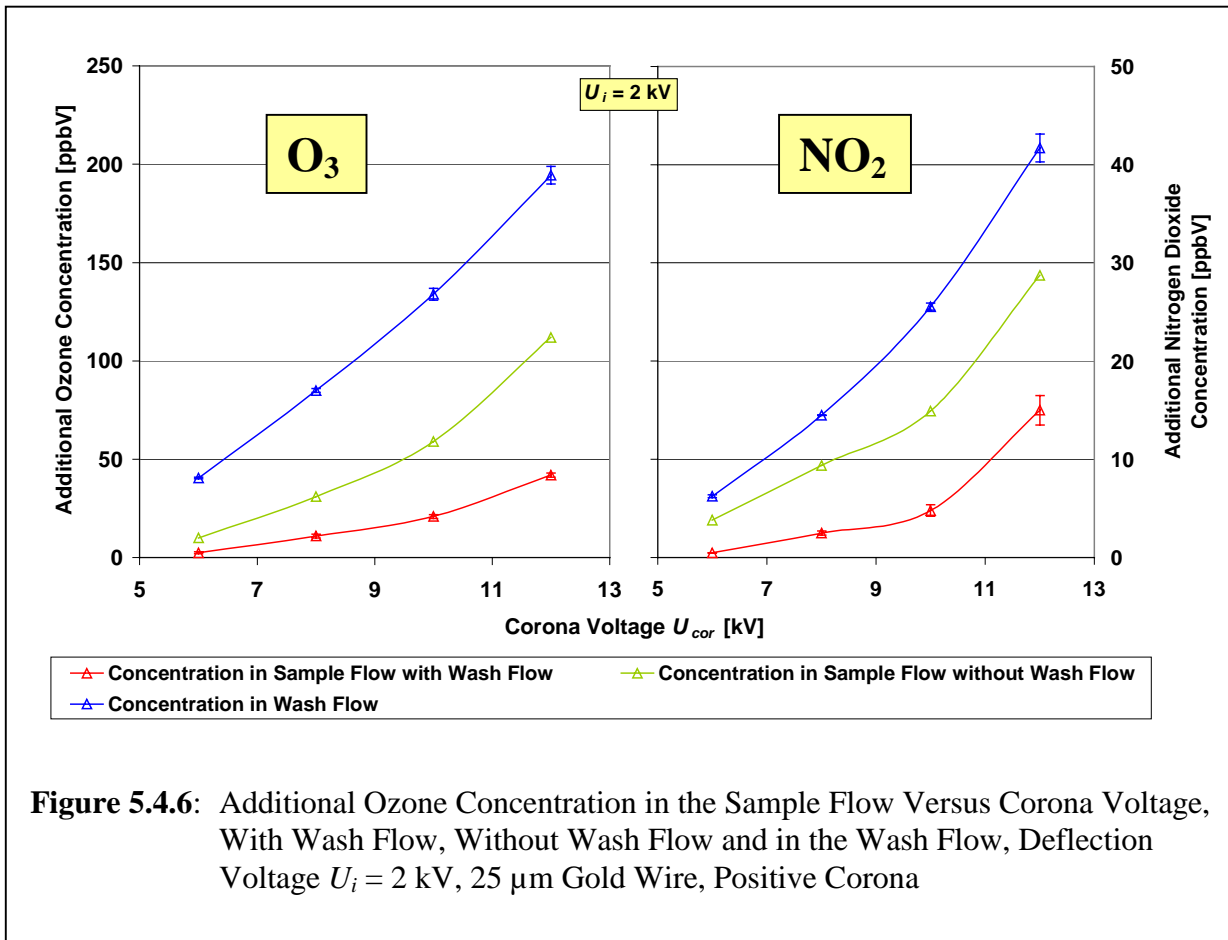
Table 5.4.1: Ozone and Nitrogen Dioxide Concentration in the Sample Flow With and Without Wash Flow and Ratio of the Concentrations for Different Corona Voltages, Deflection Voltage Ui = 2 kV, 25 µm Gold Wire, Positive Corona

Corona Voltage	U_{cor} [kV]	6	8	10	12
Ozone Concentration in Sample Flow Without Wash Flow	n_1 [ppbV]	10	31	59	112
Ozone Concentration in Sample Flow With Wash Flow	n_2 [ppbV]	2.5	11	21	42
Ratio Ozone	n_2/n_1	0.25	0.35	0.36	0.38
Nitrogen Dioxide Concentration in Sample Flow Without Wash Flow	n_3 [ppbV]	3.83	9.39	14.93	28.73
Nitrogen Dioxide Concentration in Sample Flow With Wash Flow	n_4 [ppbV]	0.49	2.5	4.8	15
Ratio Nitrogen Dioxide	n_4/n_3	0.13	0.27	0.32	0.52

It has to be noted that the concentrations in the wash flow are not representative as due to the different flow rates the mixing of the ozone with the wash air is different than it would be, when the corona would be situated directly in the sample flow. The concentrations in the wash flow can therefore only be taken as indicators for the formation of ozone and nitrogen dioxide by the corona.

The measurements were also performed with tungsten and silver wire. In order not to overload this work with redundant information, the results are not presented here. Anyhow, interesting results were obtained with silver wire, where above a critical voltage, the ozone and nitrogen dioxide concentration in the wash flow increased rapidly. Interestingly these increased concentrations did only affect the sample flow, when no wash flow was used. With wash flow, the sample flow's gas composition was not influenced by the highly increased concentration in the wash flow, but only in a manner as expected from the measurements with voltages below the critical value. The measured ozone concentration is plotted against the corona voltage in figure 5.4.7. Please note that the ozone concentration axis is in logarithmic scale. When the corona voltage is increased from 10 kV to 12 kV, the ozone concentration in the wash flow increases from 57 ppbV to approximately 7000 ppbV, the concentration in the sample flow without wash flow increases from 19 ppbV to approximately 1700 ppbV, whereas the concentration in the sample flow with wash flow increases only from 11 ppbV to 19 ppbV. The measurements were repeated and the results verified with different 25 µm silver wires. Similar results were obtained with gold wire, but the critical voltage was at a higher level, at around 16 kV. An explanation for the phenomenon could not be found in the literature. An attempt to explain it is that another reaction takes place, that requires a certain activation energy, that is supplied by the electric field in the corona region. The reaction forms non-polar ozone with none or only non-polar intermediate species. Therefore, when the wash flow is used, all newly formed gas molecules are transported away convectively with the wash flow as no radial force acts on the molecules except for diffusional forces that are negligible compared to the convective force. When there is no wash flow around the corona, no longitudinal force acts on the molecules. Hence the radial diffusional forces in counter direction of the gas concentration gradient become predominant, causing the ozone concentration in the sample flow to increase. However, this firstly proves that the wash flow is a highly effective tool for the removal of unwanted gas components in the corona region. Secondly this shows that, except for the short life time, silver wire should not be used.

Figure 5.4.7: Additional Ozone Concentration in the Sample Flow Versus Corona Voltage
With Wash Flow, Without Wash Flow and in the Wash Flow, Deflection
Voltage $U_i = 2$ kV, with 25 µm Silver Wire, Positive Corona
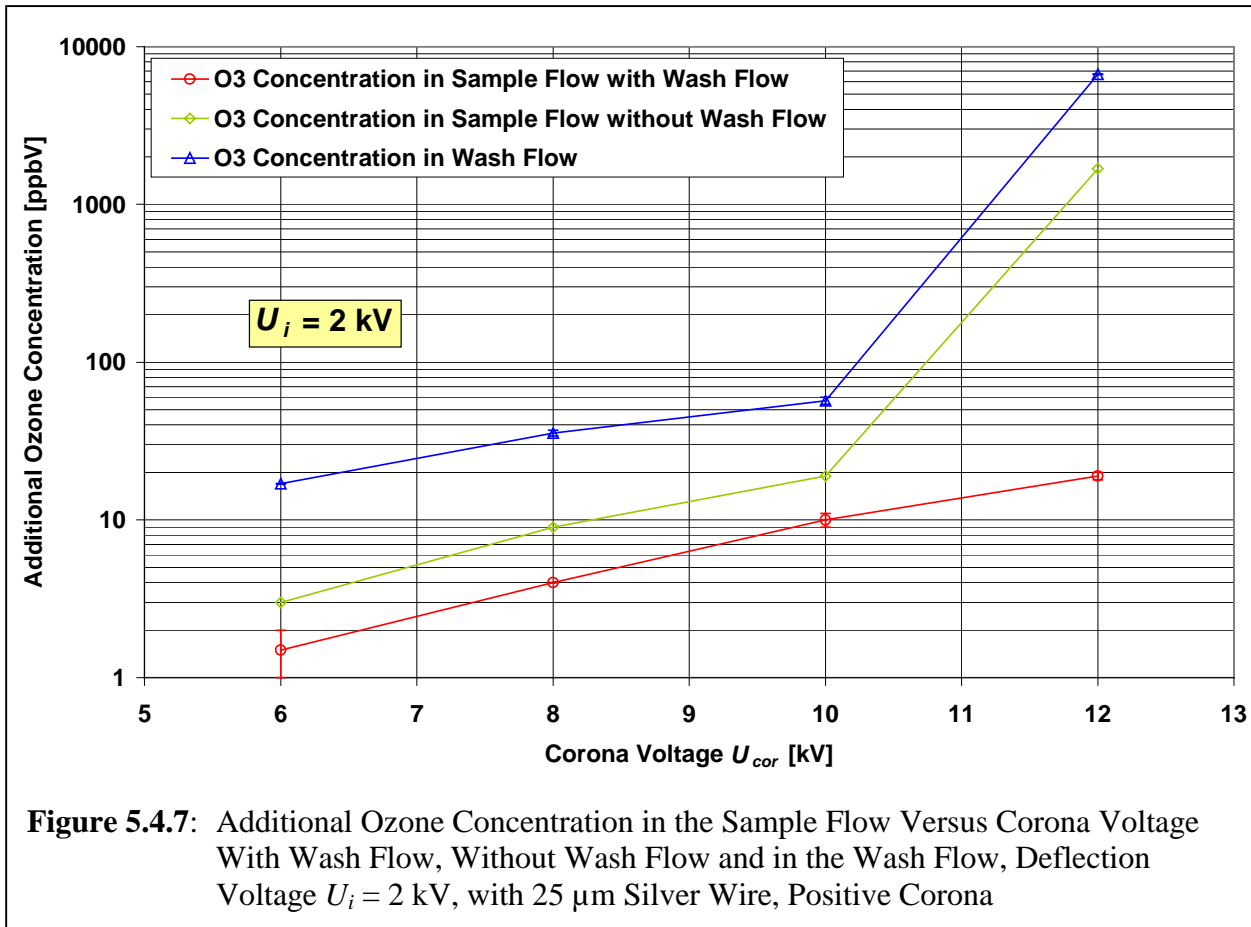
5.5 Investigations on the Material Dependent Life Cycle of a Corona Wire

In the course of the practical evaluation of the GPP, it has been found that the initially preferred silver wire broke very frequently. Detailed investigations on the life cycle of a corona wire were carried out, using the 1st prototype of the GPP as shown in appendix B to this work. Even though the geometry is slightly different, the life time of the corona wire is expected to be very similar for the first and second prototype. As the early breakage is most likely due to oxidation of the wire, which is enhanced by the electric field, the life time of a wire is determined mainly by the operating time of the wire at high voltage. For the determination of the wire life time, the GPP was continuously switched on with a corona voltage of $U_{cor} = 10$ kV. The expected life cycle of the wire, with the GPP installed in a differential particle mass monitoring system, e.g. the Differential TEOM®, where the GPP is only switched on half of the time is therefore expected to be double of that investigated here. It has been fond that 25 µm silver wire lasted for an average of 68.8 hours. 50 µm silver wires lasted for an average of 182.1 hours, 100 µm silver wires broke after averagely 301.3 hours. The life cycles, especially for the 25 µm wire, were highly fluctuating, which yields to the assumption that the wire breakage is a random process. The results of the investigations

on the lifetime of silver wires are summarized in table 5.5.1. Gold and tungsten wires were tested for more than three months without breakage.

Table 5.5.1: Life Cycle of Silver Wire with 25 µm, 50 µm and 100 µm Diameter

	25 µm	**50 µm**	**100 µm**
Average	68.8 hours	182.1 hours	301.3 hours
Minimum	23.7 hours	137.8 hours	148.5 hours
Maximum	163.5 hours	212.3 hours	599.2 hours
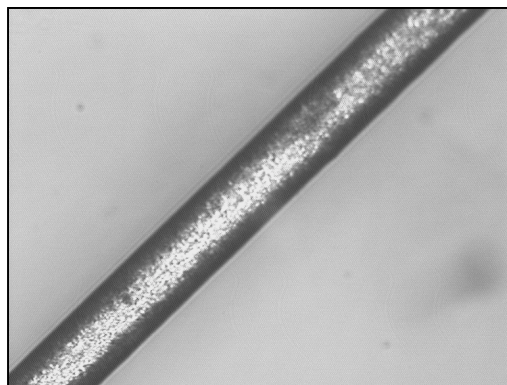
Figure 5.5.1: Unused 100 µm Silver Wire, 50 Fold Magnified
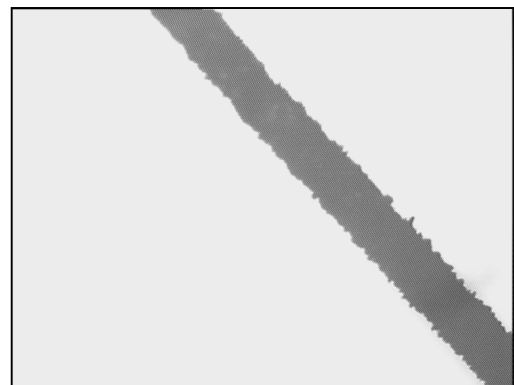
Figure 5.5.2: 100 µm Silver Wire, Used for 7 Days, 50 Fold Magnified

To study the processes on a silver wire, the surface of a 100 µm silver wire was investigated under a light microscope. The new and unused silver wire shows a quite even, metallic surface (Figure 5.5.1), whereas after 7 days operation the surface has become black and uneven (see figure 5.5.2). Figure 5.5.3 shows a 1000 fold magnified picture of the black layer on the surface of the used wire. It can be seen that the black layer has a very uneven, amorphous structure. The layer is not very rigidly connected to the silver core but can easily be wiped away, baring the thinner silver core. The transition between a zone, where the layer has been wiped away and a zone where the layer is still present is shown in figure 5.5.4. As the figure 5.5.4 shows, the diameter of the remaining core has decreased from 100 µm to 70 µm, whereas the amorphous layer has a higher diameter than the original wire. This shows that the wire obviously gets "eaten up" by the oxide layer. The oxidation of the wire surface therefore causes the silver wire to break, once the remaining diameter of the core becomes too small.
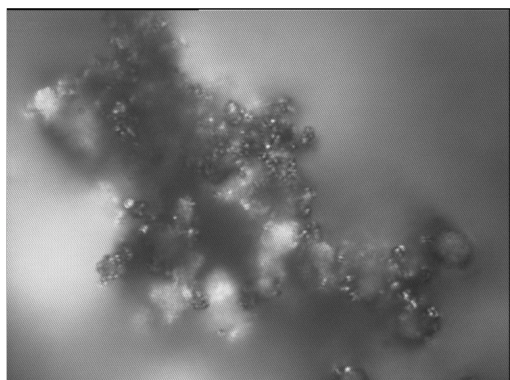
Figure 5.5.3: 1000 Fold Magnified Layer on Used Silver Wire

Approx. 140 µm

Approx. 70 µm

100 µm
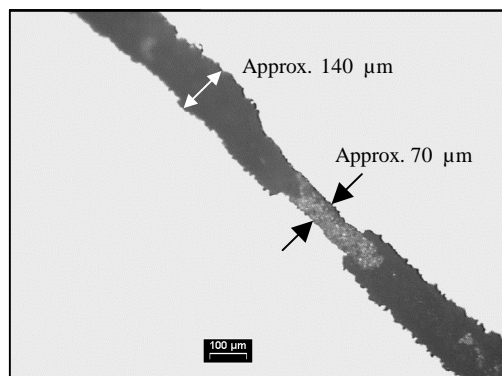
Figure 5.5.4: Transition from Core to Layer of a Used Silver Wire

5.6 Results with the GPP Employed in the Differential TEOM®, Challenged with Semi-Volatile Ammonium Nitrate Particles

A GPP equipped single sensor Differential TEOM® as per figure 2.5.3 was challenged with semi-volatile ammonium nitrate particles. A second, regular TEOM® was simultaneously fed with ammonium nitrate from the same source. The particles were generated with a ultrasonic atomizer as shown in figure 5.3.1. The differential TEOM® was operated without dryer in order only to study the effect of semi-volatile particles, evaporating from the sample filter without any side effects that might be caused by the SES system. Since the relative humidity of the aerosol, leaving the generator was constantly at approx. 20%, a further dehumidification was not required.

In order to study the effectiveness of the Differential TEOM®, the sensor was operated at 30°C and 40°C, whereas the second, regular TEOM® was operated only at 30°C. Since the data from the second TEOM® was used to evaluate the data from the differential TEOM®, it will also be referred to as reference TEOM®. It was tried to operate the reference TEOM® floating with ambient temperature, but the temperature fluctuations due to the cycles of the air conditioning in the laboratory highly affected the frequency of the TEOM®. A sample temperature of 30°C has shown to be the lowest temperature, where ambient temperature has no effect on the frequency.

Firstly, the reference and Differential TEOM® were simultaneously fed with the same aerosol. The GPP remained switched off to verify that both TEOM® sensors show the same mass concentration. Figure 5.6.1 shows that the mass concentrations from both sensors agreed well.

Figure 5.6.1: Mass Concentration of Reference TEOM® at 30°C Versus Mass Concentration of Differential TEOM® at 30°C, GPP Switched off

In the next step, the GPP got switched on and off in time intervals of 5 minutes. The frequencies of the tapered elements were recorded for further evaluation of the data. Figure 5.6.2 shows the general frequency characteristics for the Differential TEOM®, operating at 40°C and the reference TEOM®, operating at 30°C. As can be seen from the graph for the Differential, the frequency decreases during periods, when the GPP is switched off and increases during periods, when the GPP is switched on. This indicates that the filter mass increases, when the GPP is switched off, and decreases when it is switched on. I.e. when the TEOM® is operated with particle free air, ammonium nitrate particles evaporate from the filter.

Since the reference TEOM® is operated at a slightly elevated temperature, it is not in thermodynamic equilibrium with its environment. Therefore, a fraction of semi-volatile particles will also evaporate from the filter of the reference sensor. Consequently, if the Differential TEOM® accurately corrects the measured data for artefacts, the output of the Differential TEOM® should be slightly higher than that of the reference TEOM®.

In figure 5.6.3 the output of the Differential TEOM® operating at 30°C is plotted versus the mass concentration, measured with the reference TEOM® at 30°C.

Figure 5.6.2: Frequency Characteristic of the Reference TEOM® at 30°C and the Differential TEOM® at 40°C

As expected, the Differential TEOM® shows slightly higher (+3.5%) mass concentration than the reference TEOM®. The difference is most likely due to evaporation of semi-volatile material from the filters, which only in the case of the Differential TEOM® is corrected.

In the next step, the temperature of the Differential TEOM® was increased to 40°C. This

$y = 1.0354x$
$R^2 = 0.7522$

Figure 5.6.3: Mass Concentration of the Reference TEOM® at 30°C Versus Mass Concentration of the Differential TEOM® at 30°C
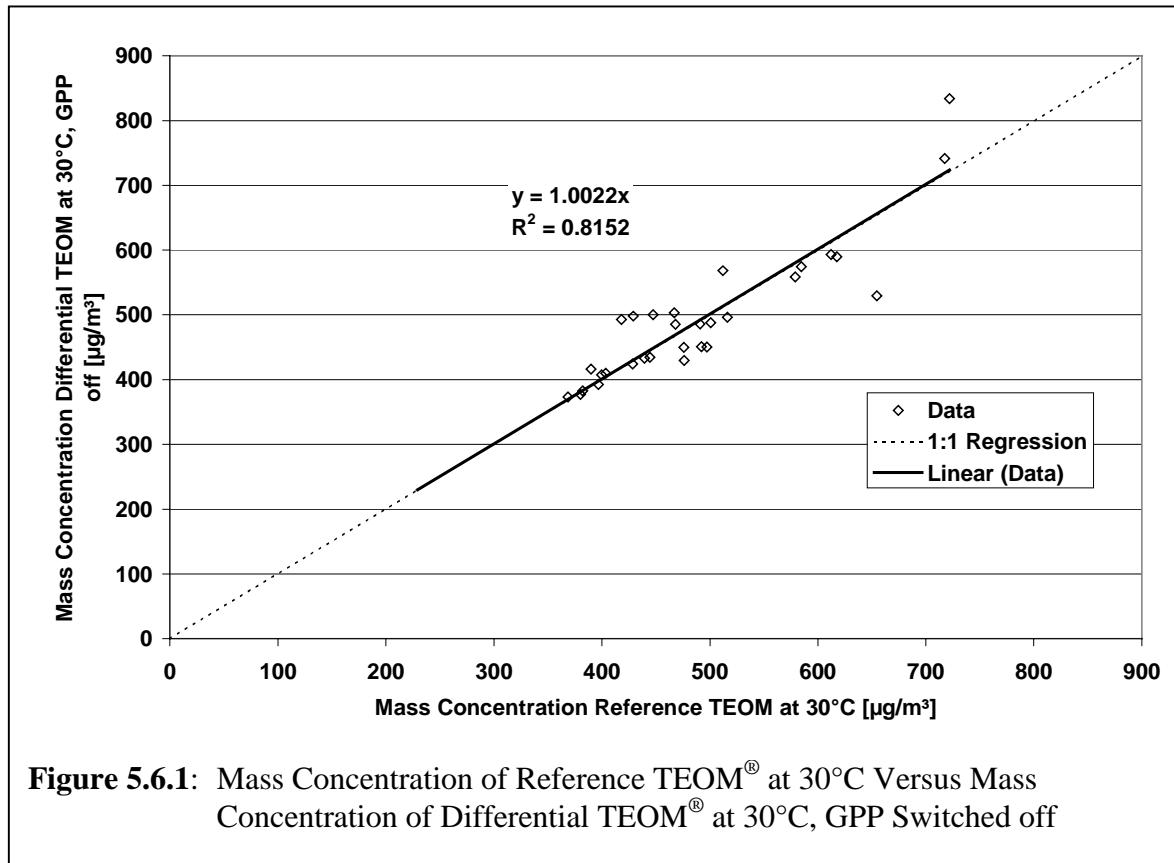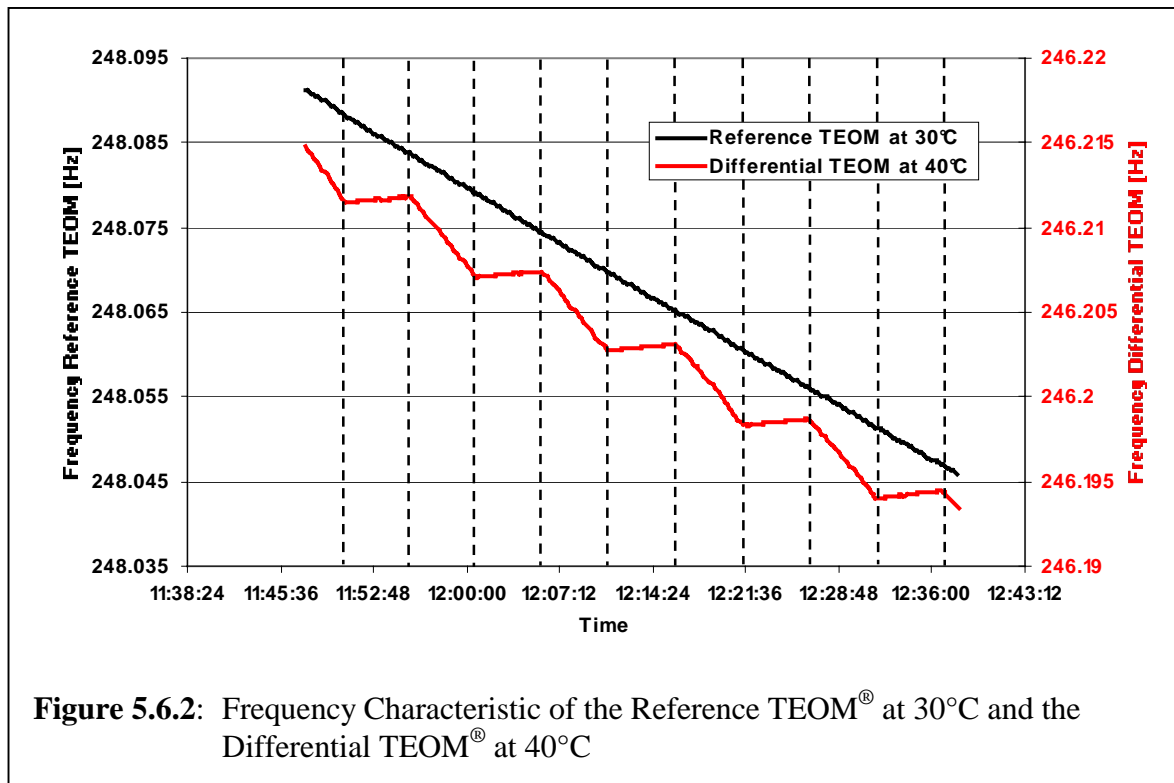
Figure 5.6.4: Mass Concentration of the Reference TEOM® at 30°C Versus Mass
Concentration of the Differential TEOM® at 40°C, GPP Switched off
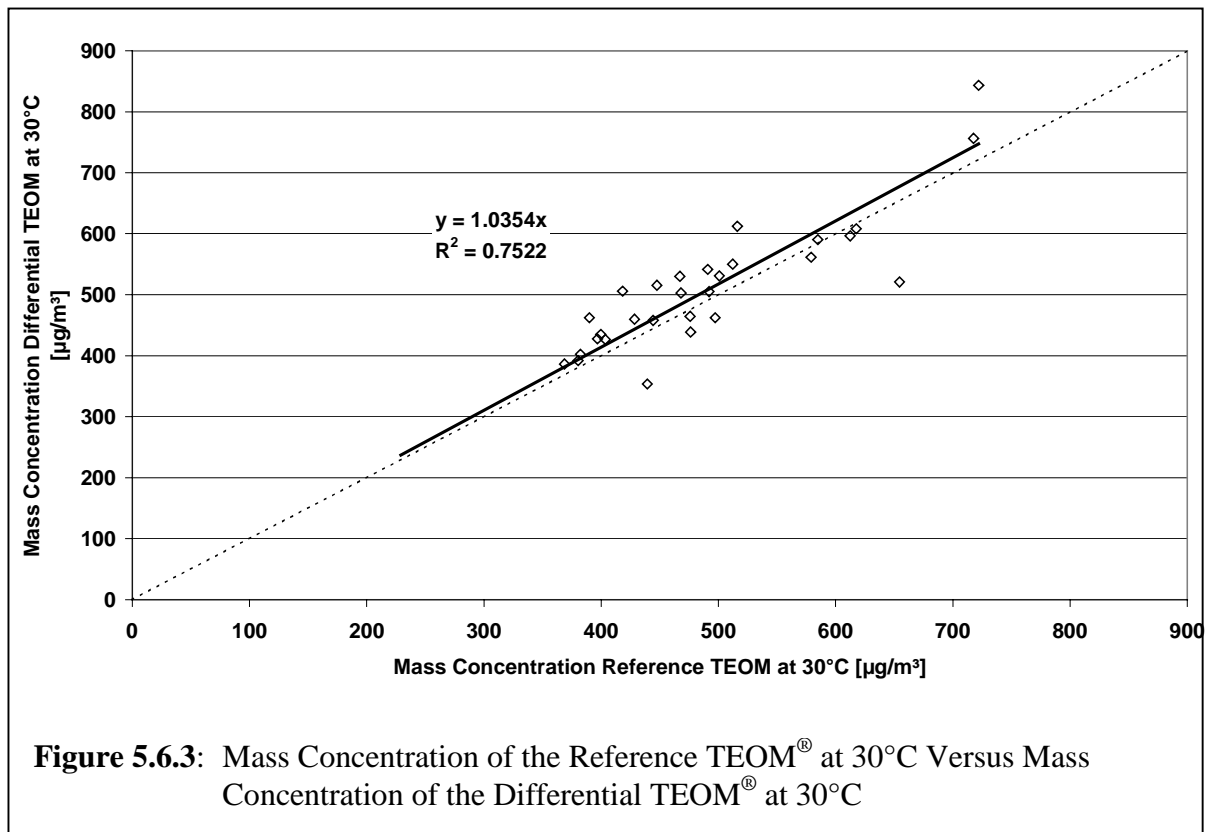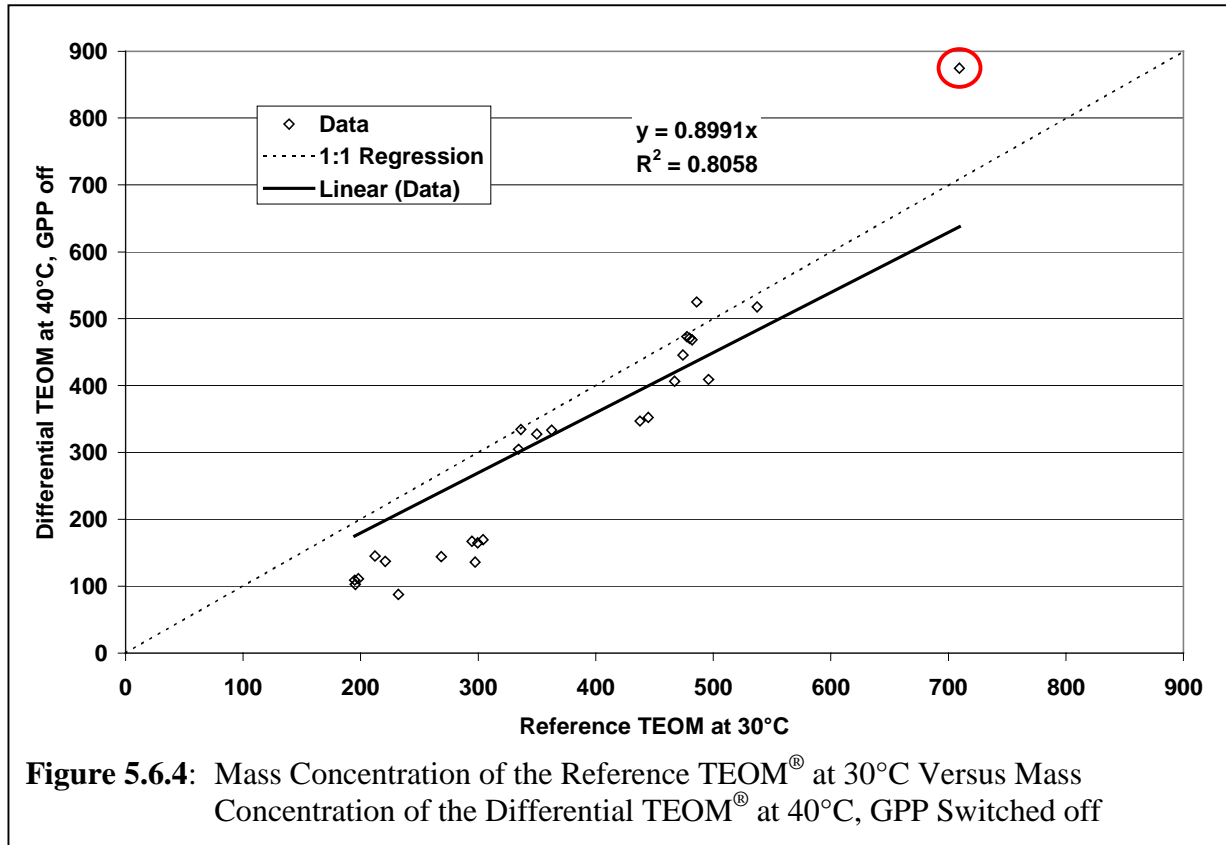
caused a higher evaporation rate from the sample filter as can be seen in figure 5.6.4. The
graph illustrates the mass concentrations from the reference TEOM® versus the uncorrected
data from the Differential TEOM®, operating at 40°C. The difference in the mass
concentrations of the two sensors is approx. 10%.

When the data of the differential TEOM® as shown in figure 5.6.4 is corrected for artefacts,
both mass concentrations agree quite well. The differences of the concentrations from the two
sensors is approximately 3.3%. The results agree well with the results from the previous
experiment where the difference was approx. 3.5%. Regarding figures 5.6.4 and 5.6.5, it can
be seen that the quite intensive scatter of the mass concentrations in figure 5.6.4 disappeared
in figure 5.6.5. A very interesting point is marked with a red circle in both graphs. The high
value of the uncorrected mass concentration of the Differential TEOM® was obviously caused
by a positive artefact, i.e. another artefact than evaporation of semi-volatile material.
However, this positive artefact was detected during the measurement with particle free air and
was therefore corrected by the Differential TEOM®. This proves that the Differential TEOM®
is able to accurately correct the mass concentration data, independent of the magnitude and
sign of the artefacts.
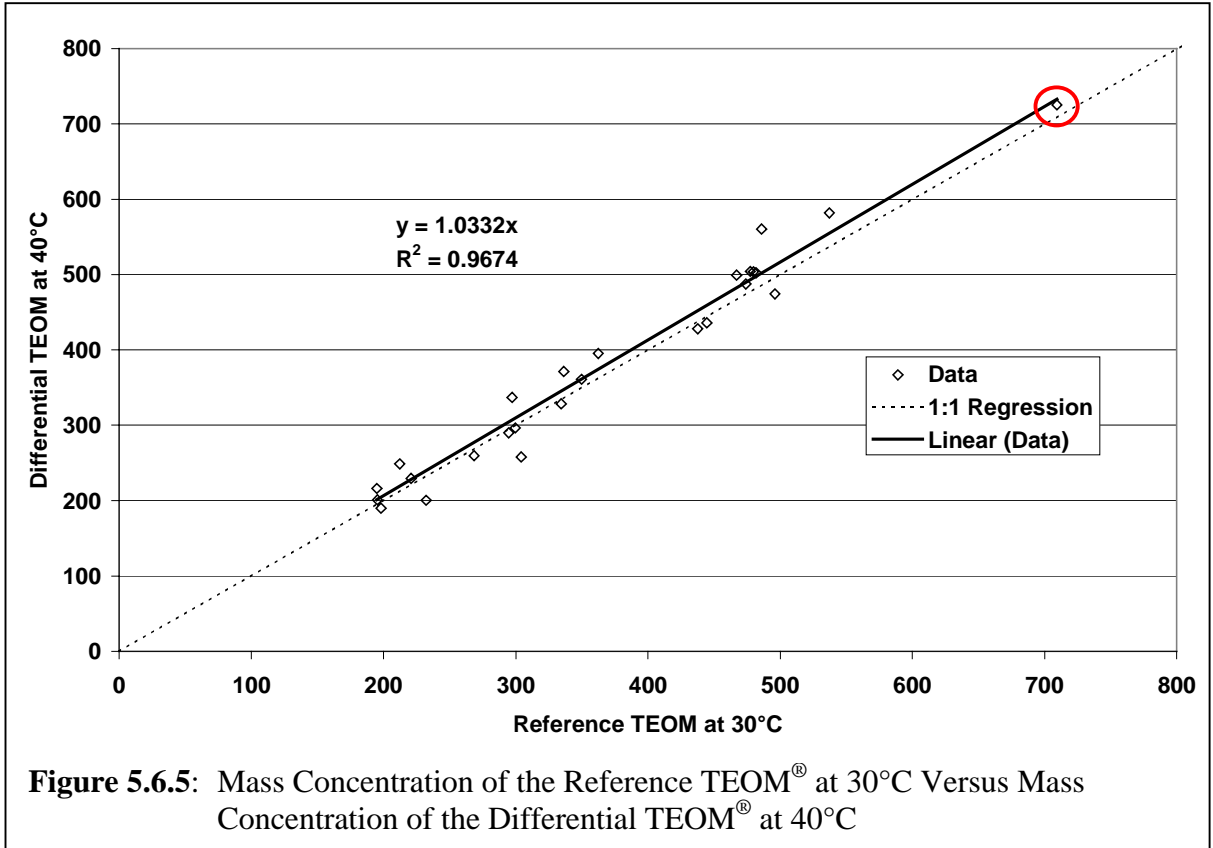
Figure 5.6.5: Mass Concentration of the Reference TEOM® at 30°C Versus Mass Concentration of the Differential TEOM® at 40°C

Chapter 6

Conclusion and Outlook

Conclusion

A Gas Particle Partitioner (GPP) has been designed and a version for employment in a differential mass measurement system, such as Differential TEOM® has been manufactured and intensively tested. The GPP does not change the thermodynamic properties of the aerosol, due to its design. The particle removal process can easily be switched on and off by switching the corona and deflection voltage. Several measures were taken to minimize the formation of gases by the corona and to avoid a mixing of these gases with the sample flow.

The investigations have shown that the GPP is able to separate gas and particles with an efficiency of approximately 100% in the particle size range $25\,\mathrm{nm} \leq d_p \leq 10.7\,\mu\mathrm{m}$. For particle diameters below 25 nm, the efficiency decreases. The t_{90} response time constant was found to be approx. 7 s plus a dead time of 3 s. The response time is in the desired range, considering the intended switching interval of the differential mass measurement system of 5 min. The effect on the gas phase could be effectively minimized. Considering the worst case to be a 100 µm gold wire, used without wash flow with negative polarity, and the optimum case to be a 25 µm gold wire, used with wash flow and positive polarity, the measures that

Figure 6.1:   Effectiveness of the Measures to Minimize an Effect on the Gas Phase
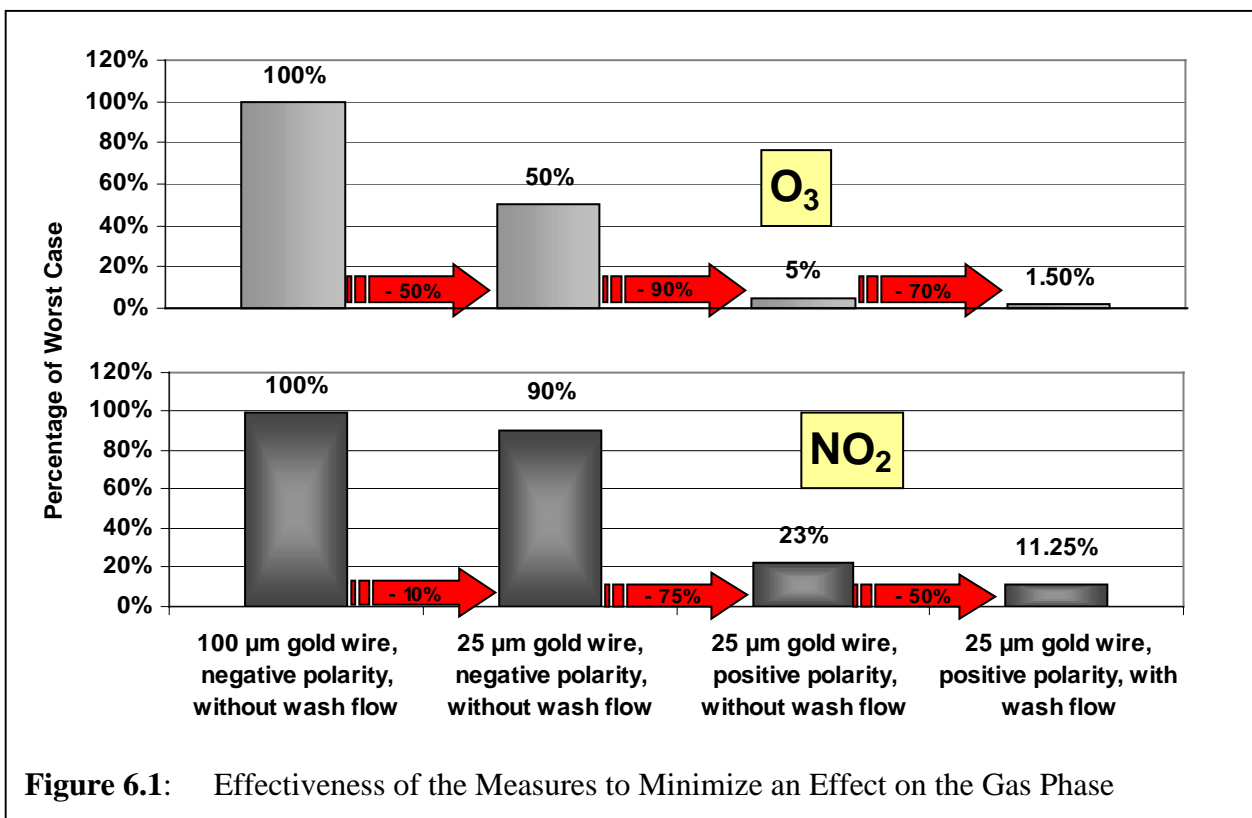
were taken to minimize the effect on the gas phase result in approximately 98.5% reduction of the additional ozone concentration in the sample flow and almost 90% of the nitrogen dioxide concentration (see figure 6.1). The use of silver wire instead of gold wire would lead to even lower concentrations, but was considered not to be practicable as the tested silver wires broke very frequently (25 µm silver wires lasted for an average of 69 hours). Due to the use of a gold wire instead of the initially suggested silver wire, the maintenance requirements for the GPP are quite low, as firstly the investigations have shown that gold wire lasts for more than three months. Secondly, cleaning intervals can be long, as only a fraction of the particles get deposited on the outer wall of the GPP, whereas a large fraction is transported out of the GPP with the excess flow. Further, the material, deposited on the outer wall does not get in contact with the sample flow and therefore a possible release of material from the outer wall does not affect the sample flow but only the excess flow. The expected maintenance interval is therefore in the range of several months. In common electrostatic precipitators, where the corona electrode is in direct contact with the aerosol, the maintenance intervals are in general much shorter, mainly due to soiling of the precipitation and corona electrode.

It can be concluded that the gas particle partitioner fulfils all the requirements as introduced for an almost ideal gas particle separator in the introduction to this work. The GPP has proven to be a reliable instrument for the highly efficient separation of gas and particles with minimized effect on the gas phase.

Outlook

The scope of applications for the GPP can be extended to any application, where the almost maintenance-free supply of particle free air is required with unaffected thermodynamic conditions of the gas and substantially no effect on the gas phase. These applications are e.g. pre-filters for gas analysers or the artefact correction with nephelometers. A version of the GPP for supplying the manifold in a gas analyser station has already been designed (see appendix D). The required sample flow rate for supplying the manifold is 50 l/min, an excess flow rate of 10 l/min has been considered sufficient for this application. Appendix D also shows a modified design of the GPP for the use in a Differential TEOM®. The modifications were made in order to allow the operation of the GPP downstream of the diffusion dryer, i.e. at low relative humidity levels. This might be required when the GPP is operated in very humid, such as tropical areas. The water content of the itself would not be a problem as the electric breakthrough field strength increases with increasing humidity, but condensation of water on surfaces inside the GPP might lead to electric flashovers (Hasenpusch, 1981). In order to assure a sufficient drying efficiency of the dryer, the total flow rate through the GPP

had to be reduced. The new design is for a total flow rate of 6 l/min, i.e. 3 l/min sample flow and 3 l/min excess flow. The disadvantage of this design compared to the current design of the differential TEOM® is that an additional flow splitter is required to split the 16.67 l/min sample flow through the inlet into the 6 l/min aerosol flow to the GPP and the sensor and an unused 10.67 l/min excess flow. One advantage of this design is that the GPP becomes smaller and less massive.

The current version of the GPP is quite heavy and massive. It is made from stainless steel and has been machined from solid cylinders. Stainless steel is advantageous as the material does not oxidize, is very rigid and can flexibly be handled on a lathe. The major disadvantage of stainless steel is its high density, causing the GPP to become quite heavy. The weight of the current version of the GPP is around 15 kg. The possibilities to reduce the weight are the use of lower flow rates (as described above) and/or the use of a different material. The requirements for the material are

1) The material must be electrically conductive (at least the surface)
2) The material must not oxidize, also in presence of high electric field strength
3) It must be possible to handle the material on a lathe or comparable tools
4) The material density should be lower than that of stainless steel

One possibility is the use of aluminium with a suitable surface coating. Uncoated aluminium would very quickly form a non-conductive oxide layer on the surface. One possible process to obtain a durable conductive surface is to coat the aluminium by yellow chroming. The only 100 nm to 300 nm thick layer on the surface is abrasion proof to an extend that is more than sufficient for static devices like the GPP. The conductivity of the chrome layer is higher than that of stainless steel. The use of aluminium would reduce the weight of the GPP to approximately one third. Bearing in mind that the realized version of the GPP is a prototype for use in the laboratory with some massive spare material on it, the weight could further be reduced by grinding away this spare material.

One possibility to further reduce the ozone concentration in the sample flow is the use of grid material other than stainless steel. Ozone is destroyed due to catalytic reactions on metal surfaces. Since the reaction rate depends on the metallic material, a grid metal, other than stainless steel might results in a further reduced ozone concentration.

In the course of the gas phase investigations, it has been found that above a critical voltage, 25 µm silver wire produced a highly increased amount of ozone and nitrogen dioxide. The corona voltage where this phenomenon started was approximately 11 kV and therefore in the intended range for the operation of the GPP. A similar effect was also observed for gold

wire, but for corona voltage above 16 kV, which is beyond the intended voltage range. Interestingly, the increased concentrations did only affect the sample flow, when the wash flow was not used.

However, it could not finally be solved which reactions lead to these rapid increases of the concentrations. Since no such processes were found in the literature, further investigation could bring new insights on the ozone and nitrogen dioxide formation from different wire materials.

Chapter 7

Summary

The goal of this work was to develop, build and test a design for a Gas Particle Partitioner (GPP) that fulfils the requirements for an ideal gas particle separator:

- Highly efficient separation of gas and particles

- Separation must be easily switchable

- No changes of the thermodynamic conditions of the aerosol

- The gas phase must remain substantially unaffected, otherwise chemical reactions might cause an additional artefact on the filter

- The response time must be short, i.e. in the range of seconds

- No or low maintenance requirement

Common gas particle separators are filtration media or electrostatic precipitators (ESP's). However, both separator types introduce changes to the aerosol (e.g. pressure drop across a filter or gas formation by corona discharge in an ESP) that do not comply with the abovementioned requirements.

Ideal gas particle separators are required e.g. in the determination of the real airborne particle mass concentrations, using a differential mass measurement system like the Differential TEOM$^{®}$ or for separating particles from the sample gas flow for gas analysers.

Under consideration of the abovementioned requirements, a Gas Particle Partitioner has been designed and a version for employment in the Differential TEOM$^{®}$ manufactured and intensively tested.

The GPP is a cylindrical and coaxial arrangement that is separated into four zones: aerosol inlet, charging zone, fractionation zone and aerosol outlet (see figure 4.1.1). The total flow rate of the realized version is 16.67 l/min as default by the standardized inlet for the Differential TEOM$^{®}$. The total flow is internally split into a 3 l/min sample flow and a 13.67 l/min excess flow. The flow splitter is designed such that no change of the particle size distribution in the aerosol occurs when the GPP is switched off, but all particles either reach the excess air flow or get deposited on the outer wall when it is active. To electrically charge the particles, the GPP utilises a corona discharge that produces unipolar ions. A strong electric field between the inner and outer electrode deflects the charged particles towards the outer

wall. It is well known that the corona discharge produces gases like ozone (e.g. Boelter et al., 1997; Chen et al., 2002) and oxides of nitrogen (e.g. Martinez and Brandvold, 1996; Griffing, 1977) but several measures were taken to minimise the influence of these gases and evaporation of deposited particles on the aerosol's gas phase. Firstly, the vicinity of the corona wire gets flushed with a particle free wash flow, which is separated from the aerosol flow and convectively carries the gases, formed by the corona, out of the GPP. Secondly, a very thin corona wire with a diameter of only $25\,\mu m$ was chosen, as this reduces the production of gases. Thirdly, positive polarity was chosen for the corona voltage as this reduces the formation of ozone essentially compared to negative polarity. Fourthly, evaporation of deposited particles in the fractionation zone does not affect the gas composition of the aerosol, as the outer electrode and the sample flow are spatially separated.

The investigations have shown that the GPP is able to separate gas and particles with an efficiency of approximately 100% for the investigated particle diameters ranging from 25 nm to 10.7 µm. Since the GPP is designed for PM_{10} particles, particle sizes above 10.7 µm have not been investigated in this work. For diameters below 25 nm, the efficiency is decreased, most likely due to insufficient charging. However, these particles almost have almost no influence on the downstream measurement of particle concentrations, due to their small mass and surface area. The particle losses have proven to be less than 1.5% of the total particle number. The sum of the t_{90} response time and the dead time of the GPP is approximately 10 s.

During the course of the experiments, the initially chosen corona wire made from silver broke very frequently so that gold was chosen as wire material, even though it produces a higher amount of ozone and nitrogen dioxide. The gas phase measurements showed that measures taken for minimization of the effect on the gas phase have led to a substantial reduction of the ozone and nitrogen dioxide concentrations. The use of positive instead of negative polarity has decreased the ozone concentration by approx. 90% and the nitrogen dioxide concentration by approx. 75%. A $25\,\mu m$ wire produced more than 50% less ozone and 10% less nitrogen dioxide than a $100\,\mu m$ wire and the use of the wash flow reduced the O_3 concentration in the sample flow by another 70% and the NO_2 concentration by 50%. Due to the design of the GPP, the thermodynamic properties of the aerosol remain unaffected.

The GPP requires very low maintenance. The soiling inside is minimized as only a fraction of particles gets deposited on the outer wall, when the GPP is switched on, whereas a large fraction is taken out by the excess flow. The gold wire did not break during 3 month tests with a corona voltage of 10 kV continuously applied to the wire. As during the operation with a

differential TEOM® the GPP is switched on only half of the time, the life time of the gold wire is expected to be more than 6 months.

The design of the GPP can flexibly be adjusted to different flow rate requirements for e.g. other applications than the Differential TEOM®. A GPP design has been developed to supply the manifold in gas analyser stations with particle free air at a sample flow rate of 50 l/min. Another GPP for the employment in the Differential TEOM® downstream of the diffusion dryer, i.e. with lower total flow rate, has also been designed.

In summary it can be concluded that the GPP allows to separate gas and particles efficiently with no change of the thermodynamic conditions of the aerosol and substantially no effect on the gas phase. All common gas particle separators either change the thermodynamic conditions (e.g. filter media, Venturi scrubbers) or the gas composition (e.g. ESP's). The GPP can therefore be considered to be very close to an ideal gas particle separator. The use of the GPP in differential particle mass monitoring systems (e.g. Differential TEOM®) will allow a very accurate and, due to the low maintenance requirement, economic determination of the real ambient particle mass concentrations. With the modified design for the supply of a manifold for gas analysers, a precise measurement of ambient gas concentrations will be possible. All artefacts caused by commonly used filter media, such as increasing pressure drop and gas adsorption/desorption, will disappear. Similar improvements are expected, when the GPP replaces the common filter media for calibration purposes in nephelometers.

Bibliography

APPEL B.R., Y. TOKIWA. **Atmospheric Particulate Nitrate Sampling Errors due to Reactions With Particulate and Gaseous Strong Acids** *Atmospheric Environment 15 (1981), 1087-1089*

APPEL B.R. **Atmospheric Sample Analysis and Sampling Artifacts** *In: Aerosol Measurement – Principles, Techniques, and Applications, K. Willeke and P.A. Baron (Eds.) Van Nostrand Reinhold, New York, 1993*

ASBACH C., T.A.J. KUHLBUSCH, H. FISSAN. **Development of an Electrostatic Partitioner for Highly Efficient Partitioning of Gas and Particles With Minimal Effect on the Gas Phase** *Aerosol Science and Technology (2003a, accepted)*

ASBACH C., T.A.J. KUHLBUSCH, H. FISSAN. **Entwicklung einer nahezu idealen Trennapparatur für Gas und Partikel** *Chemie Ingenieur Technik, (2003b, accepted)*

ASBACH C., T.A.J. KUHLBUSCH, H. FISSAN. **Online Monitor for Measurement of Real Airborne Particle Mass Concentrations** *Proceedings of QA/QC in the field of emission and air pollution control conference, Prague, (2003c, accepted)*

AWAD M.B., G.S.P. CASTLE. **Ozone Generation in an Electrostatic Precipitator With Heated Corona Wire** *Journal of the Air Pollution Control Association 25 (1975), 369-374*

AYERS G.P., M.D. KEYWOOD, J.L. GRAS. **TEOM vs. Manual Gravimetric Methods for Determination of PM2.5 Aerosol Mass Concentrations** *Atmospheric Environment 33 (1999) 3717-3721*

BIRD B. **Transport Phenomena** *John Wiley & Sons, New York, USA, 1960*

BOELTER K.J., J.H. DAVIDSON. **Ozone Generation by Indoor, Electrostatic Air Cleaners** *Aerosol Science and Technology 27 (1997), 689-708*

BRANDVOLD D.K., P. MARTINEZ, D. DOGRUEL. **Polarity Dependence of N_2O Formation From Corona Discharge** *Atmospheric Environment 23 (1989), 1881-1883*

BRONSTEIN I.N., K.A. SEMENDJAJEW. **Taschenbuch der Mathematik** *B.G. Teubner Verlag, Stuttgart, 1991*

BÜSCHER P., A. SCHMIDT-OTT, A. WIEDENSOHLER. **Performance of a Unipolar „Square Wave" Diffusion Charger With Variable *nt* Product** *Journal of Aerosol Science 25 (1994), 651-663*

CARDELLO N., J. VOLCKENS, M.P. TOLOCKA, R. WIENER, T.J. BUCKLEY. **Technical Note: Performance of a Personal Electrostatic Precipitator Particle Sampler** *Aerosol Science and Technology 36 (2002), 162-165*

CHANG C.T., C.J. TSAI, C.T. LEE, S.Y. CHANG, M.T. CHENG, H.M. CHEIN. **Differences in PM_{10} Concentrations Measured by β-Gauge Monitor and Hi-Vol Sampler** *Atmospheric Environment 35 (2001), 5741-5748*

CHEN J., J.H. DAVIDSON. **Ozone Production in the Positive DC Corona Discharge: Model and Comparison to Experiments** *Plasma Chemistry and Plasma Processing 22 (2002), 495-522*

CHOW J.C., J.G. WATSON, E.M. FUJITA, Z. LU, D.R. LAWSON, L.L. ASHBAUGH. **Temporal and Spatial Variations of PM2.5 and PM10 Aerosol in the Southern California Air Quality Study** *Atmospheric Environment 28 (1994), 2061-2080*

CYRYS J., G. DIETRICH, W. KREYLING, T. TUCH, J. HEINRICH. **PM$_{2.5}$ Measurements in Ambient Aerosol: Comparison Between Harvard Impactor (HI) and the Tapered Element Oscillating Microbalance (TEOM) System** *The Science of the Total Environment 278 (2001), 191-197*

DANALATOS D., S. GLAVAS. **Gas Phase Nitric Acid, Ammonia and Related Particulate Matter at a Mediterranean Coastal Site, Patras, Greece** *Atmospheric Environment 33 (1999), 3417-3425*

DASIBI **Operating and Service Manual 1008 Ozone Analyzer** *Dasibi Environmental Corp. (1983) ; Glendale, CA, USA*

DIN EN 12341 STANDARD. **Air Quality – Determination of the PM10 Fraction of Suspended Particulate Matter – Reference Method and Field Procedure to Demonstrate Reference Equivalence of Measurement Methods; German Version EN12341 : 1998** *Beuth Verlag, Berlin, 1998*

DOCKERY D.W., C.A. POPE, X. XU, J.D. SPENGLER, J.H. WARE, M.E. FAY, B.G. FERRIS, F.E. SPEIZER. **An Association Between Air Pollution and Mortality in Six U.S. Cities** *The New England Journal of Medicine 329 (1993), 1753-1759*

FURUUCHI M., H. FISSAN, J. HORODECKI. **Evaporation Behavior of Volatile Particles on Fibrous Filter Flushed With Particle Free Air** *Powder Technology 118 (2001), 171-179*

GEBHART J. **Optical Direct-Reading Techniques: Light Intensity Systems** *In: Aerosol Measurement – Principles, Techniques, and Applications, K. Willeke and P.A. Baron (Eds.) Van Nostrand Reinhold, New York, 1993*

GRAEDEL T.E., P.J. CRUTZEN. **Atmosphäre im Wandel** *Spektrum Akademischer Verlag, Heidelberg, 1996*

GRIFFING G.W. **Ozone and Oxides of Nitrogen Production During Thunderstorms** *Journal of Geophysical Research 82 (1977), 943-950*

HASENPUSCH O. **Hochspannungstechnik** *Franzis Verlag, München, 1981*

HERING E., R. MARTIN, M. STOHRER **Physik für Ingenieure** *VDI Verlag, Düsseldorf, 1988*

HINDS W.C. **Aerosol Technology – Properties, Behavior, and Measurement of Airborne Particles** *John Wiley & Sons, New York, 1982*

HOBBS P.V., M.P. MCCORMICK. **Aerosols and Climate** *A. Deepak Publishing, Hampton, USA, 1988*

HORODECKI J. **Untersuchung der Probenahme von Testaerosolen mit hygroskopischen und verdampfbaren Salpartikeln mit Filtern in Abhängigkeit von thermodynamischen Bedingungen** *Dissertation at the Gerhard-Mercator-University, Duisburg, 2000 (available under: http://www.ub.uni-duisburg.de/diss/diss0018/)*

JOHN A.C. **Probenahme und chemische Analytik von korngrößenfraktionierten Immissions- und Emissionsaerosolen** *Dissertation at the Gerhard-Mercator-University, Duisburg, 2002 (available under"Chemie" in: http://www.ub.uni-duisburg.de/diss/elecdiss.htm)*

JOHN W. **The Characteristics of Environmental and Laboratory-Generated Aerosols** *In: Aerosol Measurement – Principles, Techniques, and Applications, K. Willeke and P.A. Baron (Eds.) Van Nostrand Reinhold, New York, 1993*

JORDAN F. **Untersuchungen zum Partikelabscheideverhalten submikroner Partikel in Faserfiltern im elektrischen Feld** *Dissertation at the Gerhard-Mercator-University, Duisburg, 2001 (available under: http://www.ub.uni-duisburg.de/diss/elecdiss.htm)*

KENNY L.C. **Investigation on the Effects of Loading on PM2.5 Selectors** *Report by the Health and Safety Laboratory for R&P, 1998 (available under: http://www.rpco.com/assets/lit/lit01/amb0000_00114_sccreport.pdf)*

KOUTRAKIS P., J.M. WOLFSON, A. BUNYAVIROCH, S.E. FROEHLICH, K. HIRANO, J.D. MULIK. **Measurement of Ambient Ozone Using a Nitrite-Coated Filter** *Analytical Chemsitry 65 (1993), 209-214*

KUHLBUSCH T.A.J., A.C. JOHN., H. FISSAN. **Korngrößenabhängige Untersuchungen von Schwebstaub und Inhaltsstoffen** *Final Report for „Ministerium für Umwelt, Raumordnung und Landwirtschaft, NRW", 2000 (available under: http://www.uni-duisburg.de/FB9/AMT/)*

KUHLBUSCH T.A.J., A.C. JOHN, H. FISSAN. **Diurnal Variations of Aerosol Characteristics at a Rural Measuring Site Close to the Ruhr-area, Germany** *Atmospheric Environment 35, Supplement No.1 (2001), S13-S21*

LIPFERT F.W. **Filter Artifacts Associated With Particulate Measurements – Recent Evidence and Effects on Statistical Relationships** *Atmospheric Environment 28 (1994), 3233-3249*

LOEB L.B. **Electrical Coronas. Their Basic Physical Mechanisms** *University of California Press, Berkeley, 1965*

MARPLE V.A., K.L. RUBOW, B.A. OLSON **Inertial, Gravitational, Centrifugal, and Thermal Collection Techniques** *In: Aerosol Measurement – Principles, Techniques, and Applications, K. Willeke and P.A. Baron (Eds.) Van Nostrand Reinhold, New York, 1993*

MARTINEZ P., D.K. BRANDVOLD. **Laboratory and Field Measurements of NO_x Produced from Corona Discharge** *Atmospheric Environment 30 (1996), 4177-4182*

MEHLMANN A., P. WARNECK. **Atmospheric Gaseous HNO_3, Particulate Nitrate, and Aerosol Size Distributions of Major Ionic Species at a Rural Site in Western Germany** *Atmospheric Environment 29 (1995), 2359-2373*

NASHIMOTO K. **The Effect of Electrode Materials on O_3 and NO_x Emissions by Corona Discharging** *Journal of Imaging Science 32 (1988), 205-210*

OHKUBO T., S. HAMASAKI, Y. NOMOTO, J-S. CHANG, T. ADACHI. **The Effect of Corona Wire Heating on the Downstream Ozone Concentration Profiles in an Air-Cleaning Wire-Duct Electrostatic Precipitator** *IEEE Transactions on Industry Applications 26 (1990), 542-549*

PANG Y., N.L. EATOUGH, , D.J. EATOUGH. **$PM_{2.5}$ Semivolatile Organic Material at Riverside, California: Implications for the $PM_{2.5}$ Federal Reference Method Sampler** *Aerosol Science and Technology 36: 277-288, 2002*

PATASHNICK H., E. RUPPRECHT. **Continuous PM10 Measurements Using the Tapered Element Oscillating Microbalance** *Journal of Air and Waste Management 41 (1991) 1079-1083*

PATASHNICK H., G. RUPPRECHT, J.L. AMBS, M.B. MEYER. **Development of a Reference Standard for Particulate Matter Mass in Ambient Air** *Aerosol Science and Technology 34 (2001), 42-45*

PATASHNICK ET AL., UNITED STATES PATENT. **Differential Particulate Mass Monitor With Intrinsic Correction for Volatilization Losses** *United States Patent No.: US 6,205,842 B1, Mar. 27, 2001*

REIST P.C. **Aerosol Science and Technology** *Mc Graw Hill, Inc., New York, 1993*

ROBINSON R.A., R.H. STOKES. **Electrolyte Solutions. The Measurement and Interpretation of Conductance, Chemical Potential and Diffusion in Solutions of Simple Electrolytes** *Butterworths, London, 1970*

ROSE H.E, A.J. WOOD. **An Introduction to Electrostatic Precipitation in Theory and Practice** *Constable, London, 1966*

RUPPRECHT & PATASHNICK. **Operating Manual – Sample Equilibration System With Relative Humidity Module** *Rupprecht & Patashnick Co. Inc. (2000); Albany, NY, USA*

SALTER L.F., B. PARSONS. **Field Trials of the TEOM® and Partisol for PM10 Monitoring in the St. Austell China Clay Area, Cornwall, UK** *Atmospheric Environment 33 (1999) 2111-2114*

SCHWARTZ J., D.W. DOCKERY, L.M. NEAS. **Is Mortality Associated Specifically with Fine Particles?** *Journal of Air & Waste Management Association 46 (1996), 927-939*

SICKLES J.E., L.L. HODSON, W.A. MCCLENNY, R.J. PAUR, T.G. ELLESTAD, J.D. ANLAUF, H.A. WIEBE, G.I. MACKAY, H.I. SCHIFF, D.K. BUBACZK. **Field Comparison of Methods for the Measurement of Gaseous and Particulate Contributors to Acidic Dry Deposition** *Atmospheric Environment 24 (1990), 155-165*

SINGER J.G. **Combustion – Fossil Power Systems** *Combustion Engineering, Inc., Windsor, USA, 1981*

SOUTAR A., M. WATT, J.W. CHERRIE, A. SEATON. **Comparison Between a Personal PM10 Sampling Head and the Tapered Element Oscillating Microbalance (TEOM) System** *Atmospheric Environment 33 (1999) 4373-4377*

THERMO INSTRUMENTS. **Bedienungsanleitung NO-NOx-NO2-Analysator** *Thermo Instruments GmbH (1995); Dortmund, Germany*

TOWNSEND J.S. **The Theory of Ionization of Gases by Collisions** *Constable, London, 1910*

TOWNSEND J.S. **Electricity in Gases** *Oxford University Press, New York, 1915*

TSAI C.J., S.N. PERNG. **Artifacts of Ionic Species for Hi-Vol PM10 and PM10 Dichotomous Samplers** *Atmospheric Environment 32 (1998), 1605-1613*

TSI INC. **Model 3936 SMPS (Scanning Mobility Particle Sizer) Instruction Manual Revision H** *St. Paul, MN, USA, 2003 (available under: www.tsi.com)*

U.S. ENVIRONMENTAL PROTECTION AGENCY (US EPA) **Ozone: Good up High, bad Nearby** *http://www.epa.gov/oar/oaqps/gooduphigh/ (1997)*

VAN OSDEL D.W. **Wind Tunnel Test Report No. 29a – Test of the Rupprecht and Patashnick PM10 Sampler Inlet at 2 and 24 km/h** *Report by Research Triangle Institute for R&P, 1991 (available under: http://www.rpco.com/assets/lit/lit00/amb1400_00024_inlettest.pdf)*

VAN VAECK L., K. VAN CAUWENBERGHE, J. JANSSENS. **The Gas-Particle Distribution of Organic Aerosol Constituents – Measurement of the Volatilization Artefact in Hi-Vol Cascade Impactor Sampling** *Atmospheric Environment 18 (1984), 417-430*

VEREIN DEUTSCHER INGENIEURE **VDI Wärmeatlas** *VDI Verlag, Düsseldorf, 1988*

VEREIN DEUTSCHER INGENIEURE **Particulate Matter Measurement. Generation of Latex Aerosols Using Nozzle Atomizers** *VDI Guideline VDI 3491, Part 3, 1980*

VEREIN DEUTSCHER INGENIEURE **Measurement of Particulate Matter – Manual Dust Measurement in Flowing Gases Gravimetric Determination of Dust Load Plane Filter Devices** *VDI Guideline VDI 2066, Part 7, 1993*

VEREWA MEß- UND REGELUNGSTECHNIK. GMBH **F-703 Immissions-Beta-Staubmeter (Information Brochure)** *Verewa Meß- und Regelungstechnik GmbH, Mülheim/Ruhr, 1994*

VINER A.S., P.A. LAWLESS, D.S. ENSOR, L.E. SPARKS. **Ozone Generation in DC-Energized Electrostatic Precipitators** *IEEE Transactions on Industry Applications 28 (1992), 504-512*

WHITE H.J. **Entstaubung industrieller Gase mit Elektrofiltern** *VEB Deutscher Verlag für Grundstoffindustrie, Leipzig, 1969*

WILLIAMS K., C. FAIRCHILD, J. JAKLEVIC. **Dynamic Mass Measurement Techniques** *In: Aerosol Measurement – Principles, Techniques, and Applications, K. Willeke and P.A. Baron (Eds.) Van Nostrand Reinhold, New York, 1993*

WILLIAMS M., P. BRUCKMANN. **A Report on Guidance to Member States on PM10 Monitoring and Intercomparisons with the Reference Method** *European Commission Report, 13. December 2002*

WINKLER P., C.E. JUNGE **Comments on „Anomalous Deliquescence of Sea Spray Aerosols"** *Journal of Applied Meteorology 10 (1970), 159-163*

WINKLER P. **The Growth of Atmospheric Aerosol Particles as a Function of the Relative Humidity – II. An Improved Concept of Mixed Nuclei** *Journal of Aerosol Science 4 (1973), 373-387*

WITZ S., R.W. EDEN, M.W. WADLEY, C. DUNWOODY, R.P. PAPA, K.J. TORRE. **Rapid Loss of Particulate Nitrate, Chloride and Ammonium on Quartz Fiber Filters During Storage** *Journal of Air & Waste Management Association 40 (1990), 53-61*

WOLFF I. **Maxwellsche Theorie** *Springer Verlag, Berlin, 1997*

ZHANG X., P.H. MCMURRY. **Theoretic Analysis of Evaporative Losses of Adsorbed and Absorbed Species During Atmospheric Aerosol Sampling** *Environmental Science and Technology 25 (1991), 456-459*

Appendix A

Derivation of the Electric Field Strength in the Charging Zone

In Chapter 4.2.1 it was shown that the electric field strength in the charging zone in presence of space charges can be described by means of the Bernoulli differential equation

$$\frac{d}{dr}\left(r \cdot E(r)\right) = \frac{I_i \cdot r}{2\pi \cdot \varepsilon_0 \cdot l_c \cdot Z_i} \cdot \frac{1}{r \cdot E(r)} \qquad \text{(Eq. A.1)}$$

In general, Bernoulli differential equations have the form (Bronstein, 1991)

$$y' = f(x)y + g(x)y^n \quad n \neq 1 \qquad \text{(Eq. A.2)}$$

By substituting

$$\bar{y} = y^{1-n} \quad n \neq 1 \qquad \text{(Eq. A.3)}$$

the Bernoulli differential equation in equation A.2 can be transferred into the linear differential equation

$$\bar{y}' = (1-n)f(x)\bar{y} + (1-n)g(x) \qquad \text{(Eq. A.4)}$$

With the substitution $y \overset{!}{=} r \cdot E(r)$, the differential equation in equation A.1 can be written as

$$y' = \frac{I_i \cdot r}{2\pi \cdot \varepsilon_0 \cdot l_c \cdot Z_i} \cdot y^{-1} \qquad \text{(Eq. A.5)}$$

Therefore $n = -1$, $f(r) = 0$ and $g(r) = \dfrac{I_i \cdot r}{2\pi \cdot \varepsilon_0 \cdot l_c \cdot Z_i}$. Equation A.3, along with n = -1 yields to

$$\bar{y} = y^2 \qquad \text{(Eq. A.6)}$$

and along with equation A.4

$$\bar{y}' = \frac{I_i \cdot r}{\pi \cdot \varepsilon_0 \cdot l_c \cdot Z_i} \qquad \text{(Eq. A.7)}$$

Integration of equation A.7 yields to $\bar{y}$:

$$\bar{y} = \int \frac{I_i \cdot r}{\pi \cdot \varepsilon_0 \cdot l_c \cdot Z_i} dr = \frac{1}{2}\frac{I_i \cdot r^2}{\pi \cdot \varepsilon_0 \cdot l_c \cdot Z_i} + \zeta \qquad \text{(Eq. A.8)}$$

Backsubstitution of $r \cdot E(r) = y = \sqrt{\bar{y}}$ leads to the final results as given in equation 4.2.10:

$$r \cdot E(r) = \sqrt{\frac{1}{2}\frac{I_i \cdot r^2}{\pi \cdot \varepsilon_0 \cdot l_c \cdot Z_i} + \zeta}$$

and therefore

$$E(r) = \sqrt{\frac{I_i}{2\pi \cdot \varepsilon_0 \cdot l_c \cdot Z_i} + \frac{\zeta}{r^2}}$$
(Eq. A.9)

Appendix B

1st Prototype of the GPP

B.1 Design of the 1st Prototype

The first prototype was designed for a total flow rate of 8.33 l/min, which internally is split into a 3 l/min sample flow a 5.33 l/min excess air flow. It was meant to be used in a differential TEOM® set up, utilizing two TEOM® mass monitors, but only one common size selective inlet, designed for 16.67 l/min. The total flow rate is split into two halves. Each of them passes a GPP upstream of each TEOM® sensor unit (figure B.1). The total flow rate through the 1st prototype therefore was 8.33 l/min, which internally is split into a sample flow of 3 l/min and an excess air flow of 5.33 l/min. The radius of the inner electrode is 2 cm, the radius of the outer electrode is 5 cm. The resulting geometric and electric parameters are given in table B.1.

The values in table B.1 were derived as explained in chapter 3 for the 2nd prototype.

Table B.1:   Parameters of 1st Prototype

Deflection voltage	U_i [V]	1000
Voltage of Flow Splitter	U_f [V]	455.9
Radius of Flow Splitter	r_f [cm]	3.32
Length of Fractionation Zone	l_f [cm]	10
Length of Charging Zone	l_c [cm]	5

Figure B.1:   Double TEOM® Set Up for the Differential TEOM®
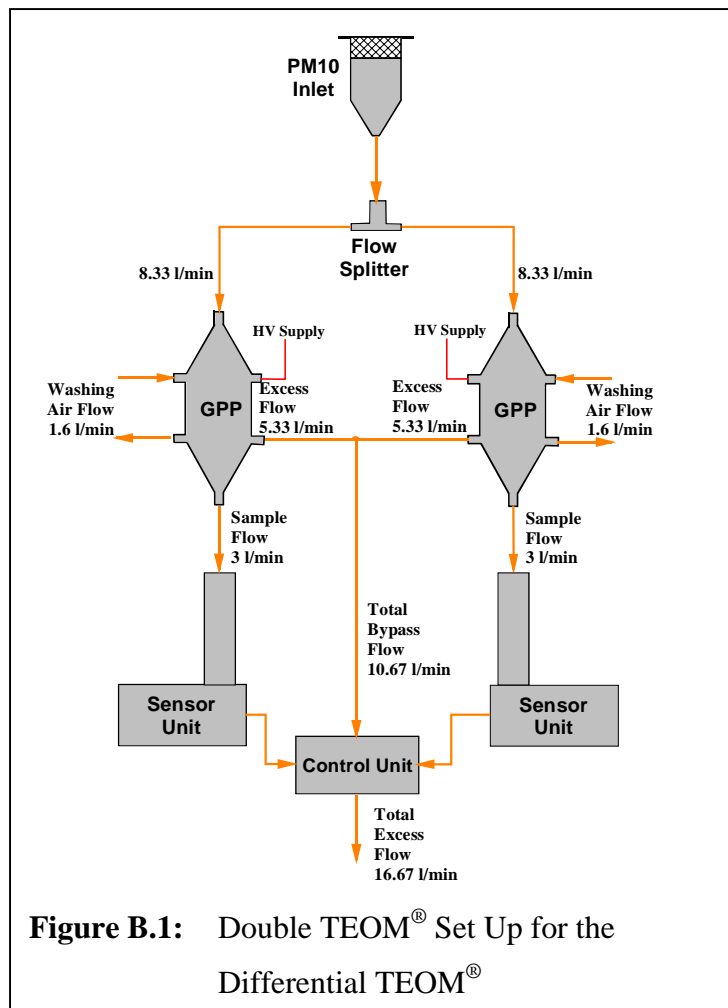
B.2 Results

The first prototype was only initially tested for separation efficiency and response time as during the course of the experiments the requirement for the development of a GPP for the differential TEOM® with single sensor set up arose. Later, the first prototype was used for the long term investigations on the life cycle of the corona wire as described in chapter 5.5.

The first experiments were performed to determine the general separation behaviour (efficiency and dynamic response) of the GPP in dependence of the corona and the deflection voltage. To determine the precipitation behaviour, a set up according to figure B.2 was used.

The different flow rates have regularly been adjusted by means of a bubble meter and maintained by mass flow controllers. Inline Filters were used to protect the flow controllers.

The voltages are applied by means of two high voltage supplies. The corona voltage U_{cor} may be adjusted by computer or manually. The supply of the inner electrode U_i and the flow split U_f is realized by a single high voltage supply only and a voltage resistor.

To measure the particle concentration in the sample flow, a condensation particle counter (TSI, CPC Model 3022) was used. Since the inlet flow of the CPC is either 0.3 l/min or 1.5 l/min and the sample flow from the GPP is 3 l/min, a flow splitter downstream of the GPP was employed. A three way valve between the flow split and the CPC allowed to measure the

Figure B.2:   Experimental set up
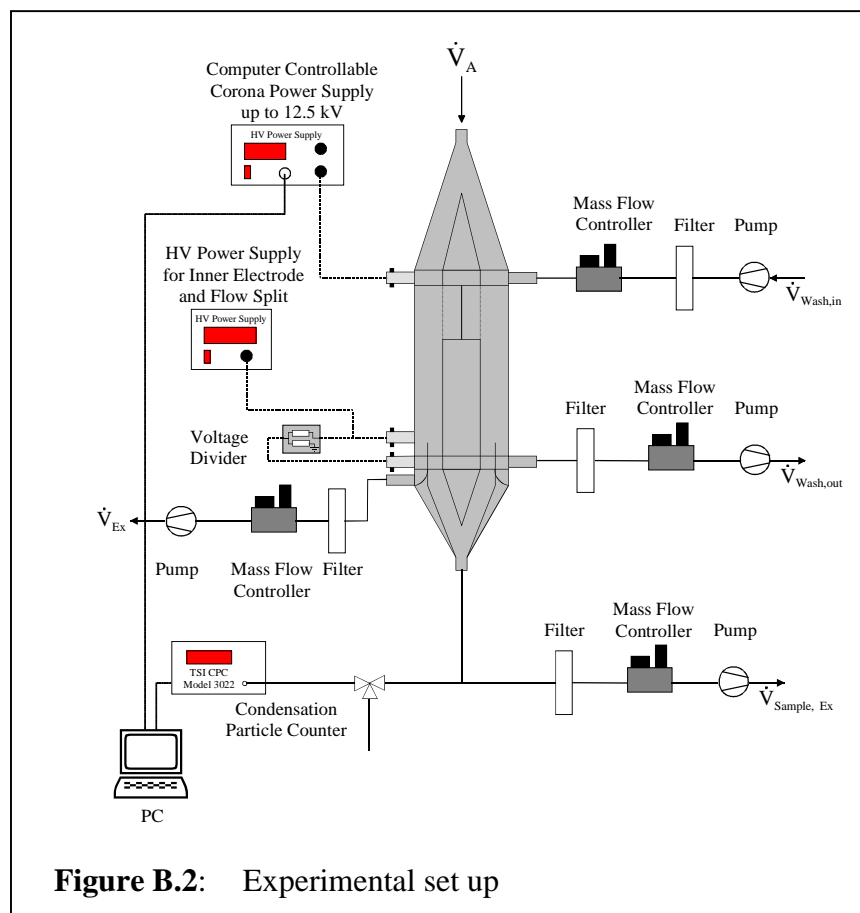
total particle concentration in ambient air. A computer software is used to read the concentrations from the CPC and to adjust the corona voltage. The software allows to apply default voltage levels and download the concentration in dedicated time steps.

A CPC was used, because it is the most sensitive instrument, so that even small changes in concentrations can be detected.

General Measurements of Separation Behaviour

The measurements were performed with ambient laboratory air. The air showed fairly constant total particle number concentrations.

Standard values that were used for the measurements, i.e.:

$$\dot{V}_{Sample} = 3\,\frac{l}{min}$$

$$\dot{V}_{Ex} = 5.33\,\frac{l}{min}$$

$$\dot{V}_{wash} = 1.6\,\frac{l}{min}$$

$$U_i = 1000\,V$$

$$U_f = 446\,V$$

The corona voltage was varied to obtain the dependence of the separation on the corona discharge voltage.

Prior to the separation behaviour measurements, the particle losses inside the GPP have been
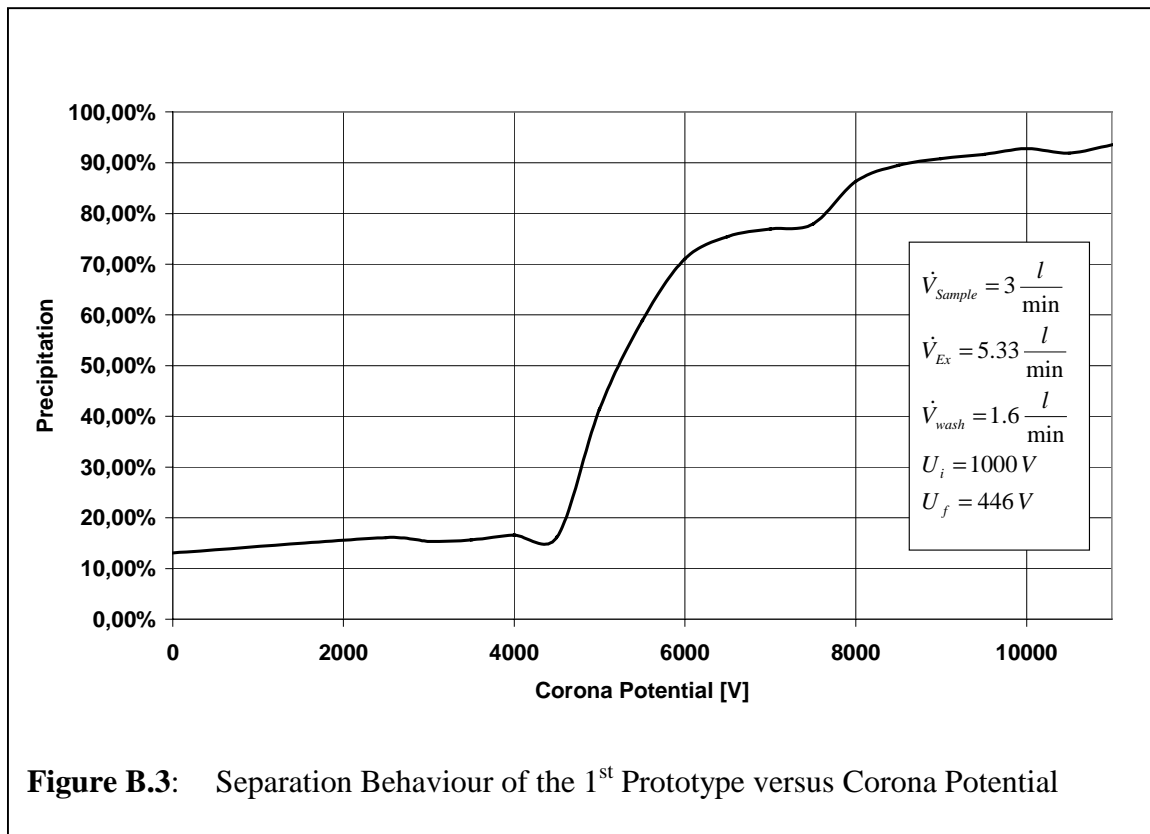

Figure B.3: Separation Behaviour of the 1st Prototype versus Corona Potential

studied. Particle losses, with no voltages applied, have shown to be low ($\approx$ 1%), if the default flow rates are kept.

For the first measurements of the separation behaviour, the standard voltages and flow rates were adjusted and the precipitation efficiency was calculated from the measured ambient and sample concentrations. The result is shown in figure B.3.

The corona potential was varied from 0 V to 11 kV. The corona potential is the voltage of the corona wire against ground potential. The actual corona voltage is the difference between the corona wire potential and the grid potential U_i, i.e. in this case, the corona voltage varied from - 1 kV to + 10 kV.

The disruptive discharge voltage is around 5 kV corona potential, i.e. at around 4 kV corona voltage. The voltage of the inner electrode was maintained at 1000 V, even if no corona voltage was applied. This results in the approximately 15% precipitation at voltages, lower than the disruptive discharge voltage, due to naturally charged particles in the air.

The maximum separation efficiency was approximately 93% for corona potential higher than 10 kV.

The next series of measurements were performed to determine a possible influence of the washing air on the precipitation efficiency. The result is shown in figure B.4.

As can be seen from the graph, no significant change of the separation behaviour occurs due to the use of the wash flow. Differences of precipitation for corona voltages, lower than the
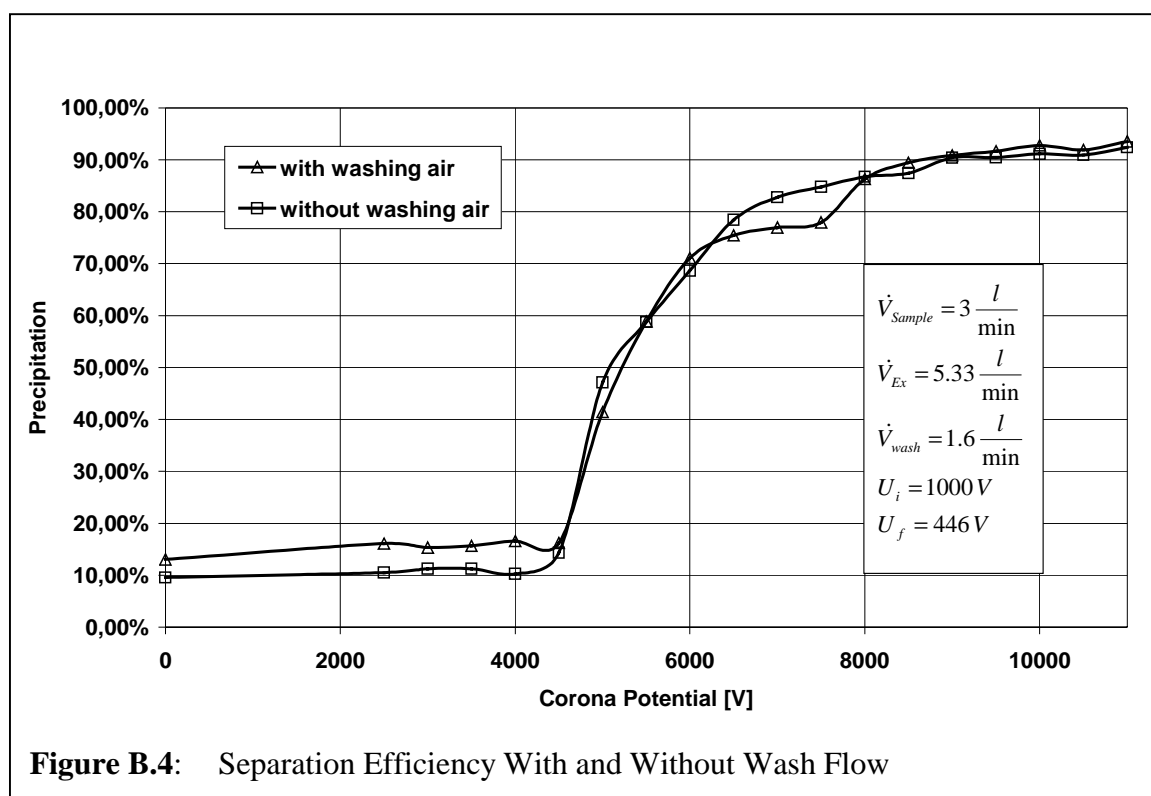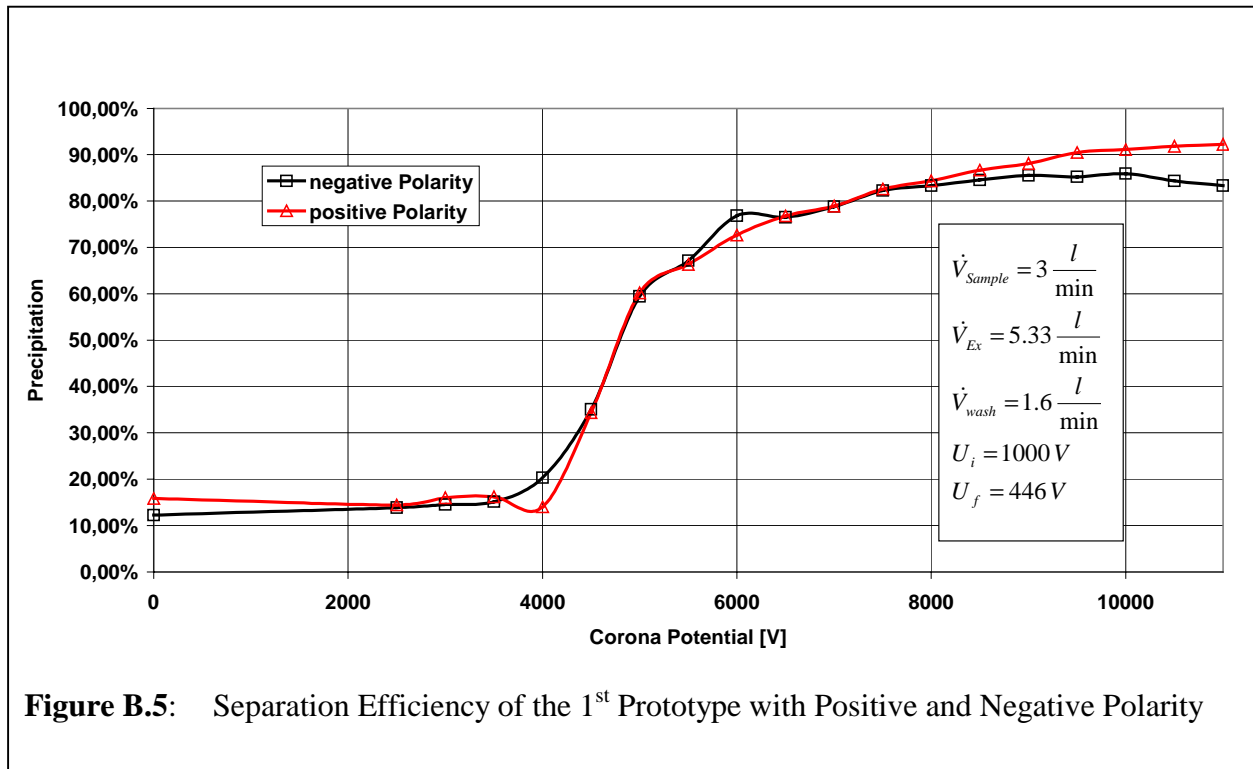

Figure B.4: Separation Efficiency With and Without Wash Flow

Figure B.5:   Separation Efficiency of the 1st Prototype with Positive and Negative Polarity

disruptive voltage may be due to different number size distribution and charge distributions, since the measurements were performed on different days.

The next step was to investigate, whether the polarity of the corona potential has a significant influence on the efficiency. Generally, a positive corona potential was chosen to be used with the GPP, because it is supposed to produce a lower amount of ozone and oxides of nitrogen. The result is shown in figure B.5. No significant differences were observed up to a corona potential of approximately 8 kV. For potentials higher than 8 kV, the efficiency was higher for positive than for negative polarity.

In the next step, the voltage of the inner electrode was increased to 1500 V, the voltage of the flow split was increased by the same factor to 669 V. A comparison of the precipitation behaviour for 1000 V and 1500 V is shown in figure B.6. Higher voltages could not be realized, since the resistors, used in the voltage divider are not suited for high voltages. For a voltage of 1500 V, the result shows a significantly increased efficiency. The maximum separation efficiency is around 96.5 %. The rest up to 100% may be due uncharged nanoparticles. This result has led to the conclusion to design the second prototype for a higher deflection voltage.
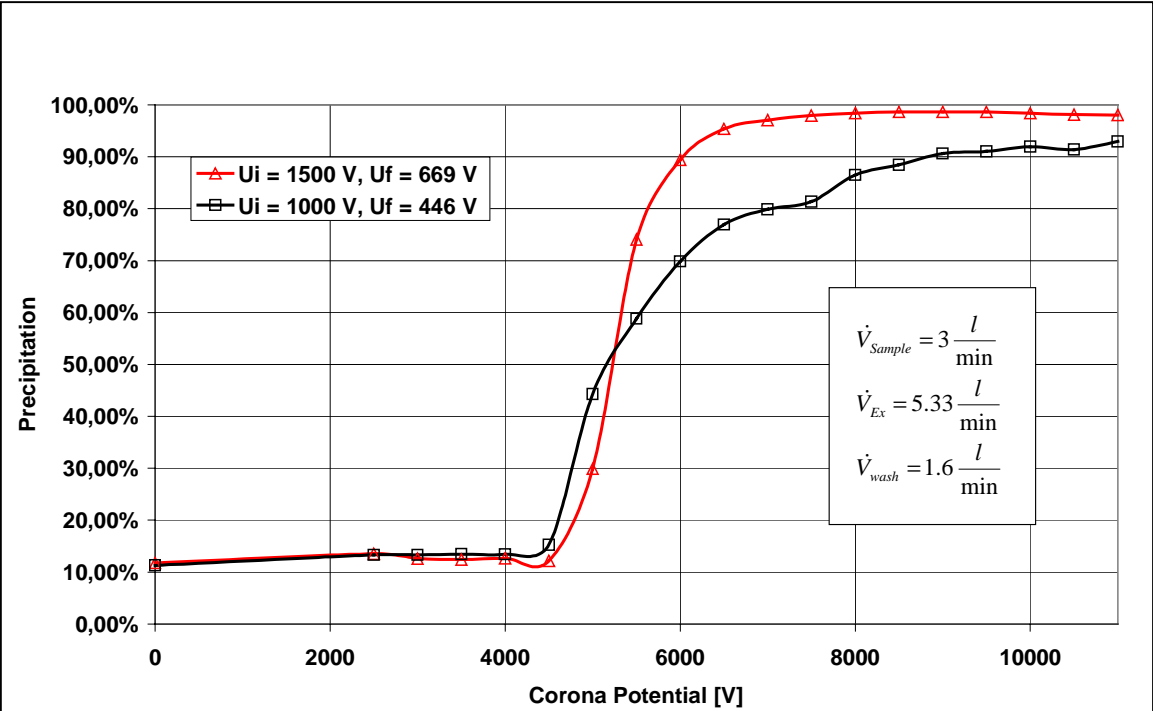
Figure B.6: Separation Efficiency with $U_i = 1000$ V and $U_i = 1500$ V

Appendix C

Ion Concentrations in the Charging Zone

This appendix is to demonstrate that the ion concentration in the charging zone is almost independent of the applied deflection voltage U_i under otherwise identical conditions. The corona voltage used in the graphs is, as described in chapter 5, the difference of the electric potentials applied to the corona wire and the grid electrode. The ion concentrations were calculated as spatial distributions as described in chapter 4.2. For better clarity of the graphs, the concentrations are potted as spatial averages for each voltage setting in figures C.1 and C.2.

Figure C.1 shows the average ion concentration n_i as a function of the corona voltage U_{cor} for deflection voltages of 2 kV and 3 kV with 25 µm gold wire. No substantial difference in the ion concentration can be observed for the two deflection voltages. Even though the ion current is higher for a higher deflection voltage (see figure 5.1.2) this does not affect the ion concentration. The reason why the ratio of the ion concentrations does not comply with the ratio of the ion currents is the difference in the applied electric field. Since the ion

Figure C.1:   Average Ion Concentration in the Charging Zone Versus Corona Voltage for Deflection Voltages of 2 kV and 3 kV for 25 µm Gold Wire
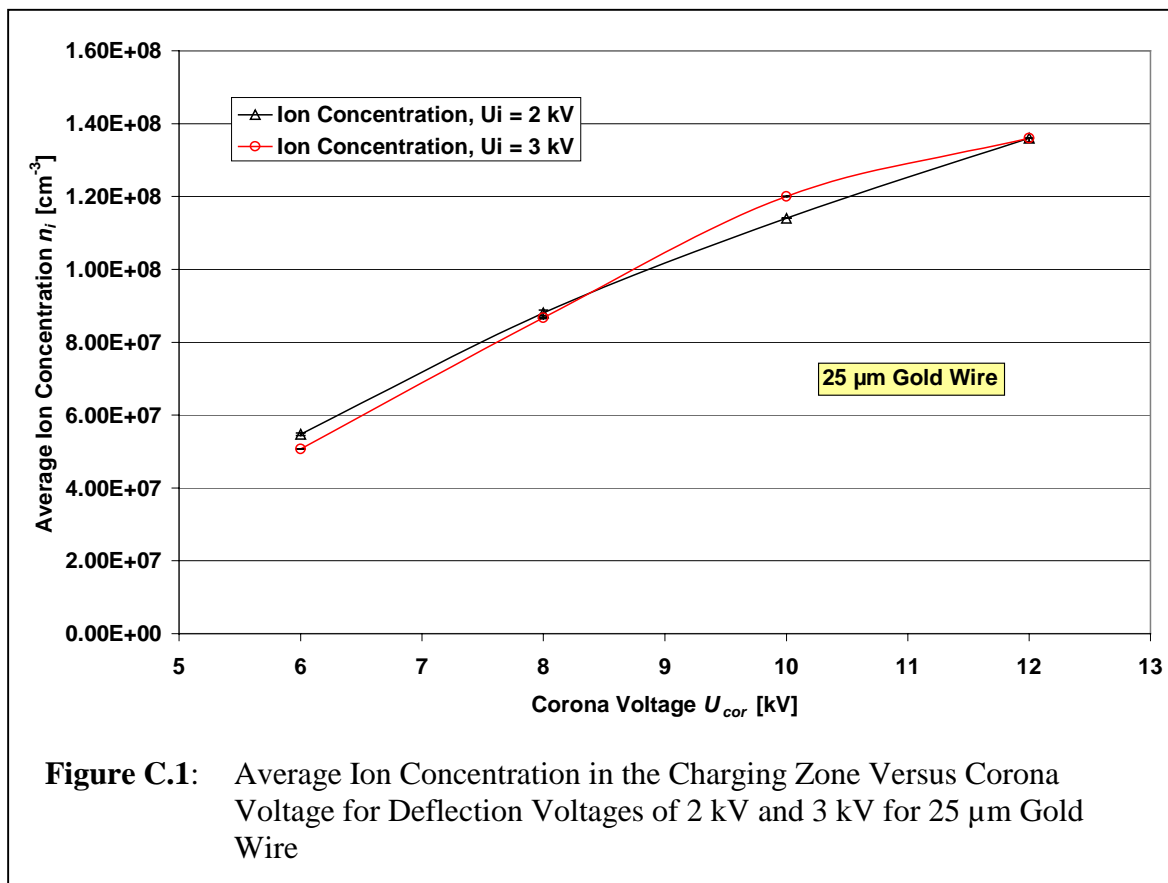
concentration is proportional to the ion current and reciprocally proportional to the electric field strength $E(r)$, the effect of the higher electric field strength almost compensates the effect of the higher ion current. Figure C.1 also shows that even for a corona voltage of 6 kV, the average ion concentration is above 10^7 cm^{-3}, which is supposed to be sufficient for efficient particle charging (Hinds, 1982). However, the investigations on the separation efficiency of the GPP have shown that a corona voltage above 10 kV, i.e. an ion concentration above 10^8 cm^{-3} is required for nearly 100% efficiency.

Figure C.2 shows the effect of different wire diameters on the ion concentration for silver wire. Wire diameters of 25 µm, 50 µm and 100 µm have been investigated. Since previous results (figure C.1) have shown that the deflection voltage only has a minor impact on the ion concentration, only the ion concentrations with a deflection voltage of 2 kV are presented in the graph. It can be seen that the wire diameter strongly influences the ion concentration in the charging zone. As can be seen from the graph, the ion concentration decreases with increasing wire diameter. This was expected, as the formation of ions near a corona wire increases with the electric field strength near the wire surface, which increases with decreasing wire diameter. With respect to figure 5.4.4, which shows the impact of the wire diameter on the gas formation as function of the corona voltage, figure C.2 gives rise to the recommendation of a 25 µm wire to be used in the GPP, concerning the highest possible charging efficiency, i.e. ion concentration, in combination with the lowest possible gas formation.
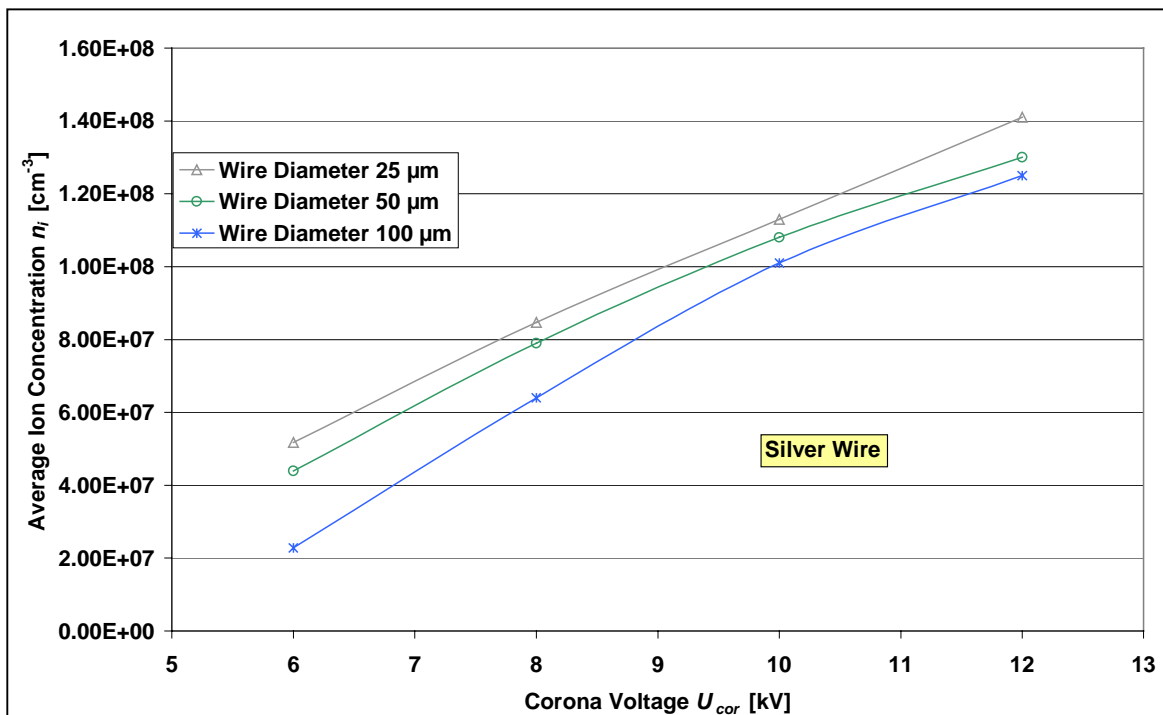
Figure C.2:   Average Ion Concentration in the Charging Zone Versus Corona Voltage for Deflection Voltages of 2 kV With Silver Wire Diameters of 25 µm, 50 µm and 100 µm

Appendix D

Designs for Different Applications

This chapter is to present two different designs for the GPP. The two designs comprise an application with the differential TEOM, where a diffusion dryer is situated upstream of the GPP and an application as a pre-filter for a set of gas analysers as used in air quality measurement stations.

The flow rate of the GPP for the differential TEOM application is lower than in the currently realized version. Only the lower flower rate allows a high ratio of purge flow to sample flow in the dryer and therefore a sufficient drying efficiency. A positive side-effect of the lower flow is that the GPP will be smaller. Negative side effect is that an additional external flow splitter is required for splitting the total flow of 16.67 l/min into the GPP-flow and the excess flow.

The sample flow rate for the gas analyser application was chosen to be 50 l/min. This allows to supply the manifold for several gas analysers in a measuring station by one GPP. The higher flow rate causes an increased size of the GPP.

Design of the GPP for Employment in the Differential TEOM Downstream of Dryer

The total flow rate of the GPP was decreased compared to the version of the GPP as presented in this work (2nd prototype), in order to achieve a high purge gas to sample gas flow in the dryer, when operated upstream of the GPP. The excess flow from the GPP was decreased from 13.67 l/min to 3 l/min, i.e. the total flow of the GPP is 6 l/min. This means that the total flow of 16.67 l/min coming from the inlet has to be split into a 6 l/min flow to the dryer/GPP and an additional 10.67 l/min flow before the dryer/GPP (see figure D.1).

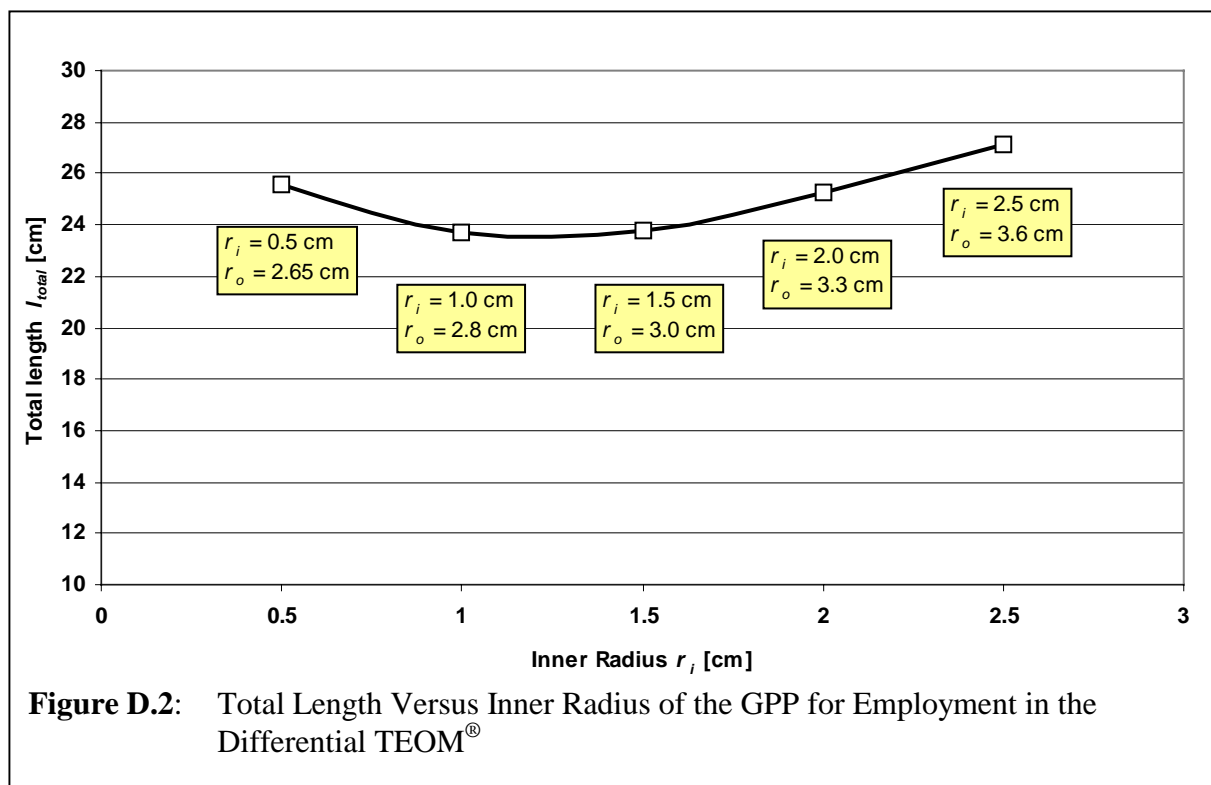For the derivation of the data for the GPP, a deflection voltage of $U_i = 2000$ V has been considered. The opening angle of inlet and outlet are $\alpha = 15°$. Table D.1 summarizes the results for different inner radii. Figure D.2 shows the total length versus the radius of the inner electrode. The total length as given in the table and the

Figure D.1: Set Up With GPP Downstream of Dryer
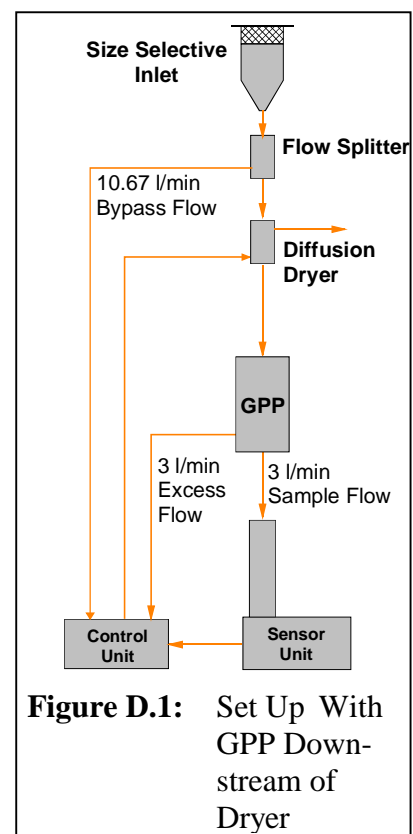
graph only comprise the theoretically calculated data as shown in the table, but no security margin, flanges or inlet/outlet connections.

Table D.1:   Dimensions of the GPP for Differential TEOM

r_i [cm]	r_o [cm]	r_f [cm]	V_{wash} [l/min]	l_{in} [cm]	l_{out} [cm]	l_c [cm]	l_f [cm]	l_{total} [cm]
0.5	2.65	1.69	0.22	7.52	3.94	4.7	9.08	25.54
1	2.8	1.969	0.88	8.08	4.98	4.7	5.60	23.66
1.5	3	2.291	2.00	8.83	6.18	4.7	3.77	23.78
2	3.3	2.676	3.48	9.95	7.62	4.7	2.73	25.29
2.5	3.6	3.067	5.59	11.07	9.08	4.7	1.99	27.13

Figure D.2:   Total Length Versus Inner Radius of the GPP for Employment in the
                    Differential TEOM®

As can be seen from the table and the graph, the minimal total length is for an inner radius of 1.0 cm (l_{total} = 23.66 cm), although the total length for an inner radius of 1.5 cm is approximately the same (l_{total} = 23.78 cm). The suggestion is to realize the version with an inner radius of 1.5 cm, as here firstly a higher corona voltage can be applied before electrical breakdown of the gas occurs and secondly the standoffs to stabilize the grid electrode in the charging zone can be manufactured more rigidly.

The Reynolds number is 289, which is far below the critical value of 2300.

In the case of an inner radius of 1.5 cm, the maximum electric field strength in the fractionation zone is 1.33 kV/cm at the surface of the inner electrode, which is far below the critical field strength in dry air of 30 kV/cm. Since in humid atmospheres, the electrical breakthrough field strength increases, an electrical breakthrough in the fractionation zone can be excluded. A higher deflection voltage could be chosen as well. In that case, the corona voltage would need to be increased and the risk of a flashover at the surface of an insulator between the potential of the inner electrode and ground level would be higher.

For the final design, two flanges of 1.5 cm each should be considered (see 2nd prototype). The upper flange should carry the supply tube for the wash flow and the voltage connector for the corona voltage. The lower flange

Figure D.3:   Comparison of 6 l/min GPP with 2nd Prototype

should carry the excess tube for the wash flow and the voltage connector for the deflection voltage. At both, inlet and outlet, a 3 cm long tube connection should be considered, ½" in diameter to easily connect the standard TEOM tubes to the GPP. Further the theoretical lengths of the charging zone and fractionation zone should slightly be increased in order to be on the safe side. The suggested length of the charger is 5 cm and of the fractionation zone also 5 cm. The dimensions of the newly designed GPP for 6 l/min are sketched in scale in comparison to the 2nd prototype in figure D.3.

Design of the GPP for Gas Analyser Application

For the gas analyser application, the GPP was designed such that it is able to supply clean air to several gas analysers simultaneously, i.e. the sample flow rate is 50 l/min. The required dimensions were calculated for different inner radii with excess flow rates of 10 l/min,
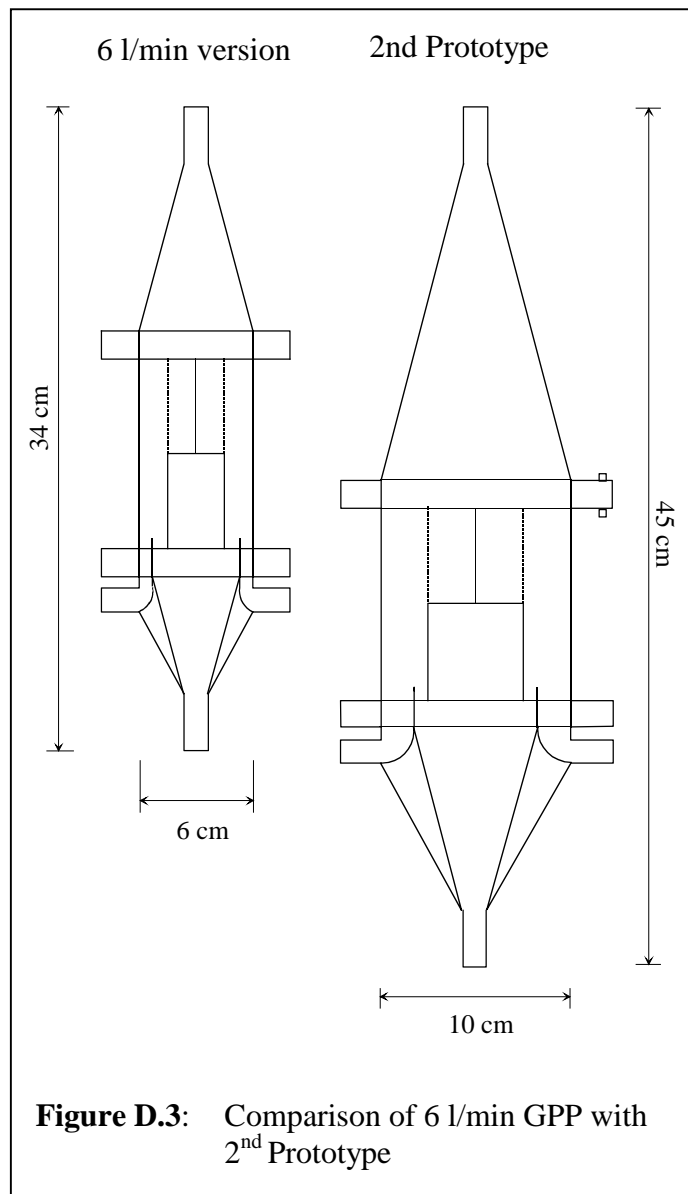
25 l/min and 50 l/min. As the dimensions become much larger than in the 2nd prototype and the 6 l/min version, a deflection voltage of 10,000 V was considered, as it is supposed to be securely manageable. For the gas analyser GPP a larger opening angle of 30° was chosen for inlet and outlet, as here the GPP is intended to operate permanently, i.e. particle losses in the inlet do not affect the effectiveness of the GPP. The resulting geometric data are shown in tables D.2 through D.4.

Table D.2:   Dimensions of Gas Analyser GPP with 10 l/min Excess Flow

r_i [cm]	r_o [cm]	r_f [cm]	V_{wash} [l/min]	l_{in} [cm]	l_{out} [cm]	l_c [cm]	l_f [cm]	l_{total} [cm]
2.5	8.59	7.192	5.55	13.78	11.36	4.7	22.4	52.23
3	8.75	7.415	7.99	14.06	11.74	4.7	19.4	49.92
3.5	8.93	7.656	10.89	14.37	12.16	4.7	17.0	48.22
4	9.14	7.922	14.21	14.73	12.62	4.7	15.0	47.04
4.5	9.37	8.207	17.99	15.13	13.12	4.7	13.3	46.25
5	9.62	8.508	22.21	15.56	13.64	4.7	11.9	45.77
5.5	9.89	8.826	26.86	16.03	14.19	4.7	10.6	45.56
6	10.17	9.153	32.03	16.52	14.75	4.7	9.6	45.54
6.5	10.48	9.501	37.56	17.04	15.36	4.7	8.7	45.76
7	10.79	9.856	43.56	17.59	15.97	4.7	7.8	46.11
7.5	11.12	10.224	50.01	18.17	16.61	4.7	7.1	46.62
8	11.47	10.491	56.90	18.76	17.07	4.7	7.7	48.24
8.5	11.82	10.875	64.24	19.37	17.74	4.7	7.1	48.89

Table D.3:   Dimensions of Gas Analyser GPP with 25 l/min Excess Flow

r_i [cm]	r_o [cm]	r_f [cm]	V_{wash} [l/min]	l_{in} [cm]	l_{out} [cm]	l_c [cm]	l_f [cm]	l_{total} [cm]
2.5	9.52	7.093	5.56	15.39	11.19	4.7	24.3	55.53
3	9.66	7.334	8.01	15.63	11.60	4.7	21.2	53.15
3.5	9.83	7.599	10.89	15.93	12.06	4.7	18.7	51.42
4	10.02	7.88	14.22	16.26	12.55	4.7	16.7	50.16
4.5	10.23	8.178	17.99	16.62	13.06	4.7	14.9	49.28
5	10.46	8.491	22.21	17.02	13.61	4.7	13.4	48.71
5.5	10.71	8.819	26.86	17.45	14.18	4.7	12.1	48.41
6	10.97	9.156	32.01	17.90	14.76	4.7	10.9	48.31
6.5	11.25	9.508	37.58	18.39	15.37	4.7	10.0	48.41
7	11.55	9.874	43.54	18.91	16.00	4.7	9.1	48.69
7.5	11.86	10.248	49.98	19.44	16.65	4.7	8.3	49.11
8	12.18	10.629	56.90	20.00	17.31	4.7	7.6	49.63
8.5	12.51	11.017	64.32	20.57	17.98	4.7	7.0	50.26

Table D.4: Dimensions of Gas Analyser GPP with 50 l/min Excess Flow

| r_i [cm]	r_o [cm]	r_f [cm]	V_{wash} [l/min]	l_{in} [cm]	l_{out} [cm]	l_c [cm]	l_f [cm]	l_{total} [cm]
2.5	10.9	7.117	5.55	17.78	11.23	4.7	26.7	60.42
3	11.02	7.377	8.00	17.99	11.68	4.7	23.6	57.97
3.5	11.17	7.658	10.89	18.25	12.16	4.7	21.1	56.16
4	11.33	7.949	14.24	18.52	12.67	4.7	18.9	54.78
4.5	11.52	8.261	18.01	18.85	13.21	4.7	17.1	53.82
5	11.73	8.568	22.20	19.22	13.74	4.7	15.5	53.13
5.5	11.95	8.92	26.88	19.60	14.35	4.7	14.1	52.73
6	12.19	9.268	31.97	20.01	14.95	4.7	12.9	52.53
6.5	12.44	9.623	37.55	20.45	15.57	4.7	11.8	52.49
7	12.71	9.991	43.54	20.91	16.21	4.7	10.8	52.64
7.5	12.99	10.366	50.00	21.40	16.85	4.7	10.0	52.92
8	13.28	10.748	56.96	21.90	17.52	4.7	9.2	53.31
8.5	13.59	11.142	64.26	22.44	18.20	4.7	8.5	53.85
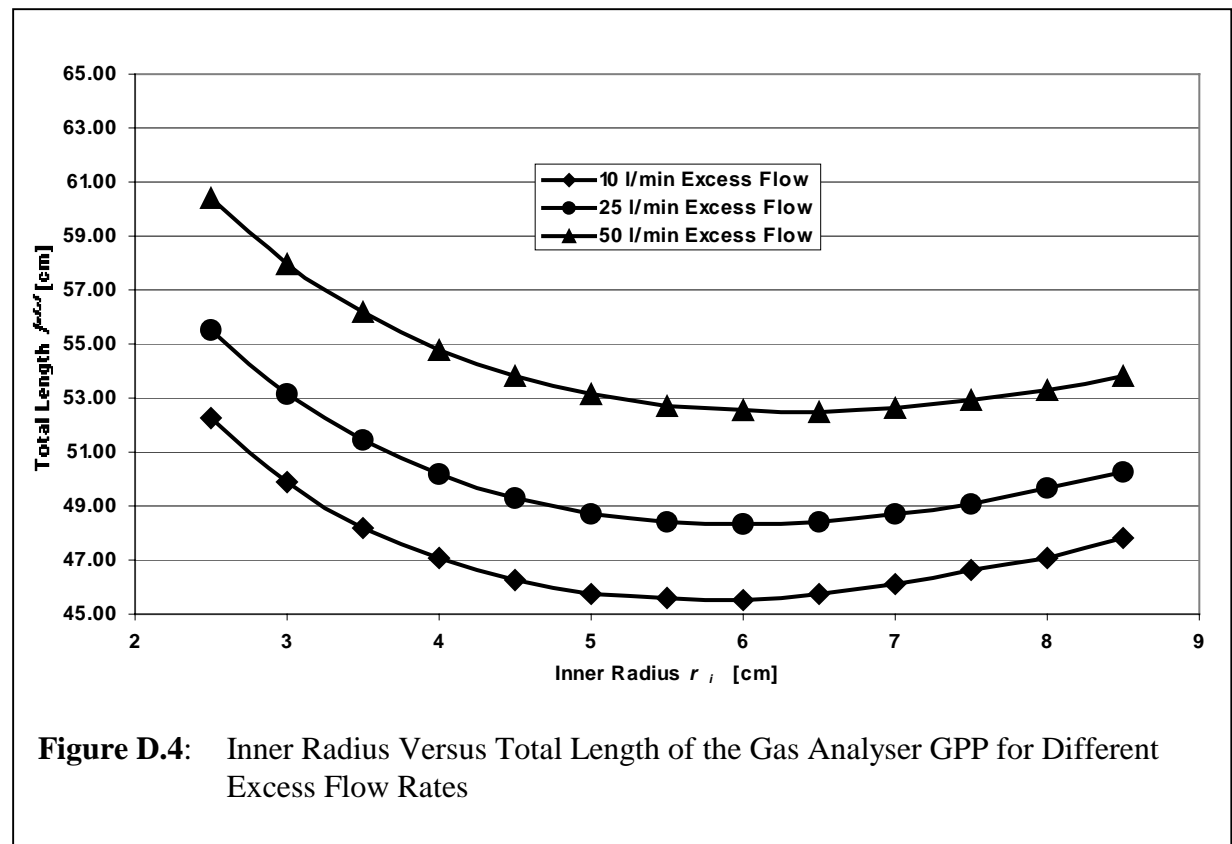
Figure D.4: Inner Radius Versus Total Length of the Gas Analyser GPP for Different Excess Flow Rates

Considering the excess flow, two opposing effects have to be taken into account. The larger the excess flow, the higher the number and mass of particles that are borne out of the GPP with the excess flow and therefore do not deposit on the outer wall. This increases the time of

the maintenance/cleaning intervals. On the other hand, the size and cost of the GPP and the required pump is increased. As the soiling inside the GPP is expected not to be substantially higehr if a 10 l/min excess flow is used instead of 25 l/min or 50 l/min, the use of 10 l/min excess flow along with 50 l/min sample flow is suggested. As can be seen from figure D.4, the total length reaches a minimum for an inner radius of $r_i = 6$ cm. In that case, the outer radius is $r_o = 10.17$ cm. In order to obtain even values for the inner and outer radius, the calculations have been repeated for an inner radius of 6 cm and outer radius of 10 cm. This causes the

Figure D.5:   Comparison of Gas Analyser GPP with 2nd Prototype
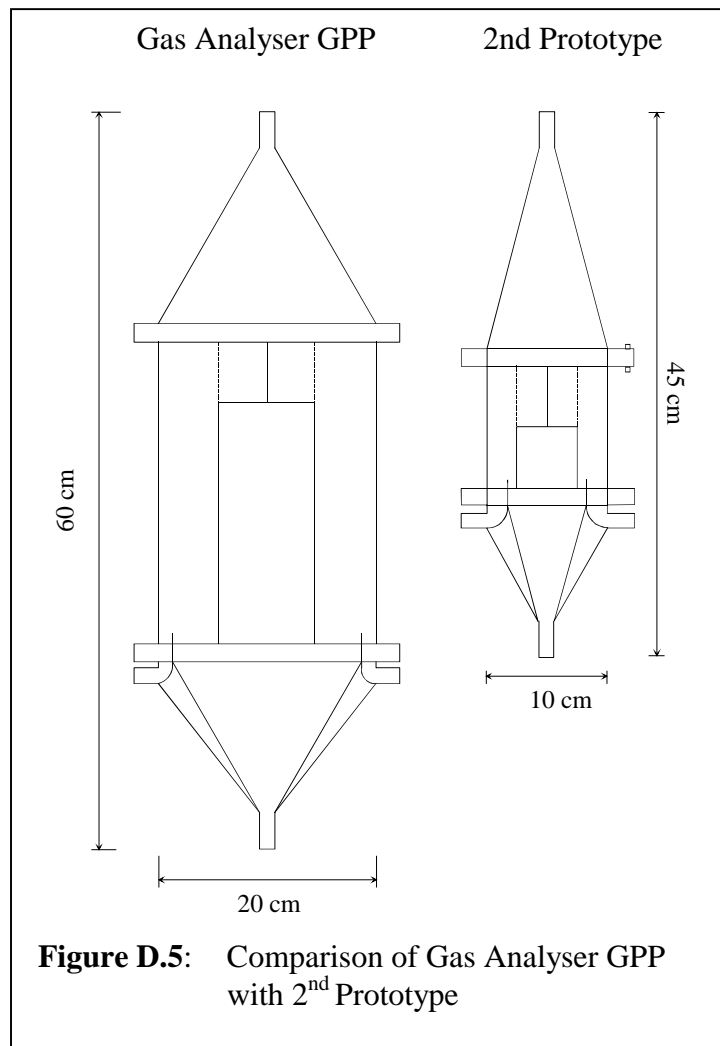
average velocity in the GPP to increase from 4.7 cm/s to 4.97 cm/s, which should not affect the effectiveness of the GPP. The Reynolds number in that version is 812 and therefore far below the critical value of 2300. The resulting values are summarized in table D.5.

Table D.5:   Gas Analyser GPP with 10 l/min Excess flow

r_i [cm]	r_o [cm]	r_f [cm]	V_{wash} [l/min]	l_{in} [cm]	l_{out} [cm]	l_c [cm]	l_f [cm]	l_{total} [cm]
6	10	9.023	33.75	16.22	14.53	5	9.267	45.017

In the case of an inner radius of 6 cm, the maximum electric field strength in the fractionation zone is 3,26 kV/cm at the surface of the inner electrode, which is far below the critical field strength in dry air of 30 kV/cm.

For the final design, two flanges of 1.5 cm each should be considered (see 2nd prototype). The upper one should carry the supply tube for the wash flow and the voltage connector for the corona voltage. The lower flange should carry the excess tube for the wash flow and the voltage connector for the deflection voltage. At both, inlet and outlet, a 3 cm long tube connection should be considered, ½" in diameter to easily connect the standard TEOM tubes to the GPP. Further slightly increased lengths of the charging zone and fractionation zone in order are recommended to be on the safe side. A length of the charger of 5 cm and a length of

the fractionation zone of 12 cm are suggested. The dimensions of the newly designed GPP for 6 l/min are sketched in scale in comparison to the 2nd prototype in figure D.5.

Two Remarks should be made, concerning the gas analyser GPP:

1) Due to the higher flow rate, the GPP becomes much bigger and therefore heavier than the 2nd Prototype. In order to reduce the weight, other material than stainless steel should be used for this version. Aluminium with a suitable coating could possibly be the choice.

2) Ambient air contains some particles, larger than 10 µm. For these particles, the sedimentation velocity cannot be neglected. The model for the GPP, as described in chapter 4, is only accurate for particles, where the sedimentation velocity v_{TS} can be neglected. The terminal settling velocity can be expressed as

$$v_{TS} = \frac{\rho_p \cdot d_p^2 \cdot g}{18 \cdot \eta} \qquad\qquad \text{(eq. D.1)}$$

Figure D.6:   Terminal Settling Velocity versus Particle Diameter
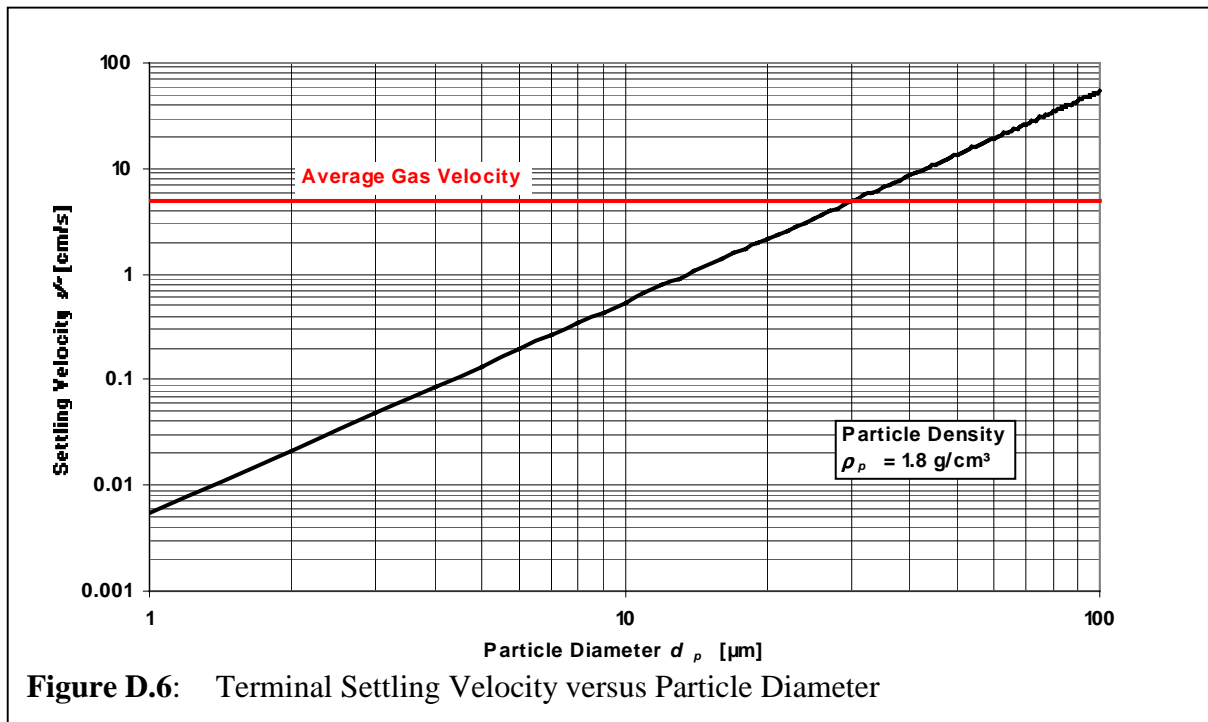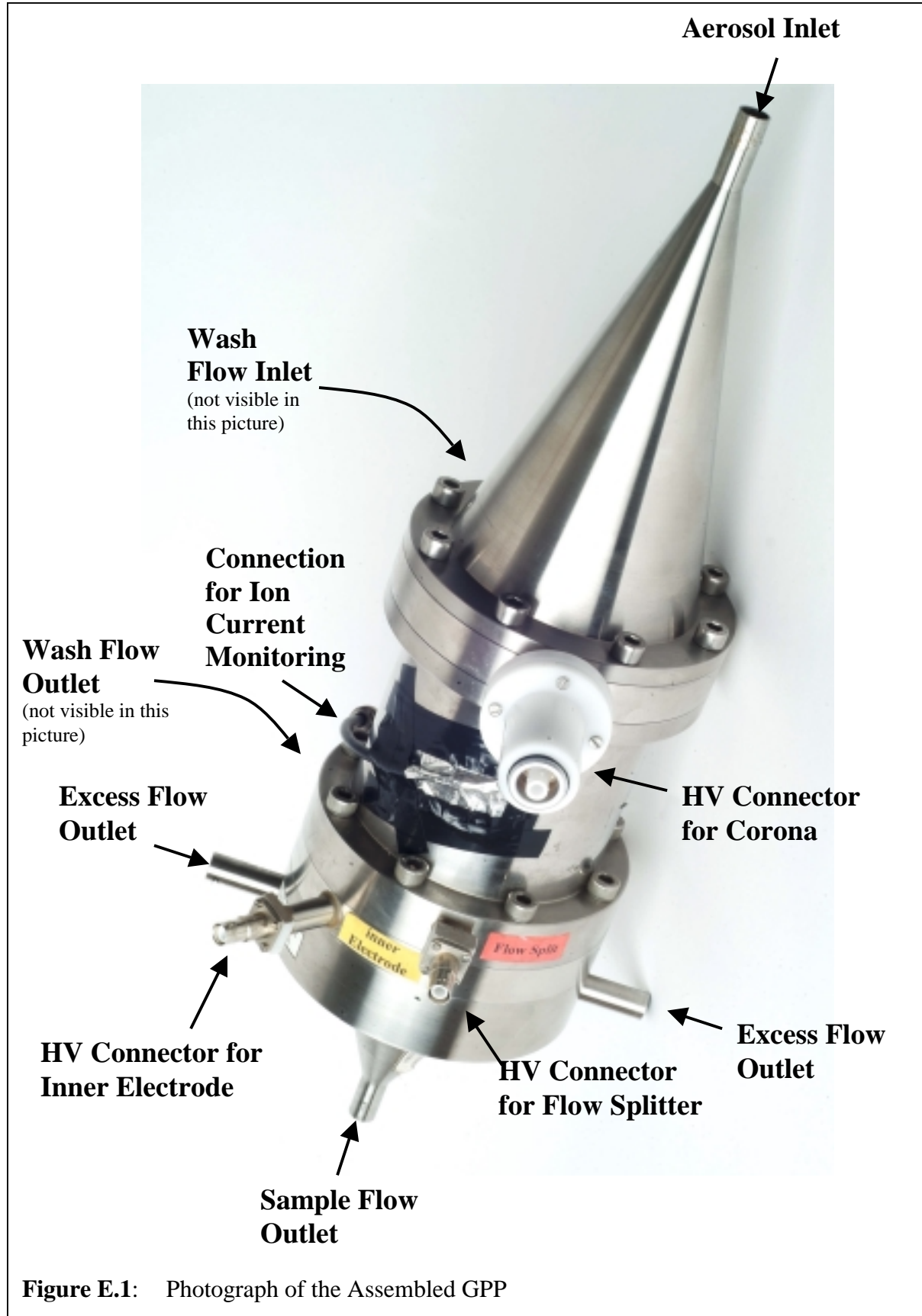
where g is the acceleration of gravity and η the viscosity of the air. In figure D.6, the terminal settling velocity is plotted against the particle diameter for a particle density of 1.8 g/cm³.
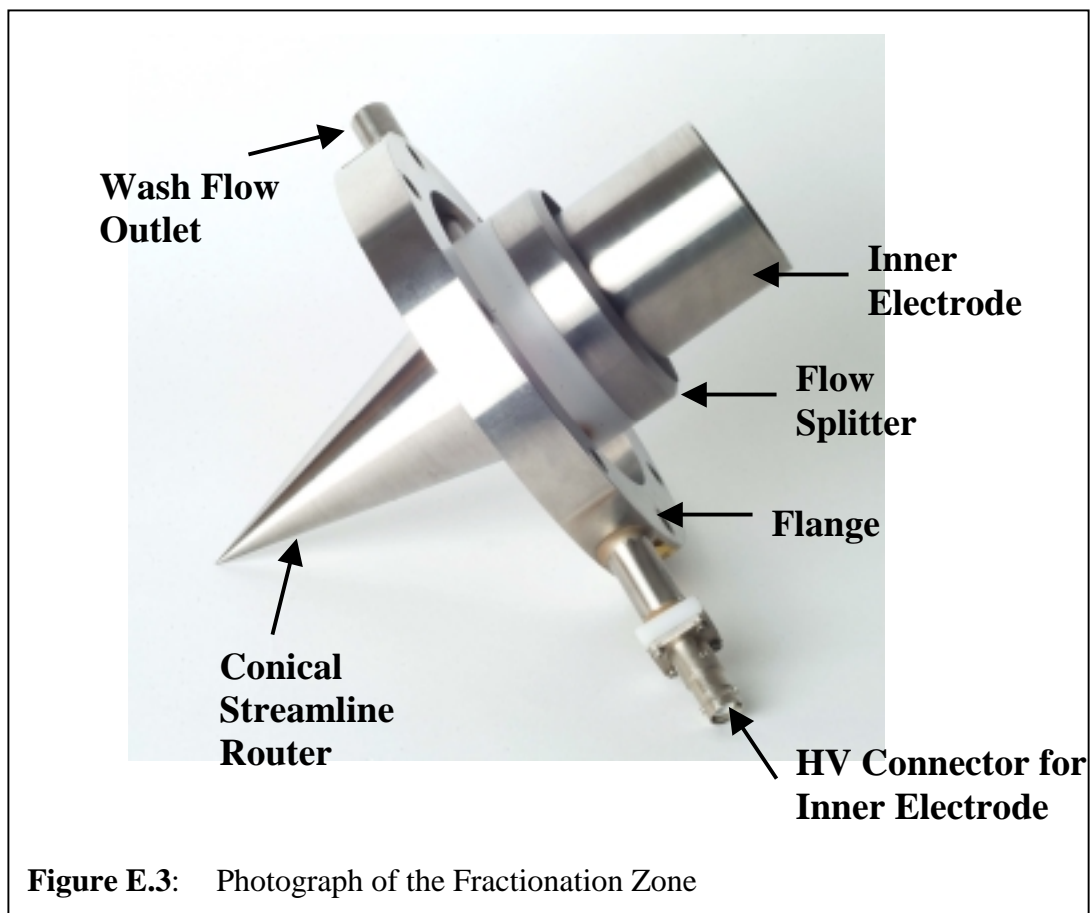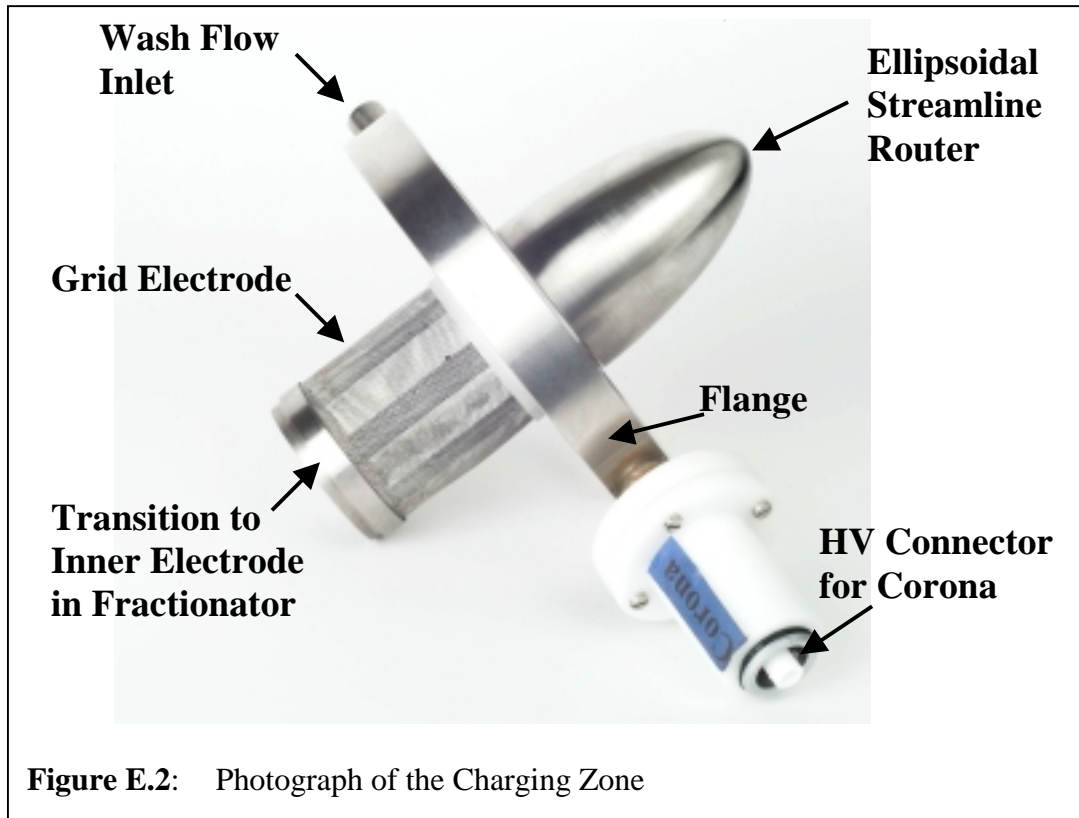
As can be seen from the graph, the terminal velocity of a 10 µm particle is 0.3 cm/s and can therefore be neglected compared to the gas velocity of 5 cm/s, whereas for a particle size of approximately 40 µm, the settling velocity is equal to the gas velocity and therefore cannot be neglected.

For the operation of the gas analyser GPP, the use of a PM10 inlet may therefore be recommendable.
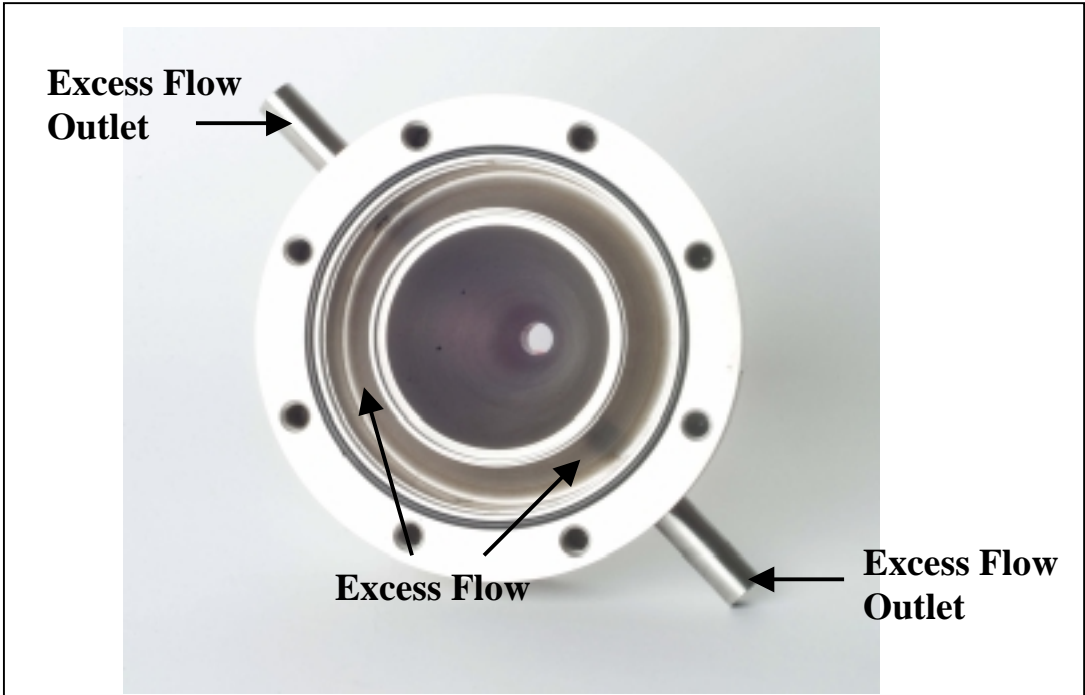
Appendix E

Photographs of the GPP

Figure E.1: Photograph of the Assembled GPP

Figure E.2:   Photograph of the Charging Zone

Figure E.3:   Photograph of the Fractionation Zone

Excess Flow Outlet

Excess Flow

Excess Flow Outlet

Figure E.4:   Photograph of the Sample and Excess Outlet

Outlet   **Fractionation Zone**   **Outer Electrode**   **Charging Zone**   **Inlet**
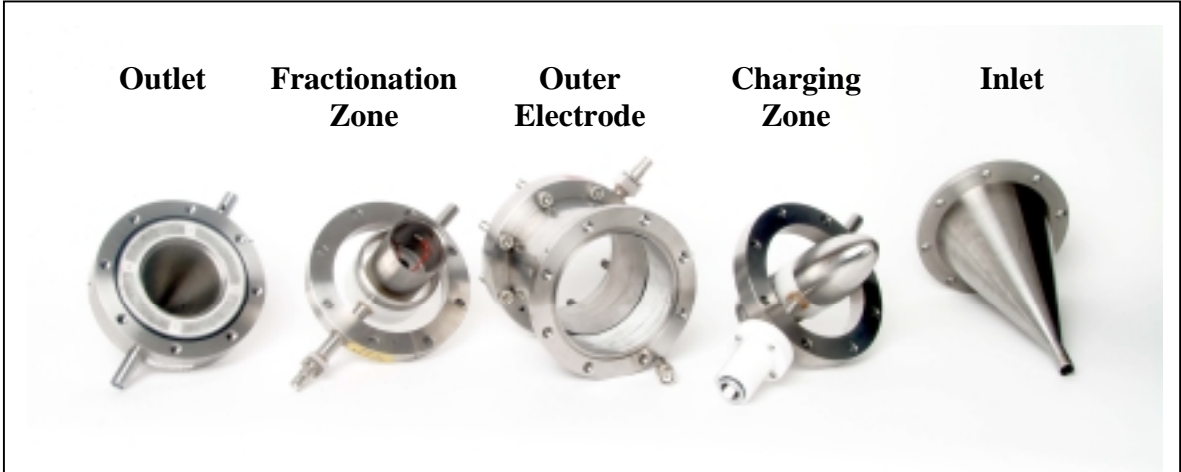
Figure E.5:   Photograph of the Disassembled GPP

Curriculum Vitae

Personal

Name:	Christof Asbach
Address:	Brücktorstr. 78 46047 Oberhausen
Email:	c.asbach@uni-duisburg.de
Date and Place of Birth:	June 29th 1974, Essen
Marital status:	not married, no children
Nationality:	Germany

Professional Experience

Since 11/2000:	Research Assistant Process and Aerosol Measurement Technology University Duisburg-Essen, Campus Duisburg Prof. Dr.-Ing. H. Fissan
07/2000 – 10/2000:	Project Engineer Babcock Prozessautomation Oberhausen

Education

05/2000:	Graduation as Diplom Ingenieur
10/1995 – 05/2000:	Studies of electrical engineering at the Gerhard-Mercator-University Duisburg
Area of specification:	Electrical power engineering

Internships

09/1998-10/1998:	Balcke Dürr & Wabag Technologies in Chennai, India (5 weeks)
03/1995-06/1995:	Elsag Bailey in Burlington, Ontario, Canada (3 months)
01/1995-02/1995:	Riley Stoker in Erie, Pennsylvania, USA (2 months)

Civilian Service, School Education

10/1993 – 12/1994:	Civilian Service (instead of military service)
06/1993:	Graduation from „Gymnasium" Specifications: Physics, Mathematics
08/1987 – 06/1993:	Bertha-von-Suttner Gymnasium, Oberhausen
08/1984 – 07/1987:	Werner Heisenberg Gymnasium, Gladbeck